From quantum transport in semiconducting nanowires to hybrid

semiconducting-superconducting qubits

by

Azarin Zarassi

B.Sc, University of Tehran, 2012

M.Sc, University of Pittsburgh, 2014

Submitted to the Graduate Faculty of

the Kenneth P. Dietrich School of Arts and Sciences in partial fulfillment

of the requirements for the degree of

Doctor of Philosophy

University of Pittsburgh

2020

UNIVERSITY OF PITTSBURGH

KENNETH P. DIETRICH SCHOOL OF ARTS AND SCIENCES

This dissertation was presented

by

Azarin Zarassi

It was defended on

August 6, 2020

and approved by

Sergey M. Frolov, Dept. of Physics and Astronomy, University of Pittsburgh

Michael J. Hatridge, Dept. of Physics and Astronomy, University of Pittsburgh

David Pekker, Dept. of Physics and Astronomy, University of Pittsburgh

Rachel Bezanson, Dept. of Physics and Astronomy, University of Pittsburgh

Paul W. Leu, Dept of Industrial Engineering, University of Pittsburgh

From quantum transport in semiconducting nanowires to hybrid semiconducting-superconducting qubits

Azarin Zarassi, PhD

University of Pittsburgh, 2020

A practical quantum computer demands a physical quantum bit (qubit) that is scalable, has a well-defined initial state, and brings together coherence with reliable control and read-out. A compelling idea is to put together a locally protected Majorana qubit with a superconducting qubit. The superconducting qubit is used to read out the Majorana states while the Majorana qubit may act as a quantum memory. This thesis presents a series of studies on quantum transport in semiconducting nanowires coupled to superconductors to investigate various platforms for realizing Majorana. These studies are followed by microwave measurements on superconducting circuits compatible with semiconducting-superconducting heterostructures.

We first evaluate the potential of Ge/Si core/shell nanowires by achieving induced superconductivity as well as estimating spin-orbit coupling. Next we explore the transport mediated by Andreev bound states formed in InSb nanowire quantum. A subgap negative differential conductance is investigated together with the coalescing Andreev resonances at zero bias relevant for the correct interpretation of Majorana experiments done on the same structures. We conclude our studies of semiconducting nanowires by exploring tunnel junctions in Sn-InSb nanowires that are prepared by in-situ shadowing using nearby nanowires and flakes. Tin shells are found to induce a hard superconducting gap persisting up to high magnetic fields. We observe the two-electron charging effect from a small superconducting island of Sn-InSb. This effect is attributed to charge parity stability, which makes this nanowire system an intriguing candidate for superconducting and topological quantum circuits.

These Sn-InSb junctions are then used as the nonlinear element in a transmon qubit design where we observe a dispersive coupling between this nanowire Josephson junction and a superconducting resonator. We also present our progress towards building a magnetic field

resilient superconducting circuit that allows integration with semiconducting and topological structures.

In the last chapter, InSb semiconducting nanowires are utilized as shadow masks prior to superconductor deposition on an InAs quantum well. We study Josephson current properties in Josephson junctions made from these nanowire shadows. Our results point to highly transparent junctions that can be developed further for hybrid superconductor-semiconductor qubit systems.

List of tables

List of figures

Preface

This dissertation is the culmination of everything I have done thus far in my life and would not have been possible without the many people I have encountered throughout this journey. I am forever grateful to my incredible advisor Sergey Frolov for his wit, contagious enthusiasm, endless patience and the ability to explain everything over and over without the slightest sign of annoyance on his face. I shall always be indebted to him for his enlightenment, supervision, and the best espresso one could find in any department[1]. I would also like to thank all members of my dissertation committee: Michael Hatridge, David Pekker, Brian D'Urso, Paul Leu, Arthur Kosowsky, and Rachel Bezanson for their insightful comments and guidance.

Conducting any part of my research would not have been possible without a teamwork and I am not a lone worker by any means. I have been so lucky to be able to work with great people from all around the world. I am thankful to my lab mates and friends at Pitt: Zhaoen Su, Dharmraj Kotekar, Jun Chen, Jen-Feng Hsu, Jens Schwenderling, Lucas Jarjat, Vince van de Sande, Hao Wu, Po Zhang, Peng Yu, Amrita Purkayastha, Bomin Zhang, Maksim Gomanko, Yifan Jiang and Tzu-Chiao Chien. I am also thankful to all the great staff of the nano fabrication facility: Esta Abelev, Susheng Tan, Matthew France, Mike McDonald, and again Jun Chen. Thank you to all the amazing and cool guys in our machine shop: Tom Gasmire, Jeff Sicher, Jeff Tomaszewski, Shawn Artman, Bill Strang. I wish to thank my wonderful mentors, colleagues, and friends from Grenoble: Silvano De Franceschi, Moïra Hocevar, and Eduardo Lee. Also, thank you to our amazing collaborators: Palmstrøm group from UCSB and Bakkers' group from Eindhoven. Special thanks to Leyla Hirschfeld for being a second mother to me and for her continuous follow-ups, making sure I submit this very dissertation on time.

Beyond all the great people I had the privilege to work with, I am blessed to be surrounded by many amazing friends throughout my thirty something years of life. They have always been by my side, whether close or from afar, offering their support and creating

---

[1]https://espressospin.org/2019/04/01/university-of-pittsburgh-physics-ranked-1-in-the-world/

meaningful moments that continue to bring joy into my life. Thank you all so very much.

Lastly, my most sincere gratitude is for my parents, Mehri and Abbas, my brother, Arash, and my sister-in-law, Forough. My eyes are full of tears writing these words and I believe that says it all about how grateful I am for their enduring support. I have always felt privileged for how they all brought me up. This dissertation is for you.

1.0   Introduction

• **Why do we care about hybrids of semiconductors and superconductors**?

Bringing semiconducting nanostructures and superconductors together leads to novel phenomena in mesoscopic physics with an ultimate goal of fault-tolerant quantum computation [1, 2, 3, 4, 5, 6]. Semiconductors can maintain their properties such as tunable carrier densities, long mean free paths, spin-orbit and Zeeman couplings while inheriting superconducting properties when proximitized to superconductors. The interplay between these properties can lead to rich and exotic physical phenomena like the formation of Majorana fermions in these condensed matter systems. In this thesis we study quantum transport in several nanostructure semiconducting systems in combination with superconductors, and evaluate their potential for future quantum computation.

The invention of the transistor at Bell labs [7] was a historical moment that enabled the exploitation of semiconductors in modern computing devices. Band structure and electronic properties of semiconductors can be engineered by intentional introduction of impurities (doping), stacking different materials on top of one another and creating heterostructures, or by means of gating. Moreover, technological advancement facilitates the miniaturization of semiconducting structures. As the size of semiconducting devices shrinks, the interactions between electrons and quantum effects at mesoscopic scale become important. For example, if the size of a transistor is reduced to nanoscale, conductance can be turned on and off periodically as the result of the Coulomb interaction between electrons and charge quantization. Such device is called a single-electron transistor [8]. In 1985, Richard Feynman stated "it seems that the laws of physics present no barriers to reducing the size of computers until bits are the size of atoms and quantum behavior holds dominant sway." This can be envisioned as encoding information in any two-level quantum system. Examples of such systems are right and left circularly polarized states of the photon, spin up and down of electrons, or two stable electronic states of trapped ions. Each of these two-level systems is called a quantum bit or, for short, qubit. In 1998, Loss and DiVincenzo proposed to use Zeeman-split single electron spin states confided in semiconducting quantum dots as qubits

and perform quantum gate operations in coupled neighboring dots [9]. The first example of such a qubit readout in single quantum dots[1] was achieved by spin-to-charge conversion followed by single-shot measurements of charge [10]. Single spin readout was followed by coherent control and manipulation of single- and two-electron spin states in double quantum dots [11, 12]. In two-electron double quantum dots, single and triplet spin states can be introduced as qubit states. The initialization and readout of these qubit states rely on Pauli spin blockade [13]: Transport of electrons between dots can be blocked by spin selection rules. For instance if each dot has one electron and they form a triplet state ((1,1)-triplet), the transport to (0,2)-singlet state will be prohibited. Moreover, Pauli spin blockade can provide information about spin mixing and relaxation mechanisms [14, 15]. For example, in the presence of a finite magnetic field, spin-orbit interaction can result in lifting of the spin blockade as it couples singlet and triplet spin states. This mechanism can be used to quantify the strength of spin-orbit coupling in a semiconductor. A strong spin-orbit interaction facilitates coherent control over single spins via an oscillating electric field generated by a local gate [16]. This quality provides a means to study the potential of a semiconducting material for qubits residing in quantum dots. Moreover, as we mention below, strong spin-orbit interaction is also one of the main ingredients for realizing Majorana modes in semiconducting nanowires-superconductor hybrids. Later in the thesis we focus on the Pauli spin blockade in double quantum dots defined in Ge/Si core/shell nanowires and estimate spin-orbit coupling in this system.

Similarly, superconductors have been one of the pillars of technological advancement since their discovery in 1911 by H. Kamerlingh Onnes. Below a certain temperature some metals lose their electrical resistivity and go through a superconducting phase transition. In 1957, Bardeen, Cooper and Schrieffer introduced the microscopic theory of superconductivity (BCS theory) [17]. In their model, below a critical temperature T_c, electrons with opposite momentum and spin can bind together and form so-called Cooper pairs. These paired electrons form a condensate which displays a gapped spectrum pinned to the Fermi level. This superconducting gap at zero temperature is related to the critical temperature, $\Delta = 1.76 k_B T_c$

---

[1]Quantum dots in semiconductors are structures that confine electrons or holes in three dimensions and make their quantum mechanical energy levels observable. Quantum dots are also referred to as artificial atoms for their quantized energy levels.

and vanishes at the transition temperature. A superconductor can support a dissipation-less current, also known as a supercurrent. Supercurrent vanishes in a bulk superconductor but can flow between two superconducting banks that are separated by a non-superconducting material (a weak link). This phenomenon, predicted by Brian Josephson in 1962, is conveniently called the Josephson effect and the physical structure that exhibits it is called a Josephson junction [18]. The transport across a Josephson junction is mediated by Andreev reflection at the interface of the superconductor and normal region [19]. Andreev reflection at each interface converts pairs of quasiparticles from the weak link with energy less than Δ to Cooper pairs in the superconductor [20]. Effectively, we can say a pair of correlated electrons (Cooper pair with charge $2e$) is transferred from one superconductor to the other, creating a supercurrent flow across the junction. Andreev reflection will be covered in more detail in the next chapter.

The first semiconductors used as weak links were thinned silicon wafers in 1974 [21]. In semiconductors, the electron density can be controlled by electrostatic gating. Consequently, the Josephson supercurrent can be controlled by a gate bias voltage in semiconducting weak links. Ten years later the gate tunability was demonstrated in p-type single crystal Si [22] and in the inversion layer on a p-type InAs [23]. In 1997, evidence of a proximity induced gap in the electron system in the inversion layer of InAs in contact with niobium superconductor was established [24]. Efforts have also been taken to improve inversion layers as well as growing heterostructured materials for buried quantum wells in planar structures, thus allowing more sophisticated device structures [25, 26, 27]. However, interface transparency seemed to be a persistent limiting issue [28, 29]. An alternative platform for hybrids of superconductor and semiconductors are semiconducting one-dimensional nanowires. Their confined structure and large surface-to-volume ratio may comparatively ease down inducing superconductivity [30]. Moreover, the ability to synthesize nanowires with tunable chemical composition, size, and morphology allows for wide variety of nanosystems ranging from photonics and electronics to biological sensors [31, 32]. In 2005, proximity induced superconductivity was achieved in n-type InAs semiconducting nanowire weak links [33] and enabled the study of supercurrent coupled with Coulomb blockade in quantum dots [34]. In such systems the magnitude of the supercurrent is controllable by gate electrodes, exhibiting a combination

of/competition between superconducting and semiconducting properties, namely Coulomb interaction, Zeeman effect and spin-orbit coupling [35, 34, 36, 37, 38]. In this thesis we investigate induced superconductivity in Josephson junctions and quantum dots defined in Ge/Si core/shell and InSb nanowires in proximity to superconductors such as NbTiN, Al and Sn. Hybrids of quantum dots coupled to superconductors further provide a platform for studying the physics of Andreev bound states - subgap quasiparticle excitations resulting from successive Andreev reflections at the interfaces [39, 40, 41, 38, 42, 43]. Andreev bound states resemble Majorana fermions. For example, they both evolve in magnetic field and form a conductance peak at zero bias voltage. Our studies of Andreev bound states formed in InSb nanowire quantum dots coupled to superconductors are helpful for the correct interpretation of Majorana experiments done in similar structures. [44, 43, 45].

A Majorana fermion is a particle that is its own antiparticle arising from specific solution to Dirac's equation proposed by Ettore Majorana in 1937 [46]. Majorana himself thought that neutrinos will be described by his solution, but the question of whether neutrinos are Majorana fermions remains open, despite significant efforts [47]. The search for Majorana fermions took an unexpected turn when they were proposed as quasiparticle excitations in exotic solid state systems, providing a path to observing what we have failed to find in nature in a man-made system [1, 48, 49, 50, 51, 4, 5]. In the middle of the superconducting gap, where $E = 0$ (Fermi level), there can exist a quasiparticle for which the annihilation and creation operation are the same, hence this particle is its own antiparticle [52]. In a 2001 theoretical proposal by Kitaev, Majorana fermions were realized at the ends of a one dimensional, spin-polarized superconductor [1]. Without spin polarization, each end of the superconductor will contain two Majorana fermions, one for each spin, and they will annihilate. In 2010, Lutchyn *et al.* [4] and Oreg *et al.* [5] took Kitaev's idea and expanded on previous proposals by Sau *et al.* [50] and Alicea [51] and proposed a practical experimental setup based on readily available semiconductor-superconductor heterostructures. Their setup consists of a ballistic semiconducting nanowire with a strong spin-orbit interaction that is in proximity with a conventional superconductor in the presence of an external magnetic field. A competition between the superconducting-induced gap and the Zeeman gap drives the system to the topological phase transition. As soon as we enter the topological phase in

the nanowire, Majorana modes are pinned to the boundaries of the system (two ends of the nanowire). A pair of Majorana bound states forms a two-level system and hence a qubit. In qubits encoded in separated Majorana fermions, the information is stored nonlocally. This protects the information from local sources of decoherence and provides a platform for fault tolerant quantum memory [2, 3].

The non-local information storage makes it very challenging to control and coherently transfer the information into and out of the system when needed. Superconducting qubits (solid state electrical circuits based on Josephson junctions), on the other hand, are easy to control, read out, and couple together [53, 54]. One can put together a superconducting qubit with Majorana fermions and form a two-qubit hybrid quantum system that leverages the advantages of both qubits via their coupling [55]. The superconducting qubit is used to read out the Majorana states, while the other qubit may act as local quantum memory. Hence, this hybrid system can be used as a building block for a full scale quantum computer. Towards the end of this work we take preliminary steps to design and fabricate superconducting circuits compatible with the semiconducting-superconducting heterostructures that we investigated.

- **What is in this thesis? - Synopsis**

We go over some background and theory related to physical concepts and structures used in the thesis in Chapter 2. Device fabrication techniques and measurement setups used throughout the thesis are explained in Chapter 3.

In Chapter 4 we evaluate the potential of Ge/Si core/shell nanowires for realizing Majorana states as well as spin based qubits. Holes in Ge/Si nanowires offer a relatively unexplored platform for such studies [56, 57, 58]. They are expected to come with long spin relaxation times owing to their p-wave wavefunction symmetry as well as their low abundance of nonzero nuclear spin isotopes in group IV materials [59]. Furthermore, the spin-orbit interaction is predicted [60] and suggested by experiments [61, 62, 63, 64] to be strong in Ge/Si core/shell nanowires. We perform transport measurements on double quantum dots made in these nanowires and extract spin-orbit coupling and g-factors by analyzing the data in the Pauli spin blockade regime. Furthermore, we observe induced superconductivity and a tunable supercurrent that persists in finite magnetic fields in NbTiN-Ge/Si-NbTiN Joseph-

son junctions. We conclude that detailed tailoring in nanowire morphology is much needed in order to enhance spin-orbit interaction and induced superconductivity to further consider this system for (non)topological qubit studies.

In Chapter 5 and Chapter 6 we explore hybrids of InSb nanowires and multiple superconductors. InSb nanowire is a promising material for implementing advanced quantum devices [65, 66]. Its high electron mobility, giant g-factor and strong spin-orbit interaction makes it one of the main candidates in the search for topological superconductivity accompanied by Majorana fermions [67, 68]. In Chapter 5 we study transport mediated by Andreev bound states formed in InSb nanowire quantum dots. We show that the nontrivial densities of states in the superconducting probes can drastically affect tunneling characteristics resulting in additional transport resonances. Accurate understanding of Andreev spectroscopy is important, because the presence of such additional resonances may complicate the interpretation of Majorana experiments done on the same structures.

In Chapter 6 we present induced superconductivity in InSb nanowires from Sn superconducting shells that persists up to a significant magnetic field. We demonstrate the two-electron charging effect that is crucial for long quasiparticle stability times. These findings open avenues for superconducting and topological quantum circuits based on new superconductor-semiconductor combinations. Until recently, the superconductors used in hybrid systems in search of topological regimes were almost exclusively Al and Nb-family superconductors. However, Al suffers from a relatively low critical magnetic field and temperature, resulting in a small induced gap. And Nb-family superconductors have failed to induce a superconducting gap void of quasiparticles, preventing the two-electron charging effect, shortening coherence times and scrambling read out of a future topological qubit.

Superconducting qubits are typically fabricated with Al and have shown incredible progress towards building a high-fidelity quantum processor [69]. However, the idea of integrating semiconducting qubits with their superconducting siblings to build a fault tolerant quantum computer naturally requires the superconducting qubits to operate in finite magnetic fields which is a limitation for Al based circuits. In Chapter 7 we present some preliminary studies on fabricating and characterizing field-resilient Nb-family superconducting microwave resonators which have been demonstrated previously to have high quality

factors [70, 71, 72]. We also make our first attempt (ongoing project) to utilize Sn-InSb nanowire Josephson junction as the nonlinear element in a transmon qubit design. The tunability of nanowire transmons and their resilience to magnetic fields enables new means of controlling the superconducting-semiconducting topological qubits [73, 74, 75, 76].

In Chapter 8 we use nanowires rather differently. We fabricate Josephson junctions on InAs two-dimensional electron gas (2DEG) by in-situ evaporating Al while InSb nanowires are serving as shadow masks [65, 66]. This technique eliminates the chemical etching process generally used to define junctions on 2DEG systems. We study the behavior of supercurrent through these junctions as a function of magnetic field and microwave excitation. Our data show a non-conventional behavior of supercurrent that may be attributed to anomalous current-phase relations of these junctions. However, we refrain from drawing conclusions as artefacts in our fabrication can introduce inhomogeneities and an alternative explanation for our observations.

At last, concluding remarks are presented in Chapter 9.

2.0   Background information

In this chapter we briefly introduce a general Hamiltonian to describe the band structure of semiconductors. We then expand the Hamiltonian by adding relevant interaction terms such as Zeeman energy and spin-orbit coupling. These terms are further investigated in quantum dot structures in Chapter 4. We briefly discuss quantum dots and the Pauli spin blockade mechanism. Next we move on to superconductivity and give an introduction to the physics of Andreev processes that we study at hybrid interfaces. Andreev spectroscopy is further investigated in Chapter 5. Supercurrents in Josephson junctions are discussed and used throughout this thesis to characterize superconductor-semiconductor interface quality and induced superconductivity (Chapter 4, Chapter 6, Chapter 8). In the final part of this chapter we give a short introduction to superconducting circuits (resonators and qubits) and we later pursue to design, characterize and incorporate them into hybrid superconducting-semiconducting circuit quantum electrodynamics devices in Chapter 7.

2.1   Hamiltonian for semiconductors[1]

The band structure of semiconductors comes from solving the Schrödinger equation for noninteracting electrons in a periodic lattice potential:

$$[\frac{-\hbar^2}{2m_e}\nabla^2 + V(\boldsymbol{r})]\psi(\boldsymbol{r}) = E\psi(\boldsymbol{r}) \tag{1}$$

where $V(\boldsymbol{r}) = V(\boldsymbol{r}+\boldsymbol{R})$ with translation vector $\boldsymbol{R}$. This periodic potential can be expanded in a Fourier series $V(\boldsymbol{r}) = \sum_{\boldsymbol{G}} V_{\boldsymbol{G}} e^{i\boldsymbol{G}\boldsymbol{r}}$ ($\boldsymbol{G}$ is a vector in the reciprocal lattice such that $\boldsymbol{G}\boldsymbol{R} = 2\pi$). Using Bloch's theorem and for a given wave vector $\boldsymbol{k}$ we can find a wavefunction that solves the Schrodinger equation:

$$\psi_{\boldsymbol{k}}(\boldsymbol{r}) = e^{i\boldsymbol{k}\cdot\boldsymbol{r}} u_{n\boldsymbol{k}}(\boldsymbol{r}) \tag{2}$$

---

[1]This section follows from Refs. [77, 78].

where $u_{n\boldsymbol{k}}(\boldsymbol{r})$ is a periodic Bloch function with translation symmetry of the lattice and n is the band index. Substituting this solution back into the Schrodinger equation we get

$$[\frac{\hbar^2}{2m_e}(-i\nabla + \boldsymbol{k})^2 + V(\boldsymbol{r})]u_{n\boldsymbol{k}}(\boldsymbol{r}) = Eu_{n\boldsymbol{k}}(\boldsymbol{r}),$$

$$([\frac{\boldsymbol{p}^2}{2m_e} + V(\boldsymbol{r})] + [\frac{\hbar}{m_e}\boldsymbol{k}\cdot\boldsymbol{p} + \frac{\hbar^2\boldsymbol{k}^2}{2m_e}])u_{n\boldsymbol{k}}(\boldsymbol{r}) = Eu_{n\boldsymbol{k}}(\boldsymbol{r}) \tag{3}$$

where $\boldsymbol{p} = -i\hbar\nabla$ is the momentum operator.

The relevant parts of the band structure for semiconducting nanostructures are close to the band gap, i.e, near the minimum of the conduction band or the maximum of the valence band.

For $\boldsymbol{k} = 0$ we can assume eigenenergies E_n corresponding to eigenfunctions $u_{n0}(\boldsymbol{r}) \equiv |n\rangle$ that can be used to expand $u_{n\boldsymbol{k}}(\boldsymbol{r})$ for arbitrary $\boldsymbol{k}$. For small $\boldsymbol{k}$ we treat $\boldsymbol{k}$-dependent terms as perturbations to calculate energy dispersions. This method is called $\boldsymbol{k}\cdot\boldsymbol{p}$ theory. We then find that the solutions of Eq. 3 are

$$E_n(\boldsymbol{k}) = E_n + \frac{\hbar^2k^2}{2m_e} + \frac{\hbar^2}{m_e^2}\sum_{m\neq n}\frac{|\langle u_{m0}|\boldsymbol{k}\cdot\boldsymbol{p}|u_{n0}\rangle|^2}{E_m - E_n}. \tag{4}$$

As in the case of free electrons this dispersion relation in the conduction band of a semiconductor is parabolic with curvature that is described by the electron's effective mass

$$\frac{1}{m_{eff}} = \frac{1}{m_e} + \frac{1}{m_e^2}\frac{|\langle u_{c0}|\boldsymbol{k}\cdot\boldsymbol{p}|u_{v0}\rangle|^2}{E_c - E_v}, \tag{5}$$

leading to eigenenergies

$$E_c(\boldsymbol{k}) = E_c + \frac{\hbar^2\boldsymbol{k}^2}{2m_{eff}} \tag{6}$$

and Hamiltonian

$$H(\boldsymbol{k}) = \frac{\hbar^2k^2}{2m_{eff}} + V(\boldsymbol{k}). \tag{7}$$

From Eq. 5 we see that the effective mass in semiconductors with large band gap $E_g = E_c - E_v$ tends to be bigger than in those with small band gaps. Eigenenergies become quantized when the wavefunction is confined by either the boundaries of the semiconductor or an external potential. When the confinement length becomes smaller than the Fermi wavelength the spatial dimensionality of the Hamiltonian is reduced. Confining the wavefunction

in one, two or three spatial dimensions then leads to a two-, one-, or zero-dimensional system, i.e., two-dimensional electron gases, one-dimensional nanowires, and quantum dots, respectively.

2.1.1 Zeeman energy

So far we have ignored the spin of electrons. The spin operator for electrons is defined as $\boldsymbol{S} = \frac{1}{2}\boldsymbol{\sigma}$, where $\boldsymbol{\sigma}$ are the Pauli matrices. The magnetic dipole moment of an electron can be described by the electronic spin via $\boldsymbol{\mu} = -\frac{1}{2}g\mu_B\boldsymbol{\sigma}$, where μ_B is the Bohr magneton. In an external magnetic field $\boldsymbol{B}$ a magnetic torque $\boldsymbol{M} = \boldsymbol{\mu} \times \boldsymbol{B}$ acts on the electron. The energy of the magnetic dipole moment in a magnetic field is then described by the Zeeman Hamiltonian

$$H_Z = -\boldsymbol{\mu} \cdot \boldsymbol{B} = \frac{1}{2}g\mu_B\boldsymbol{\sigma} \cdot \boldsymbol{B} \tag{8}$$

2.1.2 Spin-orbit interaction

Another coupling term relevant to spin is the coupling between spin and orbital motion when an electron moves in an electric field. An atom (or a crystal lattice) produces an electric field $\boldsymbol{E}$ in its rest frame. An electron orbiting around the atom with momentum $\boldsymbol{p}$ not only sees this pure electric field, but also an effective magnetic field $\boldsymbol{B'} = \frac{1}{m_e c^2}\boldsymbol{E} \times \boldsymbol{p}$ that interacts with electron spin. This field also induces a momentum-dependent spin-orbit energy $H_{SO} = \frac{g\mu_B}{2m_e c^2}(\boldsymbol{E} \times \boldsymbol{p}) \cdot \boldsymbol{\sigma}$, which is the spin-orbit coupling. The electric field is the gradient of the electrostatic potential V. In crystals the resulting spin-orbit field is

$$\boldsymbol{B}_{SO}(\boldsymbol{p}) = \frac{\mu_B}{m_e c^2}(\nabla V \times \boldsymbol{p}) \tag{9}$$

which can induce spin splitting for electrons in a lattice even with zero external field. Spin-orbit interaction can also arise from the crystal and band structure of semiconductors, for example, through Dresselhaus and Rashba spin-orbit couplings, which are most relevant to this thesis.

In binary compound crystals such as zincblende structure of InSb or InAs quantum wells, the two atoms have slightly different electronegativities to which there will be a permanent

electric field associated. This electric field will be a perturbing term for electron spins moving in the crystal's potential. This perturbation term, which comes from bulk inversion asymmetry, is referred to as the Dresselhaus contribution and is described by the following Hamiltonian [79]:

$$H_D^{bulk} \propto [\sigma_x p_x(p_y^2 - p_z^2) + \sigma_y p_y(p_z^2 - p_x^2) + \sigma_z p_z(p_x^2 - p_y^2)], \tag{10}$$

where x, y and z are along crystal directions of (100), (010) and (001), respectively. For the case of a two-dimensional electron gas (2DEG) confined along z, $\langle p_z \rangle = 0$ and $\langle p_z^2 \rangle$ is a fixed value. The Hamiltonian can be rewritten as:

$$H_D^{(001)} \propto [-\sigma_x p_x \langle p_z^2 \rangle + \sigma_y p_y \langle p_z^2 \rangle + \sigma_x p_x p_y^2 - \sigma_y p_y p_x^2] \tag{11}$$

Due to strong confinement along z, $\langle p_z^2 \rangle \gg p_x^2, p_y^2$, this Hamiltonian reduces to the so-called linear Dresselhaus spin-orbit:

$$H_D^{SO} = \beta(-\sigma_x p_x + \sigma_y p_y), \tag{12}$$

in which β depends on $\langle p_z^2 \rangle$ and also the material properties.

On the other hand, the Rashba term arises from structural inversion asymmetry [80]. "Structural" refers to the electronic band structure that is manifested by offsetting band gaps to create electron/hole confinement like in our Ge/Si core/shell nanowires or by stacking layers of different materials on top of one another to create an electron confinement in InAs quantum wells or by means of a gate voltage that creates asymmetry at the interface. There will be an electric field associated to charges confined in a quantum well and the gate or dopants on the quantum well. This electric field, too, perturbs spin. In such a case, the spin-orbit interaction can be controlled by gate voltages, which results in a confining electric field along z and the relative spin-orbit Hamiltonian will be

$$H_R \propto [\boldsymbol{E} \times \boldsymbol{p}] \cdot \boldsymbol{\sigma} = E_z(-\sigma_x p_y + \sigma_y p_x),$$
$$H_R^{SO} = \alpha(-\sigma_x p_y + \sigma_y p_x) \tag{13}$$

The proportionality factor α (the effective spin-orbit strength) depends on the material, as

well as external factors such as the orientation of the applied electric field.

Strong lateral confinement in one-dimensional quantum wires further results in $\langle p_y \rangle = 0$, which reduces Eq. 2.1.2 and Eq 2.1.2 to a single linear term dependent on p_x. The energy dispersion $\varepsilon(k) = \hbar^2 k_x^2/2m$ is split by the one-dimensional spin-orbit interaction into two parabolas to left and right moving states with fourfold degeneracy. Application of an external magnetic field opens and energy gap at $k = 0$ and states within this gap are now twofold degenerate. A combination of magnetic field and gate voltages to control the potential across the wire then allows for the tunability of spin polarization across the wire.

2.2   Quantum dots[2]

Studies of spin states in quantum dots are largely motivated by the proposals to build a spin-based quantum computer [9]. Quantum dots are semiconducting structures that confine electrons or holes in a space that is smaller than the Fermi wavelength of these charge carriers. Thus their energy levels are discrete, and quantum dots are referred to as artificial atoms. Filling dots' eigenenergies with electrons or holes follows rules from atomic physics such as Hund's rule, shell filling, etc. A schematic of a quantum dot that is connected to source and drain reservoirs through tunnel barriers and is capacitively coupled to a gate is shown in Fig. 2.1(a). This set-up allows the transport of current through the dot to be measured in response to bias voltage and gate voltage. Below we will review charge and spin transport in single and double quantum dots.

2.2.1   Single quantum dots

The basic model that can describe the physics of a quantum dot is called the Constant Interaction Model, following Hanson *et al.* [81], and is based on two assumptions. On the one hand, electrons in the dot have a capacitive coupling to source (C_S) and drain (C_D) reservoirs as well as the gate (C_g). One the other hand, the single-particle energy spectrum

---

[2]This section follows from Refs. [77, 81]

E_n is independent of these capacitive couplings. The total energy $U(N)$ of a quantum dot with N electrons (or holes) in the ground state is

$$U(N) = \frac{1}{2C}[-e(N - N_0) + C_S V_S + C_D V_D + C_G V_G]^2 + \sum_{n=1}^{N} E_n, \qquad (14)$$
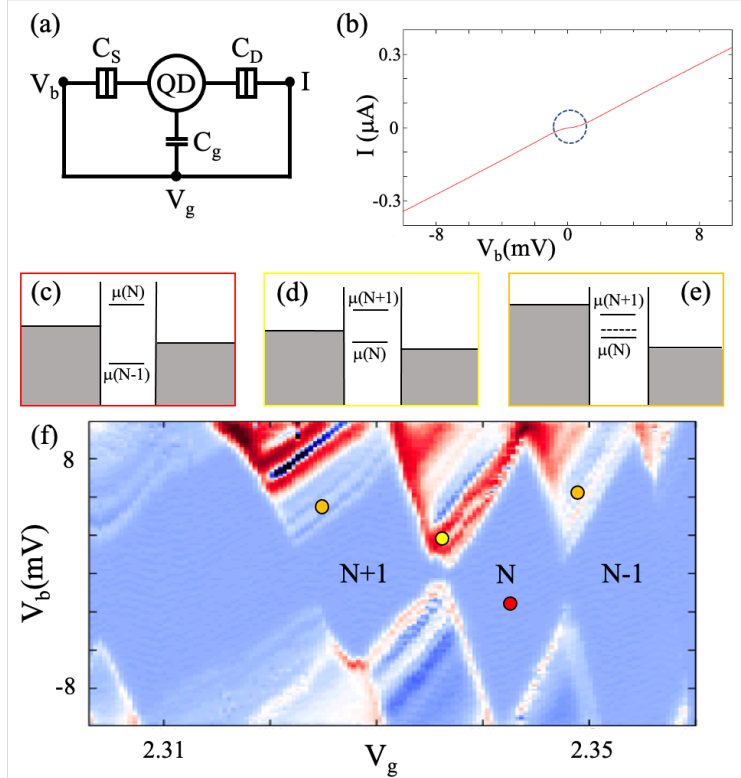
Figure 2.1: (a) Schematics of a quantum dot coupled to a source and drain contacts through tunneling barriers. The plunger gate allows us to tune the quantum mechanical energy states in the quantum dot by controlling chemical potential in the dot via capacitive coupling. The current, I through the dot measured on the drain depends of bias voltage V_b and gate voltage V_g. (b) Coulomb blockade (CB) region evident in $I - V$ trace through a quantum dot where for finite bias voltage no current passes through the dot. (c) CB schematics when there is no accessible dot levels (dot level is used as a short form for dot electrochemical potential) within the bias window. (d) Tunneling of electrons (or holes) through accessible dot level within the bias window. (e) Transport through the dot at high bias voltage where there are multiple dot levels and transition involving excited states are available for tunneling. (f) Coulomb blockade diamonds in a single quantum dot in Ge/Si core/shell nanowires defined between to adjacent gate electrodes. Color plot represents differential conductance as a function of bias and gate voltages. The number of particles in the dot is a fixed integer number N. In Ge/Si the charge carriers are holes, hence increasing the gate voltage repels holes from the dot one by one.

where N_0 compensates for background charges, V_S, V_D, and V_g are voltages on source, drain, and plunger gate, respectively. The electrochemical potential of the dot (the energy required to add the Nth electron) is then

$$\mu(N) = U(N) - U(N-1) = E_C(N - N_0 - \frac{1}{2}) - \frac{E_C}{e}(C_S V_S + C_D V_D + C_g V_g) + E_N, \quad (15)$$

where $E_C = \dfrac{e^2}{C}$ is the charging energy The electrochemical potential $\mu(N)$ then consists of two parts, an electrostatic energy to overcome the charging effect and a discrete level energy.

In transport scheme (Fig. 2.1(a)), applying a bias voltage between the source and the drain $V_b = V_S - V_D$ opens an energy window, known as bias window, between the electrochemical potential of the source, μ_S, and the drain, μ_D. Transport of electrons through the dot depends on the alignment of electrochemical potentials in the dot with respect to $\mu_S - \mu_D = -eV_b$, $\mu_S \geqslant \mu(N) \geqslant \mu_D$. If this condition is not met for at least one value of N the number of electrons on the dot remains fixed and no transport takes place. This is called the Coulomb blockade (Fig. 2.1(c)), which can be lifted by tuning voltages (Eq. 15) so that $\mu(N)$ is within the bias window (Fig. 2.1(d)).

At high source-drain bias voltage, multiple dot levels can lie within the bias window. This allows excited states to participate in tunneling transitions (Fig. 2.1(e)). For instance, for two successive ground states $GS(N)$ and $GS(N+1)$ and excited states $ES(N)$ and $ES(N+1)$ we can have transitions such as $ES(N) \leftrightarrow GS(N+1)$ and $GS(N) \leftrightarrow ES(N+1)$ fall within the bias window. These transitions manifest themselves within V-shaped regions in (bias, gate)-plane as seen in Fig. 2.1(f). The transition between $GS(N)$ and $GS(N+1)$ defines the Coulomb blockade (outside of the V-shape) and the tunneling regime (within the V-shape). Measuring the differential conductance dI/dV_b as a function of the plunger gate V_g and source–drain bias voltage V_b across a dot results in the so-called Coulomb blockade diamonds shown in Fig. 2.1(f).

Thus far, we have not included the spin of electrons in the transport studies. In a quantum dot with an odd number of electrons the spin state is either up or down. These two spins states are degenerate at zero magnetic field, thus the ground state is a spin doublet at lowest orbital. They spilt in the presence of a finite field with energy difference equal to Zeeman splitting $\Delta E_Z = g\mu_B B$. This mechanism allows for initialization and readout of

14

qubits encoded in spin-up and spin-down states of electrons in quantum dots [9, 10, 82]. For a quantum dot with an even number of electrons, the ground state is a spin singlet $|S\rangle = (|\uparrow\downarrow\rangle - |\downarrow\uparrow\rangle)/\sqrt{2}$ and the first excited states are spin triplets $|T_+\rangle = |\uparrow\uparrow\rangle$, $|T_0\rangle = (|\uparrow\downarrow\rangle + |\downarrow\uparrow\rangle)/\sqrt{2}$, and $|T_-\rangle = |\downarrow\downarrow\rangle$.

2.2.2 Double quantum dots

A double quantum dot (DQD) can be made by mutually coupling individual dots, through capacitive and/or tunnel coupling. The electrochemical potential on each dot, and hence the charge occupation (N_1, N_2), can be controlled by changing voltages on gates coupled to either dot (Fig. 2.2(a)). Transport of charge carriers from source to drain through the DQD follows this cycle: $(N_1, N_2) \rightarrow (N_1 + 1, N_2) \rightarrow (N_1, N_2 + 1) \rightarrow (N_1, N_2)$. At low source-drain bias the transport is allowed when these three charge states are energetically degenerate, and the electrochemical potential of both dots align with those of source and drain. This degeneracy point is called a triple point. Fig. 2.2(b) schematically depicts the equilibrium (N_1, N_2) charge number on each dot in the (gate, gate) plane. Such a transport plot is called a charge stability diagram. At finite source-drain bias voltage, triple points grow into so-called bias triangles, in which tunneling through excited states becomes accessible. Fig. 2.2(c) shows the charge stability diagram for a Ge/Si DQD where the charge carriers are holes in the valence band.

2.2.2.1 Pauli spin blockade

The rectification of current in DC transport through a DQD is called Pauli spin blockade [13]. The simplest case of Pauli blockade happens for the transport cycle when starting with $N_1 = 0$ and $N_2 = 1$: $(0, 1) \rightarrow (1, 1) \rightarrow (0, 2) \rightarrow (0, 1)$. When there is only one charge carrier in either one of the dots $(0, 1)$ the spin states are either spin-up or spin-down. The spin-up and spin-down states are degenerate at zero magnetic field, and at finite fields the Zeeman effect lifts the spin degeneracy. For the $(0, 2)$ charge state there are four spin states

15

possible:

$$S(0, 2) = (|\uparrow_2\downarrow_2\rangle - |\downarrow_2\uparrow_2\rangle)/\sqrt{2}$$

$$T_+(0, 2) = |\uparrow_2\uparrow_2\rangle$$

$$T_0(0, 2) = (|\uparrow_2\downarrow_2\rangle + |\downarrow_2\uparrow_2\rangle)/\sqrt{2} \tag{16}$$

$$T_-(0, 2) = |\downarrow_2\downarrow_2\rangle,$$

where triplet states are degenerate in the absence of a magnetic field. In this case a singlet ground state is favored over excited triplet states as they involve higher orbital states that are not available for small source-drain bias voltages, due to Pauli principle. The energy difference between singlet and triplet states is called the singlet-triplet splitting E_{ST}.
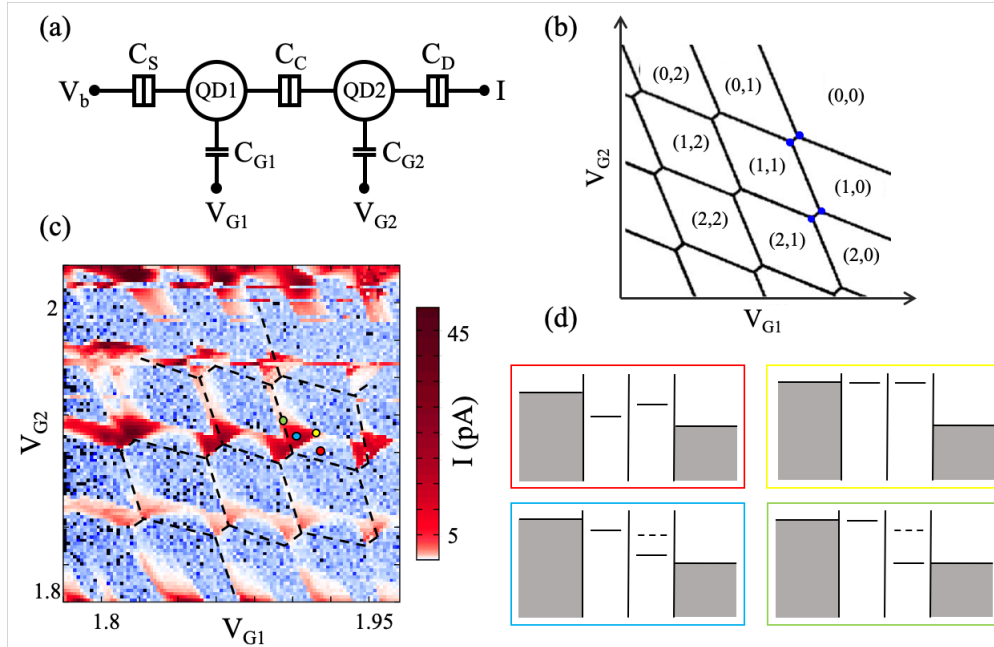
Figure 2.2: (a) Diagram of two quantum dots coupled in series. Due to capacitive couplings each gate effectively controls the chemical potential on both dots. (b) At low source-drain bias voltage transport through DQD is only possible at triple points, shown in blue. Triple points together form a hexagonal lattice. At a triple point, three different charge states are energetically degenerate. (c) Charge stability diagram of a DQD made in Ge/Si core/shell nanowires by adjacent gates. The coupling between the dots (C_C) is also controllable by a gate voltage. (d) Transport schematics of different points (color-coded) on a bias triangle that is not spin-blocked. Solid line represents ground state and dashed line is an excited state that becomes accessible when double dots level detuning increases.

Similarly, for the $(1,1)$ charge configuration, we have singlet and triplet spin states. The spin of the wavefunctions are as follow:

$$S(1,1) = (|\uparrow_1\downarrow_2\rangle - |\downarrow_1\uparrow_2\rangle)/\sqrt{2}$$
$$T_+(1,1) = |\uparrow_1\uparrow_2\rangle$$
$$T_0(1,1) = (|\uparrow_1\downarrow_2\rangle + |\downarrow_1\uparrow_2\rangle)/\sqrt{2} \tag{17}$$
$$T_-(1,1) = |\downarrow_1\downarrow_2\rangle.$$

Electrons occupy separate orbitals in neighboring dots, hence the singlet–triplet splitting at zero magnetic field is usually negligibly small. The $(0,1) \rightarrow (1,1) \rightarrow (0,2) \rightarrow (0,1)$ spin states near degeneracy points can be described by as follows [83]:

$$
\begin{aligned}
H_0 = & -\varepsilon|S(0,2)\rangle\langle S(0,2)| + \sqrt{2}t(|S(1,1)\rangle\langle S(0,2)| + |S(0,2)\rangle\langle S(1,1)|) \\
& - g\mu_B B(|T_+(1,1)\rangle\langle T_+(1,1)| - |T_-(1,1)\rangle\langle T_-(1,1)|),
\end{aligned} \tag{18}
$$

where ε is the level detuning and t is the tunnel coupling between $S(1,1)$ and $S(0,2)$. If $\varepsilon < 0$ the transport is blocked due to Coulomb blockade (red panel in Fig. 2.2(d)). For the case of $\varepsilon > 0$, if the electrons form one of the triplet states $T(1,1)$, the electron in the first dot will not be able to tunnel to the second dot, as $T(0,2)$ is too high in energy. The system remains stuck in the $(1,1)$ charge state until the electron relaxes. Once the source-drain bias is increased such that it exceeds singlet-triplet splitting, $T(0,2)$ states become available from $T(1,1)$, and the blockade is lifted. Spin blockade can also be lifted by other means such as photon-assisted tunneling and application of an external magnetic field. Some of these spin relaxation and lifting processes are discussed in detail in Ref. [81]. In Chapter 4 we thoroughly discuss spin mixing processes due to a combination of spin-orbit interaction and Zeeman splitting.

2.2.3 Spin-orbit interaction in quantum dots

In quantum dots electrons are confined in all three directions and the average momentum is zero. This property means that spin-orbit interaction does not couple the Zeeman split levels of a quantum dot with orbitals labeled with q:

$$\langle q \downarrow | H_{SO} | q \uparrow \rangle \propto \langle q | p_{x,y,z} | q \rangle \langle \downarrow | \sigma | \uparrow \rangle = 0. \tag{19}$$

However, spin-orbit interaction manifests itself as a perturbation term and couples states with different orbital numbers. Thus quantum dot states are actually admixtures of spin and orbital states:

$$
\begin{aligned}
|q \uparrow\rangle^{(1)} &= |q \uparrow\rangle + \sum_{q' \neq q} \frac{\langle q' \downarrow | H_{SO} | q \uparrow \rangle}{E_q - E_{q'} - \Delta E_Z} |q' \downarrow\rangle \\
|q \downarrow\rangle^{(1)} &= |q \downarrow\rangle + \sum_{q' \neq q} \frac{\langle q' \uparrow | H_{SO} | q \downarrow \rangle}{E_q - E_{q'} + \Delta E_Z} |q' \uparrow\rangle,
\end{aligned}
\tag{20}
$$

in which ΔE_Z is the unperturbed Zeeman energy. But this perturbation renormalizes the Zeeman energy of electrons: $\Delta E_Z^{(1)} = E_\downarrow^{(1)} - E_\uparrow^{(1)}$ and that is why what we measure in quantum dots is actually the effective g-factor. For the case of two-electron spin states, a combination of spin-orbit interaction and Zeeman splitting due to the applied field enables transitions between triplet and singlet configurations:

$$
\begin{aligned}
|Sq\rangle^{(1)} &= |Sq\rangle + \sum_{q' \neq q} \frac{\langle T_\pm q' | H_{SO} | Sq \rangle}{E_{T_\pm q'} - E_{Sq}} |T_\pm q'\rangle \\
|T_0 q\rangle^{(1)} &= |T_0 q\rangle \sum_{q' \neq q} \frac{\langle T_\pm q' | H_{SO} | T_0 q \rangle}{E_{T_\pm q'} - E_{T_0 q}} |T_\pm q'\rangle \\
|T_\pm q\rangle^{(1)} &= |T_\pm q\rangle \sum_{q' \neq q} \frac{\langle Sq' | H_{SO} | T_\pm q \rangle}{E_{Sq'} - E_{T_\pm q}} |Sq'\rangle + \sum_{q' \neq q} \frac{\langle T_0 q' | H_{SO} | T_\pm q \rangle}{E_{T_0 q'} - E_{T_\pm q}} |T_0 q'\rangle
\end{aligned}
\tag{21}
$$

2.3 Superconductivity

A superconductor can support a dissipationless current below a critical temperature T_c, and expel external magnetic fields up to a particular critical field B_c. Bardeen, Cooper and Schrieffer (BCS) developed a microscopic theory that explained thermal, transport and electromagnetic properties of superconductors [17]. In their model, the ground state of a superconductor is a condensate of pairs of electrons with opposite momentum and spin that form effective bosonic particles called Cooper pairs. This pairing is mediated by interactions between electrons and the phonon field that compensates for the Coulomb repulsion between electrons. BCS model leads to a gapped energy spectrum around Fermi level, $|E| = 2\Delta$, where Δ is the superconducting energy gap. The superconducting phase transition is characterized by a complex valued order parameter (also called superconducting pairing potential), $\Delta_k = \Delta e^{i\varphi}$, in which φ is the superconducting phase. The Hamiltonian describing this pairing can be written as:

$$H_{BCS} = \sum_{k\sigma} \epsilon_k c_{k\sigma}^\dagger c_{k\sigma} + \sum_{kl} V_{kl} c_{k\uparrow}^\dagger c_{-k\downarrow}^\dagger c_{l\uparrow} c_{-l\downarrow}, \tag{22}$$

where $\epsilon_k = \frac{(\hbar k)^2}{2m^*} - E_F$ (E_F is the Fermi energy) accounts for noninteracting electrons (in the absence of superconductivity), $c_{k\sigma}^\dagger$ ($c_{k\sigma}$) creates (annihilates) an electron with momentum k and spin σ, V_{kl} characterizes the attractive interaction between Cooper pairs. In the mean-field approximation this pairing Hamiltonian takes the form:

$$H_{BCS} = \sum_{k\sigma} \epsilon_k c_{k\sigma}^\dagger c_{k\sigma} + \sum_{k} (\Delta_k c_{k\uparrow}^\dagger c_{-k\downarrow}^\dagger + h.c.). \tag{23}$$

This Hamiltonian does not conserve particle number but spin and parity (even or odd number of particles) are conserved. The Hamiltonian can be diagonalized and written in the standard Bogoliubov-de Gennes (BdG) form:

$$\begin{aligned} H_{BCS} &= \sum_k C_k^\dagger \mathcal{H}_{BdG} C_k \\ C_k^\dagger &= \begin{pmatrix} c_{k\uparrow}^\dagger & c_{-k\downarrow} \end{pmatrix} \\ \mathcal{H}_{BdG} &= \begin{pmatrix} \epsilon_k & \Delta_k \\ \Delta_k^* & -\epsilon_k \end{pmatrix} \end{aligned} \tag{24}$$

The Schrödinger equation can be generalized to the BdG equation with plane wave solutions:

$$\mathcal{H}_{BdG} \begin{pmatrix} \psi_e(r) \\ \psi_h(r) \end{pmatrix} = E \begin{pmatrix} \psi_e(r) \\ \psi_h(r) \end{pmatrix}$$

$$\begin{pmatrix} \psi_e(r) \\ \psi_h(r) \end{pmatrix} = e^{ikr} \begin{pmatrix} \psi_e \\ \psi_h \end{pmatrix} \tag{25}$$

where for the two-component wavefunction in the electron and hole space $|\psi_{e(h)}(r)|^2$ is the probability of finding a quasiparticle in an electron-like (hole-like) state. The eigenenergies are then

$$E = \pm\sqrt{\epsilon_k^2 + |\Delta_k|^2} \tag{26}$$

and the density of states close to the Fermi energy follows from $\rho(E) \equiv \dfrac{d\epsilon}{dE}$ (depicted in Fig. 2.3(a)):

$$\rho(E) = \begin{cases} \dfrac{E}{\sqrt{E^2 - \Delta^2}} & E > \Delta \\ 0 & E < \Delta \end{cases} \tag{27}$$

2.3.1 Semiconductor-superconductor interface

Now we consider the case where a normal metal (semiconductor in our case) and a superconductor are brought together. We begin with the ideal case where there is no barrier at the interface. An electron with energy $E > \Delta$ from the semiconductor incident upon the semiconductor-superconductor interface passes through as an electron or a hole-like quasiparticle above the gap energy. However, for a normal electron with energy $E < \Delta$, there are no quasiparticle states available in the superconducting gap. When this electron reaches the interface, it reflects back to the semiconductor as a hole transferring $2e$ charge across the interface to the superconducting Cooper pair condensate. This process is known as Andreev reflection [19]. For a perfect interface with no barriers at low temperature and bias voltage, all incident electrons would undergo Andreev reflection, thus the subgap conductance would be twice that of normal state. Nevertheless, in reality there will be normal reflection in

20
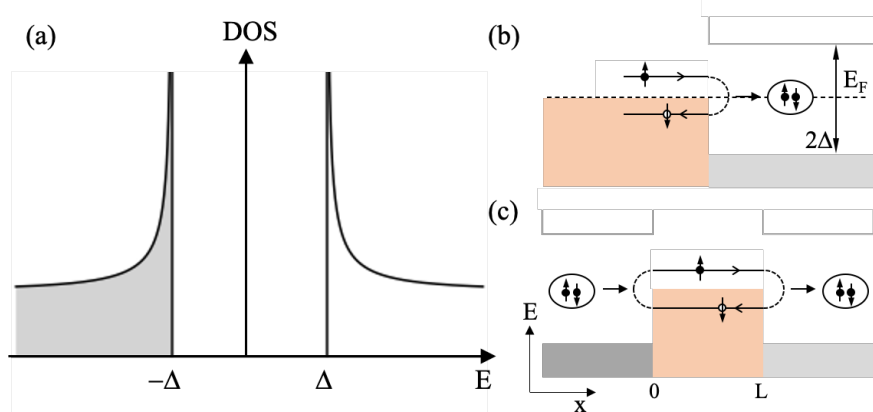
Figure 2.3: (a) Superconducting density of states with energy gap Δ, where there are no single quasiparticle states available. (b) Schematic of Andreev reflection for an incident electron with energy $E_F < E < \Delta$ at the interface of a semiconductor (orange) and a superconductor (gray). (c) Supercurrent flow between two superconducting electrodes with energy gap Δ and superconducting phases ϕ_1 and ϕ_2 that are separated by a weak link (a semiconductor in our experiments). In addition to Andreev reflection there are generally normal reflections happening at the weak link - superconductor interface due to some sort of barriers, for instance semiconductor native oxide. The normal reflections are not depicted here.

addition to Andreev reflection at the interface due to Fermi velocity mismatch of the carriers or rough interface between normal and superconducting regions. Blonder, Tinkham and Klapwijk [84] introduced a δ-function potential barrier with strength Z at the interface (so-called BTK model). Z describes the interface quality where $Z = 0$ means perfect Andreev reflection. They solved the BdG equation with plane wave ansatz to treat the transmission and reflection probabilities of an electron with energy E reaching the interface. There are four possible outcomes for an incoming electron incident at the interface: reflected as a hole $(A(E) = a^*a)$ or an electron $(B(E) = b^*b)$, transmitted as an electron $(C(E) = c^*c(\psi_e^2 - \psi_h^2))$ or hole $(D(E) = d^*d(\psi_e^2 - \psi_h^2))$ quasiparticle.

$$\Psi_{inc} = \begin{pmatrix} 1 \\ 0 \end{pmatrix} e^{ik_e r}$$

$$\Psi_{refl} = a \begin{pmatrix} 0 \\ 1 \end{pmatrix} e^{ik_h r} + b \begin{pmatrix} 1 \\ 0 \end{pmatrix} e^{-ik_e r} \qquad (28)$$

$$\Psi_{trans} = c \begin{pmatrix} \psi_e \\ \psi_h \end{pmatrix} e^{iq_e r} + d \begin{pmatrix} \psi_e \\ \psi_h \end{pmatrix} e^{-iq_h r}$$

Upon applying boundary conditions, the probability of each outcome is derived [84]. We plot Andreev and normal reflection probabilities for different values of Z in Fig. 2.4.
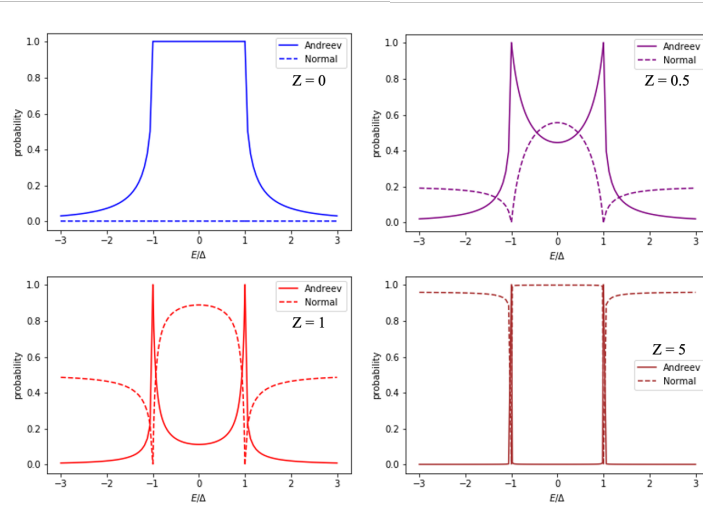
Figure 2.4: Probabilities for Andreev and normal reflections, $A(E)$ and $B(E)$ plotted for different Z values. At the two extreme limits $Z = 0$ and $Z = 5$ all electrons within the gap are Andreev and normal reflected, respectively.

2.3.1.1 Experimental relevance in the tunneling regime

When a bias voltage is applied there will be nonequilibrium quasiparticles generated at the interface. BTK model assumes the Fermi distribution for all incoming electrons and the electrochemical potential of Cooper pairs is chosen as the reference level. Hence all incoming electrons from a superconductor have a distribution function $f_0(E)$ while those

from semiconductors are described by $f_0(E - eV)$. The current across the interface must be conserved. Thus on the semiconductor side we have

$$I \sim \int_{-\infty}^{\infty} [f_{\rightarrow}(E) - f_{\leftarrow}(E)]dE \qquad (29)$$

where based on the description above $f_{\rightarrow}(E) = f_0(E - eV)$ and $f_{\leftarrow}(E) = A(E)(1 - f_{\rightarrow}(-E)) + B(E)f_{\leftarrow}(E) + [C(E) + D(E)]f_0(E)$. The current can then be rewritten as[3]

$$I \sim \int_{-\infty}^{\infty} [f(E) - f(E - eV)][1 + A(E) - B(E)]dE \qquad (30)$$

The term $1 + A(E) - B(E)$ is referred to as "transmission coefficient" from which we see Andreev reflection contributes to the current while normal reflection reduces it. The differential conductance at the interface is then

$$G(V) = \frac{dI}{dV} \sim \int \left(-\frac{df(E - eV)}{dV} \right) [1 + A(E) - B(E)]dE. \qquad (31)$$

In the tunneling regime where Z is large, $(1 + A(E) - B(E)) \longrightarrow \frac{E}{\sqrt{E^2 - \Delta^2}} = \rho(E)$ which is the superconductor density of states. Moreover, at low temperatures the derivative of the Fermi distribution reduces to a δ-function. Eq. 31 reduces to

$$G(V) = \begin{cases} \rho(eV) & Z \gg 1 \\ 1 + A(eV) - B(eV) & Z = 0 \end{cases}. \qquad (32)$$

In the tunneling regime for large Z the conductance is proportional to density of states. Therefore, a measurement of conductance is an essential spectroscopic tool to get insight into the density of states and the Andreev reflection process in a semiconductor-superconductor structure, and this model provides useful information from experimental aspects.

Blonder *et al.* also showed that the asymptotic linear $I - V$ curves derived from Eq. 30 exhibit an added "excess current" in the normal state ($eV \gtrsim \Delta$) that depends on Z, the transparency of the interface. We use an extension of this model (OBTK) [85] to deduce the transparency between Ge/Si core/shell nanowires and NbTiN superconductor in Chapter 4.

---

[3]Considering the following properties: $A(E) = A(-E)$, $A + B + C + D = 1$, $f_0(-E) = 1 - f_0(E)$.

2.3.2 Josephson effect and Andreev bound states

In 1962 Brian Josephson proposed that a supercurrent I_S can flow between two super-conducting electrodes separated by a non-superconducting region (a weak link) (Fig. 2.3(c)). The weak link can be a thin insulating layer (original Josephson's proposal), a normal metal, a semiconductor or just a narrow geometrical constriction [20]. In this thesis we study the Josephson effect in multiple Josephson junctions with semiconducting weak links (NbTiN-Ge/Si-NbTiN in Chapter 4, Al-InSb-Al in Chapter 5, Sn-InSb-Sn in Chapter 6, and Al- InAs 2DEG-Al in Chapter 8). The Josephson current in these junctions is gate voltage tunable and is sustained in relatively high magnetic fields, allowing them to potentially be used as nonlinear elements in circuit quantum electrodynamics devices for both topological and non-topological qubit designs.

The value of the supercurrent depends on the difference in the phase of the supercon-ducting wavefunction in the two electrodes $\phi = \phi_2 - \phi_1$ [18]

$$I_S(\phi) = I_c \sin\phi, \tag{33}$$

where the critical current I_c in this current-phase relation (CPR) is the maximum super-current that the junction can support. This sinusoidal CPR can successfully describe most Josephson junctions made with different materials and synthesis technologies. More gen-erally, however, CPR can deviate from simply sinusoidal form and include higher order components [86, 87, 88]

$$I_S = \Sigma[I_n sin(n\phi) + J_n cos(n\phi)] \tag{34}$$

with odd J_n terms vanishing in the presence of time-reversal symmetry, where J_n are the Bessel functions.

The flow of supercurrent through a Josephson junction can be understood by considering Cooper pair tunneling and Andreev processes at each interface. If quasiparticles in a single channel weak link stay phase coherent, they form bound states of electron-hole pairs that carry supercurrent between superconductor reservoirs with phase difference ϕ

$$I = \frac{2e}{\hbar}\frac{dE}{d\phi}, \tag{35}$$

24

where E is the energy of the bound states, known as Andreev bound states (ABS). Kulik [89] derived the wavefunction and energy levels of these excitations in a barrier-less superconducting-normal metal-superconducting junction (SNS junction and can be generalized to semiconductors depicted in Fig. 2.3(c) with a weak link with length L) by solving the BdG equation (Eq. 24) in which the order parameter is given by

$$\Delta(x) = \begin{cases} \Delta e^{i\phi_1} & x < 0 \\ 0 & 0 < x < L \\ \Delta e^{i\phi_2} & x > L \end{cases} \tag{36}$$

For $E > \Delta$ the solution is a continuous spectrum while for $E < \Delta$ there are discrete energy levels.

$$\frac{E}{\Delta}\frac{L}{\xi} = 2\arccos\frac{E}{\Delta} \pm \phi + 2\pi n \tag{37}$$

where ξ is the superconducting coherence length. For the short junction limit ($L \ll \xi$) the two lowest eigenvalues are $E^{\pm} = \pm\Delta\cos\left(\frac{\phi}{2}\right)$. Adding an interface barrier similar to BTK, Beenakker solved for ABS energies in the short junction limit [90]:

$$E^{ABS} = \pm\Delta\sqrt{\frac{cos^2(\phi/2) + Z^2}{1 + Z^2}} = \pm\Delta\sqrt{1 - T\sin^2\phi/2}, \tag{38}$$

where $T = 1/(1 + Z^2)$ is the conduction channel transmission probability. These sub-gap states with $|E^{ABS}| \lesssim \Delta$ are localized in the vicinity of the weak link and extend into the superconducting reservoirs. This allows transport through Andreev bound states as well as coupling the Andreev levels to superconducting resonators [91, 92, 93]. Substituting Eq. 38 back to Eq. 35 gives the current in a junction

$$I(\phi) = \frac{e\Delta}{2\hbar}\frac{T sin\phi}{\sqrt{1 - T sin^2(\phi/2)}}, \tag{39}$$

which reduces to Josephson current in Eq. 33 in the tunneling limit ($T \to 0$).
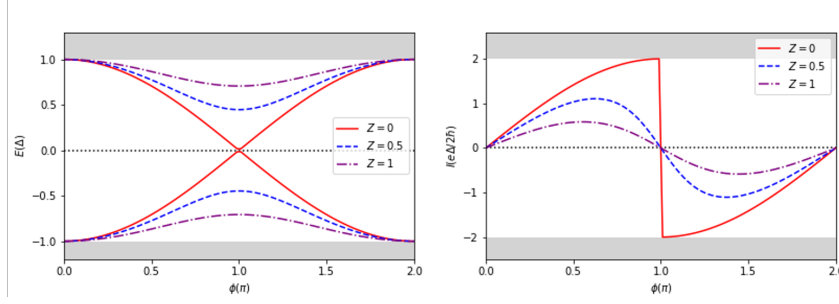
Figure 2.5: We plot Andreev bound state energy spectrum and current carried out by ABS for different interface transparencies. The continuum spectrum is shaded grey.

2.3.2.1 Andreev bound states in a quantum dot

If a quantum dot is strongly coupled to superconducting leads, ABS can be induced in the quantum dot. This results from the superconducting proximity effect, in which a transparent contact between a superconductor and a normal metal results in superconductivity in the normal region at mesoscopic scales. The Hamiltonian of this system can be written as $H = H_{QD} + H_{Lead_{L/R}} + V$. The quantum dot is modeled as a multiorbital Anderson impurity, with levels ϵ_i^D, and Coulomb interaction with charging energy U on the dot:

$$H_{QD} = \sum_{i\sigma} \epsilon_i^D d_{i\sigma}^\dagger d_{i\sigma} + U \sum_i n_{i\uparrow} n_{i\downarrow}, \tag{40}$$

where $d_\sigma^\dagger$ creates an electron in the dot and $n_{i\sigma} = d_{i\sigma}^\dagger d_{i\sigma}$. The BCS superconducting leads [20] with energy levels ϵ_k^L which allow more than one quasiparticle excitation in the superconducting lead, are described by the Hamiltonian:

$$H_{Lead_{L/R}} = \sum_{k\sigma} \epsilon_k^L c_{k\sigma}^\dagger c_{k\sigma} + \sum_k (\Delta e^{i\phi} c_{k\uparrow}^\dagger c_{-k\downarrow}^\dagger + \text{h.c.}), \tag{41}$$

in which $c_{k\sigma}^\dagger$ creates an electron with spin σ and wavevector k in the lead. And finally coupling between leads and quantum dot states through a spin-independent hopping amplitude is given by

$$V = t \sum_{ik\sigma} d_{i\sigma}^\dagger c_{k\sigma} + \text{h.c.}. \tag{42}$$

We study transport mediated by ABS in InSb nanowires with superconducting contacts in Chapter 5 in which this model is discussed in more detail.

2.3.3 Superconducting island

Let us now briefly discuss a superconducting island that is coupled to normal metal leads and a gate [20, 94]. The energy on the island at zero bias (similar to that of a quantum dot coupled to source and drain reservoirs) can be read from: $E = \frac{1}{2C_{tot}}(Q_0 + ne)^2$, where C_{tot} is the sum of all capacitances, $Q_0 = C_G V_G$ is the gate charge, and n is the number of electrons added to the island. This energy corresponds to a family of parabolas, one for each integer value of n, plotted in Fig. 2.6. At degeneracy points the value of n in the ground state changes. The electron pairing affects the potential energy on the island and modifies its ground state. If the number of conduction electrons N^4 on the island is even, the ground state is fully paired; if N is odd, the ground state should contain one quasiparticle above the energy gap Δ.
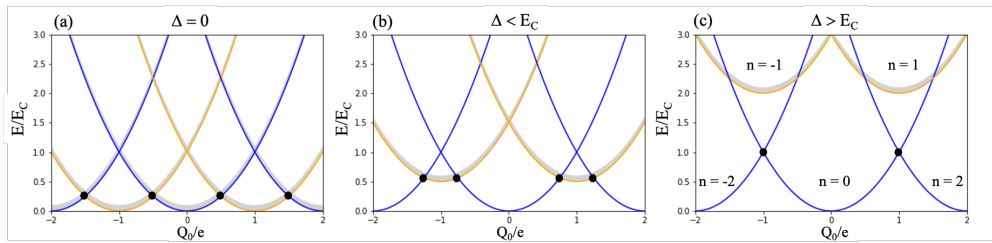
Figure 2.6: Island energy as a function of gate charge. Blue (orange) curves represent even (odd) parity. Black dots indicate degeneracy points where n in the ground state changes and charge transport without an energy barrier occurs at zero temperature. Grey shading represents a continuum of quasiparticles above the gap for odd n values or in the normal island (a) with e periodicity. (b) Superconducting island with $\Delta < E_C$. (c) Superconducting island with $\Delta > E_C$

Averin and Nazarov [95] introduced an addition energy to make a distinction between these two ground states. This energy shifts the odd N parabolas by Δ in energy while the even N parabolas stay unchanged (Fig. 2.6(b) and (c)). The relative strength of Δ and charging energy E_C on the island results in two situations: $\Delta < E_C$ and $\Delta > E_C$.

In the first case, when sweeping the gate charge, electrons enter the island one at a time. In the second situation, as the gate is swept the ground state always stays at even N transitioning from N directly to $N + 2$. This is the $2e$ charging effect, which indicates

---

[4]It is assumed that the neutral island has even number of electrons so n (excess electrons) and N (conduction electrons) have the same parity.

transport through the island without quasiparticle poisoning.

The ability to resolve charge parity on an island is essential for topological quantum computing as well as transmon qubits, where it provides a qubit state readout mechanism. In Chapter 6 we show this charge parity stability in a tin island on Sn-InSb nanowires.

2.4 Circuit quantum electrodynamics

In circuit quantum electrodynamics (circuit QED) an artificial atom is coupled to a transmission feedline through a cavity resonator. The resonators are on-chip lithographically fabricated superconducting electronic components operating at microwave frequency. The artificial atoms can be spin ensembles, quantum dots, Josephson junctions, Andreev bound states, qubits or simply a two-level system [96, 97, 98, 99, 74, 100, 101, 102]. The interaction between the artificial atom and resonators can be described by Jaynes-Cummings Hamiltonian [103].

$$H_{JC} = H_{qubit} + H_{cavity} + H_{interaction} = \frac{\hbar \omega_q}{2} \sigma^z + \hbar \omega_c (a^\dagger a + \frac{1}{2}) + \hbar g (a^\dagger \sigma_- + a \sigma_+), \quad (43)$$

where ω_q is the qubit frequency, $\sigma^z = |g\rangle\langle g| - |e\rangle\langle e|$, ω_c is the resonator frequency, $a^\dagger$ and a are photon creation and annihilation operators, g is the coupling strength between qubit and cavity, and σ_- and σ_+ are qubit lowering and raising operators, respectively. The coupling Hamiltonian describes the interaction between the qubit and the cavity, i.e, excitations can be swapped from the qubit to the resonator and vice versa.

Qubit-cavity detuning is defined as $\delta = |\omega_q - \omega_c|$. In the limit of large detuning $\delta \gg g$, the coupling term yields a dispersive spectrum and the resonator experiences a qubit-state dependent frequency shift. The dispersive approximation yields

$$H_{dispersive} = \frac{\hbar \omega_q}{2} \sigma^z + \hbar \omega_c (a^\dagger a + \frac{1}{2}) + \chi a^\dagger a \sigma^z, \quad (44)$$

where $\chi = \frac{g^2}{\delta}$ is the dispersive shift [104]. This so-called forth order term manifests itself as a change in the phase and magnitude of the transmission spectrum.

2.4.1 Superconducting resonators

Superconducting resonators are on-chip electronic circuits which demonstrate high quality factors and can have long coherence times[5]. They can mediate a strong coupling between the transmission feedline and qubits, spins in quantum dots, etc [106, 107]. They also allow for coupling of multiple qubits of different kinds through resonator modes [108, 96, 109, 110, 101, 111].

On-chip resonators are defined by patterning a thin superconducting film that is deposited onto a substrate. The superconductor is either selectively deposited or etched. The former universally results in lossier resonant circuits due to a higher surface distribution of two-level systems [112, 113, 70]. We employ two commonly used and well-developed resonator geometries in this thesis: coplanar waveguide resonators and compact LC resonators. The resonances of both kinds are controllable by design, and we can have multiple resonators with different fundamentals coupled to a transmission feedline in one chip. Below is a short introduction to them. These resonators are then utilized to build hybrid semiconductor-superconductor circuits.

2.4.1.1 Coplanar waveguide resonator

A coplanar waveguide (CPW) consists of a signal carrying center pin that is separated by a gap from the ground plane on both sides. The electric field propagates in the gap between the center pin feedline and the two ground planes. The impedance of the line is given by the geometrical properties such as center line width w, gap spacing g, superconducting film thickness t and the substrate dielectric material ε_r indicated on the bottom left panel of Fig. 2.7. These parameters are set such that the impedance of CPW matches the 50 Ω characteristic impedance of external coaxial cables to avoid partial reflection of the signal.

A CPW resonator is formed by interrupting the center pin feedline either on both ends (half-wavelength CPW) or on one end while the other end is shorted to the ground plane

---

[5]The loss of a circuit is measured by quality factor, $Q \propto \dfrac{average\ energy\ stored}{energy\ loss/second}$ [105]. Thus the quality factor is a characteristic of resonators where a higher Q means a lower loss.
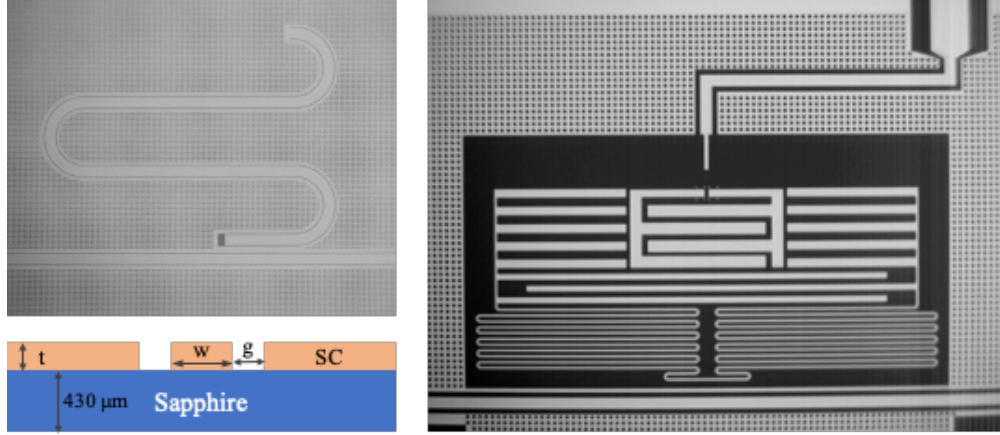
Figure 2.7: (Left) A $\lambda/4$ CPW resonator coupled to a transmission feedline. The cartoon indicates the parameters that define the impedance of a CPW that is patterned on a sapphire substrate. t is the thickness of superconducting film SC, w is the width of the CPW center pin, and g is the gap between center pin and ground plane. (Right) A transmon capacitively coupled to a compacted resonators which itself capacitively couples to a transmission feedline.

The coupling strength in this capacitive coupling scheme depends on the length of the resonator in parallel to the feedline (l_c) and the width of the ground plane between the two (g_c). The longer l_c and the smaller g_c result in stronger coupling. The coupling strength is inversely proportional to coupling quality factor Q_c.

(quarter-wavelength CPW). The resonant frequencies are given by:

$$\lambda/2 : f_n = \frac{c}{\sqrt{\varepsilon_{eff}}} \frac{n}{2l}, \qquad \lambda/4 : f_n = \frac{c}{\sqrt{\varepsilon_{eff}}} \frac{2n-1}{4l} \qquad (n = 1, 2, 3, ...), \qquad (45)$$

where $\varepsilon_{eff} = \frac{1+\varepsilon_r}{2}$ is effective dielectric permittivity of the device and l is the length of the resonator. These fundamentals are calculated considering only geometrical inductance, L_g, of the resonator in the resonant frequency expression (for quarter wavelength)

$$f_0 = \frac{1}{4l\sqrt{L_g C}}$$
$$L_g = \frac{\mu_0}{4} \frac{K(k')}{K(k)} \qquad (46)$$
$$C = 4\varepsilon_0 \varepsilon_{eff} \frac{K(k')}{K(k)},$$

where μ_0 and ε_0 are vacuum permieability and permittivity, respectively, K are complete elliptic integrals of the first kind, $k = \frac{w}{w+2g}$, and $k^2 + k'^2 = 1$.

However, the total inductance is the sum of the aforementioned geometrical inductance and the kinetic inductance. The kinetic energy attributed to moving electrons (current flowing in a wire) results in a kinetic inductance that depends on geometry as well as λ London penetration depth of the superconductor [114]:

$$L_K = \mu_0 \frac{\lambda^2}{tw} G(t, w, g)$$

$$G(t, w, g) = \frac{1}{2k^2 K^2(k)} [-\ln \frac{t}{4w} - k \ln \frac{t}{4(w + 2g)} + \frac{2(w + g)}{w + 2g} \ln \frac{g}{w + g}],$$
(47)

from which we can see that decreasing the cross sectional area of the center pin (tw) results in increasing kinetic inductance L_K as $G(t, w, g)$ is not sensitive to those parameters. This derivation uses the assumption that the film thickness is smaller than the penetration depth and the current density is uniform across the film thickness.

The resonant frequency with contributing kinetic inductance will then be

$$f_0^K = \frac{1}{4l\sqrt{(L_g + L_K)C}}.$$
(48)

Thus the resonant frequency of a CPW resonator can be modified by the ratio of kinetic inductance to total inductance. The kinetic inductance fraction is defined as

$$\alpha = \frac{L_K}{L_K + L_g}$$
(49)

and by measuring the resonant frequency f_0^K and comparing it with 45 and 46 one can find the kinetic inductance boost. In Chapter 7 we design and measure resonators based on thin film Nb alloy family superconductors in which kinetic inductance modifies the resonant frequency, resulting in shorter CPW resonators compared to thick film resonators where kinetic inductance boost is not significant.

2.4.1.2 Compact resonator

A compact resonator consists of two parallel subresonators, one with a large inductance and the other with a large capacitance. They are not considered fully lumped elements as their size is comparable to the wavelength. The inductance is provided by a thin long meandered wire and the capacitance comes from interdigitated fingers. Both the inductance and the capacitance are characterized by the total length and the width of traces as well as the spacing between them. The frequency ω_0 of a compact resonator with inductance L, capacitance C and impedance Z_0 results from following relations:

$$C = \frac{1}{\omega_0 Z_0}, \qquad L = \frac{Z_0}{\omega_0} \tag{50}$$

and does not exhibit equally spaced fundamentals.

Ref. [115] provides an extensive study on different parameter values for these resonators and their quality factors from which we extracted relevant scales for our resonator designs in Chapter 7. These parameters provide more flexibility for improving the quality factors of compact resonators compared to CPWs where only the center pin width and the gap size are changeable.

The structure of these resonators, as shown in Fig. 2.7, makes them suitable for capacitive coupling. We use a thick film Al superconductor for our first attempt to make a hybrid superconductor-semiconductor transmon qubit in Chapter 7.

2.4.1.3 Resonator quality factor measurement

As mentioned earlier the quality factor is an indication of loss mechanisms in the system at a given resonance. The higher the quality factor the longer a photon can resonate before it is lost. Measuring transmission through the feedline can give information about the resonant frequency f_r, the resonator's intrinsic quality factor Q_i, and coupling factor Q_c. This measurement is called the "hanger measurement" and comes from the hanger coupling of resonators to the transmission feedline as shown in Fig. 2.7. While measuring the transmission and sweeping the frequency through the feedline, the signal will be absorbed in a resonator at its resonant frequency. This will cause a dip in transmission and the deviation from the transmission value away from the resonance is used to extract Q_i. The width of

this dip is a measure of the loaded quality factor defined as $1/Q_l = 1/Q_i + 1/Q_c$. One can extract the values of the quality factors by fitting the Lorentzian transmission curve to the complex-valued transmission S_{21} (detailed derivation from Ref [116, 115]):

$$S_{21} = \frac{Q_c + iQ_cQ_i(2\frac{f-f_r}{f_r} + 2\frac{\delta f}{f_r})}{Q_i + Q_c + 2iQ_cQ_i\frac{f-f_r}{f_r}} \tag{51}$$

where δf is characterizing asymmetry in the lineshape. If the lineshape is symmetric then $\delta f = 0$. An example of an asymmetric hanger measurement and fitting is shown in Fig. 2.8.
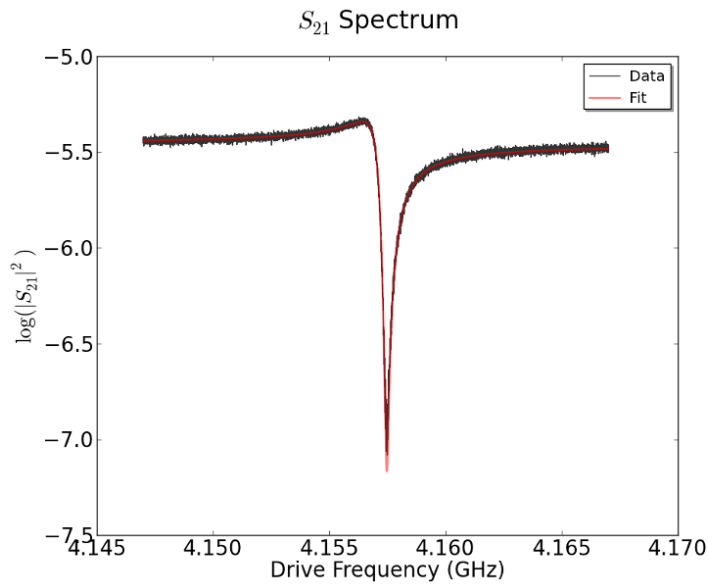
Figure 2.8: Transmission response of a 50 nm thick NbTiN quarter wavelength CPW resonator near its resonant frequency. Quality factors are extracted by fitting data using Eq. 51, $Q_i \approx 30000$ and $Q_c \approx 6000$.

2.4.2 Superconducting qubits

Superconducting qubits have shown great progress on the path of quantum information and building a quantum processor [117, 69, 118]. They are based on Josephson tunnel

junctions. The Josephson current shown in Eq. 33 results in low loss nonlinear inductance:

$$I_J = I_0 \sin \varphi$$
$$V = \frac{\hbar}{2e} \frac{d\varphi}{dt} \qquad (52)$$
$$\frac{dI_J}{dt} = \frac{2e}{\hbar} V I_0 \cos \varphi$$

By definition $V = L_J \frac{dI_J}{dt}$, thus the inductance is

$$L_J = \frac{\hbar}{2e} \frac{1}{I_0 \cos \varphi} \qquad (53)$$

If one replaces the inductor in a quantum harmonic LC oscillator by a Josephson tunnel junction which has a nonlinear inductance, the circuit can be described with an anharmonic oscillator potential. The energy levels then have different spacing, where $E_{01} \neq E_{12}$, and the two lowest levels can be used as the qubit basis. Generally, a large anharmonicity, $\alpha = E_{01} - E_{12}$, is preferred in order to address ground and excited states without exciting higher levels. One of the first circuits that was used as a two-level system was a Cooper pair box (CPB) [119]. A CPB consists of a superconducting island that is separated from a superconducting reservoir by a Josephson tunnel junction and a gate capacitor that adds charges to the island. The two levels are the charge states of Cooper pairs from the island tunneling on and off through the junction. CPB suffers from a very short coherence time as the qubit states are very sensitive to charge fluctuations. The Hamiltonian of CPB can be modified by adding additional circuit elements like capacitors and inductors. The potential energy and qubit properties such as sensitivity to charge noise and anharmonicity then can be engineered based on the relative energy scales of these circuit elements. Here we give a short introduction to two alternative qubits that we attempted to build out of hybrid superconducting-semiconducting circuits. They tackle the offset charge fluctuation by shunting the Josephson junction in two different ways: by a large capacitor (transmon) or a large inductor (fluxonium).

2.4.2.1 Transmon

A transmon [120] consists of a Josephson junction in parallel with a large shunting capacitor. The transmon is then less sensitive to charge noises by decreasing the charging energy scale $E_J \gg E_C$. Here $E_J = \frac{\hbar}{2e}I_c$ is the Josephson energy in which I_c is the junction's critical current, and $E_C = \frac{e^2}{2C}$ is the charging energy where C is the sum of the junction and external capacitances. The Hamiltonian of a transmon is the same as that of a Cooper pair box:

$$H_T = -4E_C\frac{\partial^2}{\partial\varphi^2} + E_J\cos\varphi, \tag{54}$$

where in the limit of $E_C \ll E_J$, charge ($\hat{n} = \frac{\partial}{\partial\varphi}$) is not a good quantum number anymore, and $\alpha \sim E_C$, that is reduced to orders of a couple of hundreds of MHz.

In Chapter 6 we will introduce a new superconductor-semiconductor hybrid (Sn-InSb) which exhibits 2e-charging effect. 2e-periodic charging pattern that was previously only seen in Al is an indication of long quasiparticle stability time [121]. Quasiparticle hopping between superconducting islands or single electron tunneling is a source of decoherence as fluctuations of the quasiparticle number on superconducting islands scramble qubit readout. Hence, long quasiparticle stability time is essential for long transmon lifetime as well as topological quantum computing [122, 123]. One can implement a transmon using hybrid structure as a tunnel junction which allows tuning the transmon by means of local gate voltages. The gate controls the carrier density in the semiconducting weak link which in turn modifies Josephson energy as well as qubit fundamental frequency and anharmonicity. Such devices have already been demonstrated in InAs nanowires and 2DEGs [74, 75, 100]. They have exhibited coherence times of $\sim 5\,\mu$s and demonstrated compatibility with external magnetic fields up to 100 mT. In Chapter 7 we attempt to use Sn-InSb in hybrid transmon circuit where higher critical field of tin compared to aluminum allows for entering a more robust topological regime for parity protected quantum computation [122].

2.4.2.2 Fluxonium

A Fluxonium [124] circuit consists of a Josephson junction shunted by a large inductance L and a capacitance C. This large inductance shunts charges across the junction and protects

the circuit from low-frequency charge fluctuations, even when E_J and E_C are comparable ($1 \leq E_J/E_C \leq 10$). Hence, there is no need for large shunting capacitance and anharmonicity is not reduced. The Hamiltonian then gets an added inductive term:

$$H_F = -4E_C \frac{\partial^2}{\partial \varphi^2} + \frac{E_L}{2}\varphi^2 + E_J \cos\left(\varphi - 2\pi\frac{\Phi_{ext}}{\Phi_0}\right), \qquad (55)$$

where $E_L = \frac{(\hbar/2e)^2}{L}$ is the inductive energy. The inductance is large enough such that $E_L \ll E_J$ which results in two well-separated potential minima when operated at the "sweet spot" $\Phi_{ext} = \Phi_0/2$.

The so-called "superinductance" (an inductance whose impedance exceeds the resistance quantum $h/(2e)^2 \simeq 6.5\ k\Omega$ at microwave frequencies below its self-resonant frequency $\sim 100\ nH$) [125] is conventionally provided by an array of many Al/AlO$_{\text{x}}$/Al tunnel junctions in series. Ref. [126] recently demonstrated reproducible high coherence times ($> 100\mu$s) in these conventional fluxoniums. However, the high number of many Josephson junctions per qubit could be a serious fabrication challenge. Moreover, Ref. [55] proposes a scheme where a fluxonium is coupled to a Majorana qubit for which the fluxonium needs to be able to perform in external magnetic fields for entering the topological regime. Al/AlO$_{\text{x}}$/Al tunnel junctions are not field compatible, and one can provide the superinductance needed with the high kinetic inductance of field resilient Nb family superconductors [71, 127, 128]. In Chapter 7 we study meander nanowire resonators made from thin films of disordered NbTiN superconductor sustaining their quality factors in finite magnetic fields.

3.0   Fabrication methods and experimental setups

This chapter describes the fabrication methods for Ge/Si and InSb nanowire devices as well as Josephson junction fabrication in InAs quantum well. Fabrication recipes for superconducting circuits compatible with semiconductor nanowires are also discussed. The last section of this chapter shows schematics of the measurement setups both for DC quantum transport measurements in semiconducting systems and standard microwave techniques for studying superconducting circuits.

3.1   Semiconductor structures

The Ge/Si nanowire growth was performed at the Center for Integrated Nanotechnologies (CINT), U.S. Department of Energy, Office of Basic Energy Sciences User Facility at Los Alamos National Laboratory and Sandia National Laboratories.

InSb nanowires were grown at Eindhoven University of Technology and then shipped to Santa Barbara for depositing Al and Sn shells at University of California Santa Barbara.

InAs quantum well structures were fully grown at University of California Santa Barbara.

3.1.1   Ge/Si core/shell nanowires

The Ge/Si core/shell nanowires used in this thesis were grown in a low pressure, cold wall chemical vapor deposition (CVD) system [129]. Au colloids with different diameters were used on a (111) Ge substrate to grow the Ge core with radii of $10 - 15$ nm. The Si shell thicknesses were calibrated between 1 to 4 nm [130]. The inset schematics in Fig. 3.1 shows the type II band alignment with a valence band offset of 500 meV between Ge and Si at the core/shell interface, where holes accumulate in the Ge core as the Fermi level lies just below its valence band edge. This free hole gas is present without any intentional doping in either Ge or Si which is essential in eliminating scattering processes from ionized dopants [56].

Fig. 3.1 shows room temperature gate pinch-off trace of a field effect transistor made with these nanowires where we see ambipolar behavior of charge carriers. All devices measured in this thesis are studied in the p-type depletion mode.
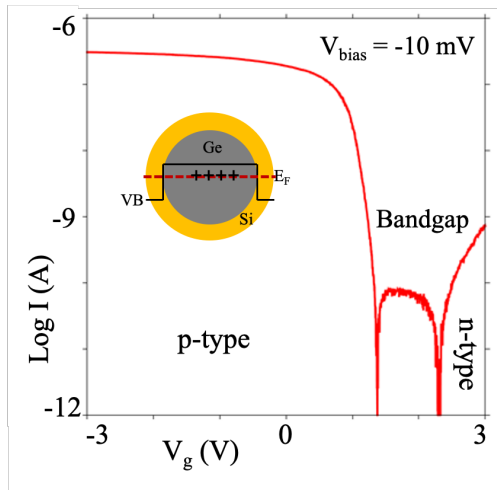
Figure 3.1: Inset: Due to an offset of 0.5 eV between Ge and Si valence bands, hole gas forms in the Ge core. Room temperature pinch-off trace of a nanowire connected to two contact leads on global back-gate chip showing ambipolarity.

Both Ge and Si are group IV elements with low abundance of nonzero nuclear spin isotopes [56], reducing hyperfine interactions. Furthermore, holes with their p-wave symmetry weakly couple to nuclear spins, if any left, increasing spin relaxation times [59]. In addition, the expected large spin-orbit interaction in the valence band [60] make these nanowires a potential platform for electrical spin manipulation as well as studies of Majorana modes.

3.1.2   InSb nanowires

The InSb nanowires used in this thesis were grown by metal-organic vapor phase epitaxy (MOVPE) with high aspect ratios [131]. They have zincblende lattice structure with a hexagonal cross section (also shown in Fig. 3.2). Their diameters are $80 - 120$ nm and they are $2 - 4$ μm long. Recent advances in engineering of these structures allow for high crystalline quality of superconductor-semiconductor junctions as well as for the precise location and size of junctions [65, 132, 133, 134]. On the one hand, the giant g-factor and strong spin-orbit interaction [135, 67] along with small band gap of ≈ 170 meV and high mobility up

to 10^4 cm^2/(Vs) makes these nanowires an extremely promising platform for Majorana studies [136]. On the other hand, the versatile nanowire weak link-superconductor compositions endorse these structures for hybrid superconducting-semiconducting qubits.

3.1.3   Epi-Al/InAs 2DEG

InAs, like InSb, benefits from small band gap energy, large Landé g-factor and strong spin-orbit interaction which are crucial for stability of non-trivial topological phases [136]. Moreover, a two-dimensional structure allows for wide variety of network design and scalability. However, a highly transparent contact between InAs quantum well and Al superconductor was achieved a few years ago which made these systems available for hybrid devices [137]. The InGaAs-InAs-InGaAs quantum well used in this thesis were grown on a semi-insulating InP (100) substrate, using a modified VG-V80H molecular beam epitaxy (MBE) system. The InAs 2DEGs mobility is ≈ 25000 cm^2/(Vs) with electron density of order of 10^{12}/cm^2 yielding mean free path of ≈ 200 nm. As shown in Fig. 3.2 InSb nanowires are deposited on quantum well's surface providing a shadow mask for Al superconducting layer.
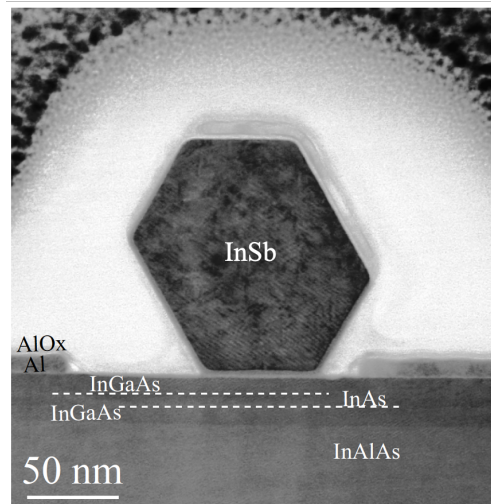
Figure 3.2: Transmission electron microscope image of the cross-section of InAs quantum well. An InSb nanowire with hexagonal cross-section is providing a shadow mask where there is a break in the Al layer deposited on the 2DEG.

3.2 Device fabrication

There are many steps in superconducting-semiconducting structure fabrication that need to be working all at once to have a full working device. In this section I will go through all fabrication steps for nanowire devices (Ge/Si, InSb, Al-InSb, and Sn-InSb), including techniques used to improve the yields of working devices, the etching process for Al-InAs 2DEG-Al devices following Ref. [138], and superconducting circuits (NbTiN and Al resonators) for hybrid qubits.

3.2.1 General fabrication process for nanowires

1. **Substrate and markers.** All nanowire devices are made on doped Si substrate covered with 285 nm thermal SiO_2. (There is an extra layer of Si_3N_4 (30 nm) deposited on the substrate to protect SiO_2 against hydroflouric acid etch used in devices in Chapter 4.1.) First, 64 bonding pads along with markers are patterned with photo-lithography followed by metal deposition (Ti/Au 5/60 nm). Then using these markers a set of fine markers are patterned across the chips with electron-beam (e-beam) lithography for alignment purposes. These fine markers map the whole chips in areas of 100×100 μm^2 which is the common writing field size used in our e-beam lithography procedure (Fig. 3.3(a)).
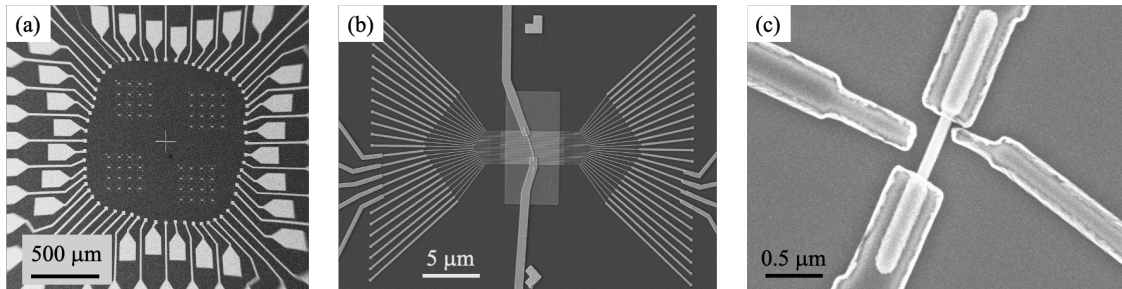
Figure 3.3: (a) An overall SEM of gate chip with bonding pads and alignment markers. (b) InSb nanowire placed on local bottom gate electrodes and contacted with source and drain leads. The gate fingers spread out and connect to bonding pads shown in panel (a). (c) InSb nanowire placed on a global backgate chip and semi-local side gates are lithographically added simultaneously with source and drain leads.

2. **Gates.** We use three gating methods: global back gate (backgate), local bottom gates (bottomgates), and local-ish side gates (sidegates) (shown in Fig. 3.3(b) and (c)).

   a. Back gate: The Si/SiO_2 substrate serves as a global back gate for Ge/Si devices in Chapter 4.1, Al-InSb devices in Chapter 5 and Sn-InSb devices in Chapter 6. Almost all nanowires are pinched off within the range of our high voltage source module which is ± 60 V.

   b. Bottom gates: Bottom gates are used to locally control the chemical potential along semiconducting nanowires and define quantum dots in series. The fabrication process of bottom gates used for devices in Chapter 4.2 and Chapter 5 are thoroughly discussed in Ref. [139]. The dielectrics used to cover bottom gates and electrically separate them from nanowires are HfO_2 by atomic layer deposition (ALD), or chemical vapor deposited (CVD) Si_3N_4. ALD grown HfO_2 is more homogeneous with lower possibility of pinholes and hence it is a more stable dielectric. Moreover, its dielectric constant is larger meaning we would be able to operate in a smaller gate voltage range.

   c. Side gates: Side gates are extra control knobs for local control of chemical potential along the nanowires with break tunnel junctions. Using back gate, we globally control the electron density along the whole nanowire and side gates will be able to effectively control the electron occupations in tunnel junctions and superconducting islands in Al-InSb and Sn-InSb devices in chapters 5 and 6.

   Side gates are also used in hybrid superconducting systems where substrates are either undoped Si or sapphire and bottom gate fabrication is not a feasible and effective design.

   In all cases sidegates are fabricated in the same step when source and drain contacts to nanowires are patterned, which I will explain below.

3. **Nanowire transfer.** We sonicate the substrate in acetone, followed by isopropyl alcohol (IPA) and O_2 plasma cleaning before putting down nanowires. Nanowires are then transferred either onto a global back gate chip or onto bottom gates. with

   a. Scanning electron microscope (SEM): Al-InSb nanowires for devices studied in Chapter 5 were transferred under SEM by Erik Bakkers's group in Eindhoven. This

technique is necessary only when nanowires are too short to be picked up under an optical microscope or there is a shortage of nanowires mother chip and is no longer needed as the growth techniques are enhancing over years and more reliable.

b. Micromanipulator: All other nanowire devices studied in this thesis are transferred using a micromanipulator under an optical microscope. We pick up nanowires with either indium tips or tungsten tips using the van der Waals force. We make indium tips from an indium bulb on a hot plate by sticking a needle into and out of it. These tips are extremely soft and bend very easily which require us to remake them after one or two nanowire transfers. The tungsten tips are harder which sometimes can break nanowires but is a faster method. One just needs to spray some IPA on the tip in case some nanowires are stuck to it and continue with the transfer.
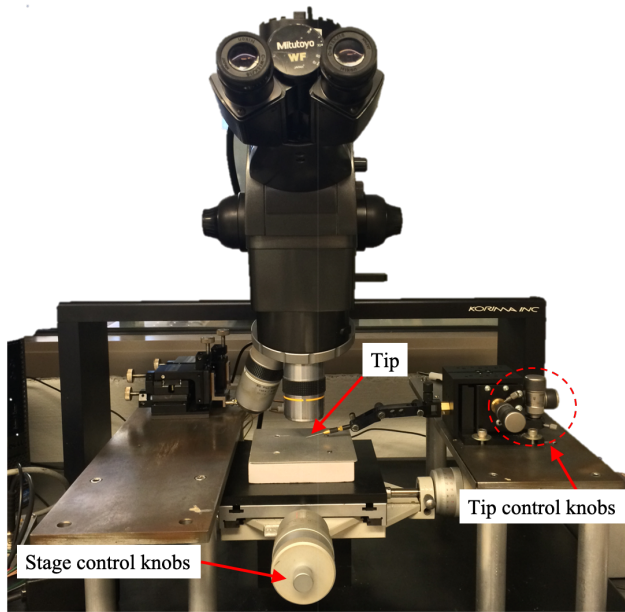
Figure 3.4: Nanowire transfer setup. The nanowire chip and Back gate or bottom gate chip are placed on the silver block. After locating the tip in the middle of eye piece field of view with 5X zoom, we switch to 100X zoom in which we can see the nanowires for picking up. The tip control knobs are most helpful for picking up nanowires and then for putting them down on the destination chip we recommend using a combination of tip and stage control knobs to slightly rob the nanowire on the surface until it falls down to the desired location.

4. **Design.** We dip the chip with nanowires in IPA and gently shake it. This removes those nanowires that are not properly laid down on the substrate. Then we image nanowires

and nearby markers with SEM. We use SEM to check for nanowires and gates quality, and to locate junctions in Al-InSb and Sn-InSb. Markers are used to align images in a CAD design program like KLayout. We then design lead contacts, side gates and bottom gate fingers for relevant devices.

5. **Coat electron beam resist.** We use PMMA (polymethyl methacrylate) as high resolution positive resist for e-beam lithography. The structures we pattern are from couple hundreds of nanometers to few microns wide, and the thickness of films we either evaporate or sputter in following steps are $60 - 150$ nm thick. Considering these geometries a successful resist profile should not be too thin (thinner than metal thickness) or too thick (larger than narrowest structure designed, for example the spacing between source and drain on nanowire). A resist that generically works for us well is PMMA 950K A4. We spin it for one minute with a speed of $3000 - 4000$ rpm which results in a homogeneous coat of $200 - 250$ nm thick. There is, however, a big problem with small size chips (smaller than 1×1 cm^2) where the resist leaves a thick and non-homogeneous profile around the edges. In this case we either increase the spinning speed or we wash away the resist and repeat the same procedure and be careful to put a smaller droplet of resist on the chip and move on with the rough edges. The thick resist on the edge in these chips with markers make it difficult to do initial alignment for e-beam patterning, but it will be manageable if three out of four corners have a reasonable resist profile. Next we need to get rid of the solvents in the resist before e-beam exposure.

   a. Baked resist: This is the common way to prepare the resist. We bake the chip at 175°C for 15 minutes. Before that we gently rub the chip on a piece of cleanroom tissue with acetone to clean the back side of the chip from any resist as this can sometimes cause charging issues and uneven focusing in the e-beam lithography machine (EBL).

   b. Cured resist: In the cases of Al-InSb and Sn-InSb nanowires we avoid baking the chip as the high temperatures can cause diffusion of Al and Sn into InSb. Instead, we cure the resist at room temperature by leaving the chip in a vacuum chamber for about 24 hours. This is also the case for InAs 2DEG Josephson junction preparation.
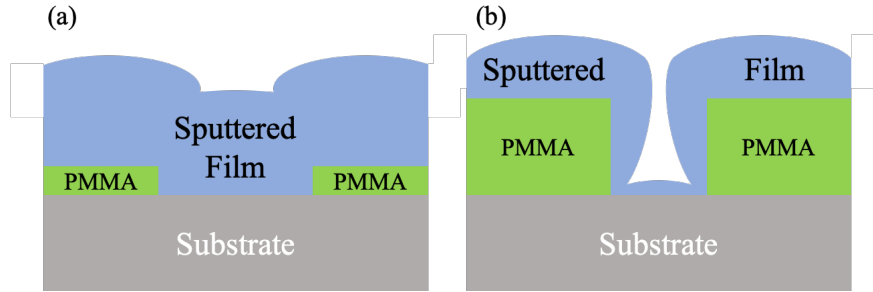
Figure 3.5: (a) The lift-off of the sputtered film may fail if the resist is too thin as it cannot strip off the substrate. (b) For narrow structures an ideal thickness of resist and sputtered film is more challenging to reach. As sputtering is non-directional the film deposits on the walls of the resist structure and prevents the exposed narrow channel to receive as much material. These issues are less severe in e-beam evaporation as it is directional, yet great caution needs to be taken for narrow structures.

6. **E-beam exposure.** In an EBL machine a focused beam of electrons attack the polymer resist molecules and break the bonds between them and leave the pattern that was designed (the case is reversed for a negative tone resist). We developed some parameters that are quite robust for most of the procedures in our laboratory. For patterns that are larger than few microns we use 60 μm aperture size to decrease the exposure time, however it is not always necessary. Other than this either a 30 μm or a 10 μm is used for all nanowire devices fabrication. The latter with e-beam accelerating voltage of 30 kV is sometimes used for sidegates that are closer than $\sim 50 - 100$ nm together. With an e-beam accelerating voltage of 10 kV for the 30 μm aperture a dose range of $110 - 160$ μC/cm^2 results in reliable and reproducible patterns.

7. **Develop.** A developer is used to fully break the bonds of polymer and remove the resist from exposed areas. We gently shake the chip in an infinity pattern for one minute in MIBK:IPA - 1:3 followed by one minute rinse in IPA. We then inspect the chip under an optical microscope to make sure there are no patterning issues such as misalignment or missed patterns. Sometimes if the resist is not cured well there are sharp edges from e-beam writing of patterns that only is resolved by striping the resist away and repeating the steps 5 through 7.

8. **Remove resist residues.** Gentle O_2 plasma cleaning (500 mTorr and 50 W for 15 seconds) is used to remove any residual of developed resist from the surface of nanowire.

9. **Surface oxide removal.** This step is perhaps the most important one resulting in a successful device with transparent contacts to a nanowire. There are three procedures used for devices studied in Chapters 4 and 5 as discussed below. However, for Al-InSb and Sn-InSb nanowires an atomic hydrogen cleaning step was done by our growth collaborators before Al and Sn deposition. Details are discussed in Chapter 6.

   a. BHF etch: A short ($\approx$ 2 s) buffered hydrofluoric acid etch seems to be removing the native oxide from Si shell on Ge/Si core/shell nanowires. The yield of junctions with low resistance are low but this method results in transparent contacts. After BHF etching for 2 seconds we deep the chip in water for one minute followed by a second deep for another one minute to make sure there is no acid residue left on the chip. A long acid etching is not recommended as it strips the PMMA. The SiO_2 of the substrate in global backgate chips is protected by CVD Si_3N_4 and the dielectric on bottomgates is HfO_2 which is immune to short BHF etching.

   b. Sulfur passivation: To remove the surface oxide on bare InSb nanowires used in Chapter 5 we use sulfur solution. (1) Mix and stir sulfur powder with ammonium sulfide with ratio of 10 mL/g for 30 minutes (use a small magnetic stir bar). (2) Dilute the ammonium solvent with water (1:250). (3) Bake the chip in the diluted solution at 55°C for 20 minutes. (4) Thoroughly rinse the chip with water and blow dry. It is extremely important to have the solvent solution fully covered with aluminum foil to block the light as light increases the etching rate and makes it less controllable (more details can be find in Peng Yu's thesis).

   c. Argon ion mill: Al-InSb and Sn-InSb nanowires are covered by few nanometers of AlO_x for protection against oxidization. Before making contacts to Al and Sn in these nanowires one needs to remove this oxide layer. This is done in deposition system using Argon atoms to gently bombard the substrate.

      i. Al-InSb. Done in AJA sputtering machine, 50 W, etch for 20 s with 40 s break to prevent hitting, for total of 6 minutes.

      ii. Sn-InSb. Done in Plassys e-beam evaporator, 250 V, 15 mA, mill for 30

seconds, wait for the chamber pressure to drop to e^{-7} mTorr (which takes $15 - 30$ minutes), mill for another 30 seconds.

10. **Metalization.**

   a. E-beam evaporation. Au, Pd, Ni were used to characterize Ge/Si nanowires in the early stages of quantum dot studies. Pd and Al were used for Al-InSb and Sn-InSb nanowire devices.

   b. Magnetron sputtering. NbTiN has been extensively used to make both ohmic and superconducting contacts to Ge/Si nanowire devices, as well as Al-InSb. However, in the latter case the superconductivity is induces by Al as it will be discussed in Chapter 5.

   Effects of stacking Al and NbTiN on Ge/Si devices will be discussed in section 3.2.3.

11. **Lift off.** We leave the chip in acetone usually for overnight to fully resolve the resist in remover and make sure of a clean and full lift off of metal layer on top of it. We use a pipette to squirt acetone to the surface of the chip and assist with lifting off of any film residues. Then we rinse the chip in IPA and blow dry.
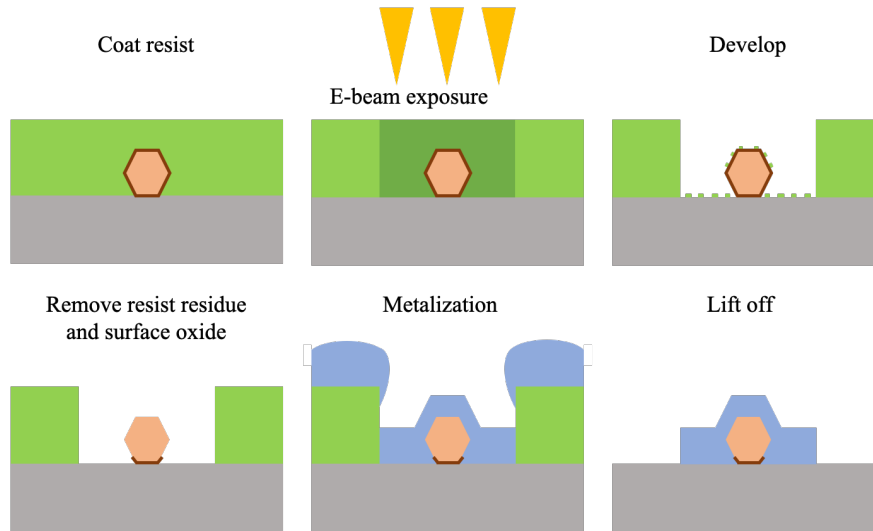
Figure 3.6: Side-view schematics of series of e-beam lithography steps introduced above. The proportions are not to scale.

12. **Post lift-off (deposition) treatments.** An essential post deposition step for Al-InSb and Sn-InSb nanowires is capping with AlO_x to terminate surface oxidation of thin Al

and Sn shells. The following procedures were used to improve contact transparency and suppress charge noises in Ge/Si devices.

a. Anneal Al

b. Encapsulate with Al_2O_3. This method is used to isolate the body of a device from the environment and prevents interaction with nearby charges. The pinch-off trace on backgate chips improved in the Coulomb blockade regime where it traced itself sweeping backgate forward and backward. However, the same method on bottomgate chips for DQD devices resulted in device instabilities such as increasing conductance as a function of time, making it impossible to further study spin transport.

3.2.2   Annealing Al in Ge/Si devices[1]

To improve the yield of transparent contacts we explore contact annealing in the presence of forming gas (5% H_2 and 95% N_2) at 1 bar. For NbTiN contacts with thin Al or Ti interlayers (3 nm), no measurable change in the saturation resistance is observed after annealing at temperatures up to 400°C for minutes. However, we observe that pure Al contacts alloy rapidly, within seconds, at temperatures as low as 180°C. Fig.3.7(a) displays the alloying of 200 nm regions next to each contact. Saturation junction resistances are reduced by more than one order of magnitude after the annealing in some devices. Low resistance (≤ 10 kΩ) devices are obtained with a high yield of $\sim 1/4$ for pure Al contacts. It is important to be aware of the Al-alloying effect because such low annealing temperature is close to the temperature used during standard nanofabrication. For example, electron beam resist PMMA is commonly baked at 175°C, so if following fabrication steps such as top gates are performed after pure Al contacts, those contacts are going to be annealed with the nanowires.

3.2.3   Effect of Al interlayer between Ge/Si nanowires and NbTiN[2]

In addition to improved contact tranparency we observe a systematic change in pinch-off voltage as a function of Al interlayer ratio to NbTiN. With increasing thickness of the Al

---

[1]This section is adapted from Ref. [140].
[2]This section is adapted from Ref. [140].
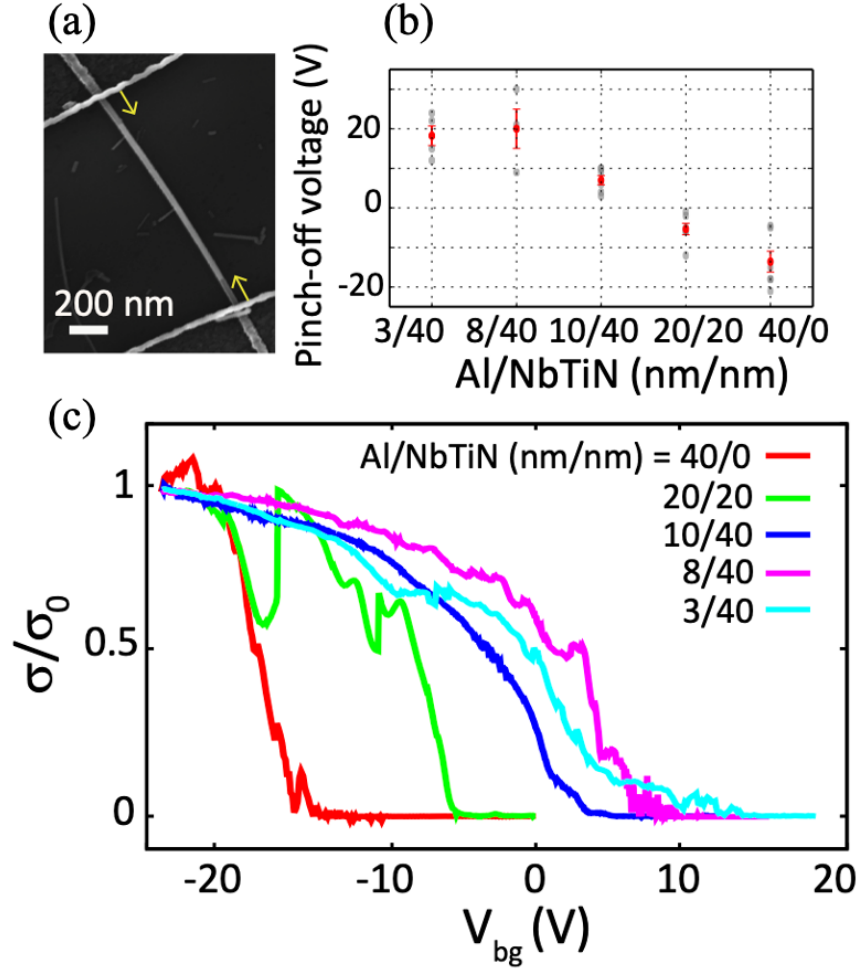
Figure 3.7: (a) Al-Ge/Si-Al device after a rapid annealing at 180°C. The arrows indicate alloyed regions of the nanowire. (b) Pinch-off voltages of 21 devices with various Al/NbTiN thicknesses. The average value for each Al/NbTiN thickness combination is indicated by the red dot. (c) Typical pinch-off traces of devices for various Al/NbTiN thickness combinations. The conductance is normalized by conductance σ_0 measured for each device at $V_{bg} = -24$ V.

interlayer, We find that the pinch-off voltages of the junctions decrease. Figs.3.7(b),(c) show the low temperature pinch-off voltage data from many unannealed devices with different Al and NbTiN layer thicknesses. Devices based on NbTiN with a thin Al interlayer have large positive pinch-off voltages. The increase of Al thickness reduces the averaged pinch-off voltages, which become negative for pure Al contacts. We argue that the pinch-off shift is due to remote doping of the nanowire due to workfunction mismatch between the Ge

core and the metal contacts. The workfunction of Ge (5.15 eV) [141] exceeds that of Al (4.06 - 4.26 eV) [142] consistent with n-doping. The workfunction of NbTiN alloy is not known, however the workfunctions of Nb (3.95 - 4.87 eV) [142] and TiN (4.5 eV) [143] are in between those of Ge and Al, which suggests lower n-doping with NbTiN than with Al. For thinner interlayers, no continuous Al film is formed and the contact is dominated by NbTiN. As Al thickness is increased, the doping of the nanowire is increasingly determined by the properties of the Al/Ge interface. The pinch-off voltages can also be affected by the interface between the nanowire and the gate dielectric. We observe that the pinch-off voltages tend to shift to more positive values when HfO_2 is used instead of Si_3N_4. Interfacial charges at the semiconductor/dielectric interfaces are likely responsible for this effect [144]. Combined, the effects of dielectric and interlayer thickness on pinch-off allow for device working point to be set to zero gate voltage, which is expected to minimize charge instabilities and gate leakage. In addition to these fabrication methods, we investigated a cooling technique for Ge/Si DQD devices to modify the pinch-off voltage further. The results of this bias cooling technique is shown in Fig. 3.8.
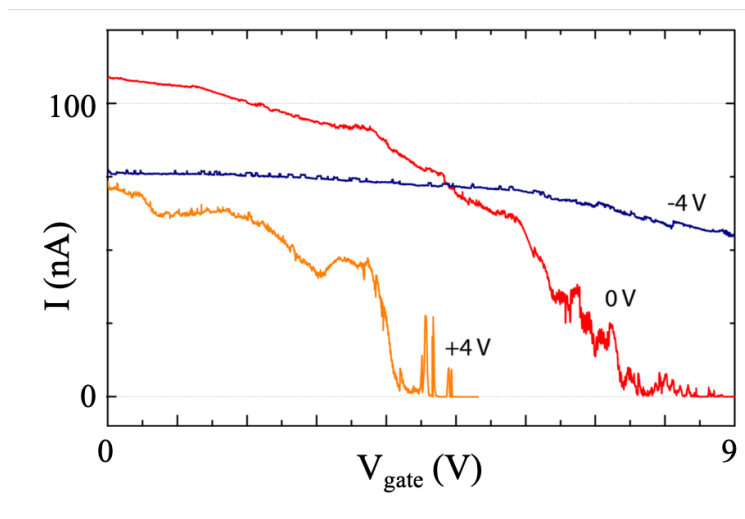
Figure 3.8: Annealing Al for bottomgate chips is not feasible as the high temperatures melt the Au electrode lines. Moreover, the HfO_2 dielectric used on bottomgates further increases the pinch-off voltage. This plot shows pinch-off trace (all bottomgates sweep together) of the same device in three subsequent cooldowns with different applied gate voltages. While cooling down from room to mK base temperature all gates are set to 0, -4 V, 4 V for red, blue, and orange traces, respectively. We evidently see the pinch-off voltage reduces and move closer to zero for orange trace.

3.2.4 Fabricating InAs quantum well smash junctions

Epitaxial growth of superconductor on two dimensional InAs quantum wells are fully demonstrated in Refs. [137, 145], in which highly transparent Josephson junctions (JJs) were demonstrated [146, 147]. Nevertheless, wet etching of the quantum well channel is inevitable in those studies to define the junction channel. Here we remove the etching step hence the junctions are immune from any chemical and physical contamination. We use InSb semiconductor nanowires grown with vapor-liquid-solid mechanism as shadow masks prior to superconductor deposition. Here we list the steps for sample preparation done by our growth collaborators:

1. The InAs 2DEG is grown following the procedure fully explained in Ref. [145] using molecular beam epitaxy (MBE) technique. Then its mobility, carrier density and sheet resistance is measured at room temperature as well as at 2 K.

2. InAs 2DEG is transferred in-vacuo (without breaking ultra high vacuum (UHV)) to a different UHV chamber. If the quantum well was grown earlier an atomic H cleaning procedure would be added to clean the surface followed by waiting time for the sample to cool down.

3. The nanowire mother chip is loaded in the same chamber. It is carefully mounted to overlap perfectly with the quantum well sample. The nanowires are brought into contact ("smash") with quantum well's surface where nanowires get transferred. The nanowires can be InSb (what we used in Chapter 8) or InAs covered by etch resistant dielectric like HfO_x.

4. Transfer the quantum well sample with nanowires smashed into, to another interconnected chamber for superconductor evaporation. Cool down the sample to ~ 85 K for 2 hours.

5. Evaporate superconductor of choice with desired thickness. We used $10 - 15$ nm Al in these experiments.

6. Cap the surface with either oxygen exposure forming a controlled native oxide in vacuum or with AlO_x from an e-beam source in the UHV, forming a slightly more impermeable controlled cap.

7. Wait for the sample to warm up for about 45 minutes.

8. Load out and unmount the sample within 1 hour of finishing superconductor evaporation. This time limit is really important as the gallium that is used to mount the sample in the chamber melts below and around room temperature and spreads like wild fire across the sample. And then the extra gallium needs to be rubbed off from the back of the sample since it still can move from back of the sample to the face of it.

After the sample has reached us we prepare the junctions for measurements. The following fabrication steps are taken:

1. **Alignment markers.** PMMA 950K A4 resist is spun and cured in a vacuum chamber to prevent diffusion of Al. Markers are patterned all over the chip with EBL (same parameters as discussed in 3.2.1) and 50 nm Pd is evaporated with e-beam evaporator. As the chips is few mm² and junctions are randomly spread throughout the whole chip numbering the markers are useful to be able to find junctions and align to markers in the following steps.
   Note. InAs quantum well chips are very fragile and mounting them on EBL stage needs extra caution for those who are used to handling Si and sapphire substrates.

2. **Design leads and bonding pads.** We then scan the chip with SEM and select junctions that are far from the edges, and design all devices with their corresponding bonding pads. Devices are consist of Josephson junctions and SQUIDs where two nanowires are found close to each other to form a loop.

3. **Deposit bonding pads.** Repeating the procedure in the first step we pattern and deposit bonding pads. We refrain from depositing Au to prevent possible formation of purple plague between Al and Au.

4. **Pattern leads.** Leads are patterned with EBL (30 μm aperture, 10 kV acceleration, dose of 200 $\mu C/cm^2$) using a negative tone resist (ma-N 2403 spun for 1 minutes with 4000 rpm) that was also cured in vacuum, and developed with maD 522 (for 70 seconds) followed by water (for 5 minutes). After developing the resist remains only where it was exposed by e-beam to define junctions' leads after etching.

5. **Etch Al and quantum well.** We exactly carried out steps fully explained in Ref. [138]

to etch Al with Transene D followed by quantum well etch.

a. Transene D in heat bath at 50° C for 10 seconds.

b. DI water in heat bath at 50° C for 20 seconds. Keep swirling in an infinity movement.

c. DI water for 60 seconds. You could change from acid tweezers to carbon tweezers after 40 seconds.

d. Blow dry with nitrogen for 1 minute.

e. 2DEG etch for 8 minutes. Use a stir bar at speed 4 to keep stirring the solution and swirl the chip at approximately 1 Hz.

   Your arms will be numb but you should keep going...

   (etch solution $\rightarrow H_2O/citric\ acid/H_3PO_4/H_2O_2 : 220mL/55mL/3mL/3mL$)

f. DI water for 40 seconds.

g. Blow dry with nitrogen for 1 minute and switch to acid tweezers.

h. Transene D in heat bath at 50° C for 10 seconds, swirl carefully.

i. DI water in heat bath at 50° C for 20 seconds, swirl vigorously.

j. DI water for 40 seconds.

k. Blow dry with nitrogen for 1 minute.

3.2.5 Fabrication processes for superconducting circuits

For superconducting resonators used in this thesis we use two different fabrication processes. One Nb-family resonators on sapphire substrate, and the other Al resonators on undoped Si substrate. For both kinds we first deposit the desired material of the desired thickness on a cleaned substrate. We then need to use similar lithography steps as explained before to define and deposit fine markers. These markers are needed when we want to add nanowires to the circuit.

3.2.5.1 Nb-family resonators

1. **Deposit superconductor.** Deposit 10 or 50 nm of NbTiN or NbN on a cleaned sapphire chip. We clean the sapphire substrate by ultrasonicating in acetone and IPA, but trying more rigorous cleaning techniques are encouraged.
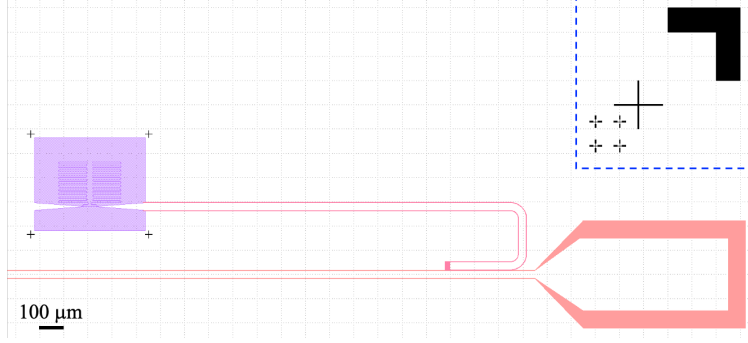
Figure 3.9: An example of design CAD showing the pink CPW transmission line and $\lambda/4$ cavity resonator, the purple meander resonator and black markers. The markers in the dashed blue box are repeated on all four corners of the chip for alignment and cutting purposes. The white area indicates the superconducting film. We note that the we are not showing squares of $4 \times 4~\mu m^2$ that will be added all over to trap magnetic vortices.

2. **Define markers.** We use 50 nm Au or Pd to achieve a reasonable contrast with Nb films under EBL. The big black marker as shown in Fig. 3.9 defines the four corner of a single resonator chip that is $2 \times 7~mm^2$. We map a 2 inch sapphire substrate with these markers.

3. **Pattern resonators.** Spin coat PMMA 950 A 4K on either the 2 inch sapphire wafer and then cut in in 4 smaller pieces or we could first cut the chip in 4 pieces and then continue with fabrication. Pattern CPW transmission line, CPW resonators, and meander resonators. We use 60 μm aperture, 20 kV acceleration, 250 $\mu C/cm^2$ dose for CPWs and 180 $\mu C/cm^2$ dose for meander resonators.

   a. **Anticharge layer.** For 10 nm thick films on a sapphire substrate one may need to add a 10 nm thick Al anticharge layer on top of the PMMA resist to avoid accumulation of electrons on the surface and drifting the beam preventing a stable patterning. If an anticharging layer is added, Developer MFCD 26 is used to remove it before developing PMMA with MIBK:IPA.

4. **Etch.** After developing we etch the patterns with mechanical ion milling (25 mA and 500 V). The etch rate is $\sim 1~nm/min$.

5. **Strip the resist.** We leave the chip in Acetone and ultrasonicate for about an hour.

The ion milling hard bakes the resist and it needs more time to be removed. We then do a $15 - 30$ minutes oxygen plasma cleaning to get rid of any resist and organic residues.

6. **Check for shorts.** We check for no electrical shorts on the chip mainly between transmission line and ground plane. The chip is now ready for cutting.

3.2.5.2 Al resonators

For these compact resonators that are made with optical lithography we first pattern and etch the resonators and then add EBL defined markers.
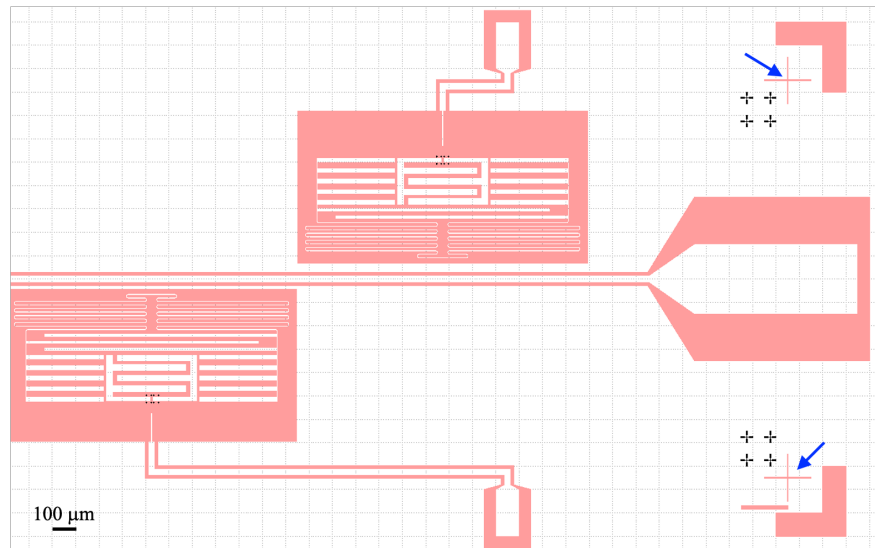
Figure 3.10: The design CAD for compact resonators coupled to a CPW transmission line and added gate lines. The pink patterns are written with optical maskless aligner followed by etching to define the resonators. The etched pink crosses pointed to by blue arrows are then used to define black fine markers with e-beam lithography.

1. **Deposit superconductor.** After cleaning an undoped pure Si wafer in Acetone and IPA followed by a 5 minute oxygen plasma cleaning we deposit 150 nm Al on the substrate.

2. **Coat resist**. For this fabrication we use optical lithography resist S1805 which we spin for 1 minute with 4000 rpm and bake at 115° for 2 minutes.

3. **Pattern resonators.** Using an optical maskless aligner we pattern CPW transmission line and compact resonators one a full 3 or 4 inch Si wafer. We used a dose of 41 mJ/cm^2.

4. **Develop and etch.** We use a solutions of MICROPOSIT 351 developer:water, 100 mL:400 mL for 2 minutes to develop S1805 resist. This alkaline developer etches Al while it is developing the resist. We also note that we found more reproducible results if we use an abundant volume of developer for a full 3 or 4 inch wafer. For example using a ratio of 50 mL:200 mK resulted in an underdeveloped pattern in some instances.

5. **Etch more.** The wet etching with developer leaves extra rough step-like edges on the patterns. We finish off etching by 15 seconds of reactive ion etching BCl_3/Cl_2, 40/50 sccm which results in sharp clean edges.

6. **Define markers.** We now can cut the full wafer in 4 smaller pieces and pattern and deposit fine markers with EBL to prepare the chip for nanowire transfer and subsequent lithography steps.

3.3 Chip carriers
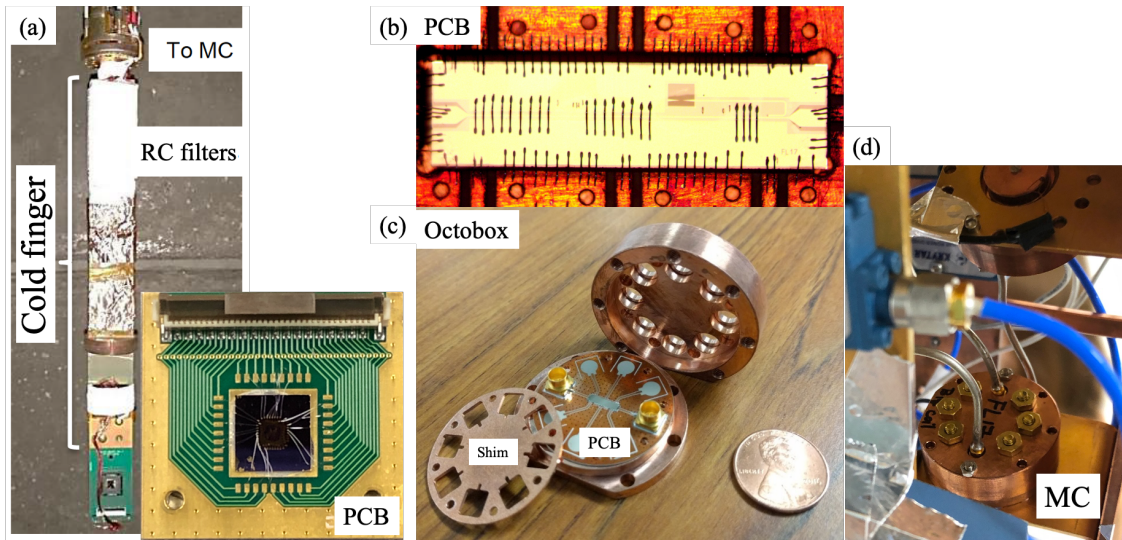
Figure 3.11: This figure is showing the chip carriers for (a) DC transport and (b, c) microwave measurements. (a) A cold finger that thermally connects to the mixing chamber (MC) stage of a dilution refrigerator from its top. The wire from room temperature to MC are thermally anchored to each stage to cool down the electrons carrying signal. The wires pass through copper powder filters which to cut out high frequency noise (up to a few GHz). Moreover, the RC filters with cutout frequency around 10 kHz are mounted on the cold finger and a wiring breakout from them goes to the printed circuit board (PCB) that holds the device chip. The inset is another version of PCB that we can use on the same cold finger. The wire bonds connects the device leads and gates to pins on the PCB. (b) A sapphire resonator chip with dimensions $2 \times 7 \ mm^2$ is mounted on and bonded to a PCB that has 8 CPW lines running on it. SMP straight plugs on PCB (limited detent Rosenberger 19S101-40ML5) connect to the center pin of CPWs. The PCB material is a copper board with Rogers AD1000 dielectric and it was ordered from Cirexx. (c) The PCB mounts on a copper Octobox and is covered by a shim to suppress extra resonances from the structure. (d) The Octobox mounts directly on the MC stage of a dilution refrigerator.

3.3.1 Dimensions in the Octobox

Table 3.1: Estimated resonant frequencies for components in an Octobox. Resonant frequency of the $\text{TE}_{nml}(\text{TM}_{nml})$ mode is: $f_{nml}^{E(M)} = \frac{c}{2\pi\sqrt{\mu_r \epsilon_r}}\sqrt{\left(\frac{p_{nm}^{E(M)}}{a}\right)^2 + \left(\frac{l\pi}{d}\right)^2}$, where $p_{nm}^{E(M)}$ are the roots of Bessel functions, $a = 19.5~mm$, $d = 11.51~mm$ are the radius and height of the Octobox. Almost are modes are outside our interest range of $2 - 8$ GHz.

Component	Length (mm)	Dielectric constant	Estimated frequency (GHz)
Octobox TE111	a, d	≈ 1 (copper)	13.8
Octobox TM010	a, d	≈ 1 (copper)	6.02
Octobox TM110	a, d	≈ 1 (copper)	9.598
Octobox TM210	a, d	≈ 1 (copper)	12.86
Octobox TM011	a, d	≈ 1 (copper)	14.34
Chip slot length (width)	7 (2)	1 (vacuum)	21.4 (74.9)
Shim slot length (width)	8.92 (5.87)	1 (vacuum)	16.8 (25.5)
Shim slot depth	0.43	1 (vacuum)	349
Bonding wires	0.75	≈ 1 (aluminum)	199

3.4 Measurement schemes
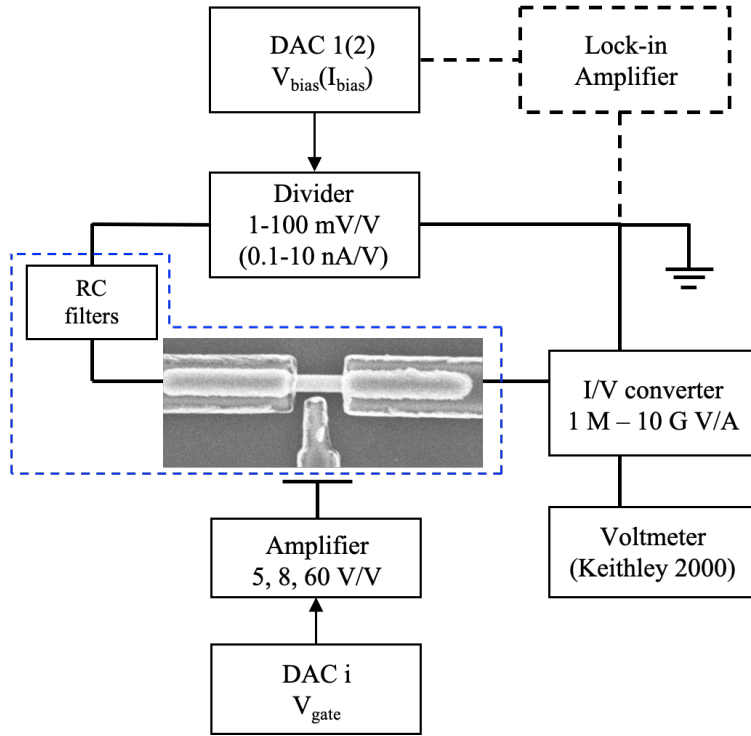
Figure 3.12: DC transport measurement setup. Voltage and current biases along with voltages on gate electrodes are applied to a device through digital to analogue converters (DACs). The voltmeter reads the measured signal from both DC and lock-in amplifiers. The lock-in signal measures the differential conductance (or resistance) with suppressed noise with the expense of longer measurement time. All DACs are powered by DC batteries to avoid interference and fluctuations from city electricity and computers. The signal from computer to DACs is carried out by an optical fiber. The breakout box between DACs and the device contains π filters at room temperature to filter noises from 10 MHz to 100 MHz. The nanowire device and RC filters in blue dashed box sit at mixing chamber stage of the dilution refrigerator.
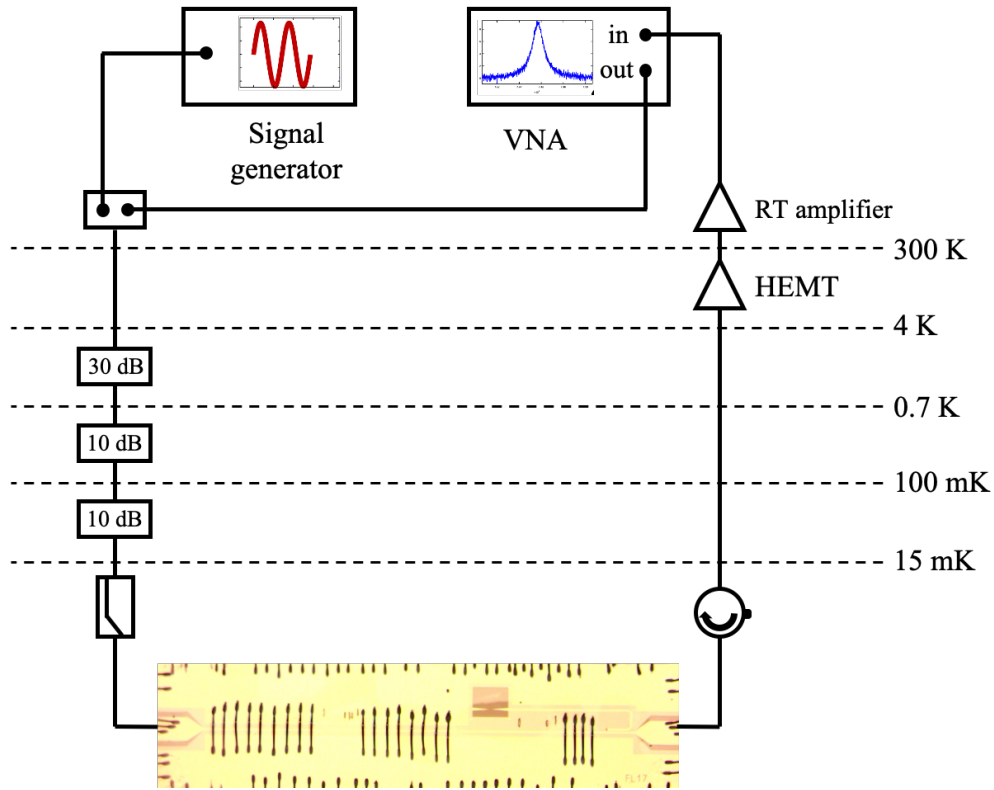
Figure 3.13: Microwave measurement setup. Cavity drive from vector network analyzer (VNA) and the spectroscopic microwave drive for two-tone continuous wave spectroscopy from a signal generator are combined in a single coax line at room temperature. The line is attenuated at the 4 K, still and 100 mK stages before connecting to an ECCOSORB (CR-124) or K&L low-pass filter then connected to the chip transmission feedline. The feedline output is then isolated by a circulator. The signal is amplified at the 4 K stage by a HEMT amplifier (LNF-LNC0.3-14A s/n 1269Z) and at room temperature by one or two Miteq amplifiers. The signal goes back to VNA and digitized and saved for processing.

4.0 Induced superconductivity and spin-orbit interaction in Ge/Si core/shell nanowires[1]

In the context of topological quantum circuits transparent contacts between high critical field superconductors and semiconductor nanowires with large spin-orbit interaction and Landé g-factor are crucial. Moreover, studies of spin blockade in quantum dots are largely motivated by the proposals to build a spin-based quantum computer [9], as spin blockade can be used for qubit initialization and readout [81, 11].

In the first section of this chapter we achieve such contacts between NbTiN and Ge/Si core/shell nanowires. We demonstrate gate-tunable supercurrent in NbTiN-Ge/Si-NbTiN junctions and observe supercurrents up to magnetic fields of 800 mT. The induced superconducting gap is characterized in the co-tunneling regime of transport through quantum dots. We then perform transport measurements on double quantum dots defined in Ge/Si core/shell nanowires in the second section to measure spin-orbit coupling by focusing on Pauli spin blockade in the regime where tens of holes occupy each dot. We estimate a lower bound on the spin-orbit parameter corresponding to an upper bound of $l_{\mathrm{so}} = 500$ nm for the Rashba spin-orbit length. We also extract effective Landé g-factors up to 8.0 from field-dependent spin blockade measurements.

---

[1]This chapter is adapted from Refs. [140, 148].

4.1 High critical magnetic field superconducting contacts to Ge/Si core/shell nanowires

4.1.1 Introduction

Josephson junctions based on semiconductor nanowires have become a fertile research platform in recent years. Charge tunability of semiconductors has been used to implement supercurrent transistors [35], Josephson π-junctions [34] and Cooper-pair beam splitters [36]. More recently, theoretical proposals for realizing Majorana zero modes in semiconductor - superconductor hybrid structures [4, 5] have led to a series of experiments that began accumulating evidence for these exotic quantum states [67, 149, 150, 151, 152, 68, 153]. Majorana studies have focused on InAs and InSb nanowires which are characterized by strong spin-orbit interaction, large effective Landé g-factors, ballistic transport along the NW, and induced superconductivity in the NW.

Ge/Si core/shell nanowires have been proposed for Majorana studies owing to the strong spin-orbit coupling in the valence band [154]. Recent experiments have established the one-dimensional hole gas [56] and ballistic quantum transport [155]. Strong spin-orbit interaction and large effective Landé g-factors have been extracted from both quantum dot and bulk nanowire measurements [62, 64, 156, 155, 148]. The last component, induced superconductivity from high critical magnetic field superconductors, is missing. Although supercurrent is observed in Al-Ge/Si-Al junctions [157], pure Al contacts are not suitable for topological quantum circuits based on Majorana zero modes due to the low bulk critical magnetic field of Al.

In this chapter, we report superconductivity in Ge/Si nanowires induced by niobium titanium nitride (NbTiN) whose critical magnetic field is large. We demonstrate the Josephson supercurrent through NbTiN-Ge/Si-NbTiN junctions to high magnetic fields of order 1 Tesla, as required for Majorana experiments. We evaluate the induced gap in the nanowire through co-tunneling in the pinched-off regime of the junctions. The devices are fabricated on doped Si substrates which serve as back gates. The substrates are covered by thermal SiO_2 (285 nm) and chemical vapor deposited Si_3N_4 (50 nm) (Fig. 4.1(a)). Ge/Si nanowires

with core diameters of 20-40 nm and shell thickness of 2 nm [158, 159, 129, 130] are randomly deposited on the substrate. The superconducting leads are patterned by electron beam lithography with nominal spacing of 200 nm followed by magnetron sputtering of NbTiN. One 3 nm interlayer of Ti (devices A and B) or Al (device C) is deposited prior to NbTiN. Before the metal deposition, two-second buffered hydrofluoric acid etch is performed to remove the native oxide on the surface of nanowires. Note that substrate has two dielectric layers and the chemical vapor deposited Si_3N_4 is used to protect SiO_2 from being etched quickly. We perform transport measurements in a dilution refrigerator with the base temperature of 40 mK.

4.1.2 Supercurrent and magnetic field dependence

Typical current-voltage (IV) characteristics are shown in Fig. 4.1(b). Because the charge carriers in Ge/Si nanowires are holes, a more negative back gate voltage V_{bg} leads to a lower normal state resistance (R_N) and a higher switching supercurrent (I_{sw}). The excess current (I_{exc}) due to Andreev reflection extracted from the IV traces is in the range of $1 - 4$ nA. Contact transparency of $\sim 50\%$ is estimated using the Octavio-Tinkham-Blonder-Klapwijk theory from the ratio $eI_{exc}R_N/\Delta \sim 0.05$, where e is the elementary charge and the bulk gap Δ is 1.7 mV given $T_c = 11$ K [85, 160]. Note that this is a lower bound estimate on the contact transparency since the ratio above is reduced for finite length junctions [161]. On the other hand, the $eI_{sw}R_N/\Delta$ ratio is 0.03 which is lower than the theoretical limit of π. Finite contact transparency and premature switching out of the supercurrent state caused by thermal activation can contribute to the reduction of the $I_{sw}R_N$ product [20]. The fact that supercurrent in Ge/Si nanowires is carried by holes which have a different momentum J than electrons in the contact superconductor may also contribute to this reduction, though this remains an open question.

Magnetic field evolution of supercurrents in two devices is presented in Figs.4.1(c,d). The switch out of the supercurrent state and into the finite voltage state corresponds to a peak in dV/dI. It is clearly visible up to 400 mT and 800 mT but can also be traced to higher fields. Both devices demonstrate monotonous decrease in I_{sw} as magnetic field
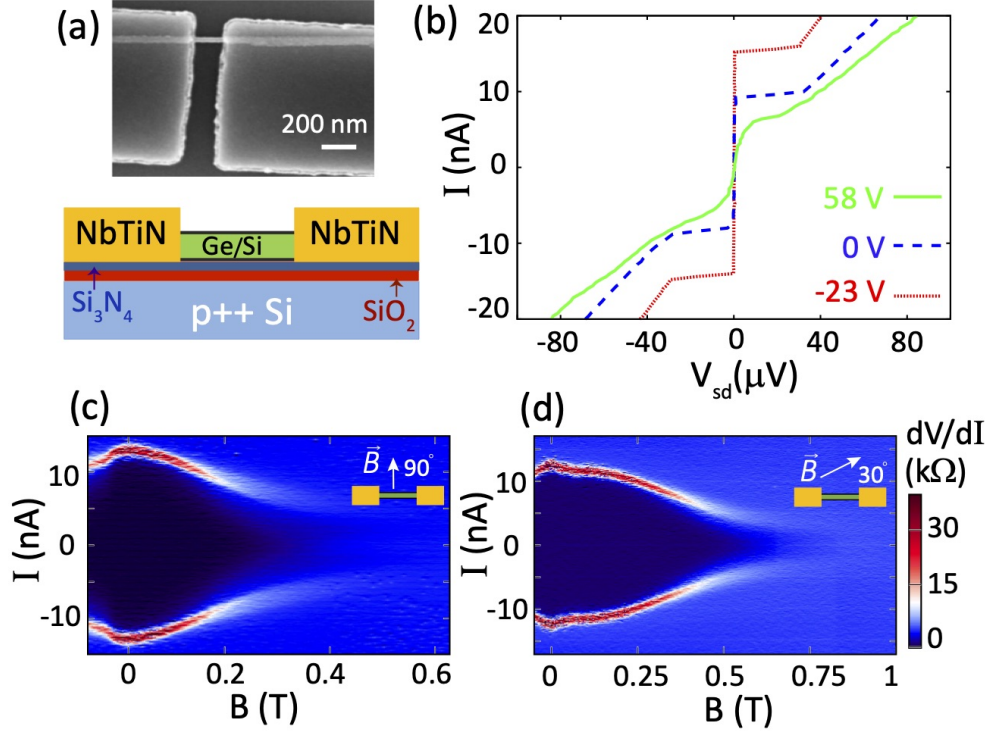
Figure 4.1: (a) (Top) Scanning electron micrograph of a Ti/NbTiN-Ge/Si-Ti/NbTiN device. (Bottom) Side view schematic of the device. (b) IV characteristics of device A at $V_{bg} = -23$ V (red), 0 V (blue) and 58 V (green). (c-d) The differential resistance dV/dI as a function of current bias and magnetic field for device A at $V_{bg} = -10$ V (panel (c)) and device B at $V_{bg} = 0$ V (panel (d)). In-plane magnetic field orientations are indicated by the cartoons.

is increased. The fact that supercurrent survives to higher fields in device B is consistent with the field aligned closer to the nanowire axis in this device, which reduces the magnetic flux threading the junction area for a given field. No nodes or oscillations in the switching current are observed up to fields of 1 Tesla, throughout the range of resolved supercurrent features. Assuming purely Fraunhofer-type interference within the junction only (zero field in the leads), the first node is expected at 300 mT for device A and 600 mT for device B. However, other geometrical factors such as the circular nanowire cross-section and Meissner effect may contribute to the absence of the nodes. The semiconductor nanowires are tuned to the multi-mode regime with several transverse one-dimensional subbands occupied, a factor which favors critical current oscillations due to inter-mode interference influenced by

magnetic field [162, 163]
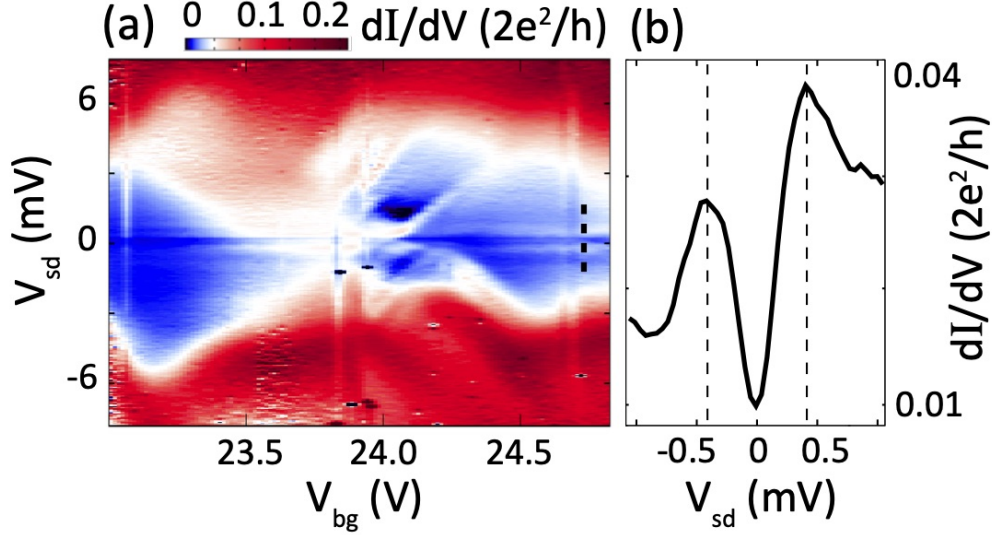
Figure 4.2: (a) Coulomb diamond measurements on an accidental quantum dot in device C in the near pinch-off regime, a dashed line marks a line cut shown in panel (b). (b) A line cut showing dI/dV as a function of the bias voltage. Peaks separated by $4\Delta_{\text{in}}$ are marked by dashed lines.

4.1.3 Induced superconducting gap

As part of evaluating the prospects of hybrid junctions studied here for the realization of Majorana zero modes, we measure the induced superconducting gap Δ_{in}. The gap is studied in the pinched-off regime through unintentional quantum dots formed in the junctions near pinch-off [164]. Fig. 4.2(a) shows differential conductance in device C as a function of back gate voltage. The boundaries of Coulomb diamonds are broadened due to co-tunneling, as the quantum dot barriers remain low. We observe a pair of sharp horizontal resonances of high differential conductance located symmetrically around zero bias at $V_{\text{sd}} = 2\Delta_{\text{in}} = \pm 440$ μV. At biases in between the peaks, conductance is suppressed but remains non-zero. Thus the induced superconducting gap here is of the so-called "soft gap" type (see Fig. 4.2(b)). This is not ideal for topological and hybrid quantum circuit applications since any subgap conductance leads to qubit decoherence. While the underline cause remains mysterious, possible attributes are disorder, quasiparticle poisoning [165, 166] and finite interface transparency. We also notice that the soft gap observed here is of the same magnitude as in the early

64

Majorana studies based on InSb nanowires [67, 152, 68]. Since the same NbTiN alloy are used in both InSb and Ge/Si cases, the soft gap measured here indicates that the soft gap is not unique to InSb-NbTiN hybrid structures and the "soft gap" may be associated to the properties of the NbTiN film, such as its granularity and alloy disorder.

4.1.4 Conclusions

We have developed and optimized superconducting contacts to Ge/Si nanowires based on NbTiN, and observed induced superconductivity up to magnetic fields of order 1 Tesla. Thus, the set of ingredients required to pursue Majorana zero modes in Ge/Si nanowires is now complete (the spin-orbit coupling term is discussed in the next section), and the integration of these ingredients in Majorana devices can begin. An induced superconducting gap of 220 μeV has been measured. The sub-gap conductance remains significant and research on suppressing the subgap conductance is desired [167].

4.2 Magnetic field evolution of spin blockade in Ge/Si nanowire double quantum dots

4.2.1 Introduction

Studies of spin blockade in quantum dots are largely motivated by the proposals to build a spin-based quantum computer [9], as spin blockade can be used for qubit initialization and readout [81, 11]. At the same time, spin blockade and its lifting mechanisms offer a direct insight into spin relaxation and dephasing processes in semiconductors and provide deeper understanding of interactions between spin localized in a quantum dot and its environment, be it the lattice and its vibrations or nuclear spins, spin-orbit interaction, or coupling to spins in nearby dots or in the lead reservoirs [168, 169, 14, 170, 15].

Holes in Ge/Si nanowires offer a relatively unexplored platform for such studies [56]. On the one hand, hyperfine interaction is expected to be greatly reduced owing to the low abundance of nonzero nuclear spin isotopes in the group IV materials [171]. Moreover, holes weakly couple to nuclear spins due to their p-wave Bloch wave symmetry, thus they are expected to come with longer spin relaxation times [59]. Heavy/light hole degeneracy may also influence the spin blockade regime [172]. On the other hand, spin-orbit interaction is predicted [60] and suggested by experiments [61, 62, 63, 64] to be strong in Ge/Si core/shell nanowires. This offers a path to electrical spin manipulation [16, 173], as well as to realizing Majorana fermions [4, 5, 67, 57].

In this work we perform transport measurements on electrostatically defined double quantum dots [81] made in Ge/Si core/shell nanowires, and detect Pauli spin blockade at several charge degeneracy points. We expand and adapt a previously developed rate equation model to analyze the magnetic-field evolution of the leakage current [174]. We also extract relatively large effective g-factors, up to 8.0 [58, 175, 156], which is promising for Majorana fermion and spin qubit implementations.

The devices are fabricated on n-doped Si substrates covered with 500 nm of thermal silicon oxide and patterned with local gate arrays of Ti/Au stripes with a center to center distance of 60 nm. The gates are covered by a 10 nm layer of HfO$_2$ dielectric. Using a

micromanipulator [176] the nanowires with a typical length of 3–5 μm, core diameter of 20–30 nm, and shell thickness of 2 nm are placed on top of these gates as shown in the inset of Fig. 4.3. After wet etching with buffered hydrofluoric acid, we sputter 15 nm of Al followed by 42 nm of NbTiN on lithographically defined source and drain electrodes to make ohmic contacts along with the contacts to the gates. We note that despite the fact that Al and NbTiN are both superconductors the contact between the leads and the nanowire has high resistance and low transparency in these devices, therefore no effects of induced superconductivity are observed on the dots as opposed to nominally the same devices that showed high contact transparency [140]. Furthermore, the applied source-drain bias exceeds the superconducting gap of NbTiN, which remains superconducting at all fields applied here. Thus we do not consider any contribution from the superconductivity of the leads on the leakage current. The measurements are performed in a dilution refrigerator at a base temperature of 30 mK.

4.2.2   Transport through double quantum dots

The double quantum dot is defined by applying positive voltages to three adjacent gates: G1 and G3 are used to set the outer barriers, and G2 defines the interdot barrier. Since all three gates are in close proximity they all influence the charge occupation of the dots, as well as all three tunneling barriers.

The main panel of Fig. 4.3 shows the measured double dot charge stability diagram which consists of a grid of charge degeneracy points connected by co-tunneling lines at higher charge occupations. Many charge degeneracy points are observed before the gate-induced energy barriers to the source and drain get too high to detect the current at the positive gate voltage extremes of the plot. This is in strong contrast with quantum dots defined using similar gates in InAs [15] or InSb [177] nanowires, where only a few charge degeneracy points are visible between complete pinch-off and the open transmission regime. The current is too low to measure at the charge degeneracy points corresponding to the last few holes in both dots, meaning that the tunneling barriers pinch off completely before the dots are emptied. In the regime studied here both dots still contain tens of holes. This is confirmed by asymmetric
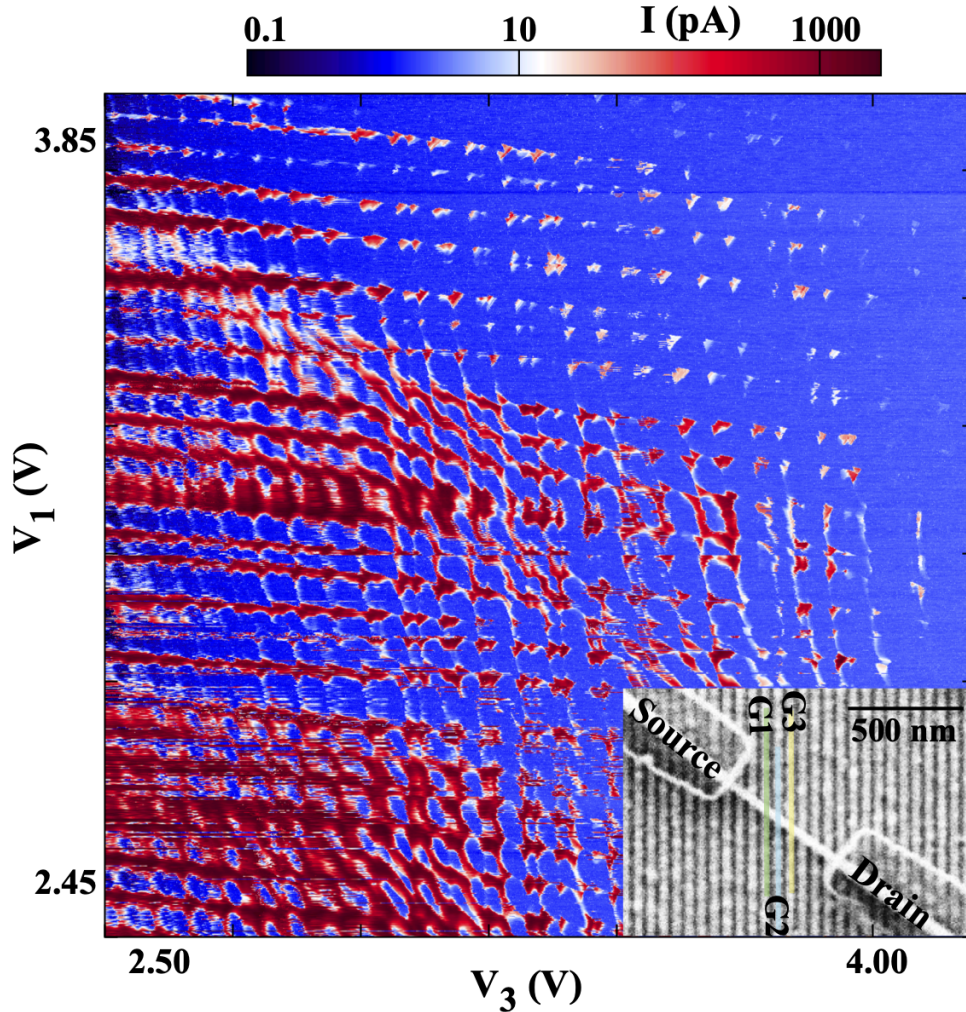
Figure 4.3: Current through the double dot as a function of voltage on G1 (V_1) versus voltage on G3 (V_3) at a fixed voltage on G2. The measurement is taken with a source-drain bias of 4 mV and at zero magnetic field. The inset shows a scanning electron micrograph of a representative Ge/Si nanowire device with Al/NbTiN lithographic contacts (labeled "Source" and "Drain") and tuning gate electrodes labeled G1 to G3. The other gates are fixed at zero voltage.

gate tuning such that as holes are expelled from one dot, the occupation of the other dot is increased and the tunneling barrier is lowered to ensure detectable current. The fact that so many holes fit in a small volume of a double dot (less than 120 nm length and 30 nm diameter) is consistent with the large effective hole masses as compared to those of electrons in III-V semiconductors, indicating that the hole wavefunctions are predominantly of a heavy-hole character.

4.2.3 Spin-orbit coupling and *g*-factor measurements in spin blocked double quantum dot configuration

In double quantum dots with multiple charges per dot, spin blockade does not necessarily occur at each (odd, odd) to (even, even) charge transition as expected for simple few-electron quantum dots [15, 177, 81, 178, 179, 180]. In fact, spin blockade may not occur for multiple transitions in a row [181]. This can be either due to the complex spin structure of the higher orbital states or due to a suppressed energy splitting between the ground state singlet and a higher orbital triplet.

When spin blockade does occur we assume that it can be effectively understood in the same way as the simplest $(1,1) \rightarrow (0,2)$ spin blockade: Close to zero detuning, the n'th hole in the source dot can only enter the drain dot if it can form a spin-singlet state with the m'th hole on the drain dot. Entering an $(n-1, m+1)$ state in a triplet configuration requires occupation of a higher orbital state which becomes energetically accessible only when an additionally applied interdot energy level detuning ε exceeds the singlet-triplet energy level splitting in the drain dot. For small detuning the system is thus expected to be blocked in one of the three triplet states, which are in principle degenerate and split in energy under the influence of a magnetic field due to the Zeeman effect. For clarity we will refer to the (n,m) states as $(1,1)$ and to the $(n-1, m+1)$ states as $(0,2)$. Current through the double dot in the spin blockade regime due to various spin non-conserving processes is referred to as the leakage current.

The primary signature of spin blockade in this study comes from the magnetic field dependence of the leakage current (Fig. 4.4), which can be explained in terms of the simple spin blockade picture described above. We vary the (1,1) to (0,2) energy level detuning, ε by scanning G1 and G3 perpendicular to the base of bias triangles (as indicated in the inset), while stepping the magnetic field. The suppressed current observed for $0 < \varepsilon \lesssim 2$ meV is associated with spin blockade, and we interpret the sudden rise in current at $\varepsilon \approx 2$ meV as the $(0,2)$ triplet states becoming energetically accessible from the $(1,1)$ triplet states, thus lifting the blockade. The associated singlet-triplet splitting of ~ 2 meV is representative of the several charge degeneracy points studied (see supplemental material).
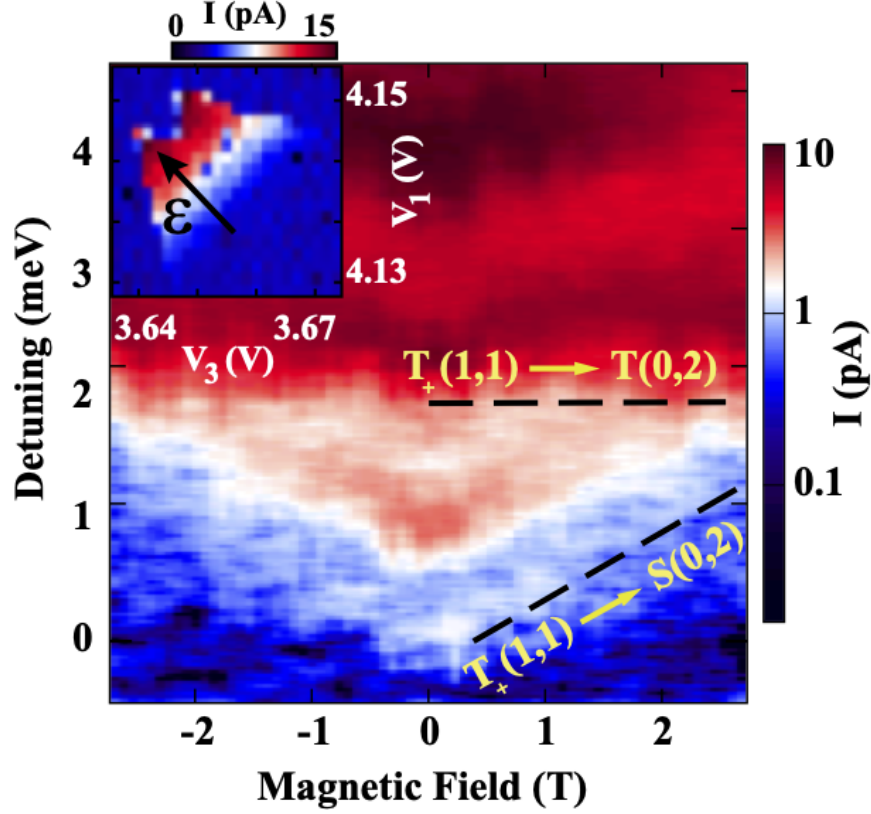
Figure 4.4: Current through the double quantum dot measured as a function of the detuning ε and the magnetic field B, with an applied source-drain voltage of $V_{SD} = 6.5$ mV. The magnetic field is applied normal to the substrate plane. The resonances associated with $T_+(1,1) \to T_+(0,2)$ and $T_+(1,1) \to S(0,2)$ transitions are marked with dashed lines. From the field dependence of the latter we find $g = 8.0 \pm 0.2$. Inset: the charge degeneracy point at finite bias with the detuning axis used in the main panel indicated by ε.

A smaller rise in the leakage current at lower detuning, marked with the tilted dashed line in Fig. 4.4, is assigned to a resonance between the lowest $(1,1)$ state T_+ and the singlet $S(0,2)$ state: Below this resonance (for smaller ε), $S(0,2)$ is energetically not accessible from the ground state $T_+(1,1)$ and the system is in Coulomb blockade. Since the energy of $S(0,2)$ is not expected to depend on the magnetic field, the B-dependence of this resonance reflects the B-dependence of the energy of $T_+(1,1)$. The pattern formed by two current resonances marked by dashed lines $T_+(1,1) \to T(0,2)$ and $T_+(1,1) \to S(0,2)$ is the main signature of spin blockade in this study. Note that a copy resonance follows the $T_+(1,1) \to S(0,2)$

70

transition in field, which is not accounted for in the simple spin blockade picture used here.

Using the slope of the resonance labeled $T_+(1, 1) \rightarrow S(0, 2)$, we obtain $g = 8.0 \pm 0.2$ for Fig. 4.4. While full g-tensor measurements were not performed, we find lower g-factors for fields deviating from normal to the substrate, in agreement with other studies (see supplemental material) [175, 156]. The highest g-factors extracted here are larger than previously reported for Ge/Si nanowires [62, 175, 156]. One possible reason for this is larger wire diameters used here: indeed, a relevant theory predicts diameter-dependent g-factors [60].

In Fig. 4.5a,b (left panels) we plot the measured leakage current in the spin blockade regime of two representative charge degeneracy points which show a qualitatively different field-dependent behavior. The current in Fig. 4.5(a) shows a single peak centered at zero field, whereas in Fig. 4.5(b) we observe a double-peak structure with a dip at zero magnetic field. We note that beyond the difference in charge numbers, we cannot independently quantify differences in other double dot parameters across the two regimes of Fig. 4.5. We speculate that the interdot tunnel coupling as well as the couplings to the leads are not the same in the two regimes.

A zero-field dip in the leakage current is known to occur in double dots hosted in materials with strong spin-orbit interaction [14, 15, 182, 183, 184]. The dip is usually explained in terms of a competition between different types of spin-mixing processes: The combination of spin-orbit interaction and Zeeman splitting due to the applied field enables transitions between triplet and singlet configurations. This mechanism becomes more efficient at higher magnetic field and thus it produces a dip in the leakage current around zero field [174]. Other processes that mix spin states, such as the hyperfine interaction between the electrons or holes and the nuclear spins in the host material [185] or spin-flip cotunneling processes with the leads [186], can be independent of the magnetic field or even become less efficient with increasing B. If one of such processes provides the dominant spin-mixing mechanism, then there will appear no dip in the current around zero field. Since the spin-orbit-mediated mechanism scales with the interdot tunnel coupling, one can expect to observe a transition from having a zero-field dip to no zero-field dip when changing the tuning of the double dot.
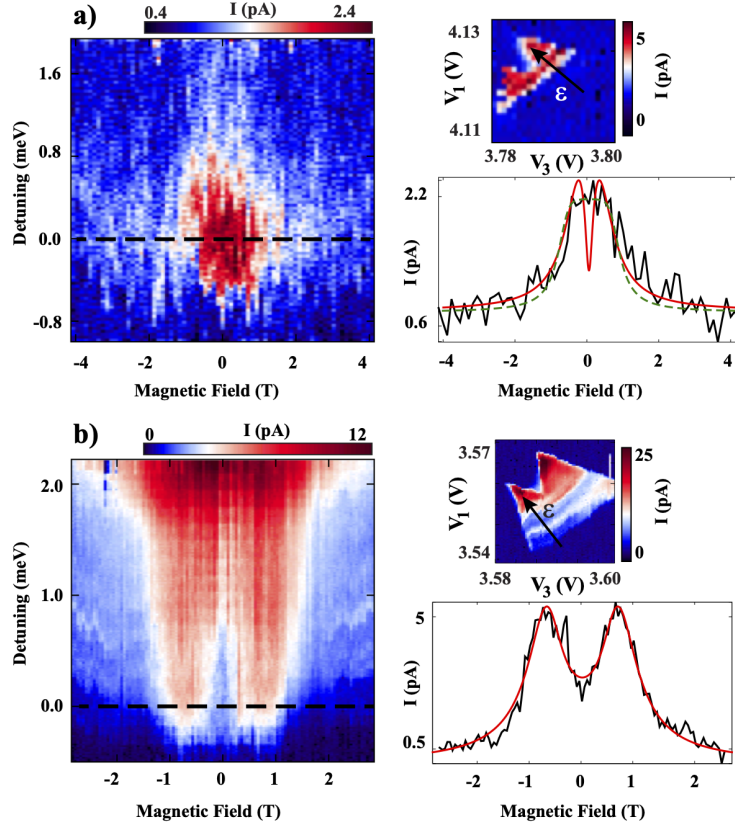
Figure 4.5: Magnetic field evolution of the leakage current in two different spin blockaded transport configurations. In both cases the field is applied in the plane of the nanowire and gates, perpendicular to the gates but making an angle of $\sim 30°$ with the wire. In the left panels we show the dependence of the leakage current on magnetic field and detuning, and on the right side we show the corresponding charge degeneracy points (top) and a line cut of the data at zero detuning (bottom). The zero-detuning cuts include fits to the theory presented in the main text. (a) In this configuration, where a bias voltage $V_{SD} = 6.5$ mV is applied, the leakage current has a single-peak structure both as function of the detuning and magnetic field. The corresponding charge stability diagram is taken at B = 5 T. In the figure we plot two different theory curves on top of the data, both with $\xi = 0.03$, $g = 4.4$, and an added constant current of 0.8 pA to account for the background signal observed in the data. We further used $\Gamma = 300$ MHz, $t = 50$ μeV, $\gamma = 0.0075$, and $\alpha = 0.4$ (solid red curve) and $\Gamma = 25$ MHz, $t = 150$ μeV, $\gamma = 0.66$, and $\alpha = 0.4$ (dashed green curve). (b) Leakage current at a different charge degeneracy point, with $V_{SD} = 4$ mV. The corresponding bias triangle is taken at B = 0 T. Here the current shows a double-peak structure in the magnetic field, which can also be seen in the zero-detuning cut. The theory curve (red solid line) uses $\xi = 0.03$, $g = 4$, $\Gamma = 256$ MHz, $t = 150$ μeV, $\gamma = 0.061$, and $\alpha = 0.37$.

72

4.2.4 Theoretical model

Ignoring the potentially more complicated nature of spin blockade in the valence band, we assume that in the present case we can describe the leakage current with a model based on the following ingredients: (i) $S(1,1)$, has the same singlet configuration as $S(0,2)$ and is thus strongly coupled to that state, with a coupling energy t. (ii) The state $S(0,2)$ decays to the drain lead with a rate Γ. Immediately after such a transition a new hole enters the system from the source, bringing it in one of the $(1,1)$ states again. (iii) $T_{\pm}(1,1)$ split off in energy when a magnetic field is applied. (iv) Spin-orbit interaction results in a coherent non-spin-conserving coupling between the $(1,1)$ triplet states and $S(0,2)$. The energy scale characterizing spin-orbit coupling t_{so} is proportional to t. (v) There can be other spin-mixing and spin-relaxation processes causing transitions between the different $(1,1)$ states.

In our data both the dip and the peak are relatively wide: they appear on a field scale of $B \sim 1$ T which is of the order of 3 K. First of all, this rules out hyperfine interaction as the dominant spin-mixing mechanism in the single-peak data of Fig. 4.5a. Hyperfine interaction is known to lift spin blockade around zero field producing a peak in current, but the width of the hyperfine peak is comparable to the typical magnitude of the effective nuclear fields in the dots. We estimate the effective nuclear fields in the present system to be less than 10 mT, which is orders of magnitude smaller than the peak width observed here [187]. Secondly, the analytic theory of Ref. [174], which is often used to extract model parameters such as the magnitude of spin-relaxation rates and $\alpha = t_{\mathrm{so}}/t$, is valid for $t, t_{\mathrm{so}}, B \ll \Gamma$ and also assumes the spin-relaxation rates to be isotropic, based on the assumption $B \ll T$, where T is the temperature. From here on we will use $\hbar = k_{\mathrm{B}} = g\mu_{\mathrm{B}} = e = 1$. In the present case, however, we have $B \gg T$ for most fields of interest, and spin relaxation will thus mostly be directed towards the $(1,1)$ ground state instead. Furthermore, the suppression of current at the highest fields could indicate that B exceeds at these fields the effective level width of $S(0,2)$ by such an amount that the system is pushed into a Coulomb blockade in the lowest-lying $(1,1)$ triplet state.

We thus cannot straightforwardly apply the theory of Ref. [174] to model the data shown in Fig. 4.5. Instead we present a modified version of the theory, where we include only spin

relaxation to the ground state and do not expand in large Γ. We start from the five-level Hamiltonian

$$H = \begin{pmatrix} 0 & iB & 0 & 0 & i\alpha t \\ -iB & 0 & 0 & 0 & i\alpha t \\ 0 & 0 & 0 & 0 & i\alpha t \\ 0 & 0 & 0 & 0 & t \\ -i\alpha t & -i\alpha t & -i\alpha t & t & 0 \end{pmatrix},$$ (56)

written in the basis $\{|T_x\rangle, |T_y\rangle, |T_z\rangle, |S\rangle, |S_{02}\rangle\}$, where $|T_{x,y}\rangle = i^{1/2 \mp 1/2}\{|T_-\rangle \mp |T_+\rangle\}/\sqrt{2}$ and $|T_z\rangle = |T_0\rangle$ are the three $(1,1)$ triplet levels and $|S\rangle$ and $|S_{02}\rangle$ the $(1,1)$ and $(0,2)$ singlets, respectively. The interdot detuning was set to zero and α parametrizes the strength of the effective spin-orbit interaction in the dots, where $\alpha \sim 1$ corresponds to the strong limit. In principle, the three α's coupling $|T_{x,y,z}\rangle$ to $|S_{02}\rangle$ can be different, constituting a vector $\boldsymbol{\alpha} = (\alpha_x, \alpha_y, \alpha_z)$ (see Ref. [174]). The length of this vector corresponds to the strength of the spin-orbit interaction and its direction is related to the direction of the effective spin-orbit field. In a physical nanowire, the precise orientation of $\boldsymbol{\alpha}$ depends on many details and is hard to predict. We therefore make the simplifying assumption that all three components are of the same magnitude. We diagonalize the Hamiltonian and use its eigenbasis to write a time-evolution equation for the density matrix [174],

$$\frac{d\hat{\rho}}{dt} = -i[H^{\mathrm{diag}}, \hat{\rho}] + \boldsymbol{\Gamma}\hat{\rho} + \boldsymbol{\Gamma}_{\mathrm{rel}}\hat{\rho}.$$ (57)

The operator $\boldsymbol{\Gamma}$ describes (i) decay of all states $|n\rangle$ (with $n = 0 \ldots 4$) to the drain lead with the rates $\Gamma|\langle n|S_{02}\rangle|^2$ and (ii) immediate reload into one of the eigenstates with the probabilities $\{1 - |\langle n|S_{02}\rangle|^2\}/4$. For the relaxation operator $\boldsymbol{\Gamma}_{\mathrm{rel}}$ we take a simple form: We assume that all four excited states relax with the same rate Γ_{rel} to the ground state. At $B = 0$ this ground state is an equal superposition of $|S_{02}\rangle$ and the optimally coupled $(1,1)$ state $|m\rangle = \{|S\rangle - i\alpha\mathbb{1} \cdot |\vec{T}\rangle\}/\sqrt{1 + 3\alpha^2}$, and for $B \to \infty$ it develops into a pure $|T_+\rangle$-state.

We first discuss this model on a qualitative level, and investigate how it differs from the model of Ref. [174]. For small fields, $B \ll \Gamma$, the different spin relaxation model used here only yields different numerical factors in some of the results. At $B = 0$ we have three blocked

states at zero energy that can relax to the hybridized $(1, 1)$–$(0, 2)$ ground state which quickly decays to the drain lead; this results on average in four holes being transported through the system in a time $3\Gamma_{\text{rel}}^{-1}$, thus yielding a leakage current of $I(0) = \frac{4}{3}\Gamma_{\text{rel}}$. Adding a finite magnetic field induces a coupling of $\sim \alpha B$ between two of the blocked states and $|m\rangle$, which provides an alternative escape route and leads to an increase of the current.

This increase becomes significant only when the rate of this escape $\sim (\alpha B)^2 \Gamma / t^2$ becomes comparable to Γ_{rel}, which happens at $B \sim (t/\alpha)\sqrt{\Gamma_{\text{rel}}/\Gamma}$. For larger fields the current tends to its maximum value $I_{\max} = 4\Gamma_{\text{rel}}$, reached when only one truly blocked state is left and on average four holes are transported in a time Γ_{rel}^{-1}. We see that this picture predicts a zero-field dip in the current of width $B_{\text{dip}} \sim (t/\alpha)\sqrt{\Gamma_{\text{rel}}/\Gamma}$ and a maximal suppression of the current, by a factor 3, at $B = 0$. This is, apart from numerical factors, the same result as found in Ref. [174].

Qualitative differences appear when we investigate what happens at even higher fields. Since Γ is finite in the present model and all relaxation is directed toward the ground state, we can enter a situation of Coulomb blockade in the $(1, 1)$ ground state $|T_+\rangle$. When we increase B, the current will thus eventually be suppressed to zero, producing in general a double-peak structure in $I(B)$. A naïve guess for the field scale where this suppression sets in would be $\sim \Gamma$: The level width of $|S_{02}\rangle$ is set by Γ, and for $B \gtrsim \Gamma$ the escape rate from $|T_+\rangle$ drops gradually to zero. However, the actual field scale of current decay is rather set by the competition of this escape rate with Γ_{rel}: Only when the B-induced suppression becomes so strong that escape from $|T_+\rangle$ is the main bottleneck for the leakage current, the decrease in current becomes significant. We thus compare this escape rate $\sim (\alpha t)^2 \Gamma / B^2$ with Γ_{rel} and find an estimate for the width of the overall double-peak structure $B_c \sim \alpha t \sqrt{\Gamma/\Gamma_{\text{rel}}}$.

We can also understand how our model could result in an apparent single-peak $I(B)$. Indeed, B_{dip} and B_c show a different dependence on the model parameters, and their ratio $B_{\text{dip}}/B_c \sim \Gamma_{\text{rel}}/\alpha^2\Gamma$ (which determines the relative visibility of the zero-field dip) could be large or small, depending on the detailed tuning of all parameters. For $B_{\text{dip}}/B_c \ll 1$ one could be in the situation where the central dip around zero field is too narrow to be observed.

We will now support these arguments with a more quantitative investigation of the model. We can solve Eq. 57 in steady state, $d\hat{\rho}/dt = 0$, and find the current from the
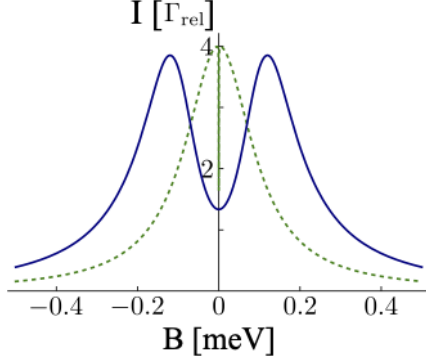
Figure 4.6: The current resulting from Eq. 58 for two different sets of parameters: $t = 120\ \mu\text{eV}$, $\alpha = 0.1$, and $\gamma = 2 \times 10^{-3}$ (solid blue curve) and $t = 3.5\ \mu\text{eV}$, $\alpha = 0.5$, and $\gamma = 10^{-4}$ (dashed green curve).

resulting equilibrium occupation probabilities $p_n = \hat{\rho}_{nn}$ as $\text{I} = \sum_n p_n \Gamma |\langle n | S_{02} \rangle|^2$, yielding

$$\text{I(B)} = \Gamma_{\text{rel}} \frac{[w - \text{B}^2 + \tau^2][w(1 + 4\gamma) + \text{B}^2 - \tau^2]}{6\gamma w^2 + 2\text{B}^2 \alpha^2 t^2}, \tag{58}$$

where we use the notation $w = \sqrt{(\text{B}^2 - \tau^2)^2 + 8\text{B}^2 \alpha^2 t^2}$, the small parameter $\gamma = \Gamma_{\text{rel}}/\Gamma$, and $\tau = t\sqrt{1 + 3\alpha^2}$ (which is the total tunnel coupling energy). To obtain Eq. 58 we assumed $\gamma \ll 1$, which we will also do below.

The current given by Eq. 58 indeed shows in general a double-peak structure. At zero field we find $\text{I}(0) = \frac{4}{3}\Gamma_{\text{rel}}$, and the current has two maxima at $\text{B} = \pm\tau$ where $\text{I} = 4\Gamma_{\text{rel}}$. The half-width of the resulting zero-field dip follows as $\text{B}_{\text{dip}} = t(\sqrt{\beta^2 + 2} - \beta)/\sqrt{2}$, where $\beta = \alpha/\sqrt{6\gamma}$. In the limit of large β (small $\sqrt{\gamma}/\alpha$) we find $\text{B}_{\text{dip}} \approx t\sqrt{3\gamma}/\alpha$. At high fields, the current drops to zero, and from Eq. 58 we find the half-width-half-maximum of the full double-peak structure to be $\text{B}_c = t(\sqrt{\beta^2 + 2} + \beta)/\sqrt{2}$ which reduces to $\text{B}_c \approx \alpha t/\sqrt{3\gamma}$ for large β. We see that in the limit of small γ these results agree with the conclusions of our qualitative discussion above.

In Fig. 4.6 we plot I(B) for two different sets of parameters, illustrating how the model can produce curves that appear to have double-peak as well as single-peak structures. The solid curve shows a clear double-peak structure, which is indeed expected since the "visibility parameter" $\text{B}_{\text{dip}}/\text{B}_c \approx 0.30$ predicts a clearly distinguishable zero-field dip. In contrast, for

the dashed curve $B_{\mathrm{dip}}/B_c \approx 0.001$. In this case, the current still has a dip around zero field; its width, however, is ~ 1000 times smaller than the overall width of the structure and therefore invisible in the plot. Depending on all other parameters, this situation could thus correspond to an experiment where the leakage current appears to have a single-peak structure.

In order to connect our model to the experimental data in Fig. 4.5 and facilitate fitting of the model parameters (see below), we include the likely scenario that g-factors in the two dots are different. The effective g-factor for a localized hole depends on many microscopic characteristics, among which the details of the confining potential [60], and is thus expected to differ from dot to dot. Recent studies on similar materials found g-factors differing by 2–5% between two dots in a double dot [184, 188]. Such differences are smaller than the error bars in our g-factor measurement, thus they cannot be verified in our devices but they need to be considered due to their strong influence on the leakage current. The effect of having different g-factors on the left and right dots (g_L and g_R) is a coherent mixing of $|T_z\rangle$ and $|S\rangle$. As a result, the single blocked state left at finite field $\{|T_z\rangle + i\alpha|S\rangle\}/\sqrt{1+\alpha^2}$ couples to the decaying state $\{|S\rangle - i\alpha|T_z\rangle\}/\sqrt{1+\alpha^2}$, thus lifting the blockade. The rate of this decay of the last blocked state is $\Gamma_\xi \sim (\xi B)^2 \Gamma/t^2$, where $\xi = \frac{1}{2}(g_L - g_R)/(g_L + g_R)$. This decay competes with Γ_{rel} for being the bottleneck for the leakage current: If $\Gamma_\xi \gtrsim \Gamma_{\mathrm{rel}}$ then the overall scale of the current will be set by Γ_ξ.

To include the effect of a finite g-factor gradient into our model, we add a term $H_\xi = \xi B\{|T_z\rangle\langle S| + |S\rangle\langle T_z|\}$ to the Hamiltonian (56). We can again solve Eq. 57 in steady state $d\hat{\rho}/dt = 0$ and arrive at an analytic expression for the current I(B) which we can fit to the data (at this point we do not assume $\gamma \ll 1$). Fixing $\xi = 0.03$, we can obtain reasonable fits to the double-peak data of Fig. 4.5b. Based on these results, we conclude that spin-orbit parameter α is in the range ~ 0.1–0.4. The single-peak data of Fig. 4.5a are harder to fit due to lack of features, thus we cannot reasonably narrow down all the fit parameters. However, theory curves with α in the same range as for the double-peak regime can show reasonable agreement, see Fig. 4.5b.

4.2.5 Conclusions

To conclude, assuming linear Rashba spin-orbit interaction as the dominant relaxation term [60] in these gate-defined double quantum dots with $\alpha = 0.1$–0.4, and a dot-to-dot distance of order 50 nm, we find a spin-orbit length of $l_{\mathrm{so}} = 100$–500 nm. While this corresponds to a substantial spin-orbit interaction, it does not greatly exceed that measured in InAs or InSb nanowires. One possibility for this could be that α is not maximal for the field orientation at which data is obtained here as a consequence of spin-orbit anisotropy [177], although the magnetic field was not oriented in the direction expected for the spin-orbit field. Another factor for lower-than-expected spin-orbit interaction is the low strain between the thin Si shell and relatively thick Ge core. Thus, it is conceivable that spin-orbit interaction can be enhanced by tailoring the nanowire morphology. A more detailed insight into spin-orbit coupling and other double dot parameters could be obtained from electric dipole spin resonance.

4.2.6 Supplemental material

4.2.6.1 Charge stability diagrams

We have measured three different nanowire devices, A, B, and C, in three different dilution refrigerators all at base temperatures below 30 mK. All three devices have the same fabrication recipe as mentioned in the main text. In this supplemental material we show more data on Device A, the device investigated in the main text, as well as data from the other two devices.

In Fig. 4.7 we show part of the charge stability diagram shown in Fig. 4.3, in both source-drain bias directions. We remove parts of the scan with lower gate values from Fig. 4.3 to improve the visibility of charge transitions with fewer hole occupation in dots and circle some charge transitions with asymmetric current near the triangles bases to illustrate how we search for spin blockaded transitions. Taking bias asymmetry near zero detuning as an initial signature of a spin blockade candidate charge degeneracy point, we study the magnetic field evolution to determine if spin blockade is present or not.

Fig. 4.8 shows the bias triangle of Fig. 4.5(b) at zero field where spin blockade is stronger,
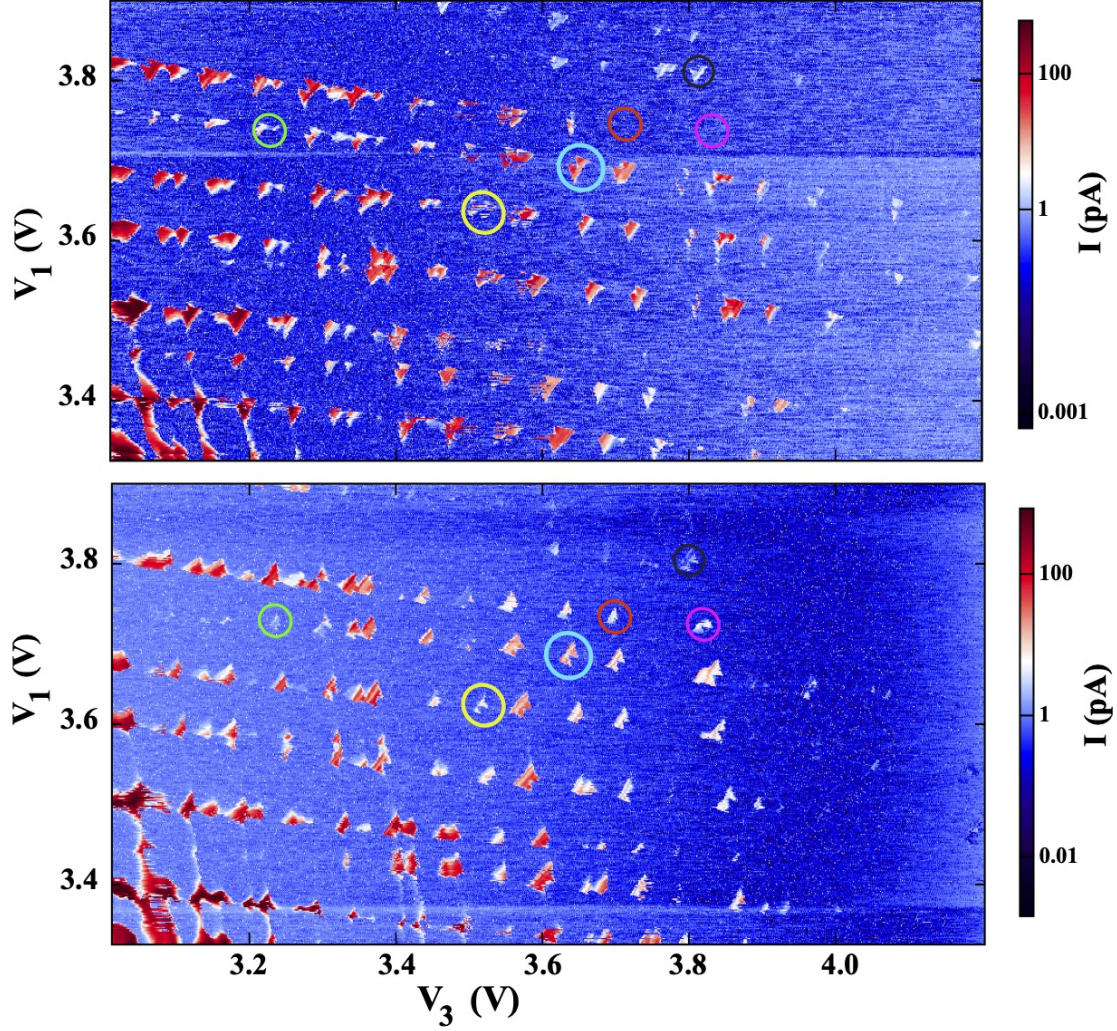
Figure 4.7: Double quantum dot charge stability diagrams in opposite bias directions (top: $V_{SD} = 4$ mV, bottom: $V_{SD} = -4$ mV). The plots show the absolute value of measured leakage current across the dots from one reservoir to the other while scanning G1 versus G3 at a fixed G2. Some charge transitions that show bias asymmetric behavior are circled.

and at finite magnetic field where the spin blockade is lifted. This figure illustrates that the current suppression due to spin blockade is sometimes a subtle effect in the presence of highly effective spin mixing mechanisms such as spin-orbit interaction.

In Fig. 4.9 we see a few charge transitions from Device B in two opposite bias directions. These transitions manifest some indicators of possible spin blockade at zero magnetic field such as suppressed current at the base of the triangles (green arrow), enhanced current on

the side of the triangles that can be related to spin exchange with the reservoir leads (yellow arrows), and triplet hats at the triangle tops (orange arrow). However, these features are not conclusive for this set of triangles. In order to accurately identify spin blockade one needs to study the magnetic field dependence of the leakage current, as shown for Device A.
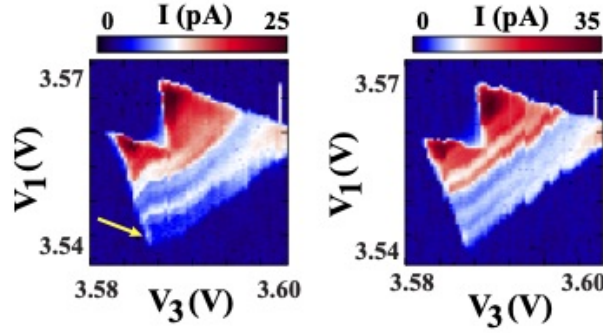
Figure 4.8: Bias triangle of Fig. 4.5b in the main text at zero magnetic field (left) and at B = −0.8 T (right) at $V_{SD} = 4$ mV. The current is suppressed at the base of the triangle (lower left) at zero field and there is an excess current at the side which can be representative of the hole exchange between the dot and the reservoir where their Fermi energy levels are equal. At finite magnetic field we can see the increase in the leakage current at the base of the triangle associated with lifting the spin blockade.

In Fig. 4.10 we present magnetic field evolution of the leakage current obtained from Device C. A similar pattern is observed here compared with Fig. 4.4, i.e. base of the triangle moves to higher detuning with applied magnetic field. The top panel shows a charge degeneracy point studied at bias voltages $V_{SD} = \pm 4$ meV. The bias triangle at positive bias is smaller than the one in opposite bias suggesting the suppression of current at its base, which we attribute to spin blockade. In the middle panel we show the leakage current as a function of detuning ε (as indicated in the top left plot) and the applied magnetic field. In this regime the the double-peak structure is observed in the field dependence at low detuning.

4.2.6.2 Positive and negative bias detuning sweeps

Fig. 4.11 shows the leakage current as a function of the magnetic field and the gate voltages controlling the detuning, for both bias directions applied across the charge degeneracy points studied in Fig. 4.4 (top) and Fig. 4.5(a) (bottom). The left panels show a field-dependent behavior of the leakage current, where the detuning at which the current sets on
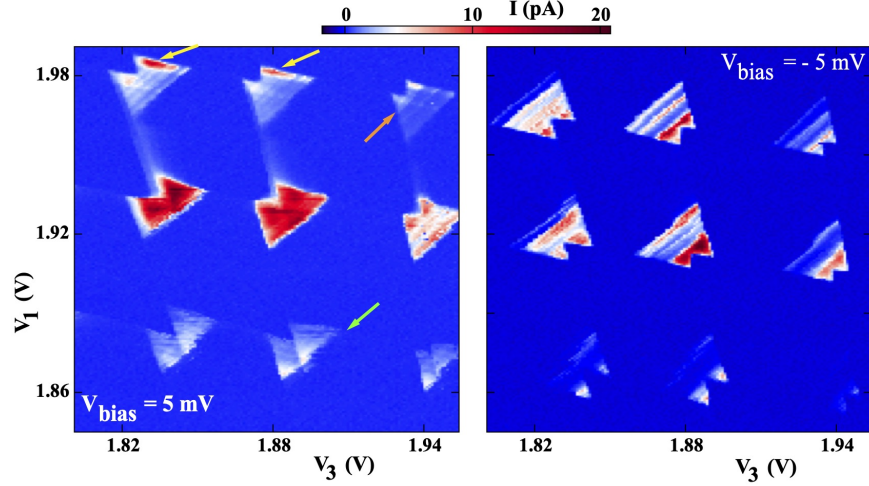
Figure 4.9: Double quantum dot charge stability diagrams of Device B in opposite bias directions. The plots show the absolute value of measured leakage current across the dots from one reservoir to the other while scanning G1 versus G3 at a fixed G2. The arrows show characteristics of spin blockade explained in the text.

increases with field, whereas in the right panels that are taken at the opposite bias direction the leakage current onsets always at the bottom of the colormap (where zero detuning is located) and the onset voltage does not demonstrate a linear magnetic field dependence. Charge instabilities are responsible for the onset voltage fluctuations, these fluctuations are not symmetric upon magnetic field reversal.

4.2.6.3 *g*-factor anisotropy

In Figs. 4.12 and 4.13 below we show multiple scans of the leakage current through different double quantum dot configurations as a function of magnetic field and detuning for Device A. As we see, not all the scans reveal very sharp steps in the current, but they are still clear enough to read off an effective *g*-factor from the slope of the resonance associated with $T_+(1,1) \to S(0,2)$ transition, as shown by dashed lines.

When extracting *g*-factors, we neglect the orbital effect of the magnetic field in the two dots on the energy of the $T_+(1,1) \to S(0,2)$ transition. The dots are likely occupied with heavy holes with a large effective mass, $m^* = 0.2 \, m_e$, for which we estimate a shift of $\approx 10\%$

81
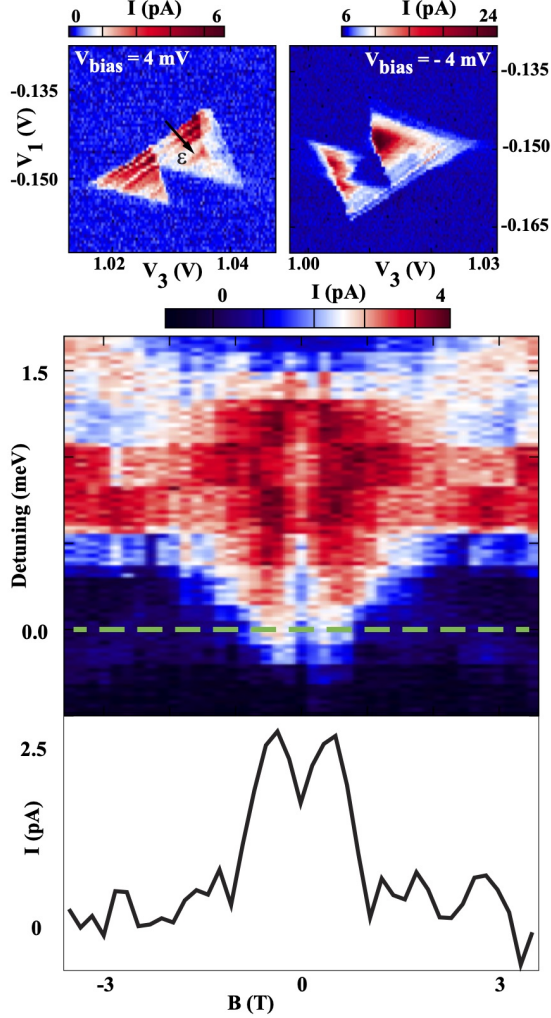
Figure 4.10: Pauli spin blockade in Device C. Top: the bias triangle in two opposite source-drain bias directions. The triangle in the left is smaller than the one on the right showing that the current at its based is suppressed. The color plot is the absolute value of the leakage current. Bottom: leakage current through the double quantum dot measured as a function of detuning and magnetic field at $V_{SD} = 4$ mV. The double-peak behavior highlighted by a line cut at zero detuning corresponds to spin blockade.

in orbital level splitting using $\Delta E = \hbar\sqrt{\omega_0^2 + \omega_c^2/4} - \hbar\omega_0$ at B = 3 T, where $\omega_c = \hbar e B/m^*$ and $\omega_0 \approx 2$ meV. At the same time, Zeeman shifts are comparable to the singlet-triplet energy level spacing in the same field range greatly exceeding the estimated orbital effect for these dots.

We apply magnetic fields in two different directions: (i) normal to the plane of the
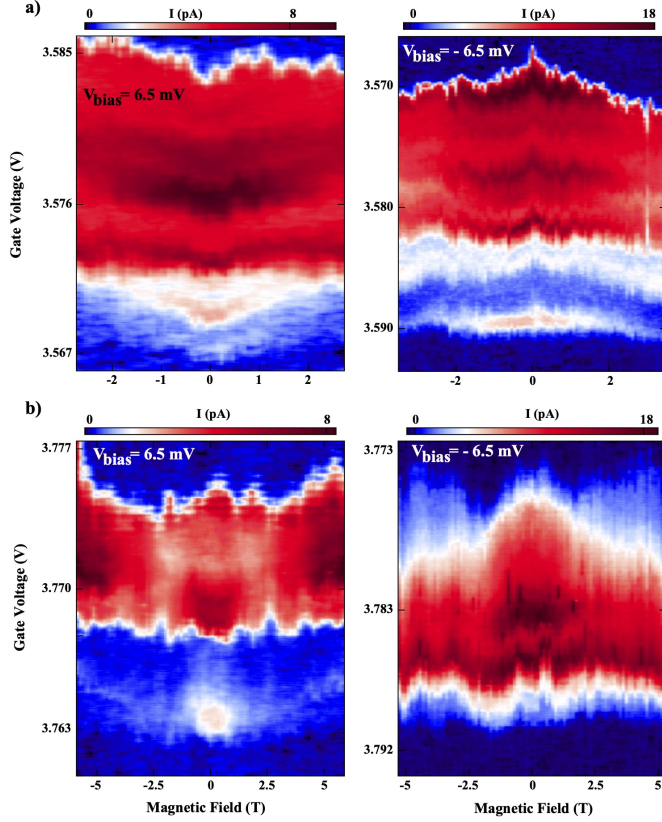
Figure 4.11: Magnetic field evolution of the leakage current in opposite bias directions for the two double quantum dot configurations shown in Fig. 4.4 (top) and Fig. 4.5(a) (bottom) in the main text. Source-drain biases are indicated in the panels

nanowire and local gates ($B_\perp$) and (ii) in-plane with the nanowire and gates, where the nanowire makes an angle of $\sim 30°$ with the field (B_z).

Fig. 4.12 shows the leakage current through a charge degeneracy point in both directions of applied magnetic field. The slopes from which we can read the effective g-factors are different for the two cases of applied field, larger for the out-of-plane magnetic field and smaller for the in-plane field.

Fig. 4.13 shows more examples of the in-plane magnetic field evolution of the leakage current at two other charge degeneracy points, where g-factor values deviate from those measured in $B_\perp$ shown in left panel of Fig. 4.12 and Fig. 4.4. Also from these scans we extract a singlet-triplet energy splitting $E_{ST} \sim 1$–2 meV.
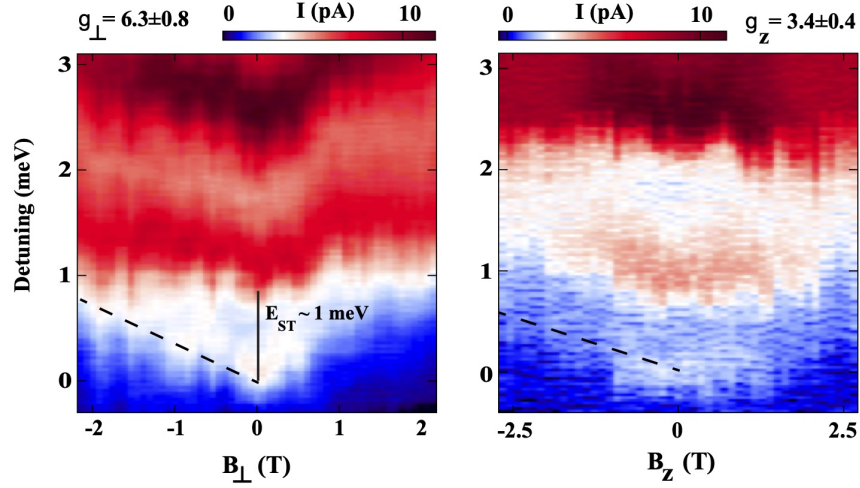
Figure 4.12: Leakage current as a function of magnetic field and detuning. Left: field is applied normal to the substrate. Right: in-plane magnetic field. The dashed lines show the slope of the resonance line moving as a function of filed and detuning from which we measure the effective *g*-factor. The solid line is used to read the singlet-triplet energy splitting. It is not trivial for the right panel to draw a solid line for this energy splitting.
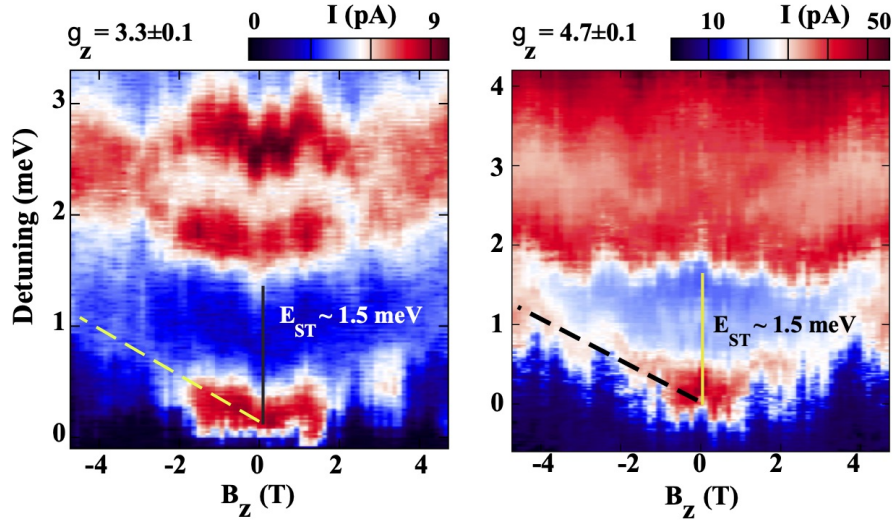
Figure 4.13: Leakage current through two different double dot configurations both as a function of in-plane magnetic field and detuning. Dashed lines are used to measure the effective *g*-factors along the direction of the magnetic field, and the singlet-triplet energy splittings are shown by solid lines.

5.0 Mirage Andreev spectra generated by mesoscopic leads in nanowire quantum dots[1]

In this chapter we study transport mediated by Andreev bound states formed in InSb nanowire quantum dots. Two kinds of superconducting source and drain contacts are used: epitaxial Al/InSb devices exhibit a doubling of tunneling resonances, while in NbTiN-InSb devices Andreev spectra of the dot appear to be replicated multiple times at increasing source-drain bias voltages. In both devices, a mirage of a crowded spectrum is created. To describe the observations a model is developed that combines the effects of a soft induced gap and of additional Andreev bound states both in the quantum dot and in the finite regions of the nanowire adjacent to the quantum dot. Understanding of Andreev spectroscopy is important for the correct interpretation of Majorana experiments done on the same structures.

5.1 Introduction

The superconductor-semiconductor hybrids are of recent interest due to the possibility of inducing topological superconductivity accompanied by Majorana bound states (MBS) [52, 190, 191, 192]. More generally, when a semiconductor is of finite size, proximity to a superconductor gives rise to subgap quasiparticle excitations, the so-called Andreev bound states (ABS), that appear due to successive Andreev reflections at the interfaces. Single ABS have been demonstrated in a variety of structures including self-assembled quantum dots, semiconductor nanowires, atomic break junctions, carbon nanotubes and graphene [193, 194, 40, 39, 195, 42, 196]. ABS exhibit many similarities to MBS, and therefore ABS can serve as a prototypical system for Majorana studies [43, 45]. Furthermore, MBS are expected to evolve from ABS across a topological phase transition [44, 153]. A powerful experimental method for investigating both MBS and ABS is via tunneling, either from a nanofabricated probe or by scanning tunneling spectroscopy [197, 198].

---

[1]This chapter is adapted from Ref. [189].

In this chapter, we focus on the mesoscopic effects within the tunneling probes. We show that the non-trivial densities of states (DOS) in the probes can drastically affect tunneling characteristics by generating multiple replicas of ABS. To experimentally investigate these effects, we use semiconductor nanowires coupled to superconductors. ABS are induced in a quantum dot by strongly coupling the dot to one superconducting contact. A second superconducting contact and a nanowire segment adjacent to it act as a tunneling probe. To explain our observations, we consider the effects of soft induced superconducting gap in the nanowire, and of additional ABS induced in nanowire segments adjacent to the dot. The surprising observation of sub-gap negative differential conductance (NDC) is found to be consistent with a peak in the DOS of the probe at zero chemical potential, which is present even at zero magnetic field. The exact origin of this anomalous DOS remains an open question. Our findings emphasize the importance of understanding the spectral structure of the measuring contacts to interpret tunneling experiments in mesoscopic systems. We expect them to be particularly relevant for the MBS search in similar nanowire devices [67, 149, 153, 68, 152].

InSb nanowires are grown using metalorganic vapor phase epitaxy (MOVPE) [131]. We investigate two devices that are drastically different both in the way they are gated and in the way superconductivity is induced. The first is an Al/InSb device which shows a two-replica tunneling spectrum that can be understood by only considering the effect of a soft induced gap in the nanowire. Building on the simpler example of an Al/InSb device, we discuss the second, NbTiN-InSb, device in which multiple replicas are observed. Properly describing this effect requires a non-trivial DOS in the leads. All measurements are performed in a dilution refrigerator with a base temperature of 30 mK.

5.2   Induced superconducting soft gap in Al/InSb nanowire

The Al/InSb device in Fig. 5.1(a) features an epitaxially-matched thin shell of Al defined by molecular beam epitaxy (MBE), with a single break in the shell around which the quantum dot is formed [65]. The wires were allowed to age in air which possibly accounts

for softer induced gap. NbTiN contacts are fabricated on top of the Al shell of the nanowire following Ref. [65], but superconductivity in the dot is primarily induced by the Al shell since NbTiN is offset back from the break in the shell. A combination of the back and side gates is used to define a quantum dot by lowering the electron density primarily near the break in the Al shell. In practice, the side gate is fixed and only the effect of the back gate is explored (see supplemental materials for quantum dot characterization). The dot is partially defined by disorder which becomes prominent at low density.

In a hard-gap superconductor-superconductor tunnel junction, conductance is expected to be zero for source-drain biases $|V| < 2\Delta/e$, where Δ is the superconducting gap which is typically 200 μeV in aluminum [199, 164]. If the probe features a soft induced gap, for example due to microscopic semiconductor-superconductor interface properties, conductance can be non-zero at lower biases. Fig. 5.1(b) illustrates how current can flow at a bias of $V < \Delta$ if a small DOS is present in the probe within the superconducting gap. Another current peak is expected when the gap edge of the probe is aligned with the ABS in the dot, therefore the same ABS is responsible for two peaks in transport.

In the Al/InSb device the conductance is non-zero for $|V| \gtrsim \Delta/e$, and two small conductance peaks are found at $V \approx \pm\Delta/e$ (Figs. 5.1(c),(d)) at zero applied magnetic field. We argue that conductance in the range $\Delta/e < V < 2\Delta/e$ is due to the soft gap effect which makes tunneling possible when the center of the induced gap in the probe is aligned with ABS level in the dot located close to the gap edge, as in Fig. 5.1(b). Still, the largest peaks at zero field are at $\pm2\Delta$, which indicates that the subgap density of states is relatively small. The resonances at $\pm2\Delta$ are accompanied by negative differential conductance (NDC) shadows around $\sim \pm0.5$ mV, which is typical for tunneling transport between two superconducting gap edges and arises due to a convolution of two DOS peaks [38].

The conductance peaks at $\pm\Delta$ and $\pm2\Delta$ evolve in magnetic field. Both resonances split into two branches, one of which moves to higher bias, while the other moves to lower bias. This indicates that we are observing Zeeman splitting of an ABS that is localized near the gap edge at zero field [38]. The spectrum is replicated because the same ABS is probed by the large density of states in the probe at $V = \Delta/e$ and by the small density of states at $V = 0/e$. This is confirmed by that fact that the branches originating from Δ are parallel

to branches originating at 2Δ at low field.

At B = 0.3 T resonances that originated from $\pm\Delta$ coalesce at zero bias, resulting in a zero-bias peak [43]. At the same field kinks are observed in higher bias resonances around V = Δ/e. The kinks appear because the positive and negative bias segments are shifted to
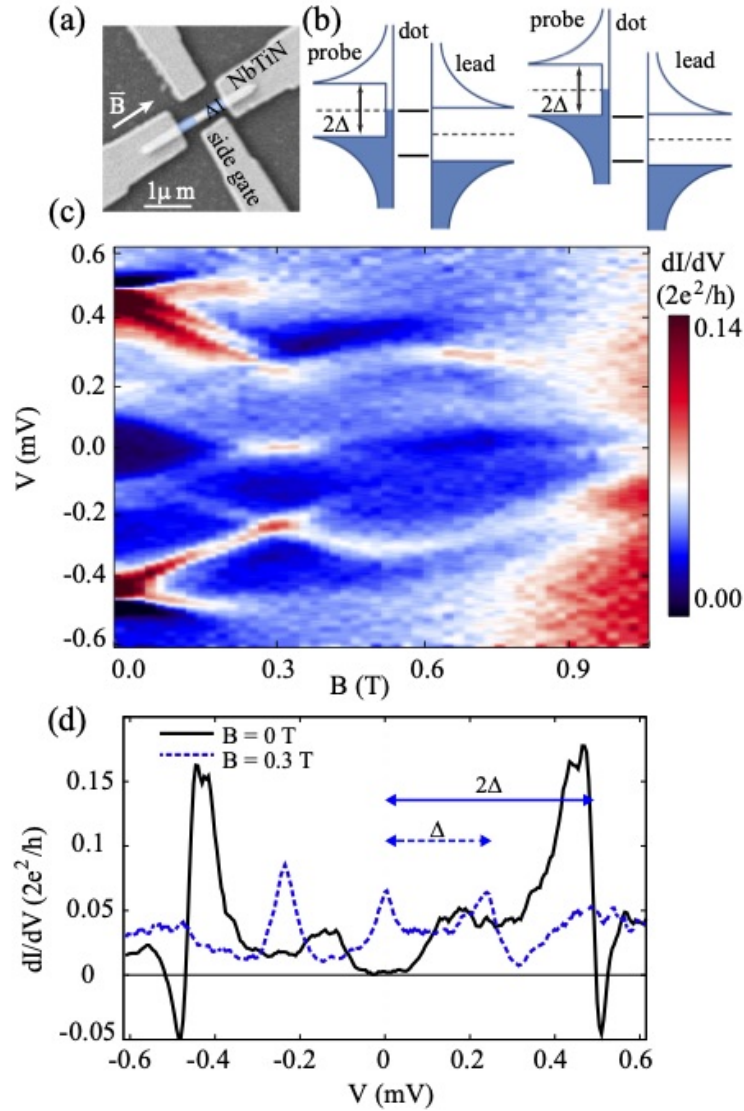
Figure 5.1: (a) scanning electron micrograph of a representative Al/InSb device. The shaded blue regions show the Al thin shell with a break in the middle. (b) Illustrative energy diagrams of a soft gap probe, a hard-gapped lead and an ABS in the dot (solid lines) for two different source drain biases V $\approx \Delta$ (left) and V $\approx 2\Delta$ (right). (c) and (d) magnetic field evolution of the two-terminal transport. The field is applied parallel to the nanowire axis.

$+\Delta$ and $-\Delta$ respectively by the probe at the gap edge. The superconducting gap in the Al shell remains virtually unchanged at B $= 0.3$ T. This can be seen because the upper branch of the 1Δ resonance meets exactly with the lower branch of the 2Δ resonance at that field. The gap collapses at higher fields and vanishes at B≈ 1.0 T. The high critical field is due to quenched orbital depairing in the thin Al shell. The low-bias replica follows the behavior of the high bias replica reaching a local maximum at B≈ 0.7 T and collapsing to zero at B≈ 1.0 T. At all fields, the replicas are separated by a bias of Δ(B)$/e$. We also note that the upper branch at $+2\Delta$ appears to split into three resonances at small fields, with two of the branches moving down, a non-universal effect which remains to be understood.

5.3 Andreev replica in NbTiN-InSb-NbTiN device

Having understood the doubling of tunneling resonances due to the soft gap effect, we now discuss the less trivial behavior of the NbTiN-InSb device in which more than two apparent replicas are observed (Fig. 5.2(a)). In this device no epitaxial Al shell is present and the nanowire directly contacts the NbTiN electrodes. This device is fabricated atop of an array of fine local gates with the center-to-center distance of 60 nm. The gate dielectric is a 10 nm thick layer of HfO$_2$. The quantum dot is fully defined by gates labeled t, p and s for "tunneling", "plunger" and "superconductor". The dot is defined close to the right superconductor and the barrier above gate s is tuned so as to strongly couple the right superconductor and the dot. The left superconductor is separated from the dot by a segment of a nanowire and a high tunneling barrier defined above gate t. We vary the occupation of the dot with voltage V$_p$ on the plunger gate. This device has been used in a previous study [200].

Data in Fig. 5.2(b) show transport through the NbTiN-InSb device as a function of plunger gate up to a high bias of 5 meV. The lowest bias resonances (closest to zero) exhibit behavior typical for ABS in quantum dots: they form a "loop" by crossing zero bias twice at approximately V$_p = 520$ mV and V$_p = 540$ mV. This is explained by the dot undergoing a singlet-doublet ground state transition at the nodes of the loop [39, 40, 42, 43]. Interestingly,
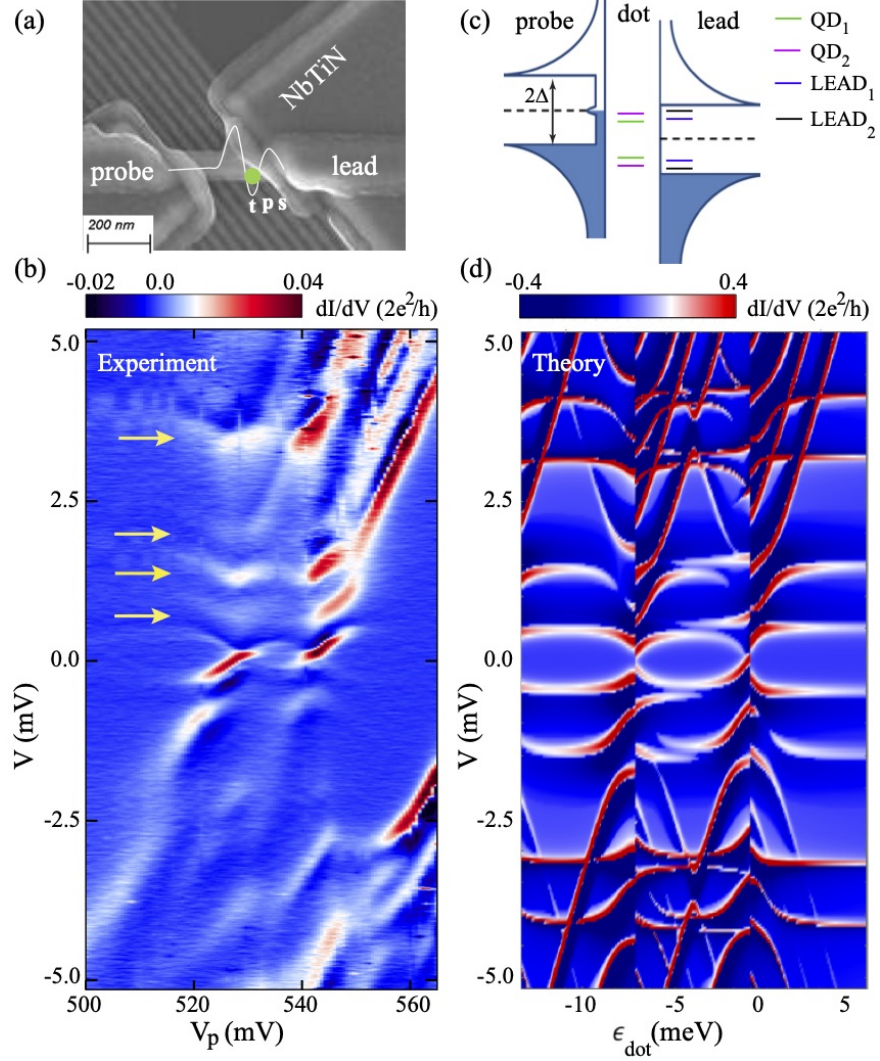
Figure 5.2: (a) Scanning electron micrograph of the NbTiN-InSb device. Green dot marks the quantum dot, white line is a conceptual confining potential set by gates t, p and s. (b) Tunneling conductance through the dot as a function of bias and V_p. Arrows point to four apparent replicas of the lowest loop-like resonance. Data obtained at zero magnetic field. (c) Illustrative energy diagram with the soft gap probe, two ABS on the dot (QD_1 and QD_2) and two ABS in the hard gap lead ($LEAD_1$ and $LEAD_2$). (d) Theoretical model results as a function of dot on-site energy ϵ_{dot}, with $QD_{1,2}$ energies $\epsilon_1^D = \epsilon_{dot}$ and $\epsilon_2^D = \epsilon_{dot} - 1.7$ meV, $LEAD_{1,2}$ energies $\epsilon_1^L = 0.5$ meV and $\epsilon_2^L = 1.5$ meV, induced pairing $\Gamma_S = 0.27$ meV, parent gap $\Delta_p = 2.7$ meV and Coulomb energy $U = 6.8$ meV.

four apparent resonances that follow the same behavior of the upper half-loop are observed at increasing values of positive bias in the gate range. The highest bias resonance is at

an energy consistent with twice the gap of bulk NbTiN, which has been measured to be close to 2 meV (data not shown). Multiple Andreev reflections are known to generate a series of subgap features, but this effect is typically observed in symmetric structures, while here s and t barriers are tuned to be highly asymmetric. We also notice that the loop-like resonances at the center of the gate range evolve smoothly into diagonal lines, most clearly for $V_p = 540 - 560$ mV. These diagonals resemble excited states of a quantum dot. This is not expected for multiple Andreev reflection.
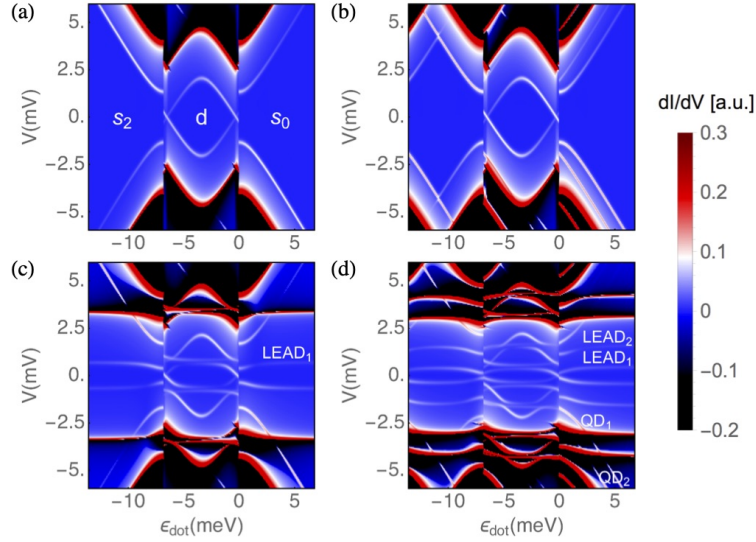
Figure 5.3: Tunneling differential conductance at zero field across a quantum dot between a soft-gap superconducting electrode and a proximitized nanowire lead with a hard gap. The quantum dot has one (a) or two (b-d) spinful levels, while the nanowire has zero (a,b), one (c) or two (d) subgap Andreev bound states. Magnetic field is zero in all panels, simulation parameters similar to those in Fig. 5.2(d).

We develop a model that includes a lead electrode with a hard gap on the right, a soft-gap electrode on the left, and a quantum dot in between. To reproduce multiple replicated spectra, we include additional ABS in the right lead, presumably confined within the nanowire segment underneath the superconductor. Good qualitative agreement is found with two ABS within the quantum dot and two ABS in the right lead, with the left lead acting as a tunneling probe (Fig. 5.2(c)). Simulated conductance data are presented in Fig. 5.2(d). The model exhibits multiple half-loop structures at higher bias, as well as the diagonal lines, which indeed originate from the excited states in the dot. The horizontal resonances that

bind the lowest loop are conventionally interpreted as the superconducting gap edge singularities. In our experiment this feature is observed at the scale of 0.4 meV, far below the NbTiN bulk gap. The model shows that the horizontal resonances are in fact the result of the hybridization of the lowest-energy ABS in the dot with the lowest-energy ABS in the lead. The state $LEAD_1$ is not sensitive to gate p therefore it appears as a horizontal resonance in the model. Calculations neglect spin-orbit coupling because the quantum dot spectra are only weakly affected by spin-orbit coupling at zero magnetic field. We also note that in practice, both devices studied in this paper likely have soft induced gaps on both sides, however essential features are well captured with soft gap only on the probe side.

In order to illustrate the role of extra ABS, in Fig. 5.3 we present the results from the same basic model, in which more and more states are added to the system in subsequent panels. Fig 5.3(a) corresponds to a single spinful ABS QD_1 in the quantum dot, and no ABS in the lead. It shows an Andreev loop around zero bias due to a soft gap probe (white), and a replica at the bulk gap edge (red). The Andreev loop separates the singlet regions (labeled s_0 and s_2 in panel a) and a central doublet region d. The three regions, which have different dot occupations (0 in s_0, 1 in d and 2 in s_2), appear separated by discontinuities in this simulation due to the self-consistent mean-field approximation used for the interactions in the quantum dot. In Fig. 5.3(b), a second ABS QD_2 is added to the quantum dot separated by 0.35 meV from QD_1. At low bias, in the blue region, this yields a pair of resonances most clearly seen in the s_0 region. At high bias $V > \Delta/e = 2.7$ mV, in the dark-red region, additional parallel lines appear as replicas of the low bias QD_1 and QD_2 resonances.

In Fig. 5.3(c) we have a single ABS in the dot QD_1 and an ABS in the lead (labeled $LEAD_1$). The latter introduces resonances that run largely parallel to the horizontal axis as in Fig. 5.2(d). However, at the points where the lead ABS is resonant with the dot ABS the features due to QD_1 and $LEAD_1$ exhibit anticrossings. The lowest bias resonance transforms into a loop confined to ±0.5 meV, well below the superconducting gap. The doublet region d contains more resonances than singlet regions s_0 and s_2 because ABS of different spins are not degenerate in this region.

In Fig. 5.3(d), we again have two ABS in the lead and two in the dot, as in Fig. 5.2(d). Comparing with Fig. 5.3(c), we can see additional loops forming in the low bias region, due

to anticrossing of LEAD_1 and LEAD_2 with QD_1 and QD_2. The higher bias loops, as probed by the soft gap in the left electrode, show a stronger bias asymmetry in terms of peak height than the primary loop around zero bias. As already discussed, all of the low-bias features develop strong replicas due to the gap edge in the probe (red) accompanied by NDC dips (black).

5.4 Negative differential conductance within the superconducting gap

In Fig. 5.4 we focus on the NDC features observed in NbTiN-InSb devices since they represent an open challenge. The unusual aspect is that NDC is observed at low bias, well within the superconducting gap (Fig. 5.4(a)). The NDC regions trace out the loop-like Andreev resonance, at certain instances dominating over the positive differential conductance part. In differential conductance measurements, NDC often appears when two peaks in the density of states are aligned in the probe and the lead. Tunneling current then exhibits a peak which translates into a peak-dip structure in differential conductance. This is why NDC is often observed when tunneling from one superconducting gap edge into another, at high bias such as in Fig. 5.1(c) at $V = 2\Delta/e$. However, NDC at very low bias would require a peak in the DOS of the probe at zero bias (Fig. 5.4(b)). Such a peak is included in the model calculation in Fig. 5.2(d), it is responsible for NDC at low bias in the model. Shifting the DOS peak in the probe to finite bias results in additional doubling of all resonant features and poorly matches the experimental data (simulation not shown).

The origin of this deduced zero-bias DOS peak, observed in several devices, is unknown at present, but it has significant implications for the interpretation of Majorana experiments done in similar devices, since MBS also manifests as a zero-bias peak. One can rule out Majorana as an explanation for this peak, because the subgap NDC is observed regardless of the presence of magnetic field which is a necessary ingredient for MBS. A plausible scenario is the presence of an accidental discrete zero-energy state in the probe region of the device. The local gates in that part were tuned to highly positive voltages to avoid creating additional quantum dots, and the superconducting contacts to the nanowire are highly transparent.

Nevertheless, some bound states may also appear in the probe segment due to its finite size. Other possibilities include though not limited to Fermi-edge singularities and Kondo effect [38, 201].
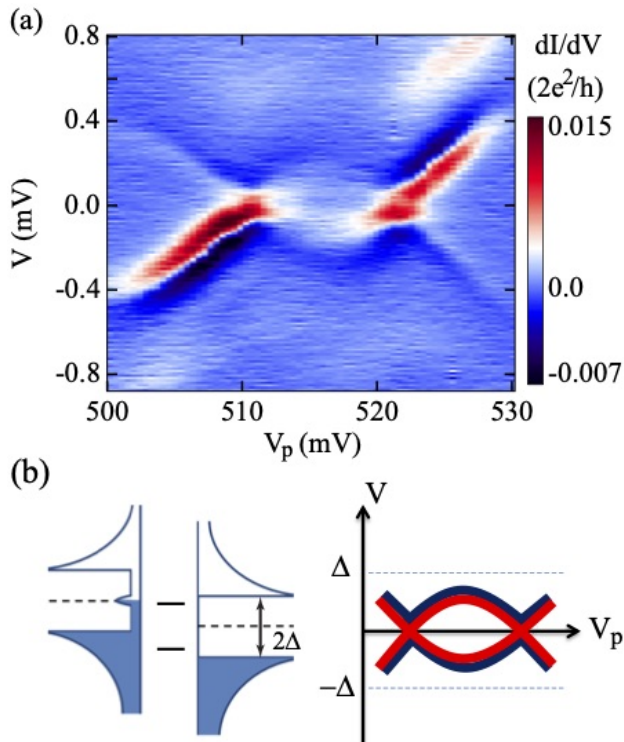
Figure 5.4: (a) Data in the regime similar to Fig. 5.2(b). (b) Illustrative energy diagram with a peak in the density of states in the left probe that aligns with ABS, and produces NDC in the loop-like structure within the superconducting gap.

5.5   Conclusion

An important conclusion for Majorana experiments is that the tunneling probe can be more complex than a Fermi level or a textbook superconducting DOS, as confined quantum states can form in the adjacent nanowire sections, resulting in additional transport resonances. The presence of such additional resonances may complicate the interpretation of experiments aimed at detecting MBS in nanowires, and should be carefully considered.

5.6 Supplemental material

Theoretical model. This section introduces the model of the form $H = H_d + H_R + V$ for the quantum dot coupled to the right hard-gap superconducting electrode. The left electrode is treated as a superconducting tunnel probe and is discussed later. The quantum dot is modeled as a multiorbital Anderson model, with levels ϵ_i^D, of the form

$$H_d = \sum_{i\sigma} \epsilon_i^D d_{i\sigma}^\dagger d_{i\sigma} + U \sum_i n_{i\uparrow} n_{i\downarrow} \tag{59}$$

where $n_{i\sigma} = d_{i\sigma}^\dagger d_{i\sigma}$. As usual, we model the coupling to the right superconductor by a self energy $\Sigma(\omega)$ that captures the induced pairing Γ_S in the dot resulting from the parent gap Δ_p. In the Bogoliubov-de Gennes basis $D_i = \left(d_{i\uparrow}, d_{i\downarrow}, d_{i\uparrow}^\dagger, d_{i\downarrow}^\dagger \right)$, this dot self-energy reads

$$\Sigma_R(\omega) = \frac{1}{2} \frac{\Gamma_S}{\sqrt{\Delta_p^2 - \omega^2}} \sum_{i\sigma} D_i^\dagger \begin{pmatrix} -\omega & 0 & 0 & -\Delta_p \\ 0 & -\omega & \Delta_p & 0 \\ 0 & \Delta_p & -\omega & 0 \\ -\Delta_p & 0 & 0 & -\omega \end{pmatrix} D_i \tag{60}$$

For the physics discussed here, it is a good approximation to solve the above superconducting Anderson Hamiltonian in a Hartree-Fock mean field approximation, hence neglecting Kondo correlations, for a discussion see e.g. Ref. [202]. Clearly, this standard model of a proximitized quantum dot does not capture in full the experimental phenomenology (in particular the replicas described in the main text), so we consider the possibility that the superconducting electrode contains additional ABSs (owing to its finite length). The ABSs are described by the term

$$H_R = \frac{1}{2} \sum_{j\sigma} \epsilon_j^L c_{j\sigma} c_{j\bar\sigma} + \text{h.c.}, \tag{61}$$

which is essentially a generalization of the so-called zero-bandwidth model to include more than one quasiparticle excitation in the superconducting lead. Note that for the case of a two orbital Anderson model coupled to a single quasiparticle excitation in the superconducting lead (see Fig. 5.3(c)) our model recovers the double dot model of Ref. [203].
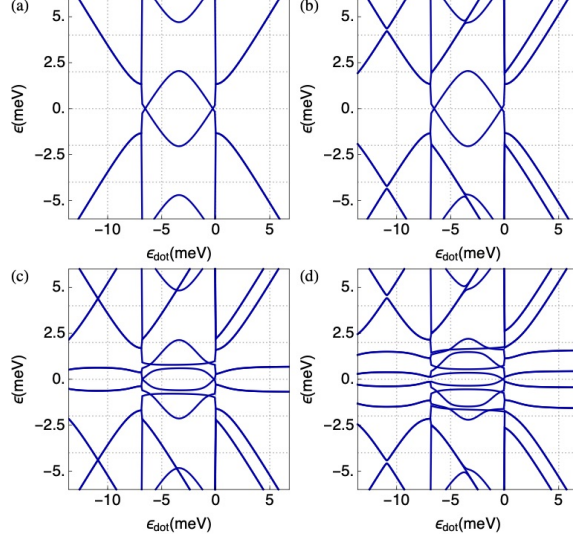
Figure 5.5: Spectra of $H = H_d + H_R + \Sigma_R$ corresponding to the transport simulations in Fig. 5.3, where the self-energy $\Sigma_R(\omega)$ of Eq. 60 is taken at $\omega = 0$.

For simplicity, we assume that the ABS are uniformly coupled to the dot states through a spin-independent hopping amplitude

$$V = t \sum_{ij\sigma} d_{i\sigma}^{\dagger} c_{j\sigma} + \text{h.c.}, \tag{62}$$

This minimal model for the quantum dot coupled to a finite-size superconducting lead fully captures the physics resulting from a microscopic model describing a quantum dot coupled to a finite proximitized nanowire (not shown).

The density of states at the dot is obtained by taking the trace over electron-like dot states $\rho(\omega) = -\frac{1}{\pi} \text{ImTr}_{\text{dot}} G$ of the retarded Green function $G = [\omega + i0 - H - \Sigma_R(\omega + i0)]^{-1}$.

Tunneling spectroscopy is performed through the left superconducting lead, that is assumed to be tunnel-coupled to the dot. Using the Keldysh formalism, it is possible to write an expression for the current in terms of Green's functions of the above model (for details, see e.g. the supplemental information of Ref. [43]. For very asymmetric situations (such that the one described here where the left superconducting lead just acts as a tunneling probe), the lengthy Keldysh expression can be simplified and one can derive a tunnel-like expression

of the current which is just a convolution of the DOS in the probe and the DOS at the quantum dot of the form

$$I \propto \int \rho(\epsilon)\rho_{probe}(\epsilon + eV)[f(\epsilon) - f(\epsilon + eV)]d\epsilon. \tag{63}$$

The density of states in the probe contains a smooth gap, modelled as a Dynes-BCS function $\rho_{probe}(\epsilon) = \mathrm{Re}\,\rho_{\mathrm{BCS}}(\epsilon + i\eta_D)$, with a phenomenological Dynes depairing imaginary part $\eta_D = 0.01$ meV and

$$\rho_{\mathrm{BCS}}(\epsilon) = \rho_0 \frac{|\epsilon|}{\sqrt{\epsilon^2 - \Delta_p^2}}, \tag{64}$$

with ρ_0 the DOS at the Fermi energy of the probe in the normal state. In simulations with a zero bias peak in the probe, the latter is added as a Gaussian of width 0.25 meV.
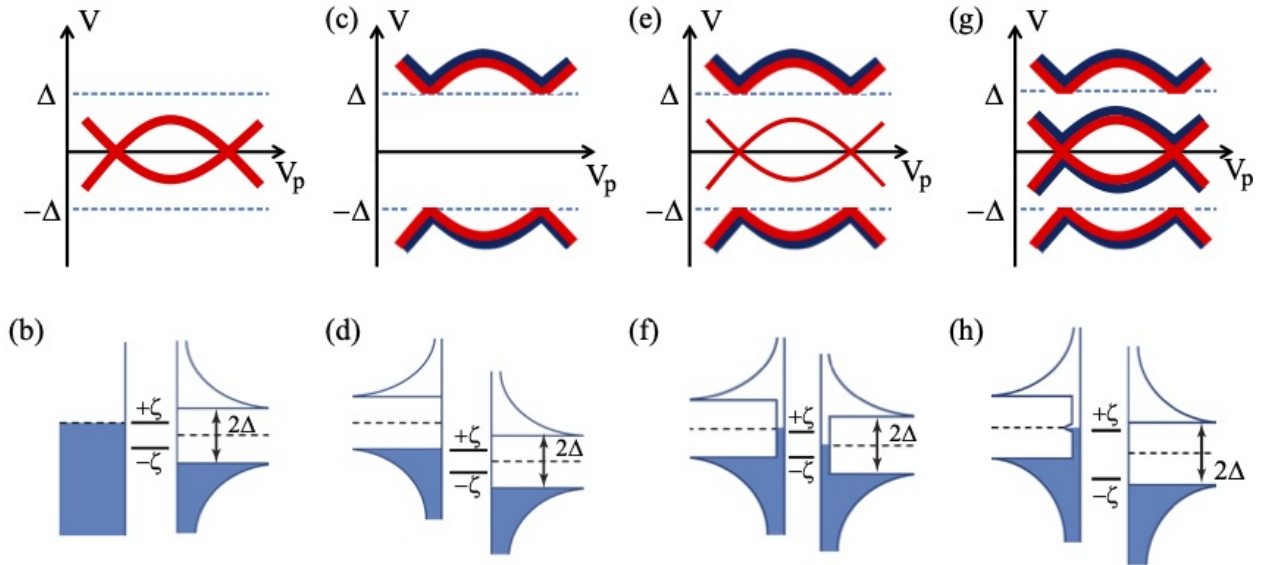
Figure 5.6: (a) Bias vs. gate plot with a normal conductor probe. Positive dI/dV resonances are depicted in red. (b) Energy diagram with ABS energy $+\zeta$ at resonance with the normal probe. (c-d) Bias vs. gate plot and energy diagram with a hard gap superconducting probe. The blue curves in (c) depict negative dI/dV resonances. (e-f) Bias vs. gate plot and energy diagram with a soft gap superconducting probe (a uniform DOS within the gap). (g) Bias vs. gate plot and energy diagram relevant for experiments on NbTiN/InSb devices. The soft gap probe has a DOS peak at zero bias, which produces NDC at low bias in (g).

Here we are showing additional data from the Al/InSb discussed in the main text as well as a second measured similar device where the Andreev replica is apparent and the

superconductivity persists also to 1 T. Moreover, there are Josephson effect measurements shown from both devices with measured switching current ≈ 5 nA. These measurements indicate that these junctions could potentially be used as the nonlinear element in hybrid qubits with Josephson energy of ≈ 2.5 GHz.
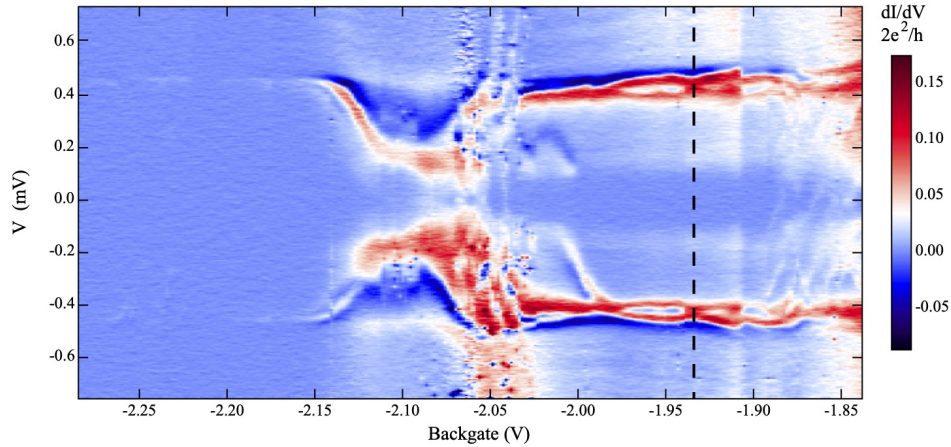
Figure 5.7: Differential conductance through the device as a function of bias and backgate voltage shows the unintentional quantum dot present in the nanowire. The linecut corresponds to the backgate voltage at which the data in Fig. 5.1 are taken. Data is obtained at zero applied magnetic fields. At negative backgate voltages below -2.15 V, current-voltage characteristics resemble a hard gap regime, however the induced gap likely remains soft and the suppressed conductance within the gap is due to an increased tunnel barrier.
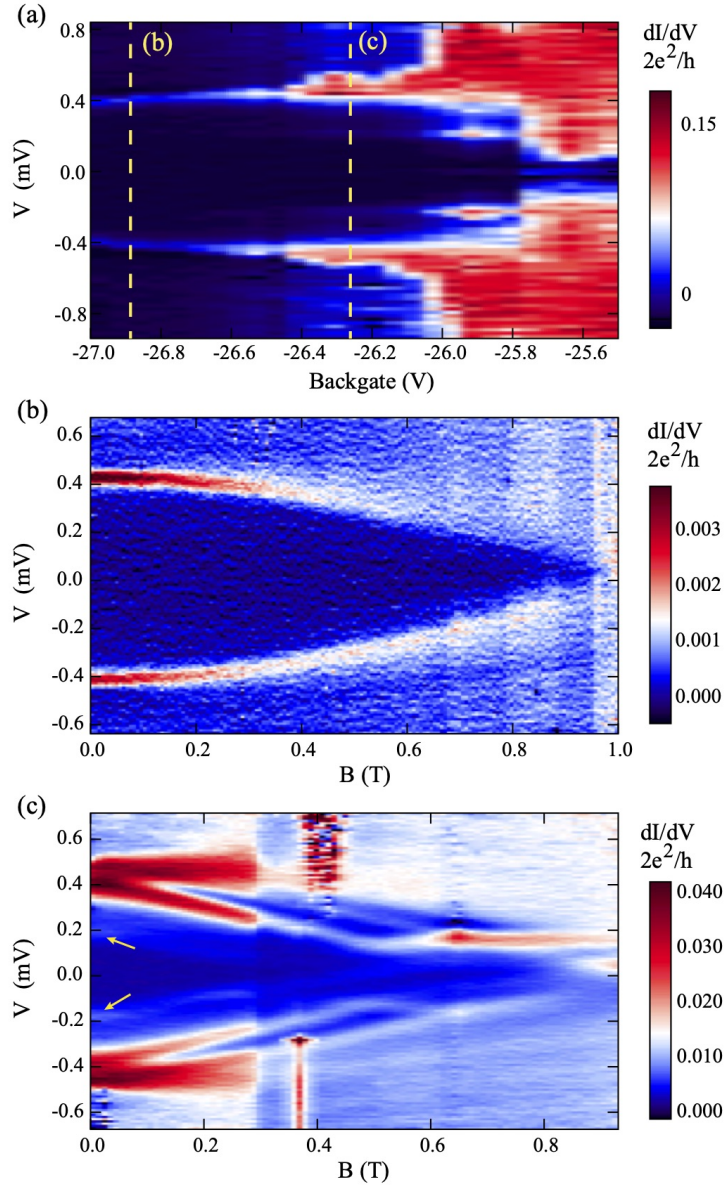
Figure 5.8: (a) Tunneling conductance through the device as a function of bias and backgate voltage. Gate voltages corresponding to panels (b) and (c) are marked with vertical dashed lines. (b) Superconducting gap with no apparent additional resonances persists up to B = 1 T. In agreement with data in Fig. 5.7, data obtained at more positive gate voltages, with more open tunnel barrier, reveal subgap structure due to soft gap: (c) There are two resonances deviating from the gap edge at finite magnetic field as well as apparent replicas of those resonances at half of the gap energy.
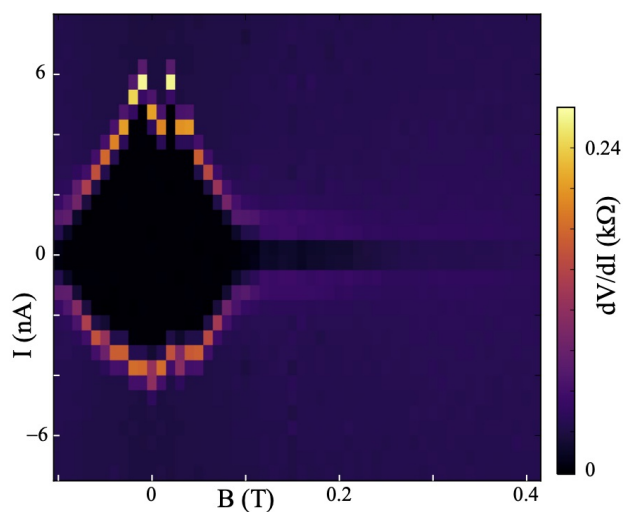
Figure 5.9: Measured differential resistance as a function of bias current and magnetic field for Al/InSb deivce of main text. The switching current decreases at 0.1 T which is critical field of Al but it persists up to higher fields consistent with gap measurements.
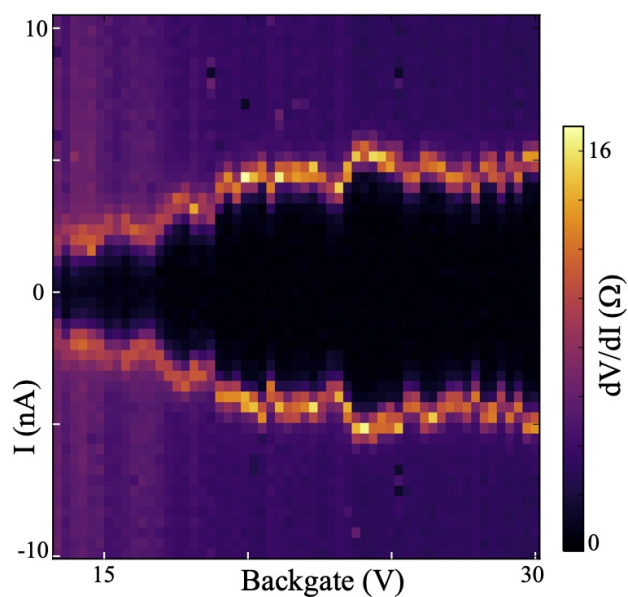
Figure 5.10: Measured differential resistance as a function of bias current and backgate voltage for second Al/InSb device. The voltage dependence of supercurrent is evident where supercurrent saturates at 30 V.

100

6.0 Parity-preserving and magnetic field resilient superconductivity in InSb nanowires with Sn shells[1]

In this chapter we study bottom-up grown semiconductor indium antimonide nanowires that are coated with shells of tin. The shells are uniform in thickness. No interdiffusion is observed at the interface between Sn and InSb. Tunnel junctions are prepared by in-situ shadowing using nearby nanowires as well as flakes. A 15 nm thick shell of tin is found to induce a hard superconducting gap in the range 600-700 μeV. Superconductivity persists up to 4 T in magnetic field. A small island of Sn-InSb exhibits the coveted two-electron charging effect, a hallmark of charge parity stability. The findings open avenues for superconducting and topological quantum circuits based on new superconductor-semiconductor combinations.

6.1 Introduction

As we enter the era of intermediate-scale quantum circuits [69, 204], materials considerations come into renewed focus through their impact on quantum gate fidelity. The most successful solid state approaches rely either on superconductors [205], or on semiconductors [206], with the future topological platform to require a hybrid of both [123]. The search continues for the ultimate material capable of delivering low intrinsic decoherence. In this context, the push for qubits based on Majorana zero modes that are expected to be topologically immune to decoherence [207, 208, 209, 210] has accelerated the discovery of high quality interfaces between superconducting metals and low-dimensional semiconductors [211, 137, 65, 212].

Only a few superconductors were explored for Majorana qubits, most notably aluminum which is also the material of choice for transmon quantum processors [69]. Among advantages of aluminum are its' self-limiting native oxide and a hard induced gap in proximate semiconductors [211, 167, 213, 65]. Due to this, aluminum is widely known to exhibit 2e

---

[1]This chapter is adapted from Ref. [134]

charging in small islands, a fundamental property that makes it a low-decoherence super-conductor [214, 215, 216, 217, 121, 151, 218, 219]. Among disadvantages of aluminum are a relatively small superconducting gap equivalent to 1 K, and a low critical magnetic field. This confines quantum computing to ultra-low temperatures and even further constrains the design of future topological qubits which will require a precise balance of several energy scales [220].

Here we present induced superconductivity in InSb nanowires [133, 131] with Sn shells. InSb is the highest electron mobility group III-V semiconductor with strong spin-orbit coupling [177] and large Landé g-factors in the conduction band [135]. These are the primary ingredients of the Majorana recipe [4, 5], making InSb an optimal material for the investigation of induced topological superconductivity [67, 150, 68, 152].

We find that InSb nanowires coupled to tin exhibit hard induced superconducting gap up to 700 μeV. Superconductivity persists to a significant magnetic field, up to 4 Tesla for 15 nm thick Sn shells. Islands of tin do exhibit 2e-periodic charging patterns. This effect is a landmark requirement for topological quantum computing as well as for transmon qubits, as it is a pre-requisite for long quasiparticle stability times. Fluctuations of the quasiparticle number on superconducting islands scramble qubit readout, while quasiparticle hopping between islands is a source of decoherence [207, 208, 209, 210, 221]. Results are obtained even though Sn and InSb exhibited no epitaxial relationship which was previously viewed as essential [167, 65].

6.2 Hard induced superconducting gap in normal metal-superconductor configuration

Our first goal is to investigate electron tunneling into Sn through InSb in the normal metal-superconductor (N-S) configuration. For this we need a nanowire with only one end covered by tin. We use the uncovered end to define a tunneling barrier and an N-contact. In order to avoid damage to InSb that results from etching away part of the Sn shell, we employ in-situ nanoscale shadowing [65, 219]. In this case it is an InSb flake, standing in front of

the nanowire, that shadows the bottom of the wire during deposition of Sn in ultra-high vacuum [132] (Fig. 6.1A). We expect that junctions defined by wet etching or lift-off would yield similar results [222, 223].
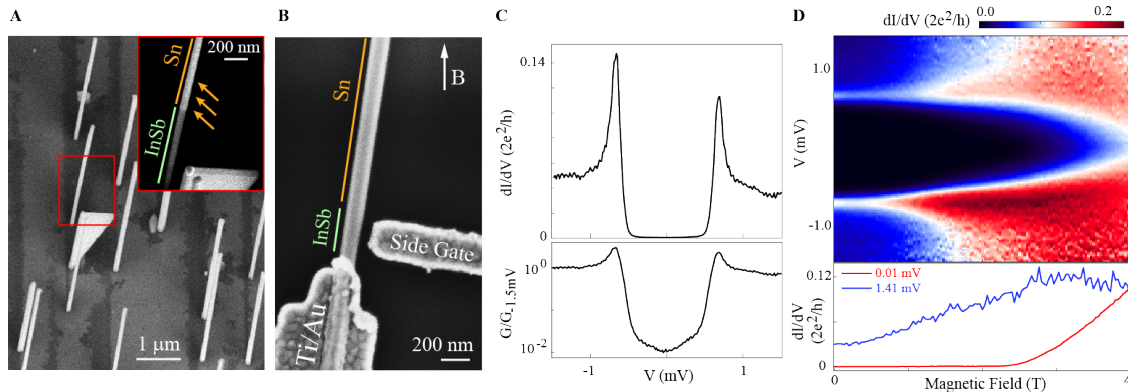
Figure 6.1: (A) Scanning electron micrograph (SEM) showing a triangular InSb flake that stood in the path of a beam of Sn atoms, shadowing the InSb nanowire standing behind. Dark streaks on the InSb substrate are also due to shadowing of the Sn beam by nanowires and flakes. The inset shows the direction of Sn beam and indicates the shadowed and exposed segments of the nanowire. (B) SEM of an N-S device (device A) with a flake-shadowed Sn-InSb nanowire and Ti/Au contacts and a side gate. Magnetic field is in the plane of the sample as shown by the arrow. (C) Zero magnetic field tunneling conductance spectrum of device A in linear scale (top) and logarithmic scale (bottom), $V_{BG} = 7.5$ V, $V_{SG} = -0.4$ V. (D) Magnetic field evolution (top) of the zero-field spectrum shown in panel (C). Line cuts at two specific source-drain bias voltages are shown in the bottom.

To prepare an N-S device the tin-coated nanowire is positioned onto a doped Si/SiO$_x$ substrate which is used as a back gate (BG) (Fig. 6.1B). A side gate (SG) is used to define and tune the tunneling barrier near the edge of the tin-free segment. The tunneling spectrum reveals a two-orders-of-magnitude suppression in conductance around zero bias (Fig. 6.1C). This so-called hard gap indicates the elimination of decoherence pathways due to disorder and spurious subgap states. A superconducting tunneling peak is at ± 680 μeV which is comparable to the gap of tin. In magnetic field, the hard gap is found to persist beyond 2 Tesla, with the gap "softening" at higher fields and fully closing around 4 Tesla (Fig. 6.1D). Magnetic field resilience is an indicator of a thin uniform shell and this resilience is another advantage of Sn since topological, spin and some superconducting qubits operate at high magnetic fields.

6.3 Transparent Josephson tunnel junction

Next, we study superconductor-superconductor (S-S) devices with both ends of the nanowire covered by tin, and only a narrow break in the shell to define an InSb weak link (Fig. 6.2A). For this we use a previously developed method of shadowing the Sn flux by criss-crossing nanowires [65]. We first study tunneling between two tin islands (Fig. 6.2B). We observe a smooth nanowire pinch off void of accidental quantum dot states. Three finite-bias resonances are observed, marked 4Δ, $4\Delta/2$ and $4\Delta/3$ in Fig. 6.2B. This sequence is a manifestation of Multiple Andreev Reflection processes, which are characteristic of transparent S-S junctions. They correspond to 615 μeV $\pm$ 10 μeV which is somewhat smaller than the gap observed in the N-S device (Fig. 6.1C). At $V_{BG} < -1$ V only the 4Δ resonance is observed. We interpret this as the superconducting tunneling regime. Because the S-S tunneling resonance is a peak in current, it appears as a peak-dip structure in conductance.

The resonance at zero bias in Fig. 6.2B is the Josephson supercurrent. This effect is best studied in the current-bias configuration (Fig. 6.2C). The switching current (I_{sw}) from superconducting to normal state is a peak in differential resistance. I_{sw} decays smoothly with more negative V_{BG}. The current-voltage characteristics are weakly hysteretic which is reflected in the asymmetry of I_{sw} in positive and negative current bias. In magnetic field, the Josephson effect is observed up to 1.5 T and remains significant with sharp switching up to 0.5 T (see Supplementary Materials). This significant field range is a positive development for schemes that require coupling and decoupling of topologically superconducting islands at finite magnetic field for Majorana fusion or braiding [224, 225]. Measurements on continuous-shell nanowires without shadow junctions yielded supercurrents in the range $20 - 30$ μA corresponding to the critical current density of 2×10^6 A/cm^2 (data in Supplementary Materials). The extracted products $I_{sw}R_N$ (R_N is the normal state resistance) are in the range $125 - 225$ μeV, which is significant, and of the same order of magnitude as the gap.
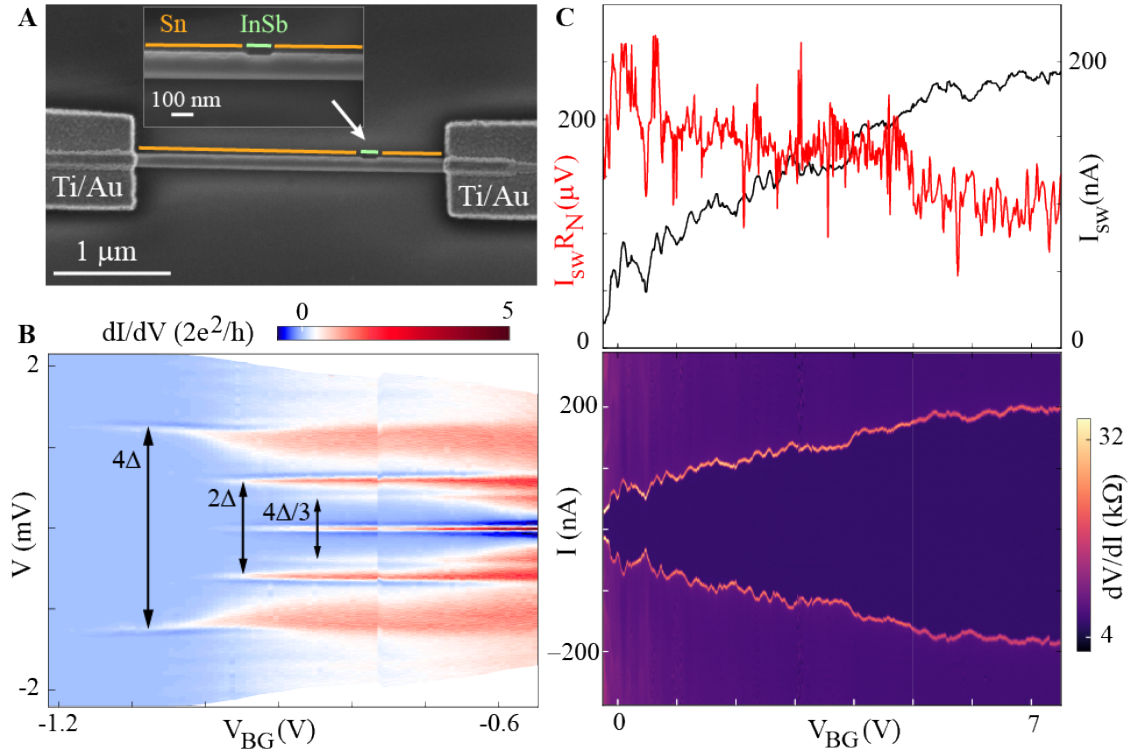
Figure 6.2: **(A)** SEM of device B (S-S device). Inset zooms in the shadow junction where Sn shell is visible. **(B)** Differential conductance as a function of source-drain voltage bias V and back gate voltage, V_{BG}. The double arrows mark resonances 4Δ, $4\Delta/2$ and $4\Delta/3$. **(C)** Differential resistance as a function of current bias I and V_{BG} (bottom). Top panel shows extracted switching current I_{sw} (black) and $I_{sw}R_N$ (red) as a function of back gate voltage.

105

6.4 2-electron tunneling through tin island

The two-electron charging effect is central for topological quantum computing because the states of a topological qubit are distinguished by even/odd island charge parity. If only 1e charging periodicity were observed, it would mean that despite a well-defined superconducting gap, electrons can be added to an island one at a time and the ability to distinguish the states of a topological qubit is scrambled. 1e periodicity is also detrimental for transmon qubits where single electron tunneling is a decoherence mechanism [221].

In Fig. 6.3 we present key findings on 2e charging of a tin island. The island is defined between two nanowire-shadow junctions in the N-S-N geometry (Fig. 6.3A). At zero magnetic field, we observe a single family of Coulomb peak resonances consistent with charging the entire island (Fig. 6.3B). At a finite magnetic field of 1 T, the frequency of Coulomb resonances doubles (Fig. 6.3C, D). We attribute data at zero field to 2e charging, and data at finite field to 1e charging. The transition from 2e to 1e is due to the superconducting gap or the lowest subgap state dropping in energy below the charging energy, which we estimate to be 0.3 meV (Figs. 6.3E, F). At finite magnetic field, it costs less energy to add electrons to the island one-by-one, while near zero field, due to hard gap superconductivity, it is advantageous to add electrons in pairs.

6.5 Interface characteristics between Sn shell and InSb nanowire

Tin is an unusual material which has two different crystal phases with a phase transition at 13°C. The low-temperature α-Sn has a diamond cubic lattice, while the high temperature β-Sn is tetragonal. The electronic properties of both phases are very different. α-Sn is a semimetal which can also be a topological insulator in monolayer form [226, 227, 228], whereas β-Sn is a metal with a superconducting transition temperature of 3.7 K.

For tin on InSb nanowires we assess the structural properties and elemental distribution using transmission electron microscopy (TEM). TEM images reveal a polycrystalline Sn shell of uniform thickness around the InSb nanowire (Fig. 6.4A): the shell features grains
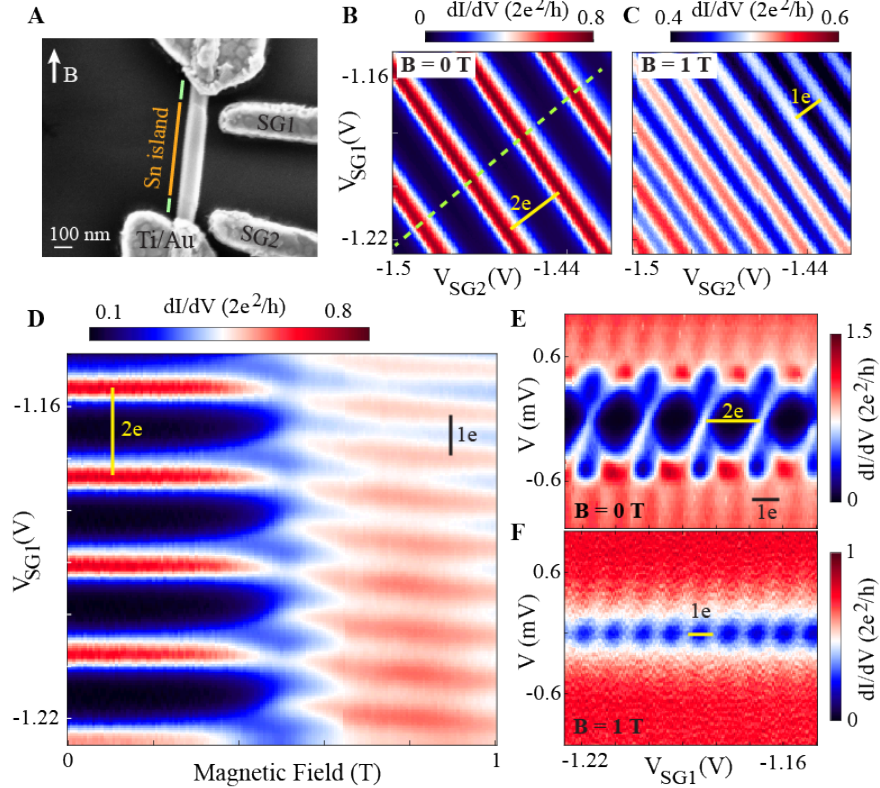
Figure 6.3: (A) SEM of device C showing the Sn island, two shadow junctions with bare InSb, side gates SG1 and SG2 and Ti/Au source-drain contacts which cover the outside Sn segments and suppress superconductivity there. (B) and (C): 2e and 1e tunneling conductance resonances measured at $V = 0$ at B = 0 T and B = 1 T, respectively. (D) Magnetic field evolution of conductance along the dashed cut in panel (B). (E) and (F): V vs gate spectroscopy at B = 0 T and B = 1 T, respectively. The duration of data acquisition for each panel is of order 1 hour, and the parity pattern is reproducible over days.

of sizes 25×25 nm to 50×60 nm (see Supplementary Materials). The Sn-InSb interface is abrupt and some Sn grains show epitaxial relationship with InSb. The high-resolution annular bright field-scanning TEM image (Fig. 6.4C) shows a section of the interface where the {111} planes of zincblende InSb are aligned with lattice planes of a Sn grain with a lattice distance of 2.04 Å. This matches the {220} interplanar distance of β-Sn. This grain is one of 13 analyzed along the same nanowire. 11 of the grains are identified as β-Sn from the fast Fourier transform analysis of the interplanar distances (Fig. 6.4C, inset). Only two of those β-Sn grains show a preferential epitaxial relationship with InSb. In contrast, α-Sn

is lattice matched to InSb and can grow epitaxially [229]. The predominantly β-Sn shell observed at room temperature by TEM is in agreement with superconductivity observed at low temperatures, suggesting that no phase transformation of Sn occurred upon device cooldown.

In addition to the uniform shell thickness, the nanowire shadow junctions used in S-S and N-S-N devices are sharp with Sn islands defined abruptly on each side of the junction
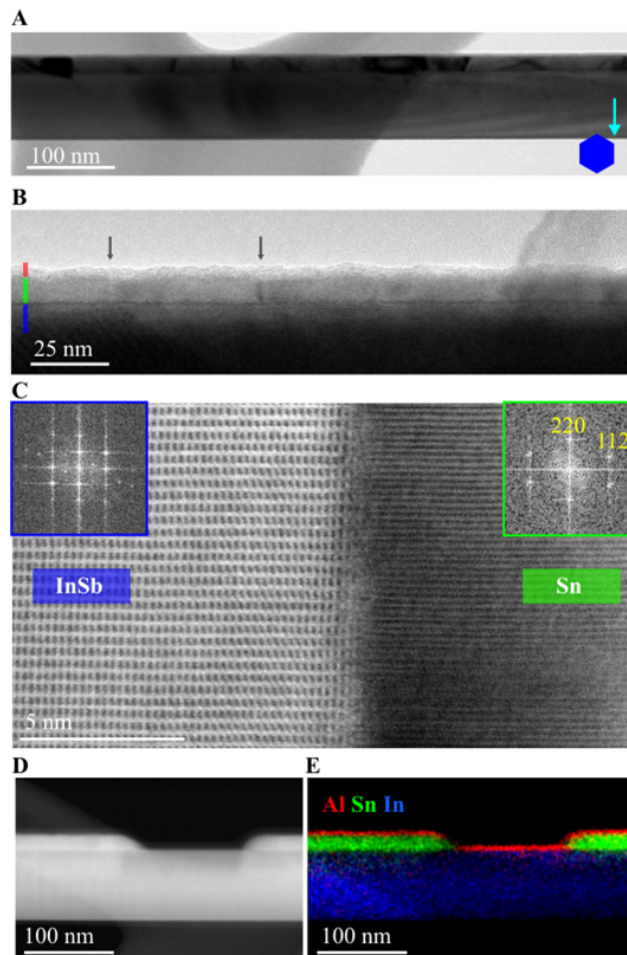
Figure 6.4: (A) Side-view TEM image along the $\langle 112 \rangle$ zone axis showing a homogeneously thin shell. (B) Higher magnification TEM of the AlO_x (red) - Sn (green) - InSb (blue) stack. The Sn grain boundaries are highlighted by arrows. (C) HR-STEM image of the Sn-InSb interface. The insets show Fourier transforms to the left and to the right of the interface. (D) High-angle annular dark-field STEM image of a shadow junction. (E) EDX elemental mapping of the shadow junction in (D). The Al-rich layer (red) corresponds to AlO_x, oxygen not shown for clarity.

(Fig. 6.4C). Energy-dispersive x-ray spectroscopy (EDX) confirms that the Sn islands are isolated from each other and no interdiffusion between Sn and In is detected (Fig. 6.4D). A uniform 3-nm-thick AlO_x passivation layer covers the entire nanowire, this layer maintains integrity and smoothness of the shell on the scale of at least 3 months. Oxidation at the Sn-InSb interfaces is not detected but cannot be fully excluded (see Supplementary Materials).

6.6   Conclusion

Our results illustrate that neither defect-free epitaxial wire-shell interfaces nor single vacuum cycle growth of nanowire and shell are crucial requirements for the demonstration of hard gap, field-resilient superconductivity and 2e charging. We conclude that the key components in attaining robust induced superconductivity are (i) removal of InSb native oxide using atomic hydrogen prior to Sn growth, followed by (ii) liquid nitrogen cooling of the nanowires during metal evaporation to produce a homogeneous ultrathin shell and (iii) immediate passivation of the wire-shell hybrid with a stable dielectric. Supplementary Figure 6.5 illustrates that when the sample is allowed to warm up without AlO_x passivation immediately after the cryogenic Sn shell growth, tin coagulates into discontinuous grains.

Without the need for epitaxial matching many more superconductor-semiconductor combinations can be tried in search for decoherence free qubit materials [219, 230, 231, 232, 223]. An immediate follow-up of our work are experiments on Sn-InSb devices in the Majorana geometry in search for clear signatures of topological superconductivity, as well as characterization of coherence times of Sn-based transmon qubits.

6.7 Supporting materials and methods

6.7.1 Nanowire growth

InSb nanowires are grown using the vapor-liquid-solid technique in a horizontal metal-organic vapor phase epitaxy reactor. The first nanowires used in this work are stemless InSb nanowires with flakes as shadow objects (Fig. 6.1A) [133, 132]. Both InSb nanowires and flakes are grown on an InSb (111)B substrate with a selective-area mask and gold as catalyst. The second type of nanowires, shown in Figs. 6.2A and 6.3B are shadowed by other nanowires [65]. The InP (100) substrates are etched to expose the two {111}B facets, on which gold particles are deposited with an offset on the two opposing facets of a trench. Nanowires grow towards each other, such that the front wire shadows the back wire. InSb wires are grown on InP stems.

6.7.2 Sn shell growth

After transit in air (from Eindhoven to Santa Barbara), nanowire chips as grown are loaded into vacuum for subsequent growth of Sn shells. The chips are gallium bonded to 3.3 mm thick, 90 mm diameter molybdenum blocks. The absence of a native nanowire surface oxide is expected to be essential in aiding in inducing a hard superconducting gap [211, 137, 65]. In order to remove the native InSb oxide, atomic hydrogen cleaning is performed in a UHV chamber with a base pressure $< 1 \times 10^{-10}$ Torr at 380°C (thermocouple temperature) for 30 minutes, at an operating pressure of 5×10^{-6} Torr consisting primarily of hydrogen ambient [65]. Once cleaned, the samples are transferred in-vacuo to an ultra-high vacuum chamber dedicated for metal evaporation (base pressure $< 5 \times 10^{-11}$ Torr). Here, the nanowire samples are cooled to 85 ± 5K (-188 ± 5°C) for 2 hours, prior to tin evaporation. 15-nm-thick tin is then evaporated from an effusion cell at a growth rate of 7.5 nm/hr and an evaporation angle close to 60° from sample normal. This shallow evaporation angle aids in-situ formation of Sn islands with nanowire or flake shadows. After Sn evaporation, while the sample is still expected to be at cryogenic temperatures (due to the thermal mass of the molybdenum block), it is moved to an interconnected UHV chamber

for the electron-beam evaporation of a 3-nm-thick shell of AlO_x, at normal incidence. This is done to prevent coagulation of the evaporated tin layer on InSb nanowires like shown in Fig. 6.5. The samples are then allowed to warm up to room temperature in vacuum.
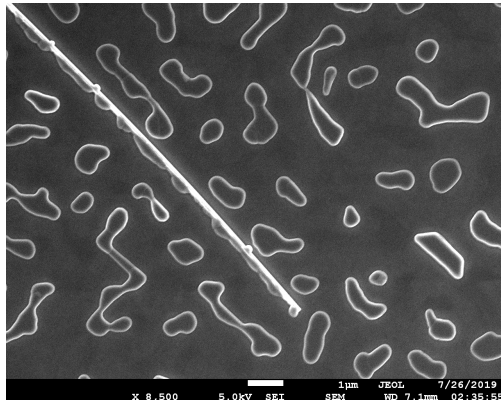
Figure 6.5: SEM image of a 15 nm tin film on an InSb nanowire grown at 85 ± 5 K that was allowed to warm up to 300 K in vacuum, without any immediate cap layer or oxidation. The tin layer coagulates to form diconnected islands or droplets on the nanowire. In a separate sample, such a film was also measured to be insulating across the wafer which confirms that the tin metal droplets are discontinuous. It was also observed that coagulation of the tin layer could be avoided by immediate oxidation of the tin film in a load lock but such films were found to show rapidly changing superconducting properties over days which was attributed to continued oxidation of the tin layer underneath. No such change was observed in tin films capped with AlO_x which were found to be robust on the scale of 3 months.

6.7.3 Device fabrication and measurements

Device fabrication is similar to previous work on wires with epitaxial Al film [65], also used in Chapter 5. We made global back gate substrates with doped and thermally oxidized Si wafers, then covered them with 75nm HfO_x to get a better dielectric layer. Wires are transferred onto substrates using a micromanipulator under an optical microscope. Contacts and gates are patterned by electron-beam lithography by curing the resist at room temperature in a vacuum chamber (operating pressure $< 1 \times 10^{-4}$ Torr) to avoid nanowire heating and potential interdiffusion of Sn and In. Argon ion milling is performed to remove the AlO_x layer before evaporating 10/150 nm of Ti/Au. Measurements are performed in a dilution refrigerator with a 30 mK base temperature using a combination of direct current and lock-in techniques. All voltage bias data are two-terminal measurements. A series

resistance of ≈ 5 kΩ due to measurement setup was taken into account in calculating conductance in all figures as well as renormalizing V axis in Figs 6.2B, 6.6, 6.7A. TEM studies were performed using a probe corrected microscope operated at 200 kV, equipped with a 100 mm^2 EDS detector.

6.7.4 Supplementary figures
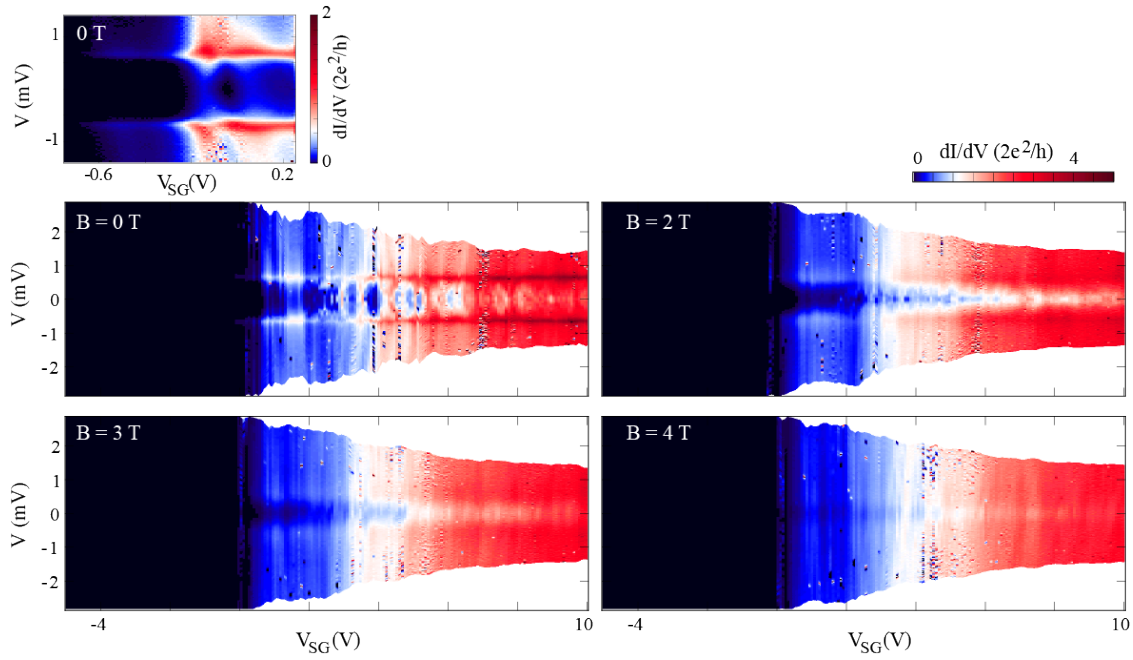
Figure 6.6: Additional gate dependence data for flake-shadowed device A studied in Fig. 6.1. Zero-field hard gap regime displays the presence of a quantum dot in the vicinity of a tunnel barrier. Soft gap is observed for higher magnetic fields up to 4T. $V_{BG} = 7.5$ V.
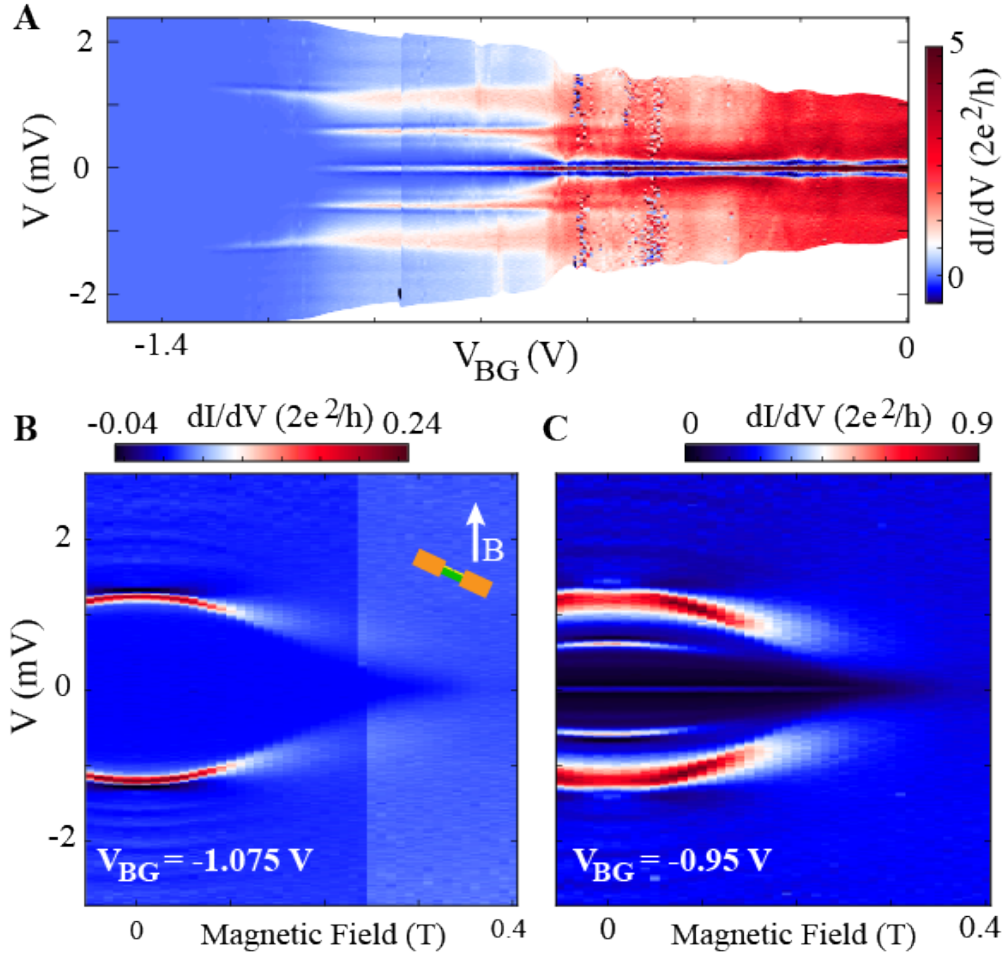
Figure 6.7: Additional data for device B studied in Fig. 6.2. (A) Differential conductance as a function of bias voltage and back gate voltage in the extended gate range compared with Fig. 6.2. (B) and (C) show magnetic field dependence at $V_{BG} = -1.075$ V, and $V_{BG} = -0.95$ V, respectively. This device is at $\approx 60°$ angle with magnetic field and as a result the gap closes at $B \approx 0.4$ T, a lower field than in devices that were aligned parallel to the field, e.g. Fig. 6.1.
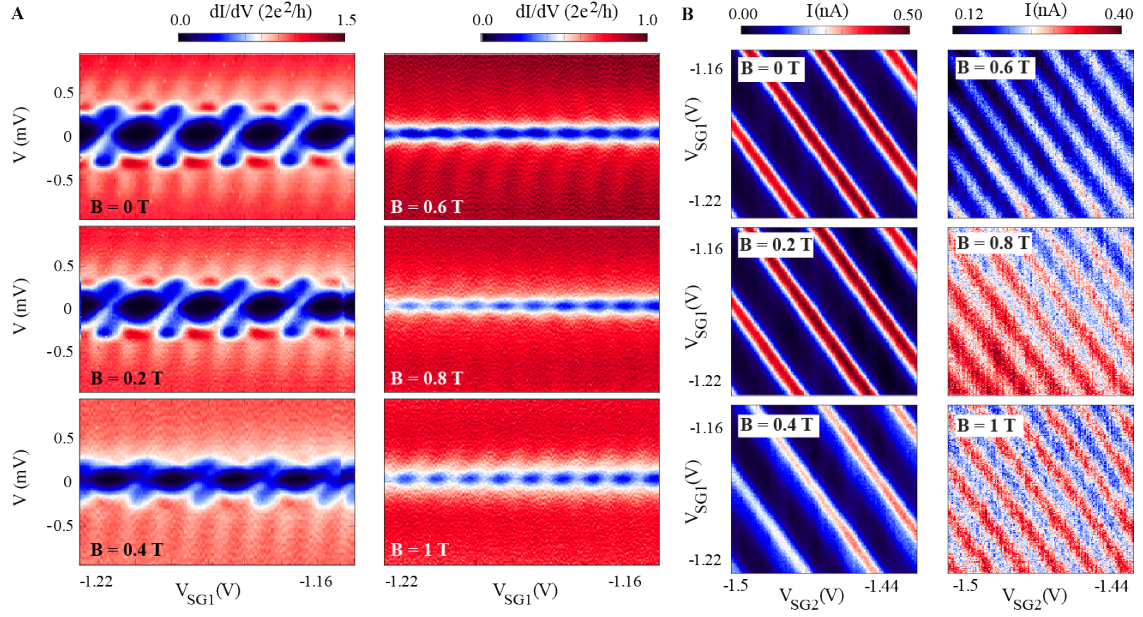
Figure 6.8: Additional data for device C studied in Fig. 6.3. (A) Bias vs a combination of SG1 and SG2 at different magnetic fields, in the same regime as Fig. 6.3E. (B) Gate dependent DC current measured at 10 μV bias. The gates are scanned in the same regime as Fig. 6.3
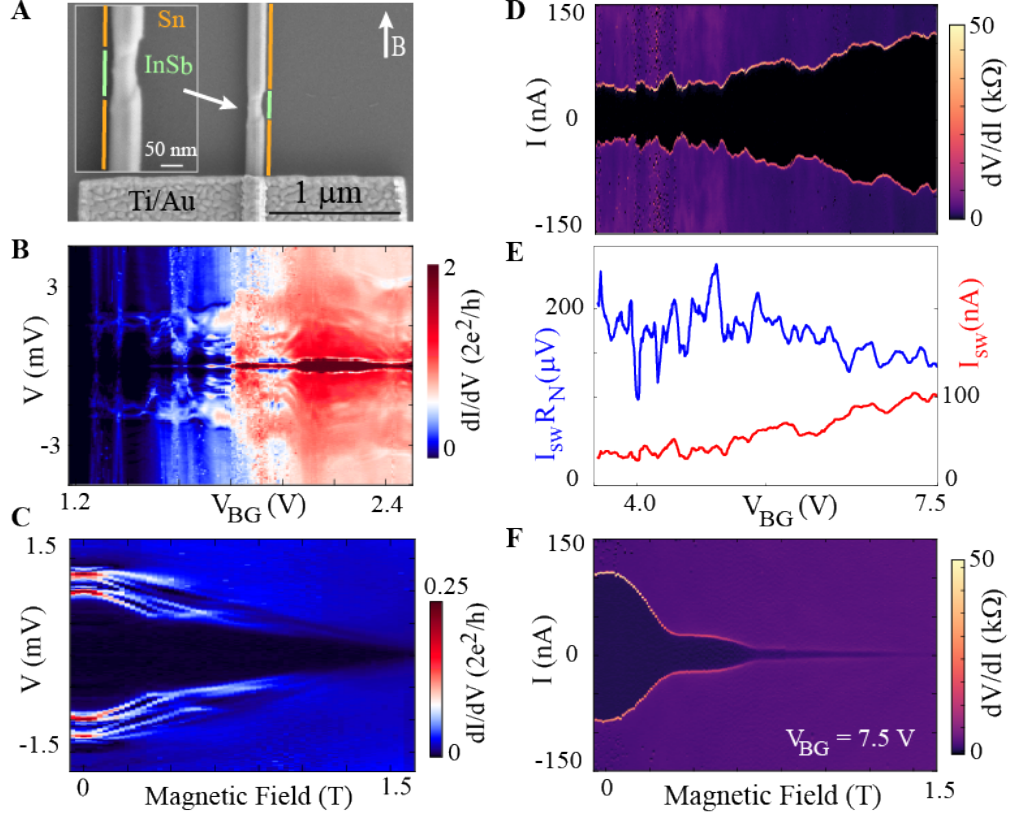
Figure 6.9: (A) SEM image of device D with a nanowire shadow defined break in the Sn shell. The electron beam resist was baked to 175°C in the process of making this device. Magnetic field is applied parallel to this device. (B) Differential conductance as a function of bias voltage and back gate voltage shows evolution from the supercurrent regime at more positive back gate to the quantum dot regime for more negative back gate. V axis is as measured and not renormalized due to series resistance. (C) Andreev bound states evolution in parallel magnetic fields at $V_{BG} = 1.4$ V. The resonances never reach zero bias due to hard gap. However, at B = $0.3 - 0.4$ T, the finite bias resonances exhibit kinks. These are the points where Andreev bound states cross zero chemical potential and undergo a ground state quantum phase transition. Resonances are shifted by $\pm\Delta(B)$ in $\pm$ bias [189]. In an N-S device a zero-bias peak would have been observed instead of finite-bias kinks. Gap remains open to 1.5 T in this device. (D) Current bias measurement in the more positive back gate regime showing the gate evolution of supercurrent. (E) Extracted $I_{sw}R_N$ (blue) and switching current (red) as a function of back gate voltage. (F) Magnetic field dependence of critical current. Josephson effect persists up to 1.5 T. This is consistent with the magnetic field decay of the induced gap (panel C). Previously, rapid decay of supercurrent in InSb nanowires was reported on the scale of 100 mT [233]. It was explained in the context of interference of supercurrent carried by multiple occupied subbands. Here, supercurrent remains significant up to 0.5 T. This can be due to shorter junctions studied, enhanced screening of magnetic field by the Meissner effect in the Sn contacts or due to a lower subband occupation.
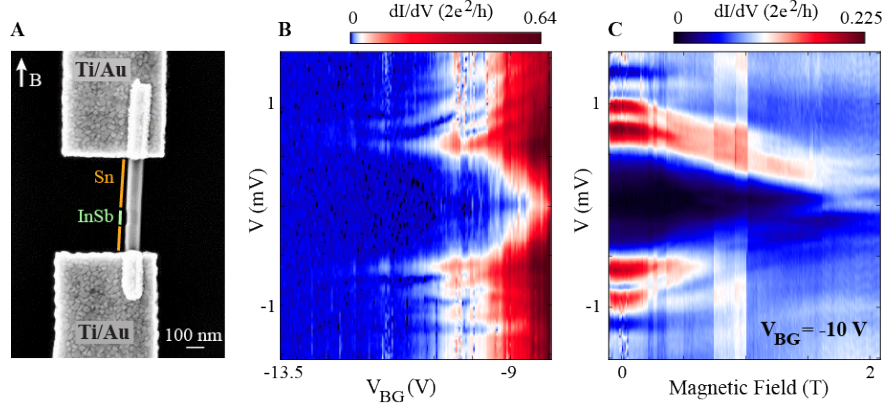
Figure 6.10: (A) SEM image of device E, a single shadow S-S device. The nanowire is aligned parallel with magnetic field. (B) Differential conductance as a function of bias and back gate voltages. V axis is as measured and not renormalized due to series resistance. (C) Magnetic field evolution of conductance at $V_{BG} = -10$ V. Near B = 1.75 T a zero bias conductance peak emerges from coalescence of two higher bias resonances. At these high magnetic fields the induced gap is soft, allowing for conductance at low bias, including the zero bias. The zero-bias peak is approximately 0.1 $2e^2/h$. We attribute this peak to a trivial zero-bias crossing by subgap Andreev states.
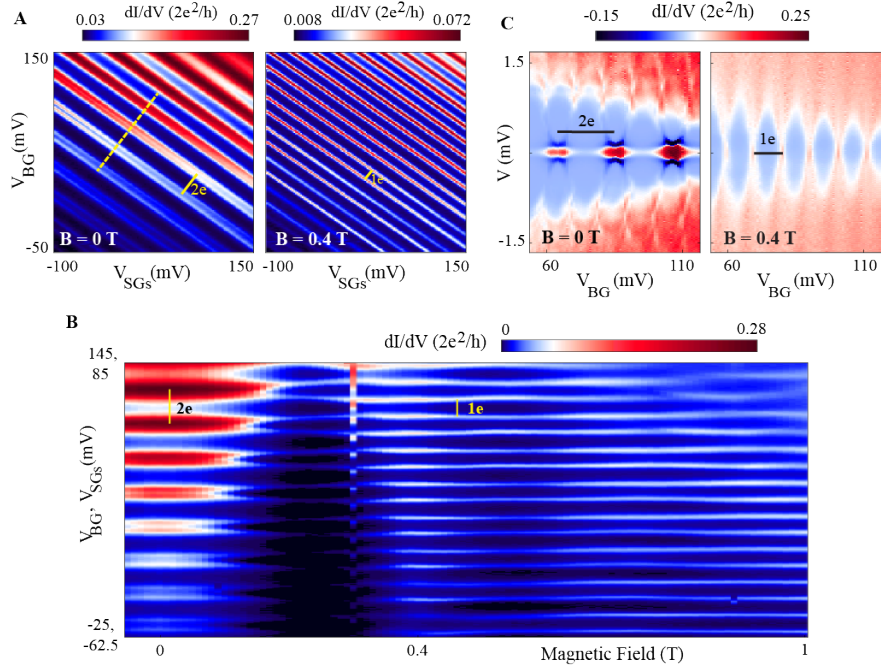
Figure 6.11: Device F is a two-shadow device of similar geometry to device C in Fig. 6.3, however with a short Sn island of order 100 nm. For this device like device D the electron beam resist was baked at 175°C in the process of making side gates and contacts. Like device C, device F has three gates: two side gates aligned with the shadow junctions and a back gate. In contrast to device C which is in the N-S-N configuration, device F is in the S-S-S configuration with the center Sn island having superconducting leads due to the Sn shell. Nanowire F is at a 30° angle with magnetic field. (A) Zero-bias conductance showing a 2e-periodic pattern of resonances at zero field and an 1e-periodic pattern at B = 0.4 T. Note that some resonances appear split. This is due to a subgap state that is lower in energy than the charging energy [218]. (B) Magnetic field evolution showing a transition from 2e-periodic to 1e-periodic pattern at finite field. (C) Differential conductance as a function of bias voltage and a combination of back gate and side gate voltages along the yellow dashed line in panel A. On the left, a zero-field scan reveals that the zero-bias conductance resonances are due to supercurrent through the S-S-S device which here manifest as zero-bias conductance peaks due to a voltage-bias measurement [234]. At finite field (right) a pattern of Coulomb diamonds is observed and no supercurrent is observed.
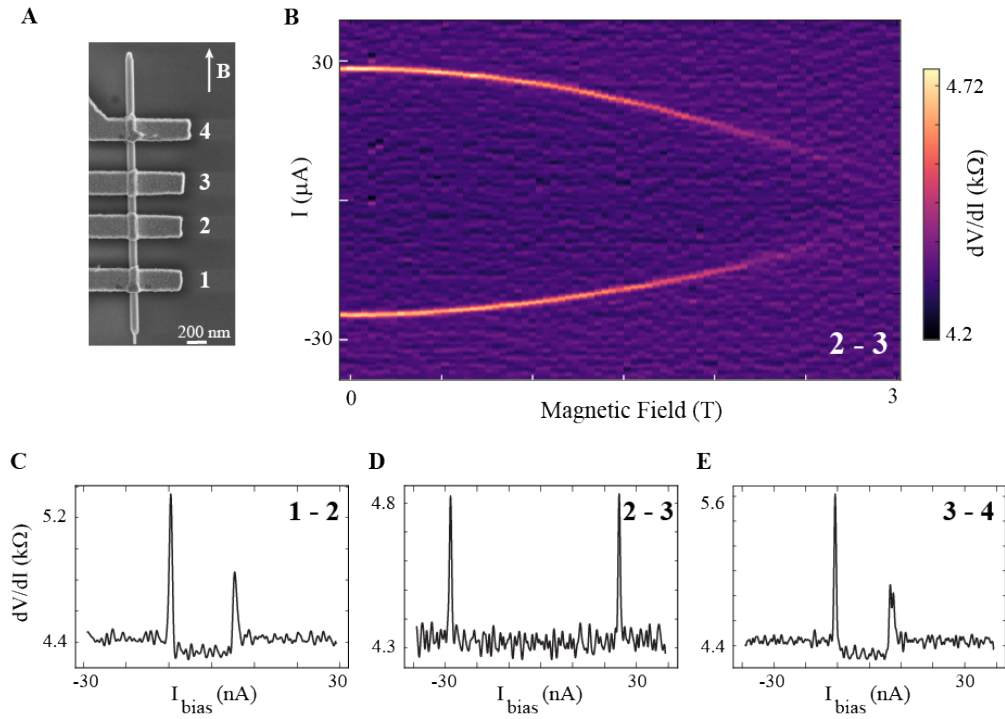
Figure 6.12: Device G has an uninterrupted Sn shell on an InSb nanowire without any shadows. The nanowire is grown on an InP stem. (A) SEM image showing 4 Ti/Au contacts labeled 1 to 4 noting different configurations for 2-terminal current bias measurements. (B) 2-terminal differential resistance as a function of bias current and magnetic field. Supercurrent persists up to 3 T, magnetic field is aligned parallel with the nanowire. (C-E) Differential resistance at zero magnetic field from different 2 terminal configurations. A variation in critical currents is observed along the shell with critical current being the highest in the central region of the nanowire. One possible explanation is the presence of grains of α-Sn which are not superconducting, with a random distribution along the nanowire.
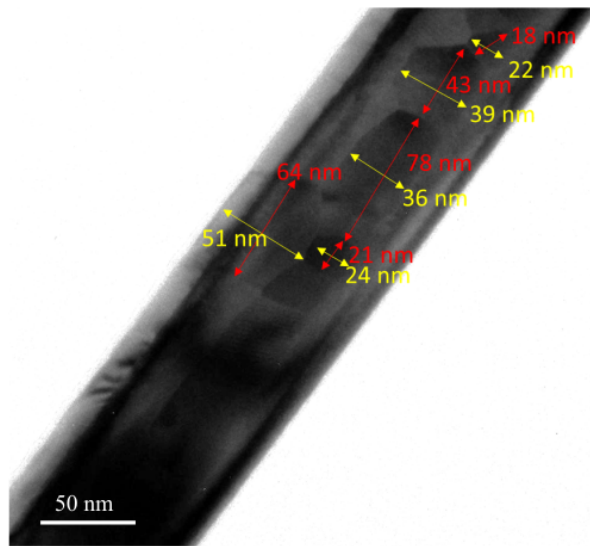
Figure 6.13: Side view bright field TEM image acquired along the $\langle 110 \rangle$ zone axis showing multiple Sn grains in the shell. Arrows and numbers are used to indicate the sizes of grains.
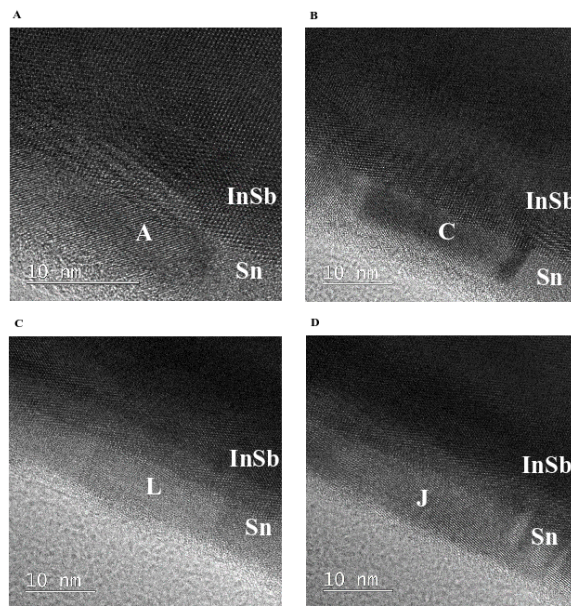
Figure 6.14: Side view TEM images of the core-shell interface, displaying four of the Sn grains listed in Table S1. (A) Grain A, which cannot unambiguously be assigned to either α-Sn or β-Sn. (B) Grain C, β-Sn grain epitaxially related to the InSb lattice. (C) Grain L, α-Sn. (D) Grain J, β-Sn.

Table 6.1: Phase identification based on lattice spacings dhkl of 13 Sn grains imaged using high resolution TEM. All dhkl values are determined from Fast Fourier Transform patterns constructed from the HRTEM images. All patterns were calibrated by InSb lattice spacings present in the same images. The 211α spacing is not allowed based on crystal symmetry, but can appear in HRTEM images. The experimental inaccuracy in the dhkl values is estimated to be 2.0 percent considering the limited number of pixels in the FFT patterns. Based on this criterion, apart from grains A and L all grains can be assigned to the β-Sn phase. Grain R is presented in Fig. 6.4

Grain	d_{hkl} (exp)	hkl β	d_{hkl} β (lit)	% deviation from lit β	hkl α	d_{hkl} α (lit)	% deviation from lit α	epitaxy
A	0.198	211	0.2010	-1.2%	311	0.1956	+1.5%	
C	0.209	220	0.2065	+1.0%	311	0.1956	+6.7%	YES
D	0.203	220	0.2065	-1.4%	311	0.1956	+4.1%	
		211	0.2010	+1.3%	-	-	-	
E	0.206	220	0.2065	-0.4%	311	0.1956	+5.1%	
F	0.205	220	0.2065	-0.5%	311	0.1956	+5.0%	
G	0.274	101	0.2772	-1.3%	211	0.264	+3.7%	
I	0.282	101	0.2772	+1.7%	211	0.264	+6.7%	
J	0.277	101	0.2772	-0.0%	211	0.264	+5.0%	
K	0.203	220	0.2065	-1.8%	311	0.1956	+3.7%	
L	0.267	101	0.2772	-3.7%	211	0.264	+1.1%	
M	0.280	101	0.2772	+1.2%	211	0.264	+6.2%	
N	0.287	200	0.2920	-0.8%	-	-	-	
R	0.204	220	0.2065	-1.2%	-	-	-	
	0.149	112	0.1472	+1.3%	-	-	-	

7.0   Superconducting-semiconducting hybrid circuits

In topological quantum computation information is stored nonlocally. This protects the information from local sources of decoherence. It also makes it very challenging to control and coherently transfer the information into and out of the system once we need it. Hybrid superconducting qubits are proposed for initialization, read-out and gate operation of topologically protected qubits through their mutual coupling [122, 55, 210]. All these schemes naturally require the superconducting qubit to perform in high magnetic fields. Thus the well-developed Al based technology is no more suitable. In the first section of this chapter we are going to present our progress towards building a fluxonium qubit that performs in finite magnetic fields. The resonators of this qubit are made of thin films of disordered superconductors with high kinetic inductance and sustain their quality factors in relatively high magnetic fields. The second section of the chapter includes our very first attempt to realize a hybrid transmon qubit where a nanowire Josephson junction is shunted by a large capacitor and is coupled to a compact resonator which in turn is capacitively coupled to a transmission feedline. The resonators in this first generation of hybrid circuit are made from Al and are not suitable for magnetic field applications.

7.1   Superconducting microwave circuits with high kinetic inductance materials in high magnetic fields

In a recent proposal, a braidonium was proposed for robust quantum information storage and manipulation, where braiding and readout are mediated by the 4π Josephson effect [210]. Braidonium's initialization and readout element is a hybrid fluxonium-Majorana qubit [55]. This fluxonium needs to perform in finite magnetic fields to allow entering the topological regime. We start with fabricating and characterizing superconducting resonators made of field resilient Nb family superconductors. Our circuits, however, have shown limited performance quality, due to fabrication drawbacks that will be explained in the coming sections.

We lay out the proposed superconducting circuit design and measurements of circuit components separately.

7.1.1 Fluxonium qubit

Fig. 7.1(a) is showing an example of a proposed fluxonium device. The qubit is inductively coupled to a cavity resonator that in turn capacitively couples to a transmission feedline. The fluxonium itself is made of a Josephson junction that is shunted by a large inductance. Moreover, a gate can be added to control the supercurrent density in a semiconducting nanowire weak link. Fig. 7.1(b) and (c) are the plots of fluxonium eigenfunctions and their corresponding transition frequencies from the fluxonium Hamiltonian:

$$H = -4E_C \frac{\partial^2}{\partial \varphi^2} + \frac{E_L}{2} \varphi^2 + E_J \cos{(\varphi - 2\pi \frac{\Phi_{ext}}{\Phi_0})}, \tag{65}$$

in which we estimate the energy scales as the following:

- Charging energy predominantly comes from stray capacitance in the circuit:
  $E_C/h \approx 2$ GHz

- Junction's critical current defines Josephson energy which can be controlled by gate in semiconducting weak links or by designed junction's area in AlO_x tunnel junctions:
  $E_J/h \approx 12$ GHz

- To enter the fluxonium regime the inductive energy has to be much smaller than charging and Josephson energies. We expect this energy to be $E_L/h \approx 0.7$ GHz.

The expected inductive energy results in a large inductance (~ 300 nH). This superinductance is provided by high kinetic inductance of thin films of disordered NbTiN superconductor that is patterned into a meander nanowire resonator [71, 128, 127].

7.1.2 Superinductance meander resonator

The superinductor element of the fluxonium is a meander nanowire resonator that can be treated as a lumped element[1]. The total inductance is dominated by the kinetic inductance

---

[1]For a lumped element the size of the circuit component is much smaller than its wavelength.
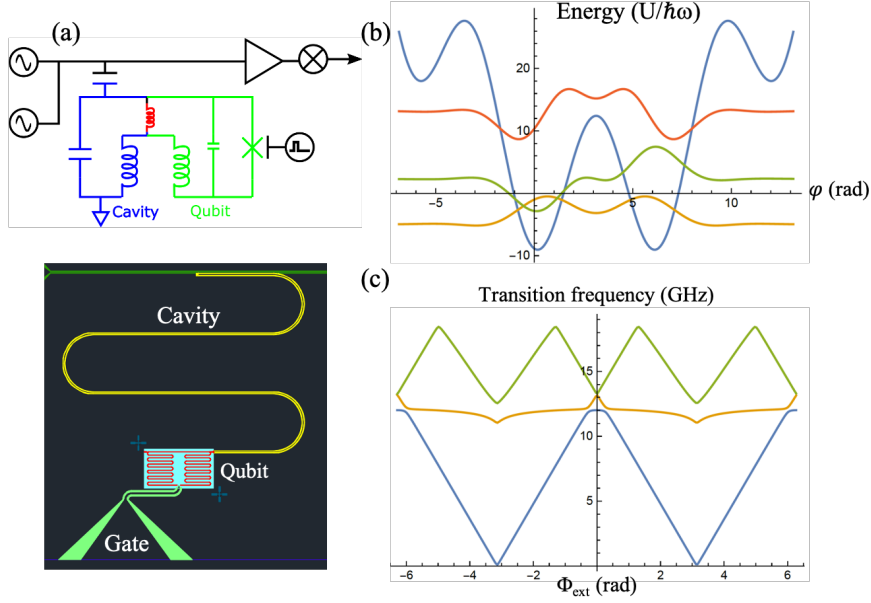
Figure 7.1: (a) Top: circuit schematics of a fluxonium qubit inductively coupled to a cavity resonator that is capacitively coupled to a transmission feedline. Bottom: design of the proposed fluxonium circuit. The red meander is the shunting inductance. (b) The effective potential energy with two well-separated potential minima and first three eigenfunctions at $\Phi_{ext} = \Phi_0/2$. (c) Spectrum of transition frequencies $g \to e$ (blue), $g \to f$ (orange), $g \to h$ (green).

and can be $100 - 1000$ nH. The kinetic inductance is estimated by length, l, width, w, and thickness of the nanowire, t, as well as the energy gap of the superconducting film [235]:

$$L_K = \frac{l}{w} \frac{R_{sq}h}{2\pi^2\Delta} \frac{1}{\tanh\left(\frac{\Delta}{2k_BT}\right)} \tag{66}$$

where R_{sq} is the sheet resistance in normal state (~ 200 $\Omega/\square$ for 10 nm thick NbTiN), h is the Plank constant, $\Delta = 1.764k_BT_c$, k_B is the Boltzmann constant, and T_c is the superconducting critical temperature (~ 12 K for NbTiN). The last part of the equation is approximately equal to one. For the resonator shown in Fig. 7.2(a) where $l \approx 5500$ μm and $w \approx 150$ nm we estimate $L_K \approx 800$ nH.

The resonators are fabricated on a sapphire substrate where a 10 nm film of NbTiN is patterned by e-beam lithography and etched away by mechanical ion milling. We couple the resonators directly to a transmission feedline that is fabricated simultaneously with the

meanders. We study their frequency response using a vector network analyzer (VNA) to obtain the resonators spectrum. Fig. 7.2(a) shows four meander resonators with different resonant frequencies coupled to a coplanar waveguide (CPW) transmission feedline. They all have qualitatively the same behavior and Fig. 7.2(b) shows the hanger measurement from a resonator with resonant frequency $f_r = 2.152$ GHz. Fitting the hanger transmission spectrum using Eq. 51 results in $Q \approx 4000$. Since these resonators are the inductive element in the qubit design their low quality factor will be restricting qubit relaxation time. The quality factor of meander resonator and qubit relaxation time are inversely related: $T_1 \sim \frac{Q}{f_r}$. Thus T_1 is limited to 2 μs.
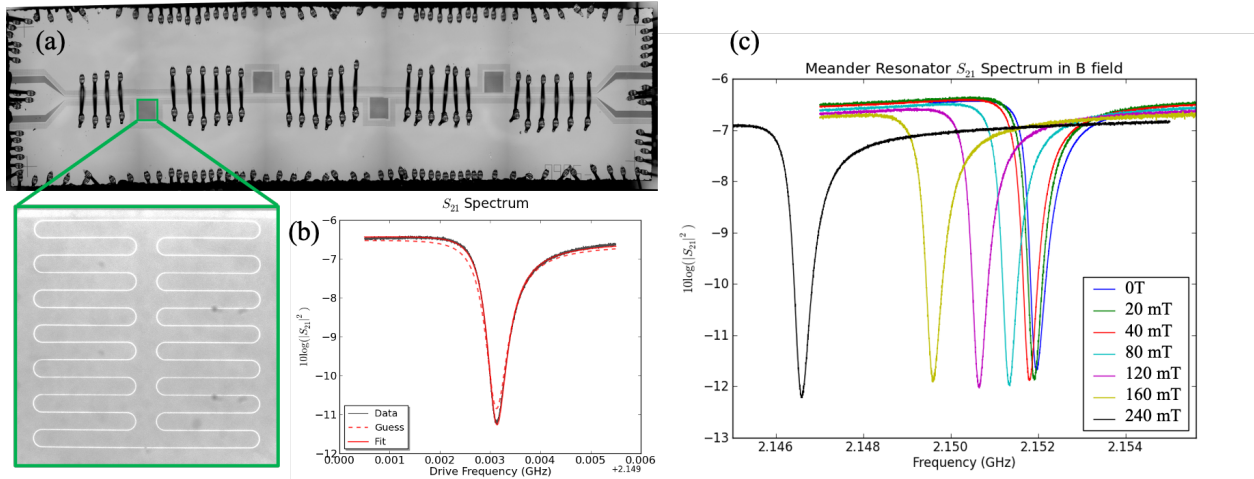
Figure 7.2: (a) Four meander resonators as enlarged in the green box are capacitively coupled to a transmission feedline. The light gray is NbTiN and the darker regions are sapphire substrate. The two ground planes on both sides of the transmission feedline are stitched bond together to avoid extra resonances on the chip. (b) Hanger measurement of a resonator where $Q_i = 5800$, $Q_c = 8100$, and $Q_l = 3400$. (c) Magnetic field resilience of these meander nanowire resonators. The downward shift in resonant frequency is evident.

We then study the performance of these resonators in finite magnetic field as shown in Fig. 7.2(c), where they sustain their quality factors of few thousands. There is a downward shift in the resonant frequency that was previously explained as the result of increased kinetic inductance due to breaking of Cooper pairs in external field [71].

This superinductor meander resonator will be inductively coupled to a quarter wavelength ($\lambda/4$) CPW resonator by sharing their center pin conductor as shown in Fig. 7.3(a).

7.1.3 Quarter wavelength coplanar waveguide resonator

The $\lambda/4$ CPW resonators are the cavities between qubit and transmission feedline. Knowledge of their quality factors is essential for example for transferring the information from the qubit to the transmission line as well as the duration of qubit pulses. We use the same fabrication and measurement technique to characterize these resonators. Resonators with different resonance frequencies are coupled to a single transmission feedline (Fig. 7.3(b)) where the complex-valued feedline transmission is used to obtain their quality factors (Fig. 7.3(c - f)). We use two superconducting films from Nb family, NbTiN and NbN. Each are studied for 10 and 50 nm thick films.
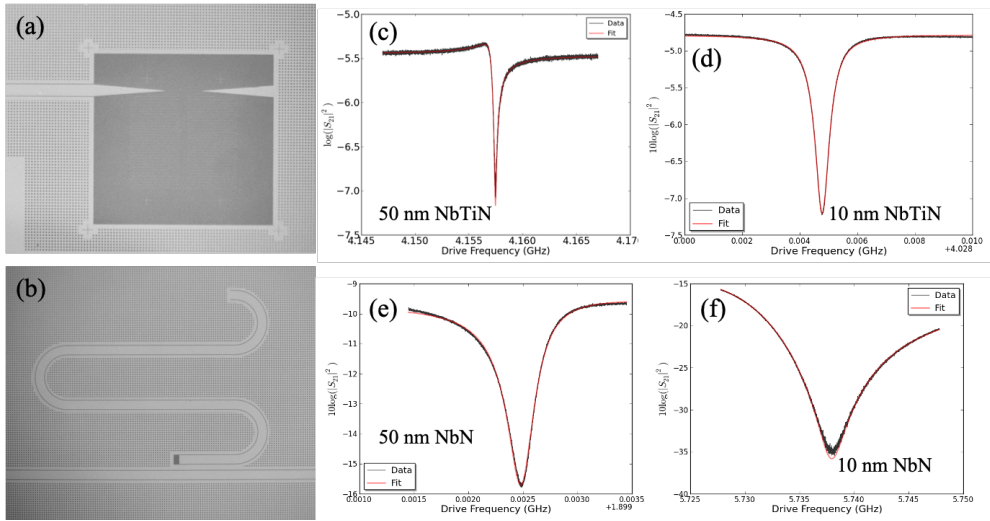
Figure 7.3: (a) Center pin of CPW resonator is tapered at its end to allow inductive coupling to meander resonator. The open end of a $\lambda/4$ resonator is a current node and that is where the inductive coupling is at its maximum. (b) A CPW resonator coupled to a transmission feedline. The small dark squares are holes in the ground plane to trap magnetic vortices on the surface [72]. The ground plane between transmission feedline and resonator's gap as well as the length of the resonator in parallel with the transmission feedline are used in simulations to determine the coupling factor, however the hanger measurements reveal a wide range of values for Q_c for different film thicknesses. (c) 50 nm thick NbTiN: $Q_i \approx 30000$, $Q_c \approx 6000$, $\alpha \approx 2$ (d) 10 nm thick NbTiN: $Q_i \approx 8000$, $Q_c \approx 24000$, $\alpha \approx 4$ (e) 50 nm thick NbN: $Q_i \approx 9000$, $Q_c \approx 9000$, $\alpha \approx 30$ (f) 10 nm thick NbN: $Q_i \approx 3000$, $Q_c \approx 500$, $\alpha \approx 80$.

Our measurements show generally higher quality factors for thicker films. Moreover, NbTiN results in higher quality resonators compare to NbN. To estimate the kinetic inductance boost in these resonators we compare the measured resonant frequency with what

is expected without kinetic inductance, $\alpha = (\frac{f_{exp}}{f_{meas}})^2 - 1$. We estimate higher boosts for thinner films and for NbN compare to NbTiN. The higher kinetic inductance in NbN results in considerably shorter resonators. One drawback of fabricating both CPW and meander resonators form NbN is an immeasurable meander resonance due to extremely high kinetic inductance boost. We made a couple of attempts on fabricating meander resonators with different lengths and failed to correspond each of them separately with a measured resonant frequency.

Moreover, the width of the transmission feedline center pin needs to be adjusted based on the thickness and kinetic inductance boost of superconducting films to match its impedance as close as possible to 50 Ω[2].

These resonators as well sustain their quality factors in finite magnetic fields. Here we show rather a peculiar behavior of two 50 nm thick NbN CPW resonators which indicates the importance of resonant frequencies in the quality factor of resonators. As evident in Fig. 7.4 the quality factors drop in magnetic field before they start to increase and go beyond zero field value. The drop in Q can be due to coupling to magnetic impurities. These impurities get pinned at higher fields where they cannot contribute to losses anymore and Q starts to retrieve its zero field value [71]. However, coupling to magnetic impurities cannot explain the increase in Q beyond $Q(B = 0)$. We point out the resonant frequencies of these two resonators shown here. At relatively small frequencies $f_r \lesssim 2$ GHz, resonators can get coupled to free electron spins at zero field resulting in reduced quality factors. At higher fields spins deviate away and decouple from the resonator prompting increased quality factors. We expect Qs to stop increasing and saturate at some finite field as shown by blue data points.

7.1.3.1 Two-level system dissipation

Our measurements of quality factors reveal values that are one order of magnitude smaller than what are reported in the literature [70, 71, 72]. These lower than expected quality factors could be due to different etching process, mechanical ion milling versus commonly used reactive ion etching method, the quality of superconducting film, the filtering in the mea-

---

[2]We design the center pin width to be $\approx$ 13.5 (32) μm for 50 (10) nm thick film. The gap for both film thicknesses is $\approx$ 2 μm.
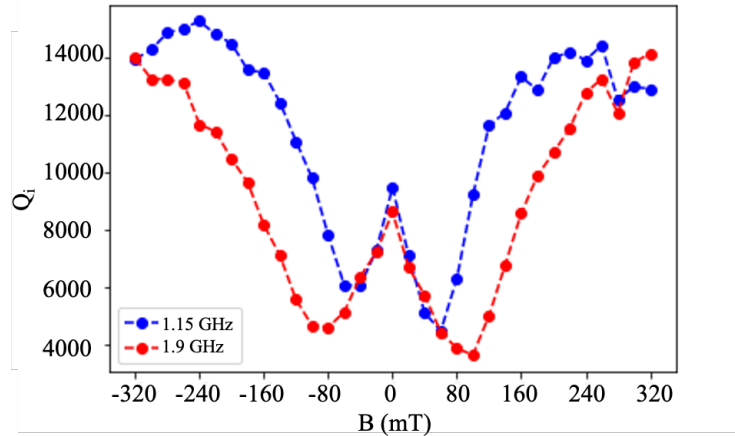
Figure 7.4: Data shown for two 50 nm NbN CPW resonators in finite magnetic fields. Q_i drops before it increases and closely reaches a saturated value. The chip sits on top of the magnet and the maximum field value cannot be reached to fully observe the saturation of Q_i.

surement setup, etc. The mechanical ion milling in particular can result in high distribution of two-level systems (TLS) that limit resonator performance. The main source of TLS are defects on the substrate and dielectric material. For example sapphire has lower density of TLS compare to SiO_2 and resonators made on sapphire substrate generally have higher quality factors. TLS are localized low-energy excitations i.e. defects that can trap charges to tunnel between spatial quantum states. At low temperatures they are polarized into ground state and ready to absorb photons from resonators which causes dissipation of energy and lowers the quality factor. However, at high power or high temperatures TLS depolarize and quality factors increase [70, 236]. We generally observe increased quality factors for all resonators we fabricated as we increase excitation power. Moreover, we study temperature dependence of NbN CPW resonators and observe Q_i increases as temperature increases until it reaches a maximum value at critical temperature of Al wire bonds where it abruptly drops. This behavior further confirms TLS are dominant loss mechanism in our resonators giving us insight on how to improve the quality factors of our resonators. Immediate actions we can take is to carefully and rigorously clean the substrate before superconducting film deposition and develop a gentle etching recipe to substitute the mechanical ion milling.

127
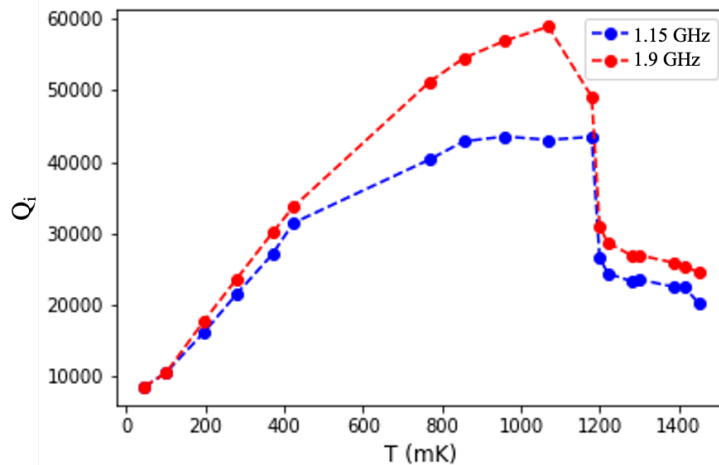
Figure 7.5: Quality factor of 50 nm NbN CPW resonators increase as temperature is rising indicating TLS are the dominant factor limiting resonator performance. The sharp drop close to 1.2 K is due to Al wire bonds transitioning to normal conductor.

7.1.4 Outlook

We fabricated a superconducting circuit including cavity and superinductor resonators with high kinetic inductance materials. These resonators maintain their quality factors in finite magnetic fields, which facilitates operation of a fluxonium qubit in external magnetic fields essential for Majorana experiments. We confirmed the lower than expected quality factors in our resonators is due to our rough etching process that introduces a high distribution of two-level systems leading to energy loss. The quality factors reported here will result in relatively short yet expected to be measurable qubit relaxation times. Next we plan to incorporate a semiconducting nanowire (Sn-InSb or Al-InSb) as the Josephson weak link to complete the fluxonium circuit. However, this imposes some fabrication kinks that need to be worked out. For example scanning electron imaging of a nanowire on an insulating sapphire substrate is close to impossible due to charging of electron beams unless we are able to take advantage of large areas of superconducting ground plane on the chip.

7.1.5   Supplementary material

To start designing resonators for desired frequencies we took trial and error approach since kinetic inductance boost was initially an unknown parameter to us. To characterize CPW resonators, we coupled 7 resonators to a single transmission feedline. They are arranged in two groups, one group has three resonators with nominal (without kinetic inductance boost) resonant frequencies around 6 GHz and the other has four resonators with nominal resonances close to 9 GHz. We also use different couplings for each resonator in each group to be able to associate the measured resonances with designed parameters. Table below is an example of such trial. The coupling distance ($d_{coupling}$) is the width of the ground plane between the gaps of the CPW resonator and transmission feedline. (-2 μm means the transmission feedline and the resonator are sharing their gap.)

Table 7.1: Design parameters and measured resonances for a set of 50 nm thick NbTiN $\lambda/4$ CPW resonators. As mentioned in the main text $\alpha = (\frac{f_{expected}}{f_{measured}})^2 - 1 \approx 2$

Label	length (μm)	f_r w/o KI (GHz)	$d_{coupling}$ (μm)	$f_measured$ (GHz)	Q_i	Q_c
6 GHz	5023	6.42	-2	not detected		
	4770	6.76	0	3.696	21800	1800
	4540	7.10	2	4.157	23700	5700
9 GHz	3352	9.62	-2	5.504	15000	400
	3235	9.97	0	5.781	13100	500
	3130	10.32	2	5.981	14800	2200
	3025	10.66	4	6.234	17800	5100

It is worth noting that the set of resonators in table 7.1 are fabricated with photo lithography technique with relatively similar quality factors with those resonators fabricated by e-beam lithography. However, the precision of photo lithography could become limiting for fabrication of meander resonators whose width are $100 - 300$ nm.

We also compare the quality factors in resonators where the superconducting film is deposited after lithography and lifted off instead of being etched away. We fabricate and measure two sets of resonators with similar design parameters as mentioned in table 7.1. These resonators result in quality factors of $\approx 2000 - 3000$ which is one order of magnitude

smaller than etched resonators. This reduced quality factor is expected due to immensely high distribution of TLS and polymer resist residue on the substrate.

7.2   Sn-InSb hybrid superconducting qubit

Superconducting qubits are projected to provide a scalable approach for building a quantum information processor [117] and they did not disappoint when quantum supremacy was achieved using a quantum processor with 53 transmon qubits coupled together [69]. These superconducting qubits are relying on $Al/AlO_x/Al$ tunnel junctions as the source of dissipationless nonlinearity that provides non degenerate energy level spacings allowing for individually addressable qubit states. Josephson coupling energy in these tunnel junctions is fixed by design and fabrication, only allowing tuning transition frequencies and coupling by flux biasing in a SQUID loop geometry. Flux-tuning is provided by superconducting loops operating in mA scale potentially causing on-chip dissipation. Moreover, in this scheme, Circuit QED is limited by aluminum's bulk critical field of ~ 10 mT. Using a semiconducting Josephson element (in particular semiconducting nanowires that enable bottom-up technology in hybrid superconducting-semiconducting devices) can provide a solution to such constraints. On the one hand, field-effect tunability of semiconducting weak-link's carrier density allows for voltage control of Josephson coupling and frequency and potentially reducing dissipation. On the other hand, using magnetic field compatible superconductors opens avenues to studying mesoscopic superconductivity and Andreev bound states in nanowire junctions [91, 92, 93], as well as readout and control of Majorana bound states [122, 237]. To date, multiple experiments realized voltage and flux tunable InAs nanowire transmon qubits [73, 74], implemented two-qubit gate operations in these hybrid transmons [109], and investigated qubit magnetic field evolution up to 70 mT where the induced superconductivity from 30-nm thick epitaxial Al shell in InAs is smeared [75]. Here we report on our first attempt to realize a hybrid transmon-like qubit using Sn-InSb nanowires that we characterized in Chapter 6. The superconductivity persists for fields above 2 T in these nanowires and gate-tunable supercurrent up to 200 nA was demonstrated which corresponds to E_J/h

up to 50 GHz allowing operation in transmon regime where $E_J \gg E_C$.

7.2.1 Nonlinear nanowire circuit

To fabricate the devices we evaporate 150 nm Al film on an undoped Si substrate. We then pattern and etch compact resonators that are capacitively coupled to a CPW transmission feedline as well as to the large interdigitated transmon capacitor as shown in Fig. 7.6(a). For etching we use a combination of chemical wet etching (MICROPOSIT 351 developer:water, 1:4 for 2 minutes[3]) followed by reactive ion etching (BCl_3/Cl_2, 40/50 sccm for 15 seconds). Next, using a micromanipulator, we place Sn-InSb nanowires between the leads of the interdigitated capacitor and contact the nanowire in a subsequent lithography step[4] (Fig. 7.6(b) and (c)).

7.2.1.1 Dispersive readout

We now verify the presence of the nonlinear nanowire Josephson element in the circuit by measuring the high power response of transmission through the feedline near the fundamental frequency of the compact cavity resonator [238]. This measurement scheme uses the dispersive readout that relies on the coupling of cavity and qubit. The Hamiltonian of a qubit-cavity system in the dispersive regime can be written as

$$H = \hbar\omega_C(a^\dagger a + \frac{1}{2}) + \hbar\omega_Q(b^\dagger b + \frac{1}{2}) + \hbar\alpha(b^\dagger b)^2 + \hbar\chi(a^\dagger a b^\dagger b) \tag{67}$$

where $a^\dagger$ (a) and $b^\dagger$ (b) are raising (lowering) operators for cavity and qubit, respectively, α is the anharmonicity of the qubit, and χ is the dispersive coupling. The energy eigenstates of this Hamiltonian is then

$$E/\hbar = \omega_C N_C + \omega_Q N_Q + \alpha N_Q^2 + \chi N_C N_Q \tag{68}$$

in which N_C and N_Q correspond to the number of photons in the linear cavity and anharmonic qubit, respectively. Eq. 68 can be rearranged to show that the cavity frequency when the

---

[3]This alkaline developer is used to develop the photolithography resist after patterning which simultaneously etches aluminum.

[4]The step by step procedure is found in Chapter 3

131
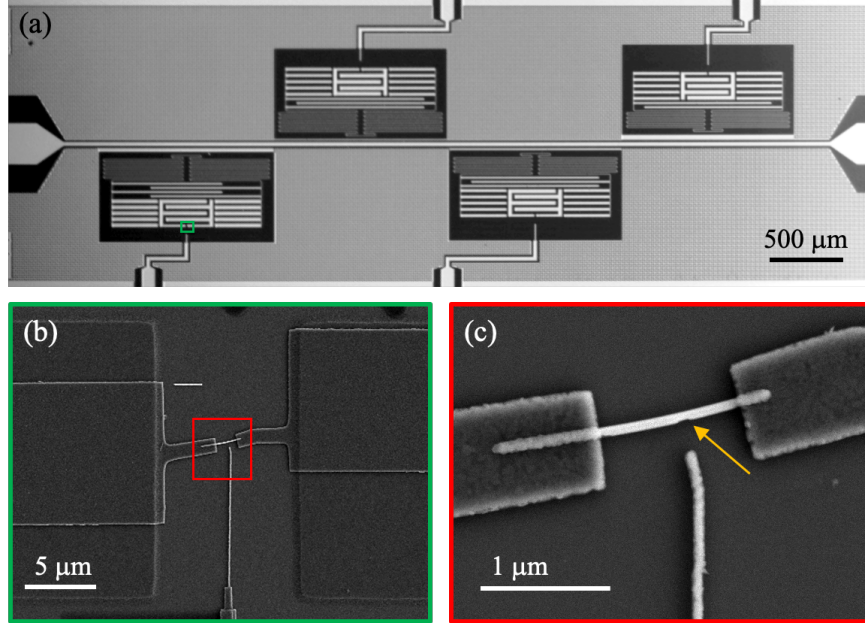
Figure 7.6: (a) Optical overview of four cavity compact resonators coupled to a common CPW transmission feedline. The interdigitated blocks of metal in the middle of the resonator provides large capacitance for the qubit resulting in a much smaller E_C than the estimated E_J from nanowire junction. The chip also contains gate lines for electrostatic tuning of the junction, which we have not used in this experiment. (b) SEM image showing the nanowire placed between leads of the interdigitated capacitor. And contacted by evaporating 150 nm Al. (c) The nanowire Josephson junction is pointed to by the orange arrow. The junction is prepared by in-situ shadowing using nearby nanowires during Sn evaporation [65].

qubit is in the excited state is shifted from when the qubit is in the ground state: $\omega_C \rightarrow \omega_C + \chi N_Q$. If we increase the driving power of the microwave tone sweeping close to the cavity frequency, the qubit photon number alters due to the cavity-qubit coupling and the cavity frequency shifts as shown in Fig. 7.7(a).

Next we search for "qubit"[5] transition frequency f_{ge} by monitoring feedline transmission at cavity frequency while sweeping a second continuous wave (two-tone CW spectroscopy). We fix the cavity drive tone at a frequency shown by the black arrow in Fig. 7.7(a). This point is chosen such that the frequency change is minimum throughout the sweeping range of the second tone, yet the dispersive shift is measurable[6]. We sweep the second tone in

---

[5] Actually all we can claim at this point is some sort of anharmonic Josephson element.

[6] We can adjust this frequency accordingly while sweeping long intervals of the second tone.
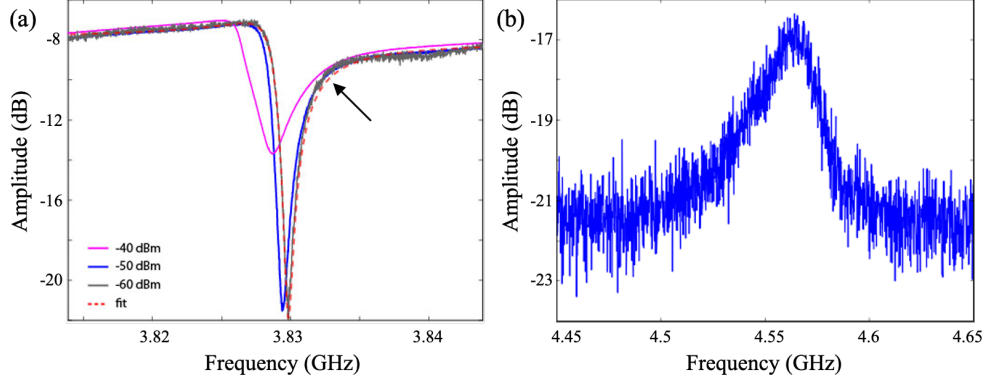
Figure 7.7: (a) High power response of transmission at the cavity frequency. The resonant frequency shifts to lower values as the power of microwave tone is increasing. The red dashed line is the fit to complex-valued feedline transmission $Q_i = 7000$ and $Q_c = 2000$. (b) Dispersive shift in the amplitude of cavity frequency response at qubit transition frequency $f_{ge} = 4.56$ GHz. $P_{drive}^{cavity} = -65$ dBm. $P_{drive}^{qubit} = -35$ dBm.

small steps of order 0.1 MHz until we observe the amplitude and phase of the cavity tone changes as shown in Fig. 7.7(b). This is the measurement of dispersive shift in the cavity that confirms presence of a nonlinear nanowire Josephson element in the superconducting circuit. It is also colloquially called the presence of "forth order term" referring to the last term in the Hamiltonian of Eq. 67.

In the two-tone CW spectroscopy the qubit drive (the second tone) is trying to rotate the qubit but cavity is trying to measure it at the same time which means cavity is dephasing the qubit, if the cavity power is high. We tried narrowing the peak in Fig. 7.7(b) by decreasing the cavity power first but we soon got limited by the signal to noise ratio (SNR) and hit the intrinsic coherence time of the qubit. Next step to make this peak narrower is to find the optimal qubit drive power. If this power is too high the peak broadens because the qubit can still rotate even if it is off resonance. We again lower the qubit drive power until we hit the SNR limit. After finding the optimal values for our setup as noted in Fig. 7.7, the width is ~ 50 MHz wide which translates into a very short qubit lifetime in the order of tens of nanoseconds ($BW = 1/T$). This short qubit relaxation time can also limit the lifetime of the cavity and explain low cavity quality factor for this compact aluminum resonator. These

resonators are expected to have high qualities in order of few hundred thousands [115]. We suspect presence of normal conductance in the nanowire channel or unwanted doping on the substrate to cause this short relaxation time. In the next set of devices we will be adding the electrostatic control knob to control the conductance through the channel and increase the supercurrent in the nanowire junction which in turn increases the Josephson coupling energy. In the supplementary section we explain how we estimated qubit parameters (f_{ge}, α and χ) based on expected Josephson inductance.

7.2.2 Outlook

We fabricated and measured a nonlinear hybrid nanowire superconducting quantum circuit. The nonlinearity is evident in high power response of the cavity resonator as well as dispersive shift in cavity resonance due to qubit photon number change. The signal bandwidth of the ground to first excited state transition frequency (f_{ge}) is ~ 50 MHz wide which translates into a very short relaxation lifetime of order of tens of nanoseconds. A common way to indirectly measure anharmonicity of the system is shown in Fig. 7.8 where increasing the power of the qubit drive tone facilitates $f_{gf}/2$ transition from which we can deduce α as explained in the caption. We were not able to detect this signal in this experiment which may have been due to the very short lifetime that causes the system to continuously lose energy and always stay in a cold state making it challenging to observe a two-photon transition to second excited state. We comment that these results are from one nanowire-resonator device and more experiments specially with added gate tunability are needed to investigate the coherence time, indicating qubit-cavity parameters and performing qubit pulses.

7.2.3 Black box quantization calculation

In this section we explain the procedure we used to estimate cavity and qubit frequencies, cavity-qubit dispersive coupling strength χ, and qubit's anharmonicity α. We use a software called Ansys HFSS (High Frequency Structure Simulator) that is a commercial finite element method solver for electromagnetic structures. Fig. 7.9(a) is showing the top view schematics of our design in the software. The red rectangle is the center pin of the CPW transmission
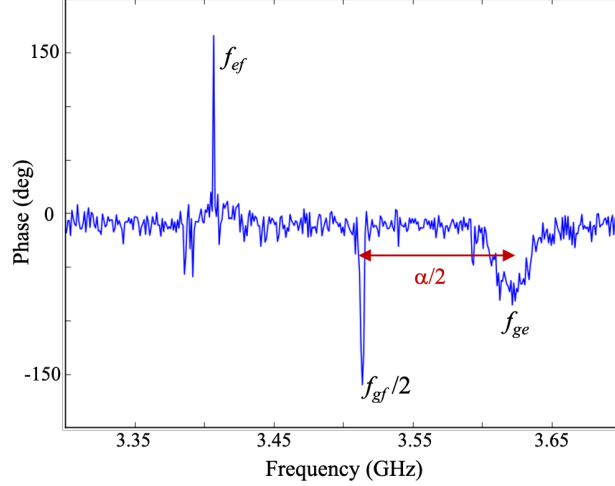
Figure 7.8: If the qubit drive power is large enough we can trigger a two photon process and transit to the second excited state, $f_{gf} = f_{ge} + f_{ef}$. However, with two-tone spectroscopy we are only able to observe one photon processes. Hence if we see a dispersion it must be from $f_{gf}/2 = f_{ge} - \alpha/2$. At finite temperature one may also be able to observe f_{ef} transition which actually requires a three-tone spectroscopy. Data courtesy of Xi Cao.

feedline. That is separated from the yellow ground plane. The light green is the substrate indicating the parts of the design that we etch in the fabrication process. The orange structure is the compact cavity resonator. The meandering lines provide its inductance while the long fingers are its capacitive part. The wide orange rectangles add to the capacitance of the resonator while they provide the coupling to the qubit. The brown interdigitated rectangles are the qubit's capacitor. Widths of orange and brown rectangles as well as the spacing between them control cavity-qubit coupling. The black square represents the Josephson junction that can be modeled as a lumped RLC element in HFSS and specify its inductance based on our estimation from junction's critical current. Initially we simulated the parameters based on $L = 3$ nH ($I_C \approx 100$ nA) which resulted in a qubit frequency ~ 6.5 GHz. However, as shown in the dispersive measurement of Fig. 7.7 the qubit frequency is ~ 4.55 GHz. We then changed the value of inductance in the simulation to get a frequency closer to the measured value: $L = 12$ nH $\rightarrow I_C = 27.5$ nA.

To get the resonant frequency of the cavity we enclose this structure with a vacuum box whose height is roughly three times larger than the substrate. We then define two wave ports
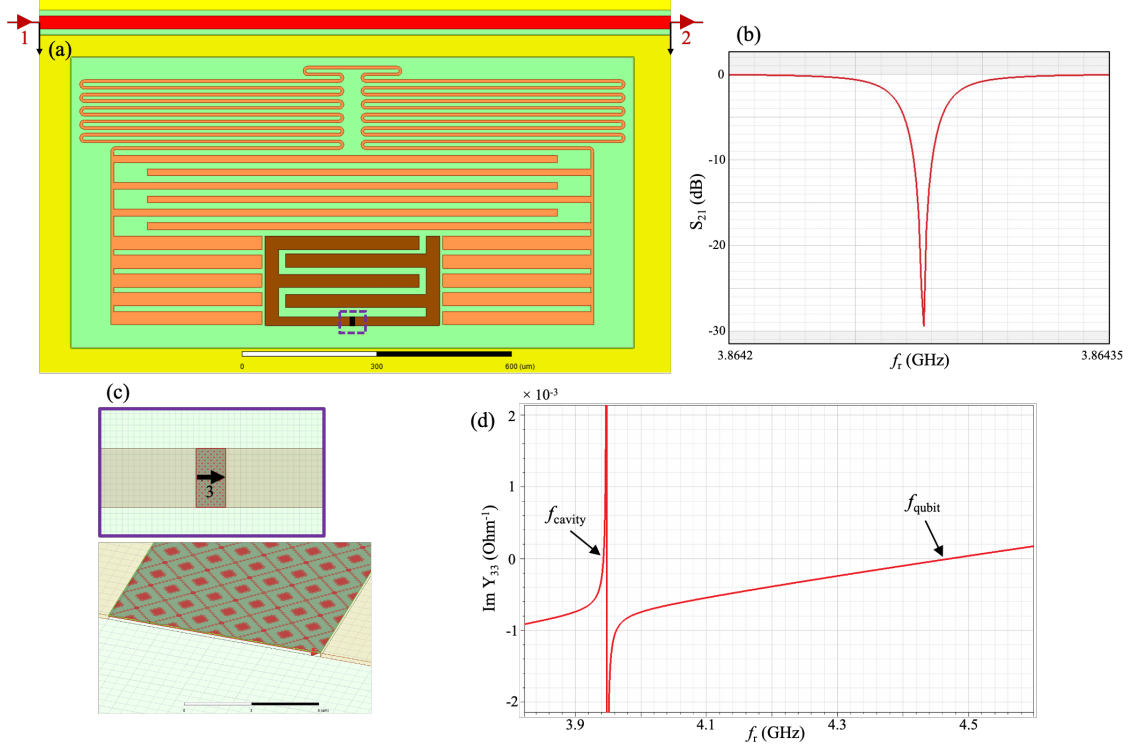
Figure 7.9: (a) Top view of the circuit design. HFSS is a 3D simulator in which we can define the thickness of the objects like 300 μm thick Si substrate. The 150 nm thick Al structures can be essentially simulated as 2D objects. To get the estimated cavity frequency we define two wave ports labeled 1 and 2 normalized to 50 Ω and sweep the frequency. The black arrows indicate the direction of the electric field from feedline's center pin to the ground plane. (b) Simulated feedline transmission response close to the cavity resonance. (c) To calculate the admittance we add a lumped port with infinite resistance connecting the capacitance block leads. The black arrow again indicates the electric field direction. (d) Imaginary part of the admittance that is used to estimate qubit frequency as well as anharmonicity and dispersive shift.

labeled as 1 and 2 in Fig. 7.9(a) to simulate the transition S_{21} through the feedline. The simulated resonance is shown in Fig. 7.9(b) which tells us where we should approximately expect the cavity resonator. This is a simulated measurement hence the internal quality factor is essentially infinity but fitting the hanger measurement the coupling quality factor is estimated in the order of hundred thousands which translates into a cavity lifetime of 50 μs. However, the measurement in Fig. 7.7(a) indicates a lower quality resonator and lifetime of 0.4 μs.

We can estimate the spectrum of the quantum circuit (α and χ) by simulating the admit-

tance at the port of the Josephson junction. This method is called Black-Box Quantization and is fully explained in Ref. [239]. If the size of the Josephson junction is negligibly smaller than the wavelength of the cavity mode, we can approximate the admittance of the linear part of the junction by putting a lumped LC port in parallel with the rest of the linear resonator. To do so we change the 2D brown blocks in part (a) of Fig. 7.9 to a 3D object and add a lumped port with infinite resistance on top the junction as shown in Fig. 7.9(c). We also terminate the red transmission feedline by 50 Ω ports. The resonant frequencies can be determined by the poles of impedance Z or roots of the admittance Y:

$$Y(\omega) \equiv Z^{-1}(\omega) = \sum_{p=1}^{M} \left(-i\omega C_p + \frac{i}{\omega L_p} + \frac{1}{R_p} \right) \tag{69}$$

where M is the number of modes, for us we have one qubit mode and one cavity mode.

The perturbed cavity-qubit Hamiltonian can be written in two linear and nonlinear parts and we quote from Ref. [239]:

$$H = H_0 + \frac{1}{2} \sum_{pp'} \chi_{pp'} \hat{n}_p \hat{n}_{p'}, \tag{70}$$

where $\hat{n}_p = a_p^\dagger a_p$. The nonlinear part is essentially similar to the last two terms of the Hamiltonian in Eq. 67. $\alpha_p \equiv \chi_{pp}$ is the anharmonicity of the first excited state of mode p and $\chi_{pp'} = \chi_{p'p}$ with $p \neq p'$ is the frequency shift of mode p due to the presence of single excitation in mode p':

$$\chi_{pp} = -\frac{L_p}{L_J} \frac{C_J}{C_p} E_C, \qquad \chi_{pp'} = -2\sqrt{\chi_{pp}\chi_{p'p'}} \tag{71}$$

Due to the presence of Josephson junction with inductance L_J and capacitance C_J all modes including the cavity mode acquire some anharmonicity, however negligible. $\dfrac{L_p}{C_p}$ can be calculated by an effective impedance that is defined as:

$$\sqrt{\frac{L_p}{C_p}} = Z_{eff}^p = \frac{2}{\omega_p \mathrm{Im}[Y'(\omega_p)]} \tag{72}$$

Thus knowing L_J it is sufficient to find the zeros of $Y(\omega)$ and the derivative of $\mathrm{Im}[Y(\omega)]$ at its zeros from Fig. 7.9(d) to calculate anharmonicity α and dispersive shift $\chi \equiv \chi_{pp'}$. Considering a Josephson junction with sinusoidal current-phase relation, with our simulations we are expecting $\alpha = 170$ MHz and $\chi = 3.7$ MHz.

137

8.0   Al-InAs-Al nanowire shadow junctions[1]

In this chapter we study supercurrent properties in Josephson junctions made with a novel shadowing method. We use semiconducting nanowires as shadow mask on the surface of InAs quantum well prior to Al deposition. The nanowires introduce breaks in the Al superconducting layer that makes an epitaxial contact with InAs. The Josephson junctions are then made by etching Al and the quantum well to only leave leads that are separated by nanowire shadows. The distance between Al electrodes is of order 100 nm, shorter than the mean free path in the quantum well ($\sim$ 200 nm). $I_c R_N$ and $I_{exc} R_N$ products in these junctions are comparable to theoretical expectations and previously reported values for epitaxial Al-InAs 2DEG Josephson junctions made with etching technique. We then perform diffraction pattern measurements, Shapiro step measurements and SQUID measurements. Diffraction pattern and interferometry measurements exhibit extra periodicity of supercurrent as the function of flux, while microwave measurements reveal half-integer Shapiro steps, all pointing at an unexpected behavior of supercurrent where the simple sinusoidal current phase relation does not fit the data. The origin of this anomaly is yet to be confirmed as we show second harmonic Josephson current and a non-uniform current density along the junction's width caused by fabrication artefacts both result in same behavior of current as a function of flux. Nonetheless, our ballistic and highly transparent junctions have the potential to be developed further for hybrid superconductor-semiconductor qubit systems as well as topological quantum circuits.

---

[1]This chapter is an ongoing project. The measurements are done by myself, L. Jarjat, and V. van de Sande. Simulations are carried out by L. Jarjat and D. Pekker. The 2DEG structure and nanowires are grown by J.S. Lee, M. Pendharkar, A. McFadden, S.D. Harrington, G. Badawy, S. Gazibegovic, R. op het Veld, E.P.A.M. Bakkers, and C.J. Palmstrøm. The TEM data are acquired by S. Tan. And the project is supervised by S.M. Frolov.

8.1 Nanowire shadowing method on two dimensional materials

Superconductor-semiconductor hybrids have been widely studied in search of topological superconductivity [52, 190, 191, 192] as well as in hybrid transmon qubits [74, 109, 75, 76]. A highly transparent contact interface between superconductor and semiconductor is the key to these studies. There are multiple superconductors exhibiting such contact to one dimensional semiconducting nanowires [65, 222, 134, 232]. However, nanowire devices require bottom-up growth and gating techniques that can be restraining. Two-dimensional electron gases (2DEGs), on the other hand, with their top-down lithography process and gate patterning allow for more liberty in complex designs and multiple device couplings [240]. Progress in hybrids of superconductors and two-dimensional systems includes demonstrating gate-tunable bipolar supercurrent in graphene [241], inducing superconductivity from field-resilient Nb-family superconductors in InGaAs [242] and InSb [243] quantum wells, achieving robust superconductivity with highly transparent contacts on InAs [137, 244] and InAlSb [245] with epitaxial Al, and realizing supercurrent in Josephson field-effect transistors carried by holes in Ge/SiGe [246, 247]. In particular, since 2016 when an epitaxial contact between Al and InAs 2DEG was achieved, this structure has become a key candidate for topological and hybrid qubit investigations [248, 212, 100].

The universal way to fabricate devices in these proximitized 2DEGs is to lithographically pattern junctions and mesas and wet etch Al and InAs quantum well stack. Here we are investigating an alternative to this ex-situ etching by exploiting an in-situ shadowing method to selectively deposit superconductor and eliminate the etching process. This allows us to produce fabrication-free interfaces between many different 2D materials or surfaces of 3D crystals and metals or superconductors. We can use this method to rapidly characterize materials combinations and interfaces qualities.

Conventional shadow masks used to suffer from low resolution patterning due to the large distance between the mask and the target substrate. With recent advancements, nano-slit shadow masks made of ~ 100 nm thick Si_3N_4 membrane on silicon were used to fabricate nanowires down to 50 nm wide and up to 100 μm long [249], as well as selective deposition of superconducting islands on nanowires for topological qubit device design [208, 250]. These

shadow masks can be cleaned and reused multiple times, however, they prove to be challenging to align with a target substrate with few micron long nanowires for selective growth of superconducting film [250]. A way to minimize the distance between the shadowing object and the target is having them on the same substrate. A method developed by Gazibegovic *et al.* uses InSb nanowires grown with an offset on opposite trenches to shadow each other during superconductor deposition and leave one, two or three breaks in the superconducting shell [65]. This method opened avenues to exploit different semiconductor nanowires, nano-flakes, or on chip etched "bridges" to be used as shadow masks during superconducting film deposition demonstrating flexible platform for growing hybrids with numerous geometries [251, 134, 232, 219].

In this Chapter we use InSb nanowires to shadow InAs 2DEG for aluminum deposition. In our method the nanowire is lying on the 2DEG's surface and their shadows are used to fabricate Al-InAs-Al Josephson junctions. In our devices we do not remove the nanowire from the surface and they could be potentially used as a self-aligned top-gate, but also they may create scattering in the quantum well. To evaluate the quality of junctions made in-situ with this technique we study the Josephson current properties and characterize the coherent charge transport across the quantum well and the interface transparency by measuring products of critical current and excess current with normal resistance. We further investigate dependence of supercurrent as a function of magnetic field (diffraction pattern measurements) and microwave excitation (Shapiro steps measurements). We then perform Josephson interferometry in dc-SQUID devices. Diffraction pattern and interferometry measurements exhibit extra periodicity of supercurrent as the function of flux, while microwave measurements reveal half-integer Shapiro steps. At first sight these measurements may suggest a strong intrinsic second order Josephson harmonic, but we point out and emphasize our peculiar device structure and fabrication artefact that can cause a non-uniform supercurrent density along the width of the junctions resulting in similar extra periodicity of Josephson current. Further work is being done as this thesis is being published to resolve this ambiguity.

8.2   Device fabrication and characterization

InGaAs/InAs/InGaAs quantum well is grown by molecular beam epitaxy (MBE) technique following the procedure fully explained in Refs. [137, 145]. The mobility of the InAs 2DEG is ≈ 25000 cm^2/(Vs) with electron density of order of 10^{12}/cm^2 yielding mean free path of ≈ 200 nm obtained from transport measurements in van der Pauw geometry (data not shown). As explained step by step in Chapter 3.2.4, prior to Al deposition a chip of previously grown InSb nanowires is transferred in the MBE machine and is brought in touch face to face with 2DEGs surface where nanowires get deposited. The chip is then transferred (without leaving the MBE) to the evaporation chamber where Al is evaporated and nanowire shadows with length of $80 - 120$ nm and width of few microns are made in-situ. Fig. 8.1(a) illustrates this procedure in cartoon. The nanowires have a layer of native oxide which prevents them from direct electric contact to the quantum well.

We start fabricating and preparing Josephson junctions for measurements by patterning and depositing Pd alignment markers mapping the chip and bonding pads around the chip. We now need to define Josephson junctions by etching the superconductor away from both ends of the finite size nanowire shadows. We use optical images of nanowires on the 2DEG's surface to find shadows and design contacts and leads, as a 10 nm deep shadow is difficult to see. For this, we pattern leads using negative tone resist (ma-N 2403). To prevent Al diffusion the resist is cured in a vacuum chamber at room temperature. The leads run continuously over a nanowire shadow. After developing, with ma-D 525 for 65 seconds and water for 5 minutes, the resist strips off where it was not exposed by electron beam. Next we etch Al and quantum well except where the leads and junctions are protected by the resist, hence the junction area is not exposed to etchants and is undamaged. Al etches away with Transene type-D and quantum well is etched by a citric acid, phosphoric acid and hydrogen peroxide solution (220:55:3:3 H$_2$O:citric acid:H$_3$PO$_4$:H$_2$O$_2$). We now have multiple junctions ready for measurements that are all expected to be $100 - 120$ nm long that is ~ 100 nm shorter than the mean free path in the quantum well and the transport is expected to be between ballistic and diffusive limit (see supplementary for all 6 measured junctions' sizes and parameters). Fig. 8.1(b) shows a transmission electron microscope (TEM) image of a
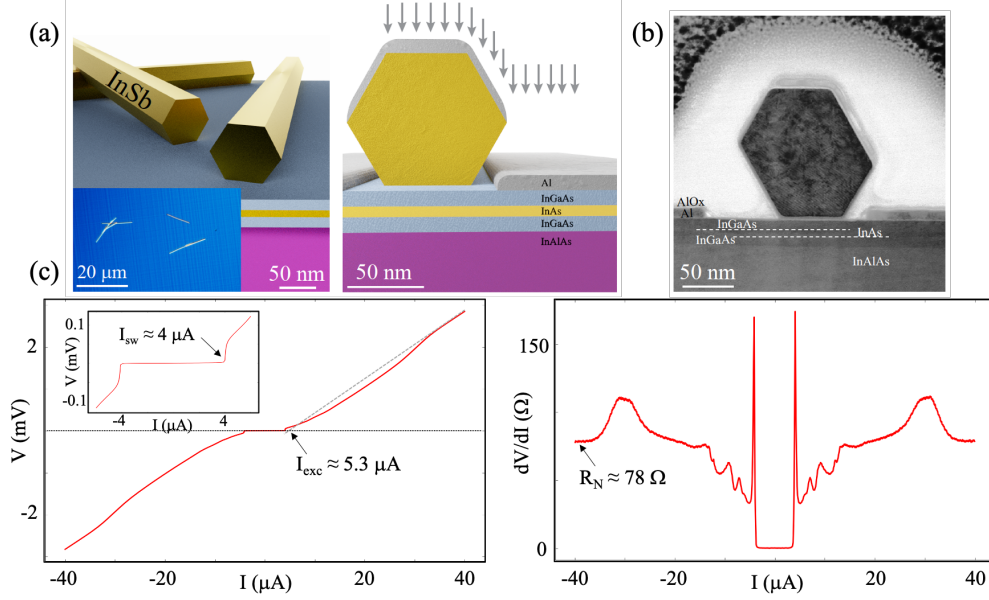
Figure 8.1: (a) Cartoon representation of transferred nanowires on InAs 2DEG's surface in MBE machine followed by Al evaporation, creating nanowire shadows instantly. The inset of the left panel is top view optical micrograph image of 2DEG surface with nanowires after Al evaporation. (b) TEM of cross-section of a device after measurements. Al-InAs quantum well heterostructure with the break defined by InSb nanowire are distinctly resulted. (c) $I - V$ characteristic of the Josephson junction discussed in the main text, where no hysteresis is visible sweeping current bias back and forth from positive to negative sides. This behavior is typical to other junctions measured in the supplementary. The dashed grey line is to extrapolate excess current I_{exc} at the intercept with $V = 0$. The inset is zoomed in to the supercurrent regime indicating measured switching current. The right panel is plotting differential resistance of $I - V$ curve revealing $R_N \approx 78~\Omega$ resulting in $I_{sw}R_N \approx 312~\mu$V and $I_{exc}R_N \approx 413~\mu$V.

junction's cross-section after measurement.

The Josephson junctions in the ballistic and diffusive limits can be characterized by products of $I_c R_N$ and $I_{exc}R_N$. R_N is the junction's normal resistance well above the superconducting gap. Right panel in Fig. 8.1(c) shows differential resistance as the function of bias current across the junction from which we extract $R_N \approx 78~\Omega$ for this junction. The critical current I_c is the maximum current that can be carried by Andreev bound states across the junction. Hence, it reflects the coherent charge transport through the semiconducting weak link and is a measure of interference transparency as well as 2DEG's mobility. The excess current I_{exc}, on the other hand, is the result of Andreev reflections involving a charge transfer

of $2e$ across the junction and primarily depends on the interface transparency [84].

The critical current can be compared to the superconducting gap by the relation $I_c R_N = \alpha \Delta / e$. Theoretical expected values of α for ballistic and diffusive limits are π and $(\pi/2)1.32$, respectively [252, 253]. We note that what experimentally is measured is the switching current I_{sw}, the current at which the junction transitions from zero-resistance to finite-voltage regime. In principle, I_{sw} and I_c should be identical but factors such as finite temperature and noise can lead to a switching current smaller than the critical current. We use the measured I_{sw} for our analysis which in the worst case gives an underestimation for our junction's quality. Inset of Fig. 8.1(c) zooms in the supercurrent region as a function of current bias across the junction from which $I_{sw} \approx 4~\mu A$. For this junction we have $I_{sw} R_N \approx 312~\mu V$, resulting in $\alpha \sim 1.5$. The superconducting gap $\Delta_{Al} \approx 210~\mu eV$ which we extract from the relation $\Delta = 1.75 k_B T_c$, in which k_B is the Boltzmann constant and T_c is the superconducting transition temperature ≈ 1.4 K for a 10 nm Al film. The excess current I_{exc} is extracted from current-voltage $(I - V)$ characteristics in the normal state where a linear fit of $V(I)$ intercepts with $V = 0$ as shown in Fig. 8.1(c). If there is no normal reflection the theoretical expected values for $\alpha' = e I_{exc} R_N / \Delta$ is $8/3$ and $\pi^2/4 - 1$ for ballistic and diffusive junction limits, respectively [85, 254]. Here again using $\Delta_{Al} \approx 210~\mu eV$ and $I_{exc} \approx 5.3~\mu A$ from our measurement $(I_{exc} R_N \approx 413~\mu V)$ we find $\alpha' \sim 1.97$ which is close to the ballistic regime. Our results are comparable to recent reported values on similar junctions made with conventional etching process [147]. α' can be directly used to extract the transparency of the interface [85, 160]. We use the analytical results in Ref. [255] and find the BTK interface transparency $Z = 0.3$ which results in the transmission probability of $T = 92\%$ $(T = 1/(1 + Z^2))$. This high interface transparency (the lower the Z the more transparent the interface) is expected due to the large contact area between the 2DEG's surface and epitaxial Al.

8.3   Supercurrent diffraction measurements

As shown earlier in Eq. 33 the current across the junction depends on the difference of superconducting phases in the leads: $I_S(\phi) = I_c \sin(\phi)$. We now define a gauge-invariant phase in the presence of an applied perpendicular magnetic field:

$$\gamma = \phi + \frac{2\pi}{\Phi_0} \oint_C \boldsymbol{A} \cdot d\boldsymbol{s}, \tag{73}$$

where $\Phi_0 = h/2e$ and $\boldsymbol{A}$ is the magnetic vector potential. The integral passing through electrodes and the weak link results in the total flux Φ enclosed by the junction:

$$\Phi = \int_{-L/2}^{L/2} \boldsymbol{A} \cdot d\boldsymbol{s} = BWL,$$

where W and L are the width and the length of the junction, respectively. The gauge-invariant phase γ along the junction can be written as

$$\gamma(x) = \phi_0 + \frac{2\pi}{\Phi_0} BW x \tag{74}$$

The Josephson current as a function of magnetic field will then be:

$$I_S(B) = \int \int_{-L/2}^{L/2} j_c(x,y) \sin\left(\phi_0 + \frac{2\pi}{\Phi_0} BW x\right) dx\, dy, \tag{75}$$

where $\int j_c(x,y)\, dy$ is the supercurrent density per unit length along x. However, here we only consider a linear supercurrent density along the width of the junction from which we can write the critical current as $I_c = j_c \times L$.

The maximum current as a function of flux threading the junction can be calculated to get the form:

$$I_S(\Phi) = I_c \left| \frac{sin(\pi\Phi/\Phi_0)}{\pi\Phi/\Phi_0} \right| \tag{76}$$

which is referred to as the "Fraunhofer diffraction pattern" due to its analogy to the case of light passing through a narrow rectangular slit, shown in Fig. 8.2(a). However, if the Josephson current is of a more general form of Eq. 34 where $I_S = \Sigma I_n \sin(n\phi)$, the supercurrent diffraction pattern deviates from the Fraunhofer pattern. In Fig. 8.2(b) we are showing the case where there is only the second harmonic present ($I_S = I_{c2}\sin 2\phi$) and as expected the periodicity of the "Fraunhofer pattern" is halved. At last Fig. 8.2(c) is depicting where a

144
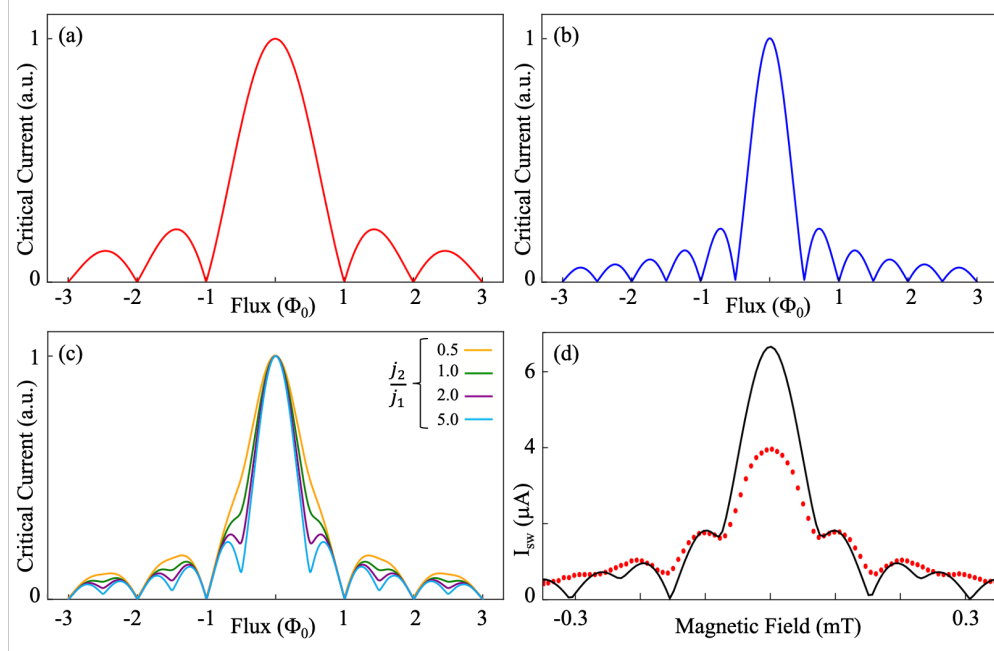
Figure 8.2: Supercurrent as a function of flux threading a Josephson junction. (a) Current-phase relation follows Josephson's prediction where $I_S = I_c \sin(\phi)$ and it resembles the simple Fraunhofer diffraction pattern. (b) The case if the supercurrent was a π periodic function of phase and second harmonic Josephson current was the only present term $I_S = I_c \sin 2\phi$. (c) If the current-phase relation deviates from the sinusoidal form where both first and second harmonic terms contribute to the flow of current the diffraction pattern results from maximizing $j_{c1} \sin(\phi(x)) + j_{c2} \sin(2\phi(x))$. As the contribution of second order increases side local dips at half flux quantum appear. (d) Red dots are the extracted points for switching current from data in Fig. 8.3. Black curve is the modeled critical current where $j_c(x) = \sin\phi + 1.77 \sin 2\phi$.

comparable mixture of first and second harmonic are present together. Next we show the resemblance of our experimental data to this case. We explore the evolution of the switching current of the Josephson junction characterized in Fig. 8.1(c) as a function of a small out-of-plane magnetic field. Fig. 8.3 is illustrating experimental diffraction measurements of this junction that is ~ 120 nm long and ~ 8 μm wide. This scan clearly deviates from a simple Fraunhofer pattern as a black arrow points to nodes at half flux quantum. The subsequent peaks are skewed that can result from self-field effect of the junction and it evidently preserves inversion symmetry, $(I, B) \rightarrow (-I, -B)$.

Fig. 8.2(d) is the extracted switching current from Fig. 8.3 where we fit the data us-
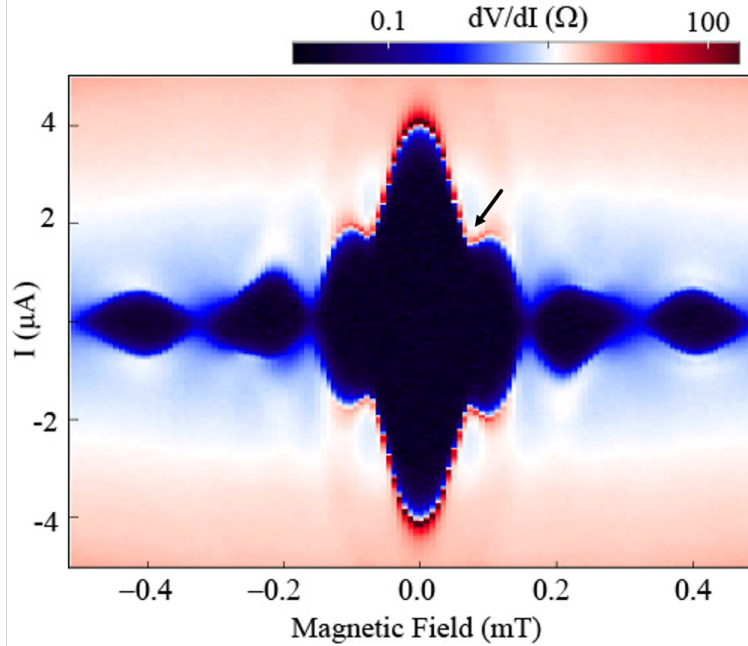
Figure 8.3: Measured differential resistance as a function of current bias I and perpendicular magnetic field. Dark blue corresponds to supercurrent regime. Dark red and white peaks are tracing supercurrent regime identify the measured switching current I_{sw}. The black arrow points to local minima at half flux quantum.

ing a supercurrent density in which both first and second harmonics are present. Doing so results in a second order Josephson current that is comparable to or higher than the first order Josephson current ($\frac{j_{c2}}{j_{c1}} = 1.77$). Such exotic current-phase relation can be realized in the vicinity of $0 - \pi$ junction transition, at which the first Josephson harmonic vanishes [256, 257, 258, 259]. However, we do not expect this to be the case for our semiconductor junctions at zero field. Additionally, in short ballistic junctions one would expect a very anharmonic current phase relation in which all higher order Josephson currents are present and the diffraction pattern resembles a Fraunhofer like pattern with no extra nodes. Such a high anomalous second order Josephson harmonic is surprising as we are not observing any contributions from higher orders.

So far we treated the supercurrent density along the junction to be uniform in calculating the integral of Eq. 75. Fig. 8.4(a) is showing a scanning electron micrograph of a typical device we studied. The dark strip in the middle of the junction is universal to all our devices

146

and represents a cross-linked polymer resist remaining on top of Al. We speculate that this feature may produce a non-uniform supercurrent density along the width of the junction, such that:

$$j_c(y) = j_{c_a}\theta(y - y_a)\sin\phi + j_{c_b}\theta(y_a - y)\theta(y - y_b)\sin\phi + j_{c_a}\theta(y_b - y)\sin\phi, \qquad (77)$$

where y is the position along the width of the junction, j_{c_a} and j_{c_b} are supercurrent densities on the two outer sides of the junctions and the middle dark strip, respectively. Varying relative j_{c_b}/j_{c_a} results in different supercurrent diffraction patterns.
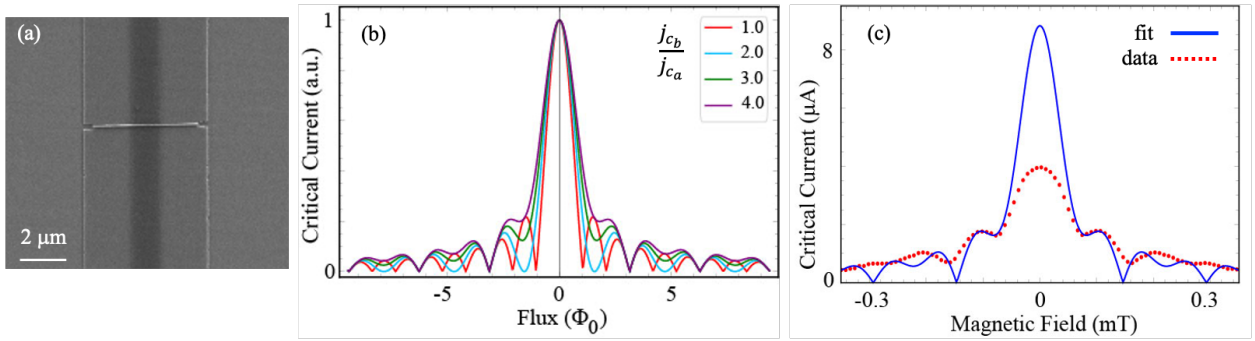
Figure 8.4: (a) SEM image of a device with residual ma-N 2403. The junction is defined underneath the nanowire where it shadows the Al superconducting layer. (b) Modeled critical current for various j_{c_b}/j_{c_a} values as indicated in the legends. For $\dfrac{j_{c_b}}{j_{c_a}} = 1$ (red curve) the supercurrent across the junction as the function of flux resembles Fraunhofer diffraction pattern. (c) Fit to the data $\dfrac{j_{c_b}}{j_{c_a}} = 3.76$, red dots extracted from Fig. 8.3.

Fig. 8.4(b) illustrates how the diffraction pattern deviates from Fraunhofer-like pattern as the relative contribution of supercurrent density of the middle part of the junction increases. We can roughly fit our data with this model assuming supercurrent density is approximately 4 times larger in the crossed-linked area than the density on either side, Fig. 8.4(c). There are, however, some features in the data, for example the lifted nodes at integer flux quanta, that could be better fit if we assume second order Josephson effect and non-uniform supercurrent density both play essential roles in our devices.

8.4   Shapiro steps

We next perform Shapiro steps measurements. We excite the junction with an ac signal with frequency f, $(\omega/2\pi)$, and measure the switching current as a function of power of this microwave signal. This results in a sequence of voltage plateaus in transport measurements at the resonance condition and these plateaus line up with integer values $nf\Phi_0$, that is a consequence of second Josephson relation:

$$\frac{d\phi}{dt} = \frac{2\pi}{\Phi_0}V(t) \longrightarrow \phi(t) = \phi_0 + \omega_0 t + \frac{2\pi}{\Phi_0\omega}V_1\sin\omega t \tag{78}$$

where $V(t) = V_0 + V_1\cos\omega t$ is the voltage across the junction and $\omega_0 = \frac{2\pi}{\Phi_0}V_0$. Substituting this relation for the phase difference across the junction back to Josephson's first relation (Eq. 33) and using Bessel functions for expansion, the supercurrent takes the form

$$I_S = I_c\sum(-1)^n J_n(\frac{2\pi}{\Phi_0\omega}V_1)\sin(\phi_0 + \omega_0 t - n\omega t), \tag{79}$$

which only contributes to the DC transport when $\omega_0 = n\omega t$ or $V_n = n\Phi_0 f$.

As expected if the current-phase relation takes the general form of Eq. 34 and second harmonic Josephson order contributes to the transport, plateaus with half-integer values $nf\Phi_0/2$ can appear. Both integer and half-integer Shapiro steps are distinctly evident in our measurements shown in Fig. 8.5(a). However, we refrain from concluding presence of second harmonic Josephson effect as inhomogeneous supercurrent density may give rise to half-integer Shapiro steps [260]. We point out that the first half-integer step in this plot which is taken at zero magnetic field is missing. The evolution of the steps in magnetic flux is shown in Fig. 8.5(b) where first half-integer step appears at B ≈ -75 μT. Missing Shapiro steps has mostly been associated with topological superconductivity [261, 262]. However, we emphasis that our junctions are in a topologically trivial state. Moreover, Landau-Zener transition between low energy and high energy Andreev bound states in highly transparent Josephson junctions is shown to be causing missing Shapiro steps [263]. This scenario may be more related to our experiments but more detailed measurements, analysis, and modeling are needed and under preparation by our group to come to a conclusion about observing half-integer and missing Shapiro steps in this system.
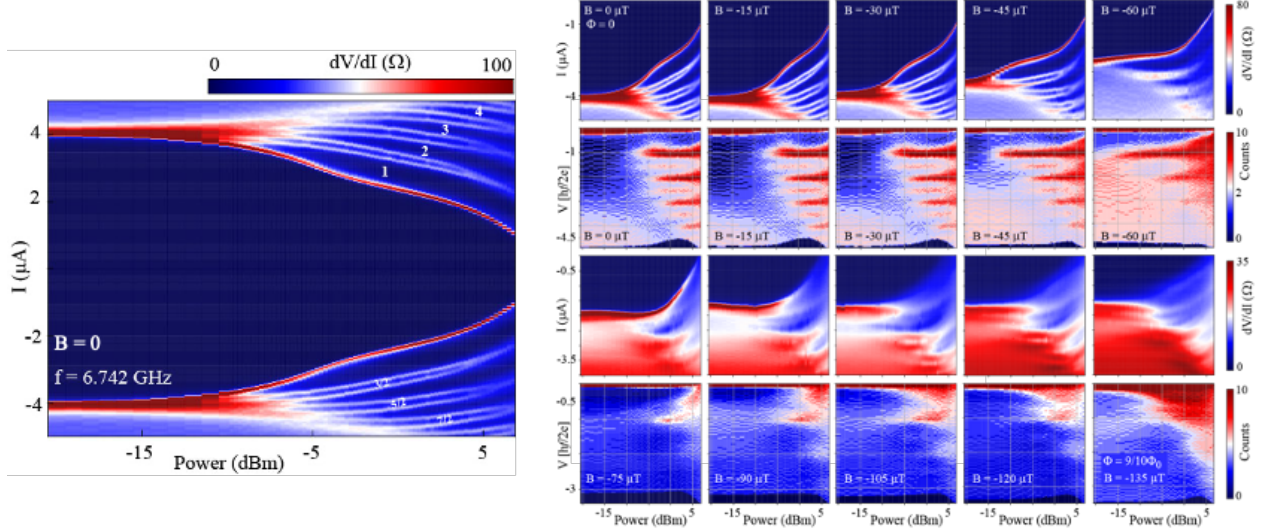
Figure 8.5: (Left) Measured differential resistance as a function of current bias I and power of applied microwave excitation at $f = 6.742$ GHz. The peaks in differential resistance correspond to Shapiro steps. Integer and half-integer voltage plateaus are marked. First half-integer plateau is missing at zero magnetic flux. (Right) Evolution of the Shapiro steps as flux threading the junction increases at $f = 6.742$ GHz. Half-integer steps start to fade away at B = -60 μT. But first half-integer step exhibits a local maximum at B $\approx$ 75 μT.

8.5 Supercurrent oscillations in superconducting quantum interference device

Next we study the switching current modulations with magnetic flux enclosed in a superconducting quantum interference device (SQUID). Fig. 8.7(a) is depicting the SQUID loop studied here which encircles two junctions denoted as JJ_a and JJ_b, that have critical current I_{c_a}, I_{c_b} and phase difference ϕ_a, ϕ_b, respectively. The supercurrent passing through the SQUID is then divided between the two junctions (assuming the two junctions have sinusoidal current-phase relation):

$$I = I_{c_a} \sin(\phi_a) + I_{c_b} \sin(\phi_b) \tag{80}$$

in which flux quantization imposes the condition:

$$\gamma = \phi_a - \phi_b = 2\pi \frac{\Phi_{ext}}{\Phi_0} + 2\pi n, \tag{81}$$

assuming the geometric inductance is negligible compared to Josephson inductance of the junctions. If $I_{c_a} = I_{c_b}$ the SQUID is called symmetric and its critical current as a function of magnetic flux Φ_{ext} is

$$I_c = 2I_{c_a} \left| cos\left(\pi\frac{\Phi_{ext}}{\Phi_0}\right)\right|. \tag{82}$$

However, practically the two junctions have different critical current values, making the SQUID asymmetric. This asymmetry is parameterized by the ratio

$$\alpha = \frac{I_{c_a} - I_{c_b}}{I_{c_a} + I_{c_b}} \tag{83}$$

which modifies the SQUID critical current:

$$I_c = (I_{c_a} + I_{c_b})\sqrt{(1-\alpha^2)\cos^2(\frac{\pi\Phi_{ext}}{\Phi_0}) + \alpha^2} \tag{84}$$

Fig. 8.6 is plotting this critical current for different values of α.
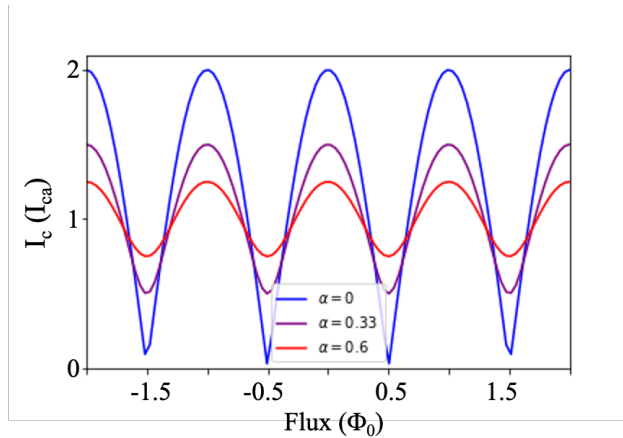
Figure 8.6: Modulations of SQUID critical current in external flux threading the loop for different asymmetry parameter α.

If $\alpha \gg 1$, meaning that the critical current of one junctions is much higher than the other, the SQUID critical current takes approximately the constant value of the larger junction with superimposed oscillations of the amplitude of the critical current of the other. This way the current-phase relation of an unknown Josephson junction can be extracted from a reference junction. Here, our junctions, however, are of similar size but could have slightly

different critical current values. Fig. 8.7(b) shows the differential resistance of our SQUID as a function of bias current and applied perpendicular magnetic field. We can distinguish typical fast SQUID oscillations of the kind shown in Fig. 8.6 superimposed by the larger scale much slower diffraction pattern from individual junctions. The junctions area are non-negligible compare to SQUID size and changing field changes flux through both junctions and the SQUID, hence this envelope function alters the amplitude of SQUID oscillations depending on the flux.
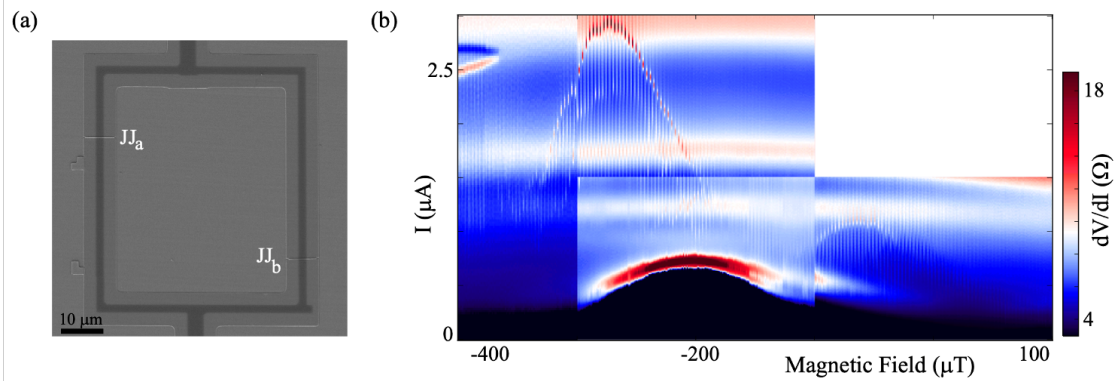
Figure 8.7: (a) Scanning electron micrograph of a SQUID loop with two junctions, JJ_a and JJ_b. The sizes of each junction is comparable to the size of the SQUID loop. (b) Differential resistance of the SQUID device exhibiting fast SQUID oscillations of the switching current enveloped by slower diffraction pattern from individual junctions. The large resistance at low current bias may be due to a "spurious junctions" in series with one of the leads causing a premature switching to normal state. In practice, if we could use a gate voltage to control the supercurrent of each junction individually we would be able to turn off the SQUID oscillations and retreat the diffraction pattern similar to what we showed in Fig. 8.3.

Fig. 8.10 in the supplementary shows the large scale SQUID oscillations upon which we zoom in different regions and obtain data shown in Fig. 8.8. We note that from data taken in Fig. 8.7(b) to these zoomed in oscillations there was a roughly 200 μT shift in magnetic field from an unexpected flux jump. The zoomed-in SQUID oscillations exhibit peculiar and rather unexpected features. In addition to different amplitude of the SQUID oscillations we observe different periodicity in different magnetic field regions. Switching current oscillations in Fig. 8.8(a) has doubled the frequency of oscillations in Fig. 8.8(c) going through a transition regime in Fig. 8.8(b).

The doubling of frequency oscillations is expected for SQUIDs made of junctions with
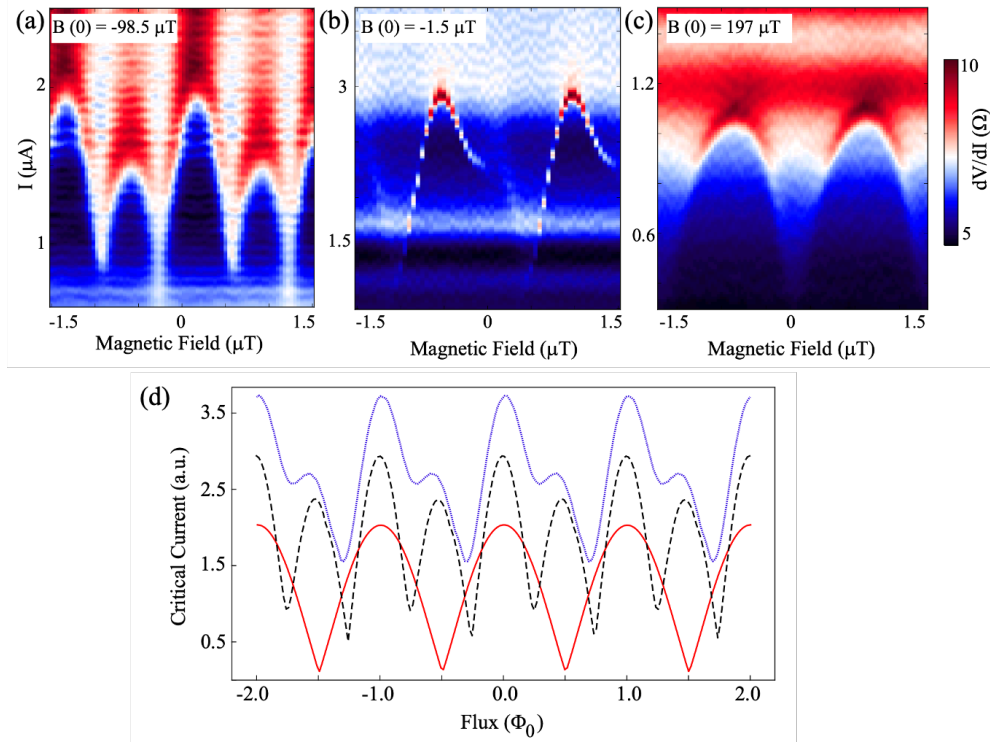
Figure 8.8: Measured differential resistance as a function of current bias and magnetic field threading the SQUID loop. Switching current pattern has half the periodicity in panel (a) compare to panel (c). Panel (b) is a transition regime in between with a distorted amplitude. A vertical line-cut is subtracted in panels (a) and (c) to increase the clarity of data. (d) Modeled critical currents for a SQUID with two non-identical Josephson junctions with first and second order Josephson harmonics. Simulation parameters used: (red solid line) $j_{c1,a} = 1.0$, $j_{c2,a} = 0.05$, $j_{c1,b} = 1.0$, $j_{c2,b} = 0.05$, (blue dotted line) $j_{c1,a} = 1.2$, $j_{c2,a} = 1.75$, $j_{c1,b} = 0.75$, $j_{c2,b} = 0.5$, (black dashed line) $j_{c1,a} = 0.6$, $j_{c2,a} = 1.2$, $j_{c1,b} = 0.4$, $j_{c2,b} = 1.0$.

a strong second order Josephson current. However, the periodicity of the pattern can be affected by the asymmetry parameter α of the SQUID. α can be flux tunable because of different critical current of the two junctions and different trapped magnetic flux nearby. Modeling a SQUID with second order Josephson current and different α parameter can produce different oscillations periodicity as shown in Fig. 8.8(d).

Again, we refrain from drawing firm conclusion on the presence of second harmonic effect due to uncertainties arising from fabrication artefacts. We would like to note that these are all preliminary analysis and require further device fabrication and measurements.

8.6   Outlook

We fabricated Josephson junctions by using a novel nanowire shadowing technique and eliminating etching mesas and junction channels. This process results in ballistic Josephson junctions with product of excess current and normal resistance comparable to theoretical value. We investigated the behavior of supercurrent as a function of flux threading junctions and observed a deviation from simple Fraunhofer diffraction pattern. Shapiro step measurements reveal both integer and half-integer voltage plateaus. Furthermore the doubling of frequency of supercurrent oscillations in a SQUID as a function of flux point out to an anomalous behavior of supercurrent in our devices. The origin of this anomaly is subject to further device fabrication and experiments in which the artefacts of fabrication are taken care of. These junctions can be utilized in semiconductor-superconductor hybrid qubits as well as the search for topological superconductivity.

The InSb nanowires used for shadowing are also etched away, where they are not covered by polymer resist. Hence, the nanowires in these devices solely are used to define the junctions. However, an immediate device enhancement is to use protected nanowires (fully covered by etch-resistant dielectric such as HfO_x) and use the nanowire as a top gate to study gate dependence of supercurrent.

8.7   Supplementary material

In this section we present extended data from devices measured in the main text, as well as data from other Josephson junctions all of which "suffer" from the crossed-link resist residue like shown in Fig. 8.4(a).

The advantage of our novel fabrication of highly transparent Josephson junctions is that its simplicity should guarantee a reasonable reproducibility rate. Out of 7 junctions fabricated and properly bonded, only one did not display supercurrent. However, the area of one junction to other is still subject to change due to fabrication artefacts. The devices also showed robust behavior in two consecutive cooldowns. The specifics of all bonded junctions

are presented in Table 8.1.

Table 8.1: Effective length L_eff of a junction of width w can be obtained from the field periodicity B_0 of the diffraction pattern. We are not considering the possible varying effective width.

Device	w $[\mu m]$	B_0 [mT]	I_{sw} $[\mu A]$	L_{eff} $[\mu m]$
1	8	0.15	4.1(0)	1.52
2	6	0.25	2.6(9)	1.28
3	6	0.28	2.9(0)	1.23
4	6	0.56	2.2(6)	0.62
5	6	0.46	2.8(2)	0.75
6	6	0.31	3.7(4)	1.01
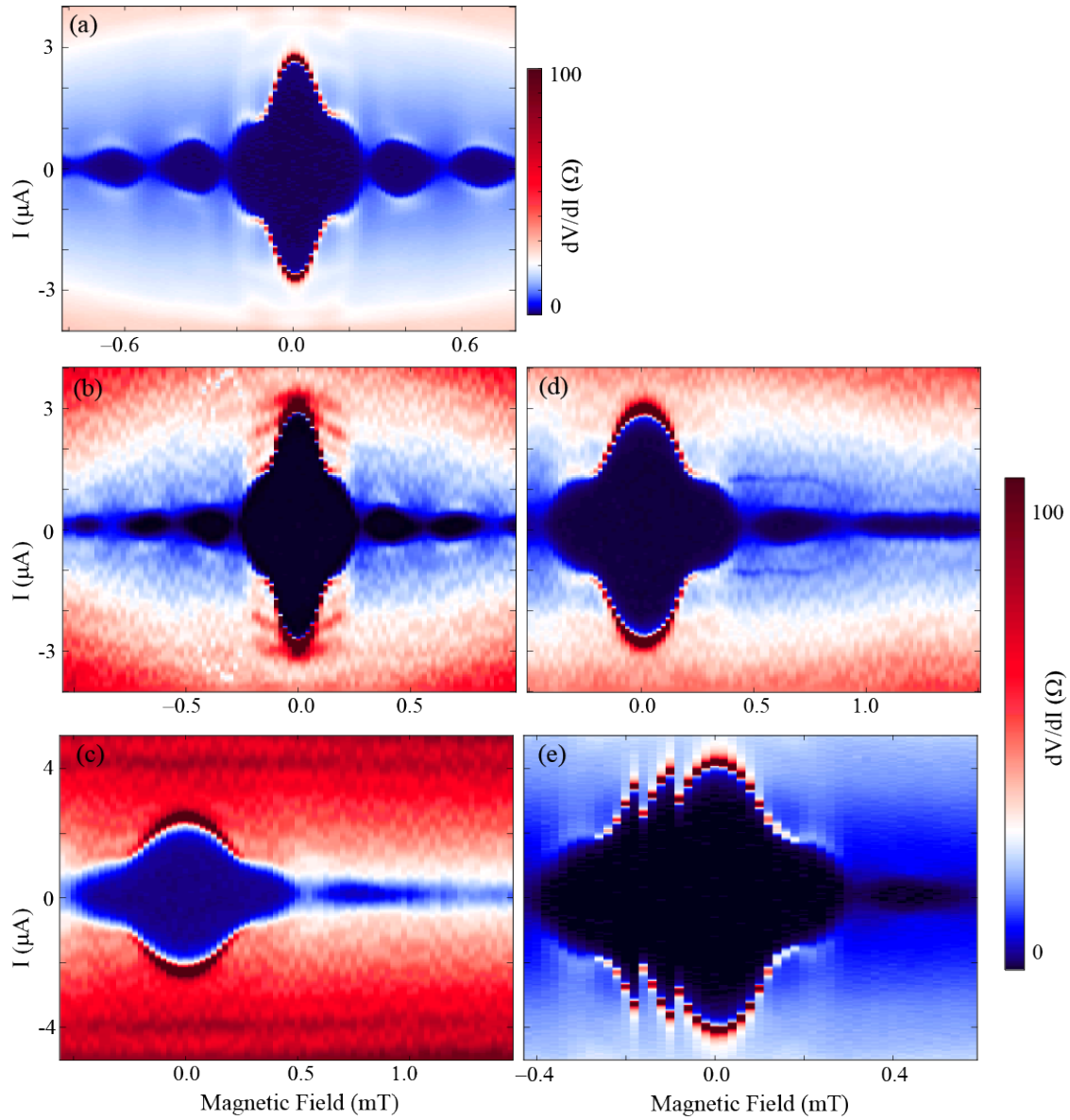
Figure 8.9: Differential resistance as a function of current bias and magnetic field for Devices 2 – 6 listed in Table 8.1. All devices show non-conventional supercurrent diffraction pattern. Device 1 is discussed in the main text.
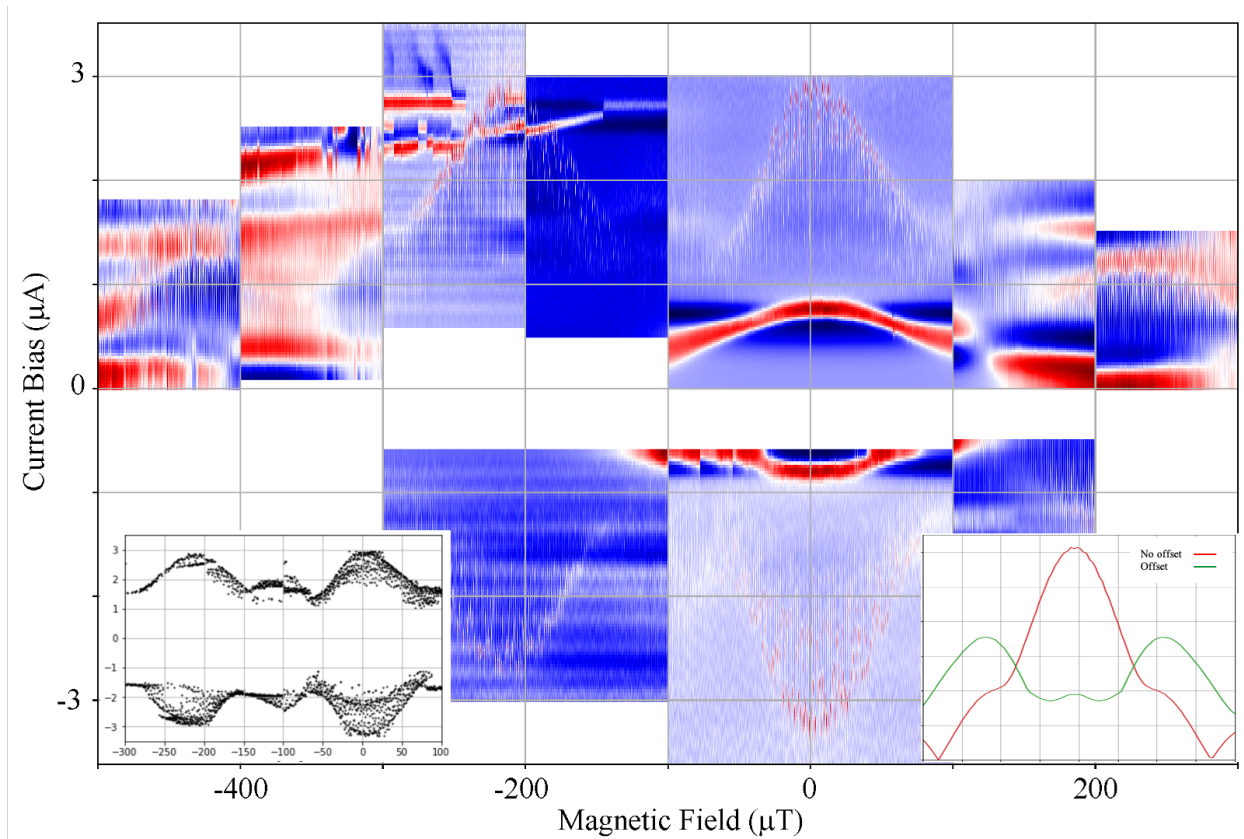
Figure 8.10: Extended SQUID oscillations. Fast SQUID oscillation are enveloped by a function that differs from expected Fraunhofer pattern. The left inset is the extracted envelope function which resembles the green curve in the right inset. Right inset: Modeled envelope function of SQUID oscillations for junctions with no offset in their zero bias (red curve) and with an offset bias (green curve), pointing out to the asymmetric SQUID with an offset in zero bias of the two junctions.
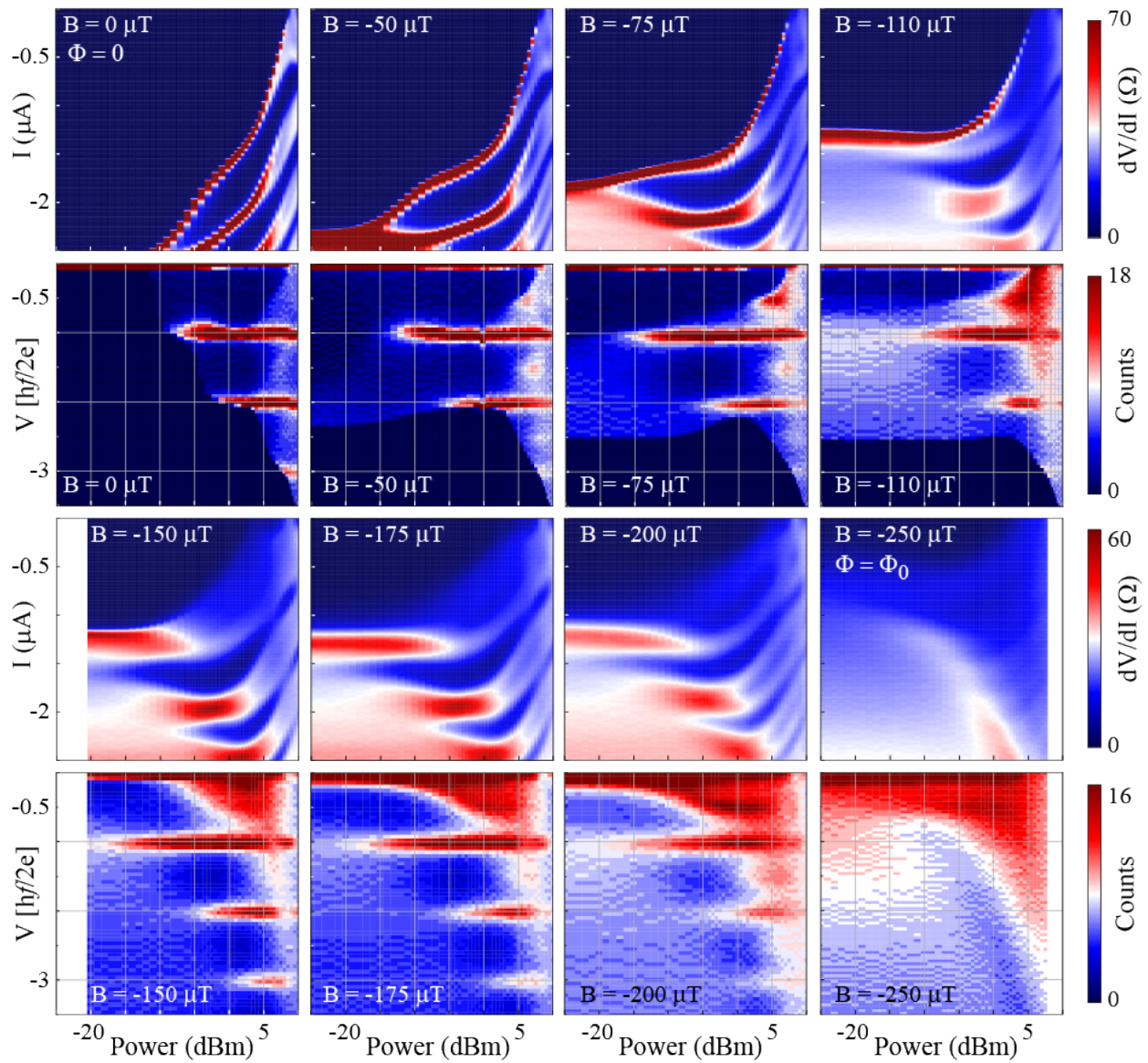
Figure 8.11: Device 2. Evolution of the Shapiro steps as flux through the junction increases at $f = 6.855$ GHz. The first half-integer step appears at B = -50 μT and displays a local maximum at B = -200 μT.

9.0   Conclusions and outlook

In this thesis we studied materials properties and quantum transport in several different nanostructures that are semiconductor nanowires coupled to superconductors. The goal of these studies is to look for an optimal platform for realizing Majorana fermions that can be developed to build a qubit that is protected against local sources of decoherence, known as topological Majorana qubit. What's more, these studies are also related to other qubit platforms such as quantum dot spin qubit and semiconductor-superconductor hybrid qubits. We started with studying physics effects such as spin-orbit coupling and induced superconductivity in Ge/Si core/shell nanowires in contact with NbTiN and Al superconductors with prospects of both Majorana fermions and quantum dot spin qubits. Then we explored quantum transport in InSb nanowires that are already extensively being investigated in Majorana studies owing to their high electron mobility, strong spin-orbit coupling and large g-factor. First we try to get a better understanding of tunneling experiments in Al-InSb and NbTiN-InSb heterostructures and then we improve the contact between InSb nanowire and superconductors where a new superconducting material (Sn) is explored. These studies are then followed by preliminary results from microwave measurements on superconducting circuits that are compatible with semiconductor-superconductor heterostructures and will be integrated in future qubit designs.

We achieved transparent superconducting contacts to Ge/Si core/shell nanowires based on NbTiN (Chapter 4). Induced superconductivity sustains up to 1 T in external magnetic fields, in good comparison to fields needed to enter the topological regime [1]. These nanowires demonstrated large effective g-factors up to 8 and substantial spin-orbit interaction corresponding to a spin-orbit length of l_{so} = 100–500 nm in gate defined double quantum dots. However, despite theoretical predictions for an extremely large spin-orbit interaction [60], the measure value in our experiments, did not exceed those measured in InAs and InSb nanowires. Possible reasons for this lower-than-expected spin-orbit coupling could be: not optimal magnetic field orientation at which data was taken due to spin-orbit anisotropy [177], and a low strain between thin Si shell and relatively thick Ge core demand-

ing tailoring nanowire morphology. Since then the quality of interface between Ge core and Si shell has been improved by in-situ HCl cleaning leading to higher hole mobility [264] and more stable quantum dot devices [265, 266]. Very recently, these enhanced nanowires showed a remarkably short spin-orbit length of $\sim$ 65 nm in similar experiments to ours done on double quantum dots focusing on Pauli spin blockade regime [267]. Another development that can be considered in tailoring these nanowires is a catalyst-free growth as Au can inevitably introduce metal contamination in the semiconducting nanowire [268]. All things considered, the valence band of Ge can be a platform for hybrid superconducting-semiconducting quantum systems [269].

We then focused on the transport mediated by Andreev bound states formed in InSb nanowire quantum dots strongly coupled to Al and NbTiN superconductors (Chapter 5). We showed that a mirage of replicated Andreev spectra can result from a tunneling probe that is more complex than a Fermi level or BCS superconducting DOS where confined Andreev bound states may form in the adjacent nanowire section under the superconductor. Moreover, a negative differential conductance within the induced superconducting gap was observed that could only be explained by a peak in the middle of the DOS of the superconducting probe. A peak at the Fermi level is one of the characteristics of Majorana zero modes and our observation could complicate the interpretation of Majorana experiments done in the similar superconductor-nanowire hybrid devices [67, 149, 153, 68, 152, 270].

Until recently, almost all experiments aiming at topological superconductivity in hybrids of superconductors and semiconducting nanowires used either Al or Nb(TiN) as the superconductor of choice. However, Al suffers from relatively low critical magnetic field and temperature, resulting in a small induced gap. And induced superconducting gap from Nb-family superconductors is generally accompanied by subgap quasiparticles, shortening coherence times and scrambling readout of a future topological qubit. Hence, we looked into another superconductor - tin. We studied induced superconductivity in InSb nanowires that are coated with uniform tin shells (Chapter 6). The induced superconducting gap is in the range of $600 - 700$ μeV and it is void of subgap states. The gap slowly shrinks in magnetic field and remains up to $\sim$ 4 T. Transparent tunnel junctions are prepared by in-situ shadowing of nearby nanowires and flakes, resulting in different geometries like S-N-S (one nanowire

shadow), N-S-N (two-nanowire shadow), and N-S (flake shadow). An immediate follow-up for N-S geometry is to explore Andreev blockade transport that may occur in double quantum dots with a superconducting lead [271] proposed in topological quantum computing schemes for Majorana state readout [225, 208, 209]. In addition to robust induced superconductivity, we observed two-electron charging effect from a tin island that is of essence for long quasiparticle stability time, which again puts this system in an immediate urge for pursuing experiments aiming at detecting topological superconductivity and Majorana zero modes, as well as for transmon qubits. Parallel to our efforts in the search of more superconductors to substitute Al and Nb(TiN), other groups have demonstrated promising results as well. Pb islands recently are found to exhibit two-electron charging effect in Pb-InAs hybrid structures [232]. A relatively large hard induced gap ~ 1.25 meV from Pb in InAs remains intact up to 8 T in magnetic field, which is remarkable. Moreover, developments in shadowing techniques allows for in-situ device fabrication with different geometries while looking for alternate superconductors [65, 230, 219].

We further plan to use Sb on a Si or sapphire substrate and explore its microwave response as well as measuring its kinetic inductance boost to evaluate the potentials of this material for transmon and fluxonium qubits. Among caveats of Sn when depositing thin films is that it may easily ball up depending on the substrate, it oxidizes and is extremely soft and scratchable. Therefore, some care needs to be taken in determining an optimal thickness in addition to capping Sn with an AlO_x layer to terminate self oxidation. In our efforts to incorporate Sn in superconducting circuits we used Sn-InSb-Sn junctions as the nonlinear element in a transmon-like design (Chapter 7.2). We observed a dispersive shift in the phase and amplitude of resonant frequency of the cavity resonator at the transition frequency of the nanowire junction. However, we were not able to perform pulse spectroscopy mainly due to a very limited lifetime of order of tens of nanoseconds. These are preliminary results that we obtained from this hybrid superconducting circuit semiconductor nanowire, in which the resonators are made of Al and not compatible with magnetic field application. Moreover, the substrate in use was a poor quality Si substrate that could further lowers the qubit lifetime. For the next step we intend to substitute Al with field resilient Nb(Ti)N resonators that we characterized in Chapter 7.1. The reason we started with Al for hybrid

superconducting-semiconducting qubit scheme was the relatively low quality factors of our Nb(Ti)N resonators in the range of few thousands to couple of tens of thousands depending on the thickness of the film from 10 nm to 50 nm. We suspect presence of a high density of two-level systems on our substrate caused by the rough mechanical ion milling process we used for etching Nb(Ti)N is primarily responsible for low quality factors. We are optimizing etching of Nb(Ti)N with different thicknesses up to 150 nm using a more gentle reactive ion etching process that should ideally increase the quality factors by one order of magnitude [70, 71, 72]. The 150 nm thick resonators then can be immediately integrated with Sn-InSb nanowires in a hybrid transmon structure [74, 73, 75] or in the future to probe spinful Andreev bound states in these nanowire junctions [92, 93, 272]. Our current thin film Nb(Ti)N resonators sustain their quality factors in finite magnetic fields and exhibit a kinetic inductance boost of $2 - 80$ depending on the thickness and material of the superconductor, which makes them suitable for a fluxonium qubit that may act as the readout circuit for topological qubits [55, 210, 273].

Another semiconducting platform of interest are 2DEGs that allow for more flexible designs than nanowires due to their top-down lithography and gating [240]. Interest in hybrids of superconductors and 2DEGs has increased specifically since 2016 when an epitaxial contact between InAs 2DEG and Al was achieved [137]. We used this platform and the nanowire shadowing idea to study Josephson properties in junctions that are prepared by nanowire shadow masks residing on the surface of the 2DEG. This way we eliminated the chemical etching process that is generally needed to define mesas and junctions on 2DEGs. However, we could risk creating scattering from the nanowire in the quantum well, which can be solved by removing the nanowire after shadow creation. Our measurements, revealed highly transparent ballistic junctions in which products of critical and excess current with normal state resistance are comparable to theoretical values. We further performed diffraction pattern measurements, Shapiro step measurements and SQUID measurements. Diffraction pattern and interferometry measurements exhibit extra periodicity of supercurrent as the function of flux, while microwave measurements reveal half-integer Shapiro steps, all pointing at an unexpected behavior of supercurrent where the simple sinusoidal current phase relation did not fit the data. The origin of this anomaly is yet to be confirmed as we showed second

harmonic Josephson current and a non-uniform current density along the junction's width caused by fabrication artefacts both could result in same behavior of current as a function of flux. To get a better understanding of behavior of supercurrent we will need to study its gate dependence. The next generation of devices that we will be studying uses same shadow mask nanowires as self-aligned top gates on top of the junction. beams unless we are able to take advantage of large areas of superconducting ground plane on the chip.

Bibliography

[1]   A. Y. Kitaev. Unpaired Majorana fermions in quantum wires. *Physics-Uspekhi*, 44:131, 2001.

[2]   A. Y. Kitaev. Fault-tolerant quantum computation by anyons. *Annals of Physic*, 303:2, 2003.

[3]   C. Nayak, S. H. Simon, A. Stern, M. Freedman, and S. Das Sarma. Non-Abelian anyons and topological quantum computation. *Reviews of Modern Physics*, 80(3):1083, 2008.

[4]   R. M. Lutchyn, J. D. Sau, and S. Das Sarma. Majorana Fermions and a Topological Phase Transition in Semiconductor-Superconductor Heterostructures. *Phys. Rev. Lett.*, 105:077001, 2010.

[5]   Y. Oreg, G. Refael, and F. von Oppen. Helical Liquids and Majorana Bound States in Quantum Wires. *Phys. Rev. Lett.*, 105:177002, 2010.

[6]   J. Alicea, Y. Oreg, G. Refael, F. von Oppen, and M. P. A. Fisher. Non-Abelian statistics and topological quantum information processing in 1D wire networks. *Nat. Phys.*, 7:412, 2011.

[7]   J. Bardeen and W. H. Brattain. The Transistor, A Semi-Conductor Triode. *Phys. Rev.*, 74:230–231, Jul 1948.

[8]   M. A. Kastner. The single-electron transistor. *Rev. Mod. Phys.*, 64:849–858, Jul 1992.

[9]   D.P. DiVincenzo and D. Loss. Quantum information is physical. *Superlattices and Microstructures*, 23(3):419 – 432, (1998).

[10]   J. M. Elzerman, R. Hanson, L. H. Willems van Beveren, B. Witkamp, L. M. K. Vandersypen, and L. P. Kouwenhoven. Single-shot read-out of an individual electron spin in a quantum dot. *Nature*, 430(6998):431–435, Jul 2004.

[11]   J. R. Petta, A. C. Johnson, J. M. Taylor, E. A. Laird, A. Yacoby, M. D. Lukin, C. M. Marcus, M. P. Hanson, and A. C. Gossard. Coherent Manipulation of Coupled Electron Spins in Semiconductor Quantum Dots. *Science*, 309(5744):2180–2184, 2005.

[12] F. H. L. Koppens, C. Buizert, K. J. Tielrooij, I. T. Vink, K. C. Nowack, T. Meunier, L. P. Kouwenhoven, and L. M. K. Vandersypen. Driven coherent oscillations of a single electron spin in a quantum dot. *Nature*, 442(7104):766–771, Aug 2006.

[13] K. Ono, D.G. Austing, Y. Tokura, and S. Tarucha. Current Rectification by Pauli Exclusion in a Weakly Coupled Double Quantum Dot System. *Science*, 297(5585):1313–1317, (2002).

[14] A. Pfund, I. Shorubalko, K. Ensslin, and R. Leturcq. Suppression of Spin Relaxation in an InAs Nanowire Double Quantum Dot. *Phys. Rev. Lett.*, 99:036801, (2007).

[15] S. Nadj-Perge, S. M. Frolov, J. W. W. van Tilburg, J. Danon, Yu. V. Nazarov, R. Algra, E. P. A. M. Bakkers, and L. P. Kouwenhoven. Disentangling the effects of spin-orbit and hyperfine interactions on spin blockade. *Phys. Rev. B*, 81:201305, May 2010.

[16] K.C. Nowack, F.H.L. Koppens, Yu.V. Nazarov, and L.M.K. Vandersypen. Coherent Control of a Single Electron Spin with Electric Fields. *Science*, 318(5855):1430–1433, (2007).

[17] J. Bardeen, L. N. Cooper, and J. R. Schrieffer. Theory of Superconductivity. *Phys. Rev.*, 108:1175–1204, Dec 1957.

[18] B. D. Josephson. Possible new effects in superconductive tunnelling. *Physics Letters*, 1(7):251–253, July 1962.

[19] A. F. Andreev. Thermal conductivity of the intermediate state of superconductors. *Sov. Phys. JETP.*, 19, 1964.

[20] M. Tinkham. *Introduction to Superconductivity: Second Edition (Dover Books on Physics) (Vol i)*. Dover Publications, second edition edition, 2004.

[21] C. L. Huang and T. Van Duzer. Josephson tunneling through locally thinned silicon wafers. *Applied Physics Letters*, 25(12):753–756, 1974.

[22] T. Nishino, M. Miyake, Y. Harada, and U. Kawabe. Three-terminal superconducting device using a Si single-crystal film. *IEEE Electron Device Letters*, 6(6):297–299, 1985.

[23] H. Takayanagi and T. Kawakami. Superconducting Proximity Effect in the Native Inversion Layer on InAs. *Phys. Rev. Lett.*, 54:2449–2452, Jun 1985.

[24] A. Chrestin, T. Matsuyama, and U. Merkt. Evidence for a proximity-induced energy gap in Nb/InAs/Nb junctions. *Phys. Rev. B*, 55:8457–8465, Apr 1997.

[25] C. Nguyen, J. Werking, H. Kroemer, and E. L. Hu. InAs-AlSb quantum well as superconducting weak link with high critical current density. *Applied Physics Letters*, 57(1):87–89, 1990.

[26] H. Takayanagi, T. Akazaki, and J. Nitta. Observation of Maximum Supercurrent Quantization in a Superconducting Quantum Point Contact. *Phys. Rev. Lett.*, 75:3533–3536, Nov 1995.

[27] J. Kutchinsky, R. Taboryski, T. Clausen, C. B. Sørensen, A. Kristensen, P. E. Lindelof, J. Bindslev Hansen, C. Schelde Jacobsen, and J. L. Skov. Decay Lengths for Diffusive Transport Activated by Andreev Reflections in Al/n-GaAs/Al Superconductor-Semiconductor-Superconductor Junctions. *Phys. Rev. Lett.*, 78:931–934, Feb 1997.

[28] P. H. C. Magnée, S. G. den Hartog, B. J. van Wees, T. M. Klapwijk, W. van de Graaf, and G. Borghs. Influence of low energy Ar-sputtering on the electronic properties of InAs-based quantum well structures. *Applied Physics Letters*, 67(24):3569–3571, 1995.

[29] K. Neurohr, A. A. Golubov, Th. Klocke, J. Kaufmann, Th. Schäpers, J. Appenzeller, D. Uhlisch, A. V. Ustinov, M. Hollfelder, H. Lüth, and A. I. Braginski. Properties of lateral Nb contacts to a two-dimensional electron gas in an InGaAs/InP. *Phys. Rev. B*, 54:17018–17028, Dec 1996.

[30] R. Agarwal. Heterointerfaces in Semiconductor Nanowires. *Small*, 4(11):1872–1893, 2008.

[31] Y. Huang, X. Duan, Y. Cui, L. J. Lauhon, K. Kim, and C. M. Lieber. Logic Gates and Computation from Assembled Nanowire Building Blocks. *Science*, 294(5545):1313–1317, 2001.

[32] C. M. Lieber. Nanoscale science and technology: Building a big future from small things. *MRS Bulletin*, 28(7):486–491, 2003.

[33] Y.-J. Doh. Tunable Supercurrent Through Semiconductor Nanowires. *Science*, 309(5732):272–275, Jul 2005.

[34] J. A. van Dam, Y. V. Nazarov, E. P. A. M. Bakkers, S. De Franceschi, and L. P. Kouwenhoven. Supercurrent reversal in quantum dots. *Nature*, 442:667–670, 2006.

[35] P. Jarillo-Herrero, J. A. van Dam, and L. P. Kouwenhoven. Quantum supercurrent transistors in carbon nanotubes. *Nature*, 439:953–956, 2005.

[36] L. Hofstetter, S. Csonka, J. Nygård, and C. Schoenenberger. Cooper pair splitter realized in a two-quantum-dot Y-junction. *Nature*, 461:960–3, 10 2009.

[37] S. Franceschi, L. Kouwenhoven, C. Schoenenberger, and W. Wernsdorfer. Hybrid superconductor-quantum dot devices. *Nature nanotechnology*, 5:703–11, 10 2010.

[38] E. J. H. Lee, X. Jiang, R. Aguado, G. Katsaros, C.s M. Lieber, and S. De Franceschi. Zero-Bias Anomaly in a Nanowire Quantum Dot Coupled to Superconductors. *Phys. Rev. Lett.*, 109:186802, Oct 2012.

[39] J-D. Pillet, C. H. L. Quay, P. Morfin, C. Bena, A. Levy Yeyati, , and P. Joyez. Andreev bound states in supercurrent-carrying carbon nanotubes revealed. *Nature Phys.*, 6:965–969, 2010.

[40] R. S. Deacon, Y. Tanaka, A. Oiwa, R. Sakano, K. Yoshida, K. Shibata, K. Hirakawa, and S. Tarucha. Tunneling Spectroscopy of Andreev Energy Levels in a Quantum Dot Coupled to a Superconductor. *Phys. Rev. Lett.*, 104:076805, Feb 2010.

[41] T. Meng, S. Florens, and P. Simon. Self-consistent description of Andreev bound states in Josephson quantum dot devices. *Phys. Rev. B*, 79:224521, Jun 2009.

[42] W. Chang, V. E. Manucharyan, T. S. Jespersen, J. Nygård, and C. M. Marcus. Tunneling Spectroscopy of Quasiparticle Bound States in a Spinful Josephson Junction. *Phys. Rev. Lett.*, 110:217005, 2013.

[43] E. J. H. Lee, X. Jiang, M. Houzet, R. Aguado, C. M. Lieber, and S. De Franceschi. Spin-resolved Andreev levels and parity crossings in hybrid superconductor-semiconductor nanostructures. *Nature nanotechnology*, 9(1):79–84, 2014.

[44] D. Chevallier, P. Simon, and C. Bena. From Andreev bound states to Majorana fermions in topological wires on superconducting substrates: A story of mutation. *Phys. Rev. B*, 88:165401, Oct 2013.

[45] C. Liu, J. D. Sau, T. D. Stanescu, and S. Das Sarma. Andreev bound states versus Majorana bound states in quantum dot-nanowire-superconductor hybrid structures: Trivial versus topological zero-bias conductance peaks. *Phys. Rev. B*, 96:075161, Aug 2017.

[46] E. Majorana. Teoria simmetrica dell'elettrone e del positrone. *Il Nuovo Cimento*, 14(4):171, 1937.

[47] F. Wilczek. Majorana returns. *Nat Phys*, 5:614 – 618, 2009.

[48] L. Fu and C. L. Kane. Superconducting Proximity Effect and Majorana Fermions at the Surface of a Topological Insulator. *Phys. Rev. Lett.*, 100:096407, Mar 2008.

[49] G. E. Volovik. Fermion zero modes at the boundary of superfluid 3He-B. *JETP Letters*, 90(5):398–401, Nov 2009.

[50] J. D. Sau, R. M. Lutchyn, S. Tewari, and S. Das Sarma. Generic New Platform for Topological Quantum Computation Using Semiconductor Heterostructures. *Phys. Rev. Lett.*, 104:040502, Jan 2010.

[51] J. Alicea. Majorana fermions in a tunable semiconductor device. *Phys. Rev. B*, 81:125318, Mar 2010.

[52] C.W.J. Beenakker. Search for Majorana Fermions in Superconductors. *Annu. Rev. Cond. Mat. Phys.*, 4(1):113–136, 2013.

[53] M. H. Devoret, A. Wallraff, and J. M. Martinis. Superconducting Qubits: A Short Review. *ArXiv e-prints*, November 2004.

[54] J. Clarke and F. K. Wilhelm. Superconducting quantum bits. *Nature*, 453:1031–1042, 2008.

[55] D. Pekker, C.-Y. Hou, V. E. Manucharyan, and E. Demler. Proposal for Coherent Coupling of Majorana Zero Modes and Superconducting Qubits Using the 4π Josephson Effect. *Phys. Rev. Lett.*, 111:107007, Sep 2013.

[56] W. Lu, J. Xiang, B.P. Timko, Y. Wu, and C.M. Lieber. One-dimensional hole gas in germanium/silicon nanowire heterostructures. *Proc. Natl Acad. Sci. USA*, 102(29):10046–10051, (2005).

[57] F. Maier, J. Klinovaja, and D. Loss. Majorana fermions in Ge/Si hole nanowires. *Phys. Rev. B*, 90:195421, (2014).

[58] F. Maier, C. Kloeffel, and D. Loss. Tunable *g* factor and phonon-mediated hole spin relaxation in Ge/Si nanowire quantum dots. *Phys. Rev. B*, 87:161305, (2013).

[59] J. Fischer, W.A. Coish, D.V. Bulaev, and D. Loss. Spin decoherence of a heavy hole coupled to nuclear spins in a quantum dot. *Phys. Rev. B*, 78:155329, (2008).

[60] C. Kloeffel, M. Trif, and D. Loss. Strong spin-orbit interaction and helical hole states in Ge/Si nanowires. *Phys. Rev. B*, 84:195314, Nov 2011.

[61] X.J. Hao, T. Tu, G. Cao, C. Zhoe, H.O. Li, G.C. Guo, W.Y. Fung, Z. Ji, G.P. Guo, and W. Lu. Strong and Tunable Spin-Orbit Coupling of One-Dimentional Holes in Ge/Si Core/Shell Nanowires. *Nano Lett.*, 10:2956 – 2960, (2010).

[62] Y. Hu, F. Kuemmeth, C.M. Lieber, and C.M. Marcus. Hole spin relaxation in Ge-Si core-shell nanowire qubits. *Nature Nanotech.*, 7:47 – 50, (2012).

[63] A.P. Higginbotham, T.W. Larsen, J. Yao, H. Yan, C.M. Lieber, C.M. Marcus, and F. Kuemmeth. Hole Spin Coherence in a Ge/Si Heterostructure Nanowire. *Nano Lett.*, 14:3582 – 3586, (2014).

[64] A.P. Higginbotham, F. Kuemmeth, T.W. Larsen, M. Fitzpatrick, J. Yao, H. Yan, C.M. Lieber, and C.M. Marcus. Antilocalization of Coulomb Blockade in a Ge/Si Nanowire. *Phys. Rev. Lett.*, 112:216806, (2014).

[65] S. Gazibegovic, D. Car, H. Zhang, S. C. Balk, J. A. Logan, M. W. A. de Moor, M. C. Cassidy, R. Schmits, D. Xu, G. Wang, P. Krogstrup, R. L. M. Op het Veld, K. Zuo, Y. Vos, J. Shen, D. Bouman, B. Shojaei, D. Pennachio, J. S. Lee, P. J. van Veldhoven, S. Koelling, M. A. Verheijen, L. P. Kouwenhoven, C. J. Palmstrøm, and E. P. A. M. Bakkers. Epitaxy of advanced nanowire quantum devices. *Nature*, 548:434, 2013.

[66] R. L. M. Op het Veld, D. Xu, V. Schaller, M. A. Verheijen, S. M. E. Peters, J. Jung, C. Tong, Q. Wang, M. W. A. de Moor, B. Hesselmann, K. Vermeulen, J. D. S. Bommer, J. S. Lee, A. Sarikov, M. Pendharkar, A. Marzegalli, S. Koelling, L. P. Kouwenhoven, L. Miglio, C. J. Palmstrøm, H. Zhang, and E. P. A. M. Bakkers. In-plane selective area InSb–Al nanowire quantum networks. *Communications Physics*, 3, 2020.

[67] V. Mourik, K. Zuo, S.M. Frolov, S.R. Plissard, E.P.A.M. Bakkers, and L.P. Kouwenhoven. Signatures of Majorana Fermions in Hybrid Superconductor-Semiconductor Nanowire Devices. *Science*, 336(6084):1003–1007, (2012).

[68] J. Chen, P. Yu, J. Stenger, M. Hocevar, D. Car, S. R. Plissard, E. P. A. M. Bakkers, T. D. Stanescu, and S. M. Frolov. Experimental phase diagram of zero-bias conductance peaks in superconductor/semiconductor nanowire devices. *Science Advances*, 3(9), 2017.

[69] F. Arute, K. Arya, R. Babbush, D. Bacon, J. C. Bardin, R. Barends, R. Biswas, S. Boixo, F. G. S. L. Brandao, D. A. Buell, et al. Quantum supremacy using a programmable superconducting processor. *Nature*, 574(7779):505–510, October 2019.

[70] A. Bruno, G. de Lange, S. Asaad, K. L. van der Enden, N. K. Langford, and L. DiCarlo. Reducing intrinsic loss in superconducting resonators by surface treatment and deep etching of silicon substrates. *Applied Physics Letters*, 106(18):182601, May 2015.

[71] N. Samkharadze, A. Bruno, P. Scarlino, G. Zheng, D. P. DiVincenzo, L. DiCarlo, and L. M. K. Vandersypen. High-Kinetic-Inductance Superconducting Nanowire Resonators for Circuit QED in a Magnetic Field. *Phys. Rev. Applied*, 5:044004, Apr 2016.

[72] J.G. Kroll, F. Borsoi, K.L. van der Enden, W. Uilhoorn, D. de Jong, M. Quintero-Pérez, D.J. van Woerkom, A. Bruno, S.R. Plissard, D. Car, E.P.A.M. Bakkers, M.C. Cassidy, and L.P. Kouwenhoven. Magnetic-Field-Resilient Superconducting Coplanar-Waveguide Resonators for Hybrid Circuit Quantum Electrodynamics Experiments. *Phys. Rev. Applied*, 11:064053, Jun 2019.

[73] T. W. Larsen, K. D. Petersson, F. Kuemmeth, T. S. Jespersen, P. Krogstrup, J. Nygård, and C. M. Marcus. Semiconductor-Nanowire-Based Superconducting Qubit. *Phys. Rev. Lett.*, 115:127001, Sep 2015.

[74] G. de Lange, B. van Heck, A. Bruno, D. J. van Woerkom, A. Geresdi, S. R. Plissard, E. P. A. M. Bakkers, A. R. Akhmerov, and L. DiCarlo. Realization of Microwave Quantum Circuits Using Hybrid Superconducting-Semiconducting Nanowire Josephson Elements. *Phys. Rev. Lett.*, 115:127002, Sep 2015.

[75] F. Luthi, T. Stavenga, O. W. Enzing, A. Bruno, C. Dickel, N. K. Langford, M. A. Rol, T. S. Jespersen, J. Nygård, P. Krogstrup, and L. DiCarlo. Evolution of Nanowire Transmon Qubits and Their Coherence in a Magnetic Field. *Phys. Rev. Lett.*, 120:100502, Mar 2018.

[76]   T. W. Larsen, M. E. Gershenson, L. Casparis, A. Kringhøj, N. J. Pearson, R. P. G. McNeil, F. Kuemmeth, P. Krogstrup, K. D. Petersson, and C. M. Marcus. A Parity-Protected Superconductor-Semiconductor Qubit. *arXiv:2004.03975*, 2020.

[77]   T. Ihn. *Semiconductor Nanostructures: Quantum states and electronic transport.* Oxford University Press, 2010.

[78]   N.W. Ashcroft and N.D. Mermin. *Solid State Physics.* HRW international editions. Holt, Rinehart and Winston, 1976.

[79]   G. Dresselhaus. Spin-Orbit Coupling Effects in Zinc Blende Structures. *Phys. Rev.*, 100:580–586, Oct 1955.

[80]   Yu. A. Bychkov and É. I. Rashba. Properties of a 2D electron gas with lifted spectral degeneracy. *Soviet Journal of Experimental and Theoretical Physics Letters*, 39:78, January 1984.

[81]   R. Hanson, L.P. Kouwenhoven, J.R. Petta, S. Tarucha, and L.M.K. Vandersypen. Spins in few-electron quantum dots. *Rev. Mod. Phys.*, 79:1217–1265, (2007).

[82]   R. Hanson, L. H. Willems van Beveren, I. T. Vink, J. M. Elzerman, W. J. M. Naber, F. H. L. Koppens, L. P. Kouwenhoven, and L. M. K. Vandersypen. Single-Shot Readout of Electron Spin States in a Quantum Dot Using Spin-Dependent Tunnel Rates. *Phys. Rev. Lett.*, 94:196802, May 2005.

[83]   Y. V. Nazarov and B. M. Yaroslav. *Quantum transport: introduction to nanoscience.* Cambridge Univ. Press, Cambridge, 2009.

[84]   G. E. Blonder, M. Tinkham, and T. M. Klapwijk. Transition from metallic to tunneling regimes in superconducting microconstrictions: Excess current, charge imbalance, and supercurrent conversion. *Physical Review B*, 25(7):4515, 1982.

[85]   M. Octavio, M. Tinkham, G. E. Blonder, and T. M. Klapwijk. Subharmonic energy-gap structure in superconducting constrictions. *Phys. Rev. B*, 27:6739–6746, 1983.

[86]   I. Sochnikov, L. Maier, C. A. Watson, J. R. Kirtley, C. Gould, G. Tkachov, E. M. Hankiewicz, C. Brüne, H. Buhmann, L. W. Molenkamp, and K. A. Moler. Nonsinusoidal Current-Phase Relationship in Josephson Junctions from the 3D Topological Insulator HgTe. *Phys. Rev. Lett.*, 114:066801, Feb 2015.

[87] C. D. English, D. R. Hamilton, C. Chialvo, I. C. Moraru, N. Mason, and D. J. Van Harlingen. Observation of nonsinusoidal current-phase relation in graphene Josephson junctions. *Phys. Rev. B*, 94:115435, Sep 2016.

[88] E. M. Spanton, M. Deng, S. Vaitiekėnas, P. Krogstrup, J. Nygård, C. M. Marcus, and K. A. Moler. Current–phase relations of few-mode InAs nanowire Josephson junctions. *Nature Physics*, 13(12):1177–1181, Aug 2017.

[89] I. O. Kulik. Macroscopic Quantization and the Proximity Effect in S-N-S Junctions. *Soviet Journal of Experimental and Theoretical Physics*, 30:944, January 1969.

[90] C. W. J. Beenakker and H. van Houten. Josephson current through a superconducting quantum point contact shorter than the coherence length. *Phys. Rev. Lett.*, 66:3056–3059, Jun 1991.

[91] D. J. van Woerkom, A. Proutski, B. van Heck, D. Bouman, J. I. Väyrynen, L. I. Glazman, P. Krogstrup, J. Nygård, L. P. Kouwenhoven, and A. Geresdi. Microwave spectroscopy of spinful Andreev bound states in ballistic semiconductor Josephson junctions. *Nature Physics*, 13(9):876–881, September 2017.

[92] M. Hays, G. de Lange, K. Serniak, D. J. van Woerkom, D. Bouman, P. Krogstrup, J. Nygård, A. Geresdi, and M. H. Devoret. Direct Microwave Measurement of Andreev-Bound-State Dynamics in a Semiconductor-Nanowire Josephson Junction. *Phys. Rev. Lett.*, 121:047001, Jul 2018.

[93] L. Tosi, C. Metzger, M. F. Goffman, C. Urbina, H. Pothier, Sunghun Park, A. Levy Yeyati, J. Nygård, and P. Krogstrup. Spin-Orbit Splitting of Andreev States Revealed by Microwave Spectroscopy. *Phys. Rev. X*, 9:011010, Jan 2019.

[94] M. T. Tuominen, J. M. Hergenrother, T. S. Tighe, and M. Tinkham. Even-odd electron number effects in a small superconducting island: Magnetic-field dependence. *Phys. Rev. B*, 47:11599–11602, May 1993.

[95] D. V. Averin and Yu. V. Nazarov. Single-electron charging of a superconducting island. *Phys. Rev. Lett.*, 69:1993–1996, Sep 1992.

[96] G. Allison, A. Oiwa, S. Kumar, D. DiVincenzo, M. Ketchen, K. Hirakawa, H. Takayanagi, and S. Tarucha. A superconducting resonator designed for coupling to spin based qubits in quantum dots. *Journal of Physics: Conference Series*, 245:012024, sep 2010.

[97] Y. Kubo, C. Grezes, A. Dewes, T. Umeda, J. Isoya, H. Sumiya, N. Morishita, H. Abe, S. Onoda, T. Ohshima, V. Jacques, A. Dréau, J.-F. Roch, I. Diniz, A. Auffeves, D. Vion, D. Esteve, and P. Bertet. Hybrid Quantum Circuit with a Superconducting Qubit Coupled to a Spin Ensemble. *Phys. Rev. Lett.*, 107:220501, Nov 2011.

[98] K. D. Petersson, L. W. McFaul, M. D. Schroer, M. Jung, J. M. Taylor, A. A. Houck, and J. R. Petta. Circuit quantum electrodynamics with a spin qubit. *Nature*, 490:380–383, 2012.

[99] Y.-Y. Liu, J. Stehlik, C. Eichler, M. J. Gullans, J. M. Taylor, and J. R. Petta. Semiconductor double quantum dot micromaser. *Science*, 347(6219):285–287, 2015.

[100] L. Casparis, M. R. Connolly, M. Kjaergaard, N. J. Pearson, A. Kringhøj, T. W. Larsen, F. Kuemmeth, T. Wang, C. Thomas, S. Gronin, and et al. Superconducting gatemon qubit based on a proximitized two-dimensional electron gas. *Nature Nanotechnology*, 13(10):915–919, Jul 2018.

[101] P. Scarlino, D. J. van Woerkom, U. C. Mendes, J. V. Koski, A. J. Landig, C. K. Andersen, S. Gasparinetti, C. Reichl, W. Wegscheider, K. Ensslin, and et al. Coherent microwave-photon-mediated coupling between a semiconductor and a superconducting qubit. *Nature Communications*, 10(1), Jul 2019.

[102] G. Burkard, M. J. Gullans, X. Mi, and J. R. Petta. Superconductor–semiconductor hybrid-circuit quantum electrodynamics. *Nature Reviews Physics*, 2(3):129–140, Jan 2020.

[103] E. T. Jaynes and F. W. Cummings. Comparison of quantum and semiclassical radiation theories with application to the beam maser. *Proceedings of the IEEE*, 51(1):89–109, 1963.

[104] A. Blais, R. Huang, A. Wallraff, S. M. Girvin, and R. J. Schoelkopf. Cavity quantum electrodynamics for superconducting electrical circuits: An architecture for quantum computation. *Phys. Rev. A*, 69:062320, Jun 2004.

[105] D.M. Pozar. *Microwave Engineering*. Addison-Wesley series in electrical and computer engineering. Addison-Wesley, 1990.

[106] L. Frunzio, A. Wallraff, D. Schuster, J. Majer, and R. Schoelkopf. Fabrication and characterization of superconducting circuit QED devices for quantum computation. *IEEE Transactions on Applied Superconductivity*, 15(2):860–863, 2005.

[107] M. Trif, V. N. Golovach, and D. Loss. Spin dynamics in InAs nanowire quantum dots coupled to a transmission line. *Phys. Rev. B*, 77:045434, Jan 2008.

[108] L. DiCarlo, J. M. Chow, J. M. Gambetta, Lev S. Bishop, B. R. Johnson, D. I. Schuster, J. Majer, A. Blais, L. Frunzio, S. M. Girvin, and et al. Demonstration of two-qubit algorithms with a superconducting quantum processor. *Nature*, 460(7252):240–244, Jun 2009.

[109] L. Casparis, T. W. Larsen, M. S. Olsen, F. Kuemmeth, P. Krogstrup, J. Nygård, K. D. Petersson, and C. M. Marcus. Gatemon Benchmarking and Two-Qubit Operations. *Phys. Rev. Lett.*, 116:150505, Apr 2016.

[110] D. J. van Woerkom, P. Scarlino, J. H. Ungerer, C. Müller, J. V. Koski, A. J. Landig, C. Reichl, W. Wegscheider, T. Ihn, K. Ensslin, and A. Wallraff. Microwave Photon-Mediated Interactions between Semiconductor Qubits. *Phys. Rev. X*, 8:041018, Oct 2018.

[111] F. Borjans, X. G. Croot, X. Mi, M. J. Gullans, and J. R. Petta. Resonant microwave-mediated interactions between distant electron spins. *Nature*, 577(7789):195–198, Dec 2019.

[112] J. Gao, M. Daal, A. Vayonakis, S. Kumar, J. Zmuidzinas, B. Sadoulet, B. A. Mazin, P. K. Day, and H. G. Leduc. Experimental evidence for a surface distribution of two-level systems in superconducting lithographed microwave resonators. *Applied Physics Letters*, 92(15):152505, Apr 2008.

[113] R. Barends, N. Vercruyssen, A. Endo, P. J. de Visser, T. Zijlstra, T. M. Klapwijk, P. Diener, S. J. C. Yates, and J. J. A. Baselmans. Minimal resonator loss for circuit quantum electrodynamics. *Applied Physics Letters*, 97(2):023508, Jul 2010.

[114] K. Watanabe, K. Yoshida, T. Aoki, and S. Kohjiro. Kinetic Inductance of Superconducting Coplanar Waveguides. *Japanese Journal of Applied Physics*, 33(Part 1, No. 10):5708–5712, oct 1994.

[115] K. Geerlings. *Improving Coherence of Superconducting Qubits and Resonators*. PhD thesis, Yale University, 2013.

[116] M. S. Khalil, M. J. A. Stoutimore, F. C. Wellstood, and K. D. Osborn. An analysis method for asymmetric resonator transmission applied to superconducting devices. *Journal of Applied Physics*, 111(5):054510, Mar 2012.

[117] M. H. Devoret and R. J. Schoelkopf. Superconducting Circuits for Quantum Information: An Outlook. *Science*, 339(6124):1169–1174, 2013.

[118] M. Kjaergaard, M. E. Schwartz, J. Braumüller, P. Krantz, J. I.-J. Wang, S. Gustavsson, and W. D. Oliver. Superconducting Qubits: Current State of Play. *Annual Review of Condensed Matter Physics*, 11(1):369–395, Mar 2020.

[119] Y. Nakamura, Yu. A. Pashkin, and J. S. Tsai. Coherent control of macroscopic quantum states in a single-Cooper-pair box. *Nature*, 398(6730):786–788, Apr 1999.

[120] J. Koch, T. M. Yu, J. Gambetta, A. A. Houck, D. I. Schuster, J. Majer, A. Blais, M. H. Devoret, S. M. Girvin, and R. J. Schoelkopf. Charge-insensitive qubit design derived from the Cooper pair box. *Phys. Rev. A*, 76:042319, Oct 2007.

[121] P. Joyez, P. Lafarge, A. Filipe, D. Esteve, and M. H. Devoret. Observation of parity-induced suppression of Josephson tunneling in the superconducting single electron transistor. *Phys. Rev. Lett.*, 72:2458–2461, Apr 1994.

[122] F. Hassler, A. R. Akhmerov, and C. W. J. Beenakker. The top-transmon: a hybrid superconducting qubit for parity-protected quantum computation. *New Journal of Physics*, 13(9):095004, sep 2011.

[123] R. M. Lutchyn, E. P. A. M. Bakkers, L. P. Kouwenhoven, P. Krogstrup, C. M. Marcus, and Y. Oreg. Majorana zero modes in superconductor–semiconductor heterostructures. *Nature Reviews Materials*, 3(5):52–68, May 2018.

[124] V. E. Manucharyan, J. Koch, L. I. Glazman, and M. H. Devoret. Fluxonium: Single Cooper-Pair Circuit Free of Charge Offsets. *Science*, 326(5949):113–116, 2009.

[125] M. T. Bell, I. A. Sadovskyy, L. B. Ioffe, A. Yu. Kitaev, and M. E. Gershenson. Quantum Superinductor with Tunable Nonlinearity. *Phys. Rev. Lett.*, 109:137003, Sep 2012.

[126] L. B. Nguyen, Y. Lin, A. Somoroff, R. Mencia, N. Grabon, and V. E. Manucharyan. High-Coherence Fluxonium Qubit. *Phys. Rev. X*, 9:041041, Nov 2019.

[127] T. M. Hazard, A. Gyenis, A. Di Paolo, A. T. Asfaw, S. A. Lyon, A. Blais, and A. A. Houck. Nanowire Superinductance Fluxonium Qubit. *Phys. Rev. Lett.*, 122:010504, Jan 2019.

[128] D. Niepce, J. Burnett, and J. Bylander. High Kinetic Inductance NbN Nanowire Superinductors. *Physical Review Applied*, 11(4), Apr 2019.

[129] S. A. Dayeh, W. Tang, F. Boioli, K. L. Kavanagh, H. Zheng, J. Wang, N. H. Mack, G. Swadener, J. Y. Huang, L. Miglio, K. Tu, and S. T. Picraux. Direct Measurement of Coherency Limits for Strain Relaxation in Heteroepitaxial Core/Shell Nanowires. *Nano Letters*, 13(5):1869–1876, 2013.

[130] B.-M. Nguyen, Y. Taur, S. T. Picraux, and S. A. Dayeh. Diameter-Independent Hole Mobility in Ge/Si Core/Shell Nanowire Field Effect Transistors. *Nano Letters*, 14(2):585–591, 2014.

[131] S. R. Plissard, D. R. Slapak, M. A. Verheijen, M. Hocevar, G. W. G. Immink, I. van Weperen, S. Nadj-Perge, S. M. Frolov, L. P. Kouwenhoven, and E. P. A. M. Bakkers. From InSb Nanowires to Nanocubes: Looking for the Sweet Spot. *Nano Letters*, 12(4):1794–1798, 2012.

[132] S. Gazibegovic, G. Badawy, T. L. J. Buckers, P. Leubner, J. Shen, F. K. de Vries, S. Koelling, L. P. Kouwenhoven, M. A. Verheijen, and E. P. A. M. Bakkers. Bottom-Up Grown 2D InSb Nanostructures. *Advanced Materials*, 31(14):1808181, 2019.

[133] G. Badawy, S. Gazibegovic, F. Borsoi, S. Heedt, C. Wang, S. Koelling, M. A. Verheijen, L. P. Kouwenhoven, and E. P. A. M. Bakkers. High Mobility Stemless InSb Nanowires. *Nano Lett.*, 19(6):3575–3582, June 2019.

[134] M. Pendharkar, B. Zhang, H. Wu, A. Zarassi, P. Zhang, C. P. Dempsey, J. S. Lee, S. D. Harrington, G. Badawy, S. Gazibegovic, J. Jung, A. H. Chen, M. A. Verheijen, M. Hocevar, E. P. A. M. Bakkers, C. J. Palmstrøm, and S. M. Frolov. Parity-preserving and magnetic field resilient superconductivity in indium antimonide nanowires with tin shells. *arXiv:1912.06071*, 2019.

[135] H. A. Nilsson, P. Caroff, C. Thelander, M. Larsson, J. B. Wagner, L. Wernersson, L. Samuelson, and H. Q. Xu. Giant, Level-Dependent g Factors in InSb Nanowire Quantum Dots. *Nano Lett.*, 9(9):3151–3156, September 2009.

[136] J. D. Sau, S. Tewari, R. M. Lutchyn, T. D. Stanescu, and S. Das Sarma. Non-Abelian quantum order in spin-orbit-coupled semiconductors: Search for topological Majorana particles in solid-state systems. *Phys. Rev. B*, 82:214509, Dec 2010.

[137] J. Shabani, M. Kjaergaard, H. J. Suominen, Y. Kim, F. Nichele, K. Pakrouski, T. Stankevic, R. M. Lutchyn, P. Krogstrup, R. Feidenhans'l, S. Kraemer, C. Nayak, M. Troyer, C. M. Marcus, and C. J. Palmstrøm. Two-dimensional epitaxial superconductor-semiconductor heterostructures: A platform for topological superconducting networks. *Phys. Rev. B*, 93:155402, Apr 2016.

[138] M. Kjaergaard. *PROXIMITY INDUCED SUPERCONDUCTING PROPERTIES IN ONE AND TWO DIMENSIONAL SEMICONDUCTORS.* PhD thesis, Copenhagen University, 2015.

[139] Z. Su. *ANDREEV BOUND STATES IN SUPERCONDUCTOR-QUANTUM DOT CHAINS.* PhD thesis, University of Pittsburgh, 2017.

[140] Z. Su, A. Zarassi, B.M. Nguyen, J. Yoo, S.A. Dayeh, and S.M. Frolov. High critical magnetic field superconducting contacts to Ge/Si core/shell nanowires. *ArXiv e-prints:1610.03010*, (2016).

[141] J. Hölzl, F. K. Schulte, and H. Wagner. *Solid Surface Physics.* Springer Berlin Heidelberg, 1979.

[142] W. M. Haynes and D. R. Lide. *CRC Handbook of Chemistry and Physics : A Ready-reference Book of Chemical and Physical Data.* CRC, 2011.

[143] C. Henkel, S. Abermann, O. Bethge, P. Klang, and E. Bertagnolli. Impact of sputter deposited TaN and TiN metal gates on ZrO2/Ge and ZrO2/Si high-k dielectric gate stacks. In *2009 10th International Conference on Ultimate Integration of Silicon*, pages 197–200, 2009.

[144] W. Lu, Y. Dai, F. Wang, and B. Jin. Impact of native defects and impurities in HfO2 and Si3N4 on charge trapping memory devices: A first principle hybrid functional study. *phys. Status Solidi (b)*, 2016.

[145] J. S. Lee, B. Shojaei, M. Pendharkar, A. P. McFadden, Y. Kim, H. J. Suominen, M. Kjaergaard, F. Nichele, H. Zhang, C. M. Marcus, and C. J. Palmstrøm. Transport Studies of Epi-Al/InAs Two-Dimensional Electron Gas Systems for Required Building-Blocks in Topological Superconductor Networks. *Nano Letters*, 19(5):3083–3090, 2019.

[146] M. Kjaergaard, H.J. Suominen, M.P. Nowak, A.R. Akhmerov, J. Shabani, C.J. Palmstrøm, F. Nichele, and C.M. Marcus. Transparent Semiconductor-Superconductor In-

176

terface and Induced Gap in an Epitaxial Heterostructure Josephson Junction. *Physical Review Applied*, 7(3), Mar 2017.

[147] W. Mayer, J. Yuan, K. S. Wickramasinghe, T. Nguyen, M. C. Dartiailh, and J. Shabani. Superconducting proximity effect in epitaxial Al-InAs heterostructures. *Applied Physics Letters*, 114(10):103104, 2019.

[148] A. Zarassi, Z. Su, J. Danon, J. Schwenderling, M. Hocevar, B. M. Nguyen, J. Yoo, S. A. Dayeh, and S. M. Frolov. Magnetic field evolution of spin blockade in Ge/Si nanowire double quantum dots. *Phys. Rev. B*, 95:155416, Apr 2017.

[149] A. Das, Y. Ronen, Y. Most, Y. Oreg, M. Heiblum, and H. Shtrikman. Zero-bias peaks and splitting in an Al-InAs nanowire topological superconductor as a signature of Majorana fermions. *Nature Physics*, 8(12):887–895, 2012.

[150] M. Deng, C. L. Yu, G. Y. Huang, M.s Larsson, P. Caroff, and H. Xu. Anomalous zero-bias conductance peak in a Nb–InSb nanowire–Nb hybrid device. *Nano letters*, 12(12):6414–6419, 2012.

[151] S. M. Albrecht, A. P. Higginbotham, M. Madsen, F. Kuemmeth, T. S. Jespersen, J. Nygård, P. Krogstrup, and C. M. Marcus. Exponential protection of zero modes in Majorana islands. *Nature*, 531:206–209, 2016.

[152] Ö. Gül, H. Zhang, J. D. S. Bommer, M. W. A. de Moor, D. Car, S. R. Plissard, E. P. A. M. Bakkers, A. Geresdi, K. Watanabe, T. Taniguchi, et al. Ballistic Majorana nanowire devices. *Nature nanotechnology*, 13:192, 2018.

[153] M. T. Deng, S. Vaitiekenas, E. B. Hansen, J. Danon, M. Leijnse, K. Flensberg, J. Nygård, P. Krogstrup, and C. M. Marcus. Majorana bound state in a coupled quantum-dot hybrid-nanowire system. *Science*, 354(6319):1557–1562, 2016.

[154] J. Klinovaja and D. Loss. Composite Majorana fermion wave functions in nanowires. *Phys. Rev. B*, 86:085408, 2012.

[155] D. Kotekar-Patil, B. M. Nguyen, J. Yoo, S. A. Dayeh, and S. M. Frolov. Quasi-ballistic quantum transport through Ge/Si core/shell nanowires. *Nanotechnology*, 28(38):385204, Sep 2017.

[156] M. Brauns, J. Ridderbos, A. Li, E. P. A. M. Bakkers, and F. A. Zwanenburg. Electric-field dependent g-factor anisotropy in Ge-Si core-shell nanowire quantum dots. *Phys. Rev. B*, 93:121408, 2016.

[157] J. Xiang, A. Vidan, M. Tinkham, R. M. Westervelt, and C. M. Lieber. Ge/Si nanowire mesoscopic Josephson junctions. *Nat Nano*, 1:208–213, 2006.

[158] S. A. Dayeh, A. V. Gin, and S. T. Picraux. Advanced core/multishell germa-nium/silicon nanowire heterostructures: Morphology and transport. *Appl. Phys. Lett.*, 98(16), 2011.

[159] S. A. Dayeh, N. H. Mack, J. Y. Huang, and S. T. Picraux. Advanced core/multishell germanium/silicon nanowire heterostructures: The Au-diffusion bottleneck. *Appl. Phys. Lett.*, 99(2), 2011.

[160] K. Flensberg, J. B. Hansen, and M. Octavio. Subharmonic energy-gap structure in superconducting weak links. *Phys. Rev. B*, 38:8707–8711, 1988.

[161] S. Abay, D. Persson, H. Nilsson, F. Wu, H. Q. Xu, M. Fogelström, V. Shumeiko, and P. Delsing. Charge transport in InAs nanowire Josephson junctions. *Phys. Rev. B*, 89:214508, 2014.

[162] D. Averin and A. Bardas. ac Josephson Effect in a Single Quantum Channel. *Phys. Rev. Lett.*, 75:1831–1834, 1995.

[163] J. C. Cuevas, A. Martín-Rodero, and A. L. Yeyati. Hamiltonian approach to the trans-port properties of superconducting quantum point contacts. *Phys. Rev. B*, 54:7366–7379, 1996.

[164] K. Grove-Rasmussen, H. I. Jørgensen, B. M. Andersen, J. Paaske, T. S. Jespersen, J. Nygård, K. Flensberg, and P. E. Lindelof. Superconductivity-enhanced bias spec-troscopy in carbon nanotube quantum dots. *Phys. Rev. B*, 79:134518, Apr 2009.

[165] S. Takei, B. M. Fregoso, H. Hui, A. M. Lobos, and S. Das Sarma. Soft Superconducting Gap in Semiconductor Majorana Nanowires. *Phys. Rev. Lett.*, 110:186803, 2013.

[166] T. D. Stanescu, R. M. Lutchyn, and S. Das Sarma. Soft superconducting gap in semiconductor-based Majorana nanowires. *Phys. Rev. B*, 90:085302, 2014.

[167] W. Chang, S. M. Albrecht, T. S. Jespersen, F. Kuemmeth, P. Krogstrup, J Nygård, and C. M. Marcus. Hard gap in epitaxial semiconductor–superconductor nanowires. *Nat Nano*, 10:232–236, 2015.

[168] F.H.L. Koppens, J.A. Folk, J.M. Elzerman, R. Hanson, L.H. Willems van Beveren, I.T. Vink, H.P. Tranitz, W. Wegscheider, L.P. Kouwenhoven, and L.M.K. Vandersypen. Control and Detection of Singlet-Triplet Mixing in a Random Nuclear Field. *Science*, 309(5739):1346–1350, (2005).

[169] A.C. Johnson, J.R. Petta, J.M. Taylor, A. Yacoby, M.D. Lukin, C.M. Marcus, M.P. Hanson, and A.C. Gossard. Triplet-singlet spin relaxation via nuclei in a double quantum dot. *Nature*, 435:925 – 928, (2005).

[170] A. Pfund, I. Shorubalko, K. Ensslin, and R. Leturcq. Spin-state mixing in InAs double quantum dots. *Phys. Rev. B*, 76:161308, (2007).

[171] Y. Hu, H.O.H. Churchill, D.J. Reilly, J. Xiang, C.M. Lieber, and C.M. Marcus. A Ge/Si heterostructure nanowire-based double quantum dot with integrated charge sensor. *Nature Nanotech.*, 2:622 – 625, (2005).

[172] F. Pei, E.A. Laird, G.A. Steele, and L.P. Kouwenhoven. Valley-spin blockade and spin resonance in carbon nanotubes. *Nature Nanotech.*, 7:630 – 634, (2012).

[173] S. Nadj-Perge, S.M. Frolov, E.P.A.M. Bakkers, and L.P. Kouwenhoven. Spin-orbit qubit in a semiconductor nanowire. *Nature*, 468:1084 – 1087, (2010).

[174] J. Danon and Yu.V. Nazarov. Pauli spin blockade in the presence of strong spin-orbit coupling. *Phys. Rev. B*, 80:041301, (2009).

[175] S. Roddaro, A. Fuhrer, P. Brusheim, C. Fasth, H.Q. Xu, L. Samuelson, J. Xiang, and C.M. Lieber. Spin States of Holes in Ge/Si Nanowire Quantum Dots. *Phys. Rev. Lett.*, 101:186802, (2008).

[176] K. Flöhr, M. Liebmann, K. Sladek, H. Y. Günel, R. Frielinghaus, F. Haas, C. Meyer, H. Hardtdegen, T. Schäpers, D. Grützmacher, and M. Morgenstern. Manipulating InAs nanowires with submicrometer precision. *Review of Scientific Instruments*, 82(11):113705, (2011).

[177] S. Nadj-Perge, V. S. Pribiag, J. W. G. van den Berg, K. Zuo, S. R. Plissard, E. P. A. M. Bakkers, S. M. Frolov, and L. P. Kouwenhoven. Spectroscopy of Spin-Orbit

Quantum Bits in Indium Antimonide Nanowires. *Phys. Rev. Lett.*, 108:166801, Apr 2012.

[178] A. C. Johnson, J. R. Petta, C. M. Marcus, M. P. Hanson, and A. C. Gossard. Singlet-triplet spin blockade and charge sensing in a few-electron double quantum dot. *Phys. Rev. B*, 72:165308, Oct (2005).

[179] H. W. Liu, T. Fujisawa, Y. Ono, H. Inokawa, A. Fujiwara, K. Takashina, and Y. Hirayama. Pauli-spin-blockade transport through a silicon double quantum dot. *Phys. Rev. B*, 77:073310, Feb (2008).

[180] N. Shaji, C. B. Simmons, M. Thalakulam, L. J. Klein, H. Qin, H. Luo, D. E. Savage, M. G. Lagally, A. J. Rimberg, R. Joynt, M. Friesen, R. H. Blick, S. N. Coppersmith, and M. A. Eriksson. Spin blockade and lifetime-enhanced transport in a few-electron Si/SiGe double quantum dot. *Nat Phys*, 4:540 – 544, (2008).

[181] H. O. H. Churchill, A. J. Bestwick, J. W. Harlow, F. Kuemmeth, D. Marcos, C. H. Stwertka, S. K. Watson, and C. M. Marcus. Electron-nuclear interaction in 13C nanotube double quantum dots. *Nat Phys*, 5:321 – 326, (2009).

[182] G. Yamahata, T. Kodera, H.O.H. Churchill, K. Uchida, C.M. Marcus, and S. Oda. Magnetic field dependence of Pauli spin blockade: A window into the sources of spin relaxation in silicon quantum dots. *Phys. Rev. B*, 86:115322, (2012).

[183] R. Li, F.E. Hudson, A.S. Dzurak, and A.R. Hamilton. Pauli Spin Blockade of Heavy Holes in a Silicon Double Quantum Dot. *Nano Lett.*, 15:7314 – 7318, (2015).

[184] H. Bohuslavskyi, D. Kotekar-Patil, R. Maurand, A. Corna, S. Barraud, L. Bourdet, L. Hutin, Y.-M. Niquet, X. Jehl, S. De Franceschi, and et al. Pauli blockade in a few-hole PMOS double quantum dot limited by spin-orbit interaction. *Applied Physics Letters*, 109(19):193101, Nov 2016.

[185] O.N. Jouravlev and Yu.V. Nazarov. Electron Transport in a Double Quantum Dot Governed by a Nuclear Magnetic Field. *Phys. Rev. Lett.*, 96:176804, (2006).

[186] W.A. Coish and F. Qassemi. Leakage-current line shapes from inelastic cotunneling in the Pauli spin blockade regime. *Phys. Rev. B*, 84:245407, (2011).

[187] W.J. Childs and L.S. Goodman. Hyperfine Structure of Ge^{73} in the $^3P_1$ and $^3P_2$ Atomic States and the Nuclear Magnetic Dipole Moment of Ge^{71}. *Phys. Rev.*, 141:15–21, (1966).

[188] B. Voisin, R. Maurand, S. Barraud, M. Vinet, X. Jehl, M. Sanquer, J. Renard, and S. De Franceschi. Electrical Control of g-Factor in a Few-Hole Silicon Nanowire MOSFET. *Nano Lett.*, 16:88 – 92, (2016).

[189] Z. Su, A. Zarassi, J.-F. Hsu, P. San-Jose, E. Prada, R. Aguado, E. J. H. Lee, S. Gazibegovic, R. L. M. Op het Veld, D. Car, S. R. Plissard, M. Hocevar, M. Pendharkar, J. S. Lee, J. A. Logan, C. J. Palmstrøm, E. P. A. M. Bakkers, and S. M. Frolov. Mirage Andreev Spectra Generated by Mesoscopic Leads in Nanowire Quantum Dots. *Phys. Rev. Lett.*, 121:127705, Sep 2018.

[190] J. Alicea. New directions in the pursuit of Majorana fermions in solid state systems. *Rep. Prog. Phys.*, 75(7):076501, 2012.

[191] S. R. Elliott and M. Franz. *Colloquium* : Majorana fermions in nuclear, particle, and solid-state physics. *Rev. Mod. Phys.*, 87:137–163, 2015.

[192] R. Aguado. Majorana quasiparticles in condensed matter. *La Rivista del Nuovo Cimento*, 40:523, 2017.

[193] T. Sand-Jespersen, J. Paaske, B. M. Andersen, K. Grove-Rasmussen, H. I. Jørgensen, M. Aagesen, C. B. Sørensen, P. E. Lindelof, K. Flensberg, and J. Nygård. Kondo-Enhanced Andreev Tunneling in InAs Nanowire Quantum Dots. *Phys. Rev. Lett.*, 99:126603, Sep 2007.

[194] A. Eichler, M. Weiss, S. Oberholzer, C. Schönenberger, A. Levy Yeyati, J. C. Cuevas, and A. Martín-Rodero. Even-Odd Effect in Andreev Transport through a Carbon Nanotube Quantum Dot. *Phys. Rev. Lett.*, 99:126602, Sep 2007.

[195] T. Dirks, T. L. Hughes, S. Lal, B. Uchoa, Y. F. Chen, C. Chialvo, P. M. Goldbart, and N. Mason. Transport through Andreev bound states in a graphene quantum dot. *Nature Phys.*, 7:386–390, 2011.

[196] L. Bretheau, Ç. Girit, H. Pothier, D. Esteve, and C. Urbina. Exciting Andreev pairs in a superconducting atomic contact. *Nature*, 499(7458):312, 2013.

[197] A. Yazdani, B. A. Jones, C. P. Lutz, M. F. Crommie, and D. M. Eigler. Probing the local effects of magnetic impurities on superconductivity. *Science*, 275(5307):1767–1770, 1997.

[198] M. Ruby, F. Pientka, Y. Peng, F. von Oppen, B. W. Heinrich, and K. J. Franke. Tunneling Processes into Localized Subgap States in Superconductors. *Phys. Rev. Lett.*, 115:087001, Aug 2015.

[199] M. Ruby, F. Pientka, Y. Peng, F. von Oppen, B. W. Heinrich, and K. J. Franke. End States and Subgap Structure in Proximity-Coupled Chains of Magnetic Adatoms. *Phys. Rev. Lett.*, 115:197204, Nov 2015.

[200] Z. Su, A. B. Tacla, M. Hocevar, D. Car, S. R. Plissard, E. P. A. M. Bakkers, A. J. Daley, D. Pekker, and S. M. Frolov. Andreev molecules in semiconductor nanowire double quantum dots. *Nature Communications*, 8:585, 2017.

[201] A. K. Geim, P. C. Main, N. La Scala, L. Eaves, T. J. Foster, P. H. Beton, J. W. Sakai, F. W. Sheard, M. Henini, G. Hill, and M. A. Pate. Fermi-edge singularity in resonant tunneling. *Phys. Rev. Lett.*, 72:2061–2064, Mar 1994.

[202] A. Martin-Rodero and A. Levy Yeyati. The Andreev states of a superconducting quantum dot: mean field versus exact numerical results. *Journal of Physics: Condensed Matter*, 24(38):385303, 2012.

[203] K. Grove-Rasmussen, G. Steffensen, A. Jellinggaard, M. H. Madsen, R. Zitko, J. Paaske, and J. Nygard. Yu-Shiba-Rusinov screening of spins in double quantum dots. *arXiv preprint arXiv:1711.06081*, 2017.

[204] C. Figgatt, A. Ostrander, N. M. Linke, K. A. Landsman, D. Zhu, D. Maslov, and C. Monroe. Parallel entangling operations on a universal ion-trap quantum computer. *Nature*, 572(7769):368–372, August 2019.

[205] P. Krantz, M. Kjaergaard, F. Yan, T. P. Orlando, S. Gustavsson, and W. D. Oliver. A quantum engineer's guide to superconducting qubits. *Applied Physics Reviews*, 6(2):021318, 2019.

[206] C. Kloeffel and D. Loss. Prospects for spin-based quantum computing in quantum dots. *Annu. Rev. Condens. Matter Phys.*, 4(1):51–81, 2013.

[207] T. Hyart, B. van Heck, I. C. Fulga, M. Burrello, A. R. Akhmerov, and C. W. J. Beenakker. Flux-controlled quantum computation with Majorana fermions. *Phys. Rev. B*, 88:035121, Jul 2013.

[208] T. Karzig, C. Knapp, R. M. Lutchyn, P. Bonderson, M. B. Hastings, C. Nayak, J. Alicea, K. Flensberg, S. Plugge, Y. Oreg, C. M. Marcus, and M. H. Freedman. Scalable designs for quasiparticle-poisoning-protected topological quantum computation with Majorana zero modes. *Phys. Rev. B*, 95:235305, Jun 2017.

[209] S. Plugge, A. Rasmussen, R. Egger, and K. Flensberg. Majorana box qubits. *New Journal of Physics*, 19(1):012001, 2017.

[210] J. P.T. Stenger, M. Hatridge, S. M. Frolov, and D. Pekker. Braiding quantum circuit based on the 4 π Josephson effect. *Physical Review B*, 99(3):035307, 2019.

[211] P. Krogstrup, N. L. B. Ziino, W. Chang, S. M. Albrecht, M. H. Madsen, E. Johnson, J. Nygård, C. M. Marcus, and T. S. Jespersen. Epitaxy of semiconductor–superconductor nanowires. *Nature Materials*, 14:400, 2015.

[212] A. Fornieri, A. M. Whiticar, F. Setiawan, E. Portolés, A. C. C. Drachmann, A. Keselman, S. Gronin, C. Thomas, T. Wang, R. Kallaher, et al. Evidence of topological superconductivity in planar Josephson junctions. *Nature*, 569(7754):89–92, Apr 2019.

[213] Ö. Gül, H. Zhang, F. K. de Vries, J. van Veen, K. Zuo, V. Mourik, S. Conesa-Boj, M. P. Nowak, D. J. van Woerkom, M. Quintero-Pérez, et al. Hard Superconducting Gap in InSb Nanowires. *Nano Letters*, 17(4):2690, 2017.

[214] L. J. Geerligs, V. F. Anderegg, J. Romijn, and J. E. Mooij. Single Cooper-pair tunneling in small-capacitance junctions. *Phys. Rev. Lett.*, 65:377–380, Jul 1990.

[215] M. T. Tuominen, J. M. Hergenrother, T. S. Tighe, and M. Tinkham. Experimental evidence for parity-based 2e periodicity in a superconducting single-electron tunneling transistor. *Phys. Rev. Lett.*, 69:1997–2000, Sep 1992.

[216] P. Lafarge, P. Joyez, D. Esteve, C. Urbina, and M. H. Devoret. Measurement of the even-odd free-energy difference of an isolated superconductor. *Phys. Rev. Lett.*, 70:994–997, Feb 1993.

[217] T. M. Eiles, J. M. Martinis, and M. H. Devoret. Even-odd asymmetry of a super-conductor revealed by the Coulomb blockade of Andreev reflection. *Phys. Rev. Lett.*, 70:1862–1865, Mar 1993.

[218] J. Shen, S. Heedt, F. Borsoi, B. van Heck, S. Gazibegovic, R. L. M. Op het Veld, D. Car, J. A. Logan, M. Pendharkar, S. J. J. Ramakers, et al. Parity transitions in the superconducting ground state of hybrid InSb-Al Coulomb islands. *Nature Communications*, 9(1):4801, November 2018.

[219] D. J. Carrad, M. Bjergfelt, T. Kanne, M. Aagesen, F. Krizek, E. M. Fiordaliso, E. Johnson, J. Nygård, and T. S. Jespersen. Shadow Epitaxy for In Situ Growth of Generic Semiconductor/Superconductor Hybrids. *Advanced Materials*, 32(23):1908411, Apr 2020.

[220] H. Pan and S. Das Sarma. Physical mechanisms for zero-bias conductance peaks in Majorana nanowires. *Phys. Rev. Research*, 2:013377, Mar 2020.

[221] K. Serniak, M. Hays, G. de Lange, S. Diamond, S. Shankar, L. D. Burkhart, L. Frunzio, M. Houzet, and M. H. Devoret. Hot Nonequilibrium Quasiparticles in Transmon Qubits. *Phys. Rev. Lett.*, 121:157701, Oct 2018.

[222] S. T. Gill, J. Damasco, B. E. Janicek, M. S. Durkin, V. Humbert, S. Gazibegovic, D. Car, E. P. A. M. Bakkers, P. Y. Huang, and N. Mason. Selective-Area Superconductor Epitaxy to Ballistic Semiconductor Nanowires. *Nano Letters*, 18(10):6121–6128, 2018.

[223] S. A. Khan, C. Lampadaris, A. Cui, L. Stampfer, Y. Liu, S. J. Pauka, M. E. Cachaza, E. M. Fiordaliso, J. Kang, S. Korneychuk, T. Mutas, J. E. Sestoft, F. Krizek, R. Tanta, M. C. Cassidy, T. S. Jespersen, and P. Krogstrup. Transparent Gatable Superconducting Shadow Junctions. *arXiv:2003.04487*, 2020.

[224] B. van Heck, A. R. Akhmerov, F. Hassler, and C. W. J. Beenakker. Coulomb-assisted braiding of Majorana fermions in a Josephson junction array. *New J. Phys.*, 14:035019, 2012.

[225] D. Aasen, M. Hell, R. V. Mishmash, A. Higginbotham, J.n Danon, M. Leijnse, T. S. Jespersen, J. A. Folk, C. M. Marcus, K. Flensberg, and J. Alicea. Milestones Toward Majorana-Based Quantum Computing. *Phys. Rev. X*, 6:031016, Aug 2016.

[226] Y. Xu, B. Yan, H. Zhang, J. Wang, G. Xu, P. Tang, W. Duan, and S. Zhang. Large-Gap Quantum Spin Hall Insulators in Tin Films. *Phys. Rev. Lett.*, 111:136804, Sep 2013.

[227] C. Xu, Y. Chan, Y. Chen, P. Chen, X. Wang, C. Dejoie, M. Wong, J. A. Hlevyack, H. Ryu, H. Kee, et al. Elemental Topological Dirac Semimetal: α-Sn on InSb(111). *Phys. Rev. Lett.*, 118:146402, Apr 2017.

[228] X. Zheng, J. Zhang, B. Tong, and R. Du. Epitaxial growth and electronic properties of few-layer stanene on InSb (1 1 1). *2D Materials*, 7(1):011001, oct 2019.

[229] R. F. C. Farrow, D. S. Robertson, G. M. Williams, A. G. Cullis, G. R. Jones, I. M. Young, and P. N. J. Dennis. The growth of metastable, heteroepitaxial films of α-Sn by metal beam epitaxy. *Journal of Crystal Growth*, 54(3):507–518, 1981.

[230] M. Bjergfelt, D. J. Carrad, T. Kanne, M. Aagesen, E. M. Fiordaliso, E. Johnson, B. Shojaei, C. J. Palmstrøm, P. Krogstrup, T. S. Jespersen, et al. Superconducting vanadium/indium-arsenide hybrid nanowires. *Nanotechnology*, 30(29):294005, 2019.

[231] N. A. Güsken, T. Rieger, P. Zellekens, B. Bennemann, E. Neumann, M. I. Lepsa, T. Schäpers, and D. Grützmacher. MBE growth of Al/InAs and Nb/InAs superconducting hybrid nanowire structures. *Nanoscale*, 9(43):16735–16741, 2017.

[232] T. Kanne, M. Marnauza, D. Olsteins, D. J. Carrad, J. E. Sestoft, J. de Bruijckere, L. Zeng, E. Johnson, E. Olsson, K. Grove-Rasmussen, and J. Nygård. Epitaxial Pb on InAs nanowires. *arXiv:2002.11641*, 2020.

[233] K. Zuo, V. Mourik, D. B. Szombati, B. Nijholt, D. J. van Woerkom, A. Geresdi, J. Chen, V. P. Ostroukh, A. R. Akhmerov, S. R. Plissard, et al. Supercurrent Interference in Few-Mode Nanowire Josephson Junctions. *Phys. Rev. Lett.*, 119:187704, Nov 2017.

[234] J. van Veen, A. Proutski, T. Karzig, D. I. Pikulin, R. M. Lutchyn, J. Nygård, P. Krogstrup, A. Geresdi, Leo P. Kouwenhoven, and John D. Watson. Magnetic-field-dependent quasiparticle dynamics of nanowire single-Cooper-pair transistors. *Phys. Rev. B*, 98:174502, Nov 2018.

[235] A. J. Annunziata, D. F. Santavicca, L. Frunzio, G. Catelani, M. J Rooks, A. Frydman, and D. E. Prober. Tunable superconducting nanoinductors. *Nanotechnology*, 21(44):445202, oct 2010.

[236] W. D. Oliver and P. B. Welander. Materials in superconducting quantum bits. *MRS Bulletin*, 38(10):816–825, 2013.

[237] E. Ginossar and E. Grosfeld. Microwave transitions as a signature of coherent parity mixing effects in the Majorana-transmon qubit. *Nature Communications*, 5(1):4772, September 2014.

[238] L. S. Bishop, E. Ginossar, and S. M. Girvin. Response of the Strongly Driven Jaynes-Cummings Oscillator. *Phys. Rev. Lett.*, 105:100505, Sep 2010.

[239] S. E. Nigg, H. Paik, B. Vlastakis, G. Kirchmair, S. Shankar, L. Frunzio, M. H. Devoret, R. J. Schoelkopf, and S. M. Girvin. Black-Box Superconducting Circuit Quantization. *Phys. Rev. Lett.*, 108:240502, Jun 2012.

[240] M. Hell, M. Leijnse, and K. Flensberg. Two-Dimensional Platform for Networks of Majorana Bound States. *Phys. Rev. Lett.*, 118:107701, Mar 2017.

[241] H. B. Heersche, P. Jarillo-Herrero, J. B. Oostinga, L. M. K. Vandersypen, and A. F. Morpurgo. Bipolar supercurrent in graphene. *Nature*, 446(7131):56–59, Mar 2007.

[242] K. Delfanazari, R. K. Puddy, P. Ma, T. Yi, M. Cao, Y. Gul, I. Farrer, D. A. Ritchie, H. J. Joyce, M. J. Kelly, and C. G. Smith. Proximity induced superconductivity in indium gallium arsenide quantum wells. *Journal of Magnetism and Magnetic Materials*, 459:282–284, August 2018.

[243] C. T. Ke, C. M. Moehle, F. K. de Vries, C. Thomas, S. Metti, C. R. Guinn, R. Kallaher, M. Lodari, G. Scappucci, T. Wang, et al. Ballistic superconductivity and tunable π–junctions in InSb quantum wells. *Nature Communications*, 10(1), Aug 2019.

[244] M. Kjaergaard, F. Nichele, H. J. Suominen, M. P. Nowak, M. Wimmer, A. R. Akhmerov, J. A. Folk, K. Flensberg, J. Shabani, C. J. Palmstrøm, and et al. Quantized conductance doubling and hard gap in a two-dimensional semiconductor–superconductor heterostructure. *Nature Communications*, 7(1), Sep 2016.

[245] W. Mayer, W. F. Schiela, J. Yuan, M. Hatefipour, W. L. Sarney, S. P. Svensson, A. C. Leff, T. Campos, K. S. Wickramasinghe, M. C. Dartiailh, I. Zutic, and J. Shabani. Superconducting proximity effect in InAsSb surface quantum wells with in-situ Al contact, 2019.

[246] F. Vigneau, R. Mizokuchi, D. C. Zanuz, X. Huang, S. Tan, R. Maurand, S. M. Frolov, A. Sammak, G. Scappucci, F. Lefloch, and et al. Germanium Quantum-Well Josephson Field-Effect Transistors and Interferometers. *Nano Letters*, 19(2):1023–1027, Jan 2019.

[247] N. W. Hendrickx, M. L. V. Tagliaferri, M. Kouwenhoven, R. Li, D. P. Franke, A. Sammak, A. Brinkman, G. Scappucci, and M. Veldhorst. Ballistic supercurrent discretization and micrometer-long Josephson coupling in germanium. *Phys. Rev. B*, 99:075435, Feb 2019.

[248] H. J. Suominen, M. Kjaergaard, A. R. Hamilton, J. Shabani, C. J. Palmstrøm, C. M. Marcus, and F. Nichele. Zero-Energy Modes from Coalescing Andreev States in a Two-Dimensional Semiconductor-Superconductor Hybrid Platform. *Phys. Rev. Lett.*, 119:176805, Oct 2017.

[249] H. D. Tong, H. V. Jansen, N. R. Tas, V. J. Gadgil, E. T. Carlen, and A. van den Berg. Simple Technique for Direct Patterning of Nanowires using a Nanoslit Shadow-Mask. In *TRANSDUCERS 2007 - 2007 International Solid-State Sensors, Actuators and Microsystems Conference*, pages 191–194, 2007.

[250] M. Pendharkar. *Molecular Beam Epitaxy of Low Dimensional Electron Systems for Topological Quantum Computation*. PhD thesis, University of California Santa Barbara, 2019.

[251] F. Krizek, T. Kanne, D. Razmadze, E. Johnson, J. Nygård, C. M. Marcus, and P. Krogstrup. Growth of InAs Wurtzite Nanocrosses from Hexagonal and Cubic Basis. *Nano Letters*, 17(10):6090–6096, 2017. PMID: 28895746.

[252] K. K. Likharev. Superconducting weak links. *Rev. Mod. Phys.*, 51:101–159, Jan 1979.

[253] I. O. Kulik and A. N. Omel'Yanchuk. Contribution to the microscopic theory of the Josephson effect in superconducting bridges. *Soviet Journal of Experimental and Theoretical Physics Letters*, 21:96, February 1975.

[254] S.N. Artemenko, A.F. Volkov, and A.V. Zaitsev. On the excess current in microbridges S-c-S and S-c-N. *Solid State Communications*, 30(12):771 – 773, 1979.

[255] G. Niebler, G. Cuniberti, and T. Novotn. Analytical calculation of the excess current in the Octavio–Tinkham–Blonder–Klapwijk theory. *Supercond. Sci. Technol*, 22:85016–7, 08 2009.

[256] N. M. Chtchelkatchev, W. Belzig, Yu. V. Nazarov, and C. Bruder. π-0 transition in superconductor-ferromagnet-superconductor junctions. *Journal of Experimental and Theoretical Physics Letters*, 74(6):323–327, Sep 2001.

[257] J. J. A. Baselmans, T. T. Heikkilä, B. J. van Wees, and T. M. Klapwijk. Direct observation of the transition from the conventional superconducting state to the π state in a controllable josephson junction. *Phys. Rev. Lett.*, 89:207002, Oct 2002.

[258] S. M. Frolov, D. J. Van Harlingen, V. A. Oboznov, V. V. Bolginov, and V. V. Ryazanov. Measurement of the current-phase relation of superconductor/ferromagnet/superconductor π josephson junctions. *Phys. Rev. B*, 70:144505, Oct 2004.

[259] M. J. A. Stoutimore, A. N. Rossolenko, V. V. Bolginov, V. A. Oboznov, A. Y. Rusanov, D. S. Baranov, N. Pugach, S. M. Frolov, V. V. Ryazanov, and D. J. Van Harlingen. Second-harmonic current-phase relation in josephson junctions with ferromagnetic barriers. *Phys. Rev. Lett.*, 121:177702, Oct 2018.

[260] C. Vanneste, C. C. Chi, W. J. Gallagher, A. W. Kleinsasser, S. I. Raider, and R. L. Sandstrom. Shapiro steps on current-voltage curves of dc SQUIDs. *Journal of Applied Physics*, 64(1):242–245, 1988.

[261] J. Wiedenmann, E. Bocquillon, R. S. Deacon, S. Hartinger, O. Herrmann, T. M. Klapwijk, L. Maier, C. Ames, C. Brune, C. Gould, A. Oiwa, K. Ishibashi, S. Tarucha, H. Buhmann, and L. W. Molenkamp. 4π-periodic Josephson supercurrent in HgTe-based topological Josephson junctions. *Nature Communications*, 7:10303, 2016.

[262] D. Laroche, D. Bouman, D. J. van Woerkom, A. Proutski, C. Murthy, D. I. Pikulin, C. Nayak, R. J. J. van Gulik, J. Nygård, P. Krogstrup, et al. Observation of the 4π-periodic Josephson effect in indium arsenide nanowires. *Nature communications*, 10(1):245, 2019.

[263] M. C. Dartiailh, J. J. Cuozzo, W. Mayer, J. Yuan, K. S. Wickramasinghe, E. Rossi, and J. Shabani. Missing shapiro steps in topologically trivial josephson junction on inas quantum well. *arXiv:2005.00077*, 2020.

[264] S. Conesa-Boj, A. Li, S. Koelling, M. Brauns, J. Ridderbos, T. T. Nguyen, M.A. Verheijen, P.M. Koenraad, F. A. Zwanenburg, and Erik P.A.M. Bakkers. Boosting Hole Mobility in Coherently Strained [110]-Oriented Ge-Si Core-Shell Nanowires. *Nano letters*, 17(4):2259–2264, 4 2017.

[265] M. Brauns, J. Ridderbos, A. Li, W. G. van der Wiel, E. P. A. M. Bakkers, and F. A. Zwanenburg. Highly tuneable hole quantum dots in Ge-Si core-shell nanowires. *Applied Physics Letters*, 109(14):143113, 2016.

[266] F. N. M. Froning, M. K. Rehmann, J. Ridderbos, M. Brauns, F. A. Zwanenburg, A. Li, E. P. A. M. Bakkers, D. M. Zumbühl, and F. R. Braakman. Single, double, and triple quantum dots in Ge/Si nanowires. *Applied Physics Letters*, 113(7):073102, 2018.

[267] F. N. M. Froning, M. J. Rančić, B. Hetényi, S. Bosco, M. K. Rehmann, A. Li, E. P. A. M. Bakkers, F. A. Zwanenburg, D. Loss, D. M. Zumbühl, and F. R. Braakman. Strong spin-orbit interaction and g-factor renormalization of hole spins in Ge/Si nanowire quantum dots. *arXiv:2007.04308*, 2020.

[268] X. Zhang, W. Jevasuwan, Y. Sugimoto, and N. Fukata. Controlling Catalyst-Free Formation and Hole Gas Accumulation by Fabricating Si-Ge Core-Shell and Si-Ge-Si Core-double shell Nanowires. *ACS Nano*, 13(11):13403–13412, 2019.

[269] G. Scappucci, C. Kloeffel, F. A. Zwanenburg, D. Loss, M. Myronov, J. Zhang, S. De Franceschi, G. Katsaros, and M. Veldhorst. The germanium quantum information route, 2020.

[270] P. Yu, J. Chen, M. Gomanko, G. Badawy, E. P. A. M. Bakkers, K. Zuo, V. Mourik, and S. M. Frolov. Non-Majorana states yield nearly quantized conductance in superconductor-semiconductor nanowire devices. *arXiv:2004.08583*, 2020.

[271] D. Pekker and S. M. Frolov. Andreev Blockade in a Double Quantum Dot with a Superconducting Lead. *arXiv:1810.05112*, 2018.

[272] M. Hays, V. Fatemi, K. Serniak, D. Bouman, S. Diamond, G. de Lange, P. Krogstrup, J. Nygård, A. Geresdi, and M. H. Devoret. Continuous monitoring of a trapped superconducting spin. *Nature Physics*, Jul 2020.

[273] M. Pita-Vidal, A. Bargerbos, C. Yang, D. J. van Woerkom, W. Pfaff, N. Haider, P. Krogstrup, L. P. Kouwenhoven, G. de Lange, and A. Kou. A gate-tunable, field-compatible fluxonium. *arXiv:1910.07978*, 2019.